LITHOGEOCHEMICAL FOOTPRINT OF ALTERATION AND MINERALIZATION AT THE MESKAN PB-ZN DEPOSIT (HAKKARI, SOUTHEAST ANATOLIA)

A THESIS SUBMITTED TO
THE GRADUATE SCHOOL OF NATURAL AND APPLIED SCIENCES
OF
MIDDLE EAST TECHNICAL UNIVERSITY

BY

GÖKSU KARATAŞ

IN PARTIAL FULFILLMENT OF THE REQUIREMENTS
FOR
THE DEGREE OF MASTER OF SCIENCE
IN
GEOLOGICAL ENGINEERING

APRIL 2024

Approval of the thesis:

LITHOGEOCHEMICAL FOOTPRINT OF ALTERATION AND MINERALIZATION AT THE MESKAN PB-ZN DEPOSIT (HAKKARI, SOUTHEAST ANATOLIA)

submitted by **GÖKSU KARATAŞ** in partial fulfillment of the requirements for the degree of **Master of Science** i**n Geological Engineering, Middle East Technical University** by,

Prof. Dr. Naci Emre Altun

Dean, **Graduate School of Natural and Applied Sciences** _____

Prof. Dr. Erdin Bozkurt

Head of the Department, **Geological Engineering, METU** _____

Assist. Prof. Dr. Ali İmer

Supervisor, **Geological Engineering, METU** _____

Examining Committee Members:

Prof. Dr. Kaan Sayıt

Geological Engineering, METU _____

Assist. Prof. Dr. Ali İmer

Supervisor, Geological Engineering, METU _____

Assoc. Prof. Dr. Fatma Toksoy Köksal

Geological Engineering, METU _____

Prof. Dr. Tolga Oyman

Geological Engineering, Dokuz Eylül University _____

Prof. Dr. Halim Mutlu

Geological Engineering, Ankara University _____

Date: 26.04.2024

I hereby declare that all information in this document has been obtained and presented in accordance with academic rules and ethical conduct. I also declare that, as required by these rules and conduct, I have fully cited and referenced all material and results that are not original to this work.

Name, Last name: Göksu Karataş

Signature:

ABSTRACT

LITHOGEOCHEMICAL FOOTPRINT OF ALTERATION AND MINERALIZATION AT THE MESKAN PB-ZN DEPOSIT (HAKKARI, SOUTHEAST ANATOLIA)

Karataş, Göksu
Master of Science, Geological Engineering
Supervisor: Assoc. Dr. Ali İmer

April 2024, 139 pages

The Meskan carbonate-hosted Pb-Zn deposit, located in the Hakkari district in SE Anatolia, formed along the northern passive margin of the Arabian Platform. The predominant components of the host rocks consist primarily of carbonate micrite mudstones and claystones, with a lesser proportion of interlaminated grainstone-mudstone formations. These rock units are mainly composed of calcite, with dolomite present in smaller quantities. Additionally, hydrothermal processes have influenced these rocks, resulting in the alteration and partial replacement of calcite and dolomite by sulfides, barite, and carbonates (predominantly calcite). Banded dolomitic alteration (zebra dolomite) and dolomite-matrix breccias are associated with mineralization. The sulfide mineralization is characterized primarily by very fine to medium-grained pyrite dominance, along with sphalerite, galena and marcasite. Mineralization textures are mostly massive, disseminated, interbeds and banded zebra texture, brecciated, and colloform banding, and recrystallization textures. Additionally, recrystallization textures with cataclastic deformation and framboidal pyrite are observed in thin and polished sections.

In this study, a detailed lithogeochemical characterization of the stratigraphic units including the mineralized levels at Meskan was attempted. For this purpose a total of 439 drill core samples were analyzed for their major, minor, and trace element compositions (including total C and S) through ICP-ESMS and XRF methods. Based on their lithogeochemical characteristics, these samples were classified into five chemostratigraphic packages, in which Zn-Pb mineralization appears to be hosted by relatively pure carbonate rocks with low siliciclastic contents. Both petrography and XRD analysis of host rock samples demonstrate that dolomite is present only in small amounts within the altered and mineralized rocks. It occurs locally as a hydrothermal replacement phase within rocks exhibiting zebra-like textures. Dolomitization is not play a significant role in the Meskan succession. The ore host rocks exhibit a relatively lower amount of organic material compared to the surrounding strata.

Lithogeochemical analysis including with carbon and sulfur analysis and provide critical insights into the geological and mineralogical characteristics of the Meskan deposit and establishment of relationships between rock geochemical signatures and mineralization. Contents of SiO_2, Al_2O_3, K_2O, TiO_2, and most of the trace elements content are depleted in the main mineralized zone, whereas As, Cd, CaO, Fe_2O_3, Ge, Sb, Pb, Tl, and Zn values are enriched in these zone. Lack amount of HFSE may imply that these carbonates are mostly pure and depleted in silt amount. Cs is found to be enriched in pyrite, sphalerite, galena samples with respect to barren (but pyritic) zebra carbonates in main sulfide mineralization zone. The REE values demonstrate that the carbonates of Meskan deposit in main mineralized zone possess high Eu/ Eu* ratio (avg= 0.27), and low Ce/ Ce* ratio (avg= 1.78). The contrast values between Eu and Ce concludes that the characterisation of mineralized unit in Meskan deposit is controlled by detrital input and this unit is depleted in clastic sediments with respect to other units.

Keywords: Meskan deposit, Hakkari, carbonate-hosted Pb-Zn, lithogeochemistry

ÖZ

MESKAN PB-ZN YATAĞINDA ALTERASYON VE CEVHERLEŞMENİN LİTOJEOKİMYASAL AYAK İZLERİ (HAKKARİ, GÜNEYDOĞU ANADOLU)

Karataş,Göksu
Yüksek Lisans, Jeoloji Mühendisliği
Tez Yöneticisi: Dr. Öğr. Üyesi Ali İmer

Nisan 2024, 139 sayfa

Karbonatlarla ilişkili olarak gelişmiş bir Pb-Zn yatağı olan Meskan, GD Anadolu'daki Hakkari maden bölgesinde, tektonik olarak Arap Platformu'nun kuzey pasif kenarında yer almaktadır. Ana kayaların baskın bileşenleri çoğunlukla karbonat mikrit çamurtaşları ve kiltaşlarıdır; yer yer danetaşı-kiltaşı formasyonları bulunmaktadır. Bu kaya birimleri genellikle kalsit içerirken, daha az miktarda dolomit bulunmaktadır. Ayrıca, hidrotermal süreçler bu kayaları etkilemiş, kalsit ve dolomitin kısmi olarak sülfürler, baritler ve karbonatlar (genellikle kalsit) tarafından değiştirilmesine neden olmuştur. Zebra bantlı dolomitik alterasyon ve dolomit-matriks breşler mineralizasyon ile ilişkilendirilmiştir. Sülfür mineralizasyonu, çok ince ve orta taneli pirit baskınlığı ile karakterize olup; sfalerit, galen ve markazit ile birlikte bulunmaktadır. Mineralizasyon dokuları genellikle kütlesel, yayılmış, aralıklar ve bantlı zebra doku, breşli ve kolloform bantlama ve yeniden kristalleşme dokularından oluşmaktadır. Ayrıca, incelenen ince ve cilalanmış kesitlerde kataklastik deformasyon ve çerçevesi pirit ile yeniden kristalleşme dokuları gözlemlenmiştir.

Bu çalışmada, Meskan'daki mineralleşmiş seviyeler de dahil olmak üzere stratigrafik birimlerin detaylı bir litokimyasal karakterizasyonu ortaya çıkarılmaya çalışılmıştır. Bu amaçla, toplam 439 kuyu çekirdeği örneği, ICP-ESMS ve XRF yöntemleriyle ana, minör ve iz element bileşimleri (toplam C ve S dahil) açısından analiz edilmiştir. Litojeokimyasal özelliklerine dayanarak, bu örnekler beş kemostratigrafik pakette sınıflandırılmış; Zn-Pb mineralleşiminin, düşük silisiklastik içeriğe sahip nispeten saf karbonat kayalar tarafından barındırıldığı gözlemlenmiştir. Ana kaya örneklerinin petrografisi ve XRD analizi, dolomitin değiştirilmiş ve mineralleşmiş kayaçlarda yalnızca az miktarda bulunduğunu göstermektedir. Bu, zebra benzeri dokular sergileyen kayalar içinde, hidrotermal bir değişim evresi olarak lokal olarak meydana gelmiştir. Dolomitleşme, Meskan'da önemli bir rol oynamamaktadır. Cevher ana kayaçları, çevredeki kaya tabakalarına göre organik madde açısından nispeten daha azdır.

Karbon ve kükürdün yanı sıra litokimyasal analizler, Meskan yatağının jeolojik ve mineralojik özelliklerini ve kayaç litokimyasal imzaları ile mineralizasyon arasındaki ilişkilerin belirlenmesine kritik bir katkı sağlamaktadır. SiO_2, Al_2O_3, K_2O, TiO_2 ve iz elementlerin çoğunluğu, ana mineralize zonun içinde tükenmiştir; As, Cd, CaO, Fe_2O_3, Ge, Sb, Pb, Tl ve Zn değerleri ise bu bölgede zenginleştirilmiştir. HFSE'nin az miktarı, bu karbonatların genellikle saf olduğunu ve alüvyon miktarında tükenmiş olduğunu gösterebilir. Cs, ana sülfür mineralleşme zonunda, verimsiz (ancak piritli) zebra karbonatlarına kıyasla pirit, sfalerit ve galenit örneklerinde zenginleşmiş olarak bulunmuştur. NTE değerleri, Meskan yatağındaki ana mineralize zonun karbonatlarının yüksek Eu/Eu* oranına (ortalama=0.27) ve düşük Ce/Ce* oranına (ortalama=1.78) sahip olduğunu göstermektedir. Eu ve Ce arasındaki zıtlık değerleri, Meskan yatağındaki mineralize birimin, alüvyon girişimine bağlı olduğunu ve bu birimin diğer birimlere göre klasik tortular açısından tükenmiş olduğunu sonuçlandırmıştır.

Anahtar Kelimeler: Meskan yatağı, Hakkari, karbonat barındıran Pb-Zn, litojeo kimya

To My Family

ACKNOWLEDGMENTS

First of all, I would like to thank Assist. Prof. Dr. Ali İmer, my advisor, in particular for his advice, encouragement, support, criticis, and insight not only throughout thesis study, but also throughout my entire career. I appreciate his patience and the amount of time he spent providing advice and mentorship to me.

I am appreciative to Dr. Mustafa Yücel Kaya for providing background petrographic information on carbonate rocks.

Additionally, I would like to express my gratitude to First Quantum Minerals for permission for Meskan project. I special express my thanks to Tim Ireland, the Principal Exploration Geologist, for his all-endless support and comments. Gökhan Okan Yıldız, the District Geologist of the exploration department, his critical interpretation and insights, and were instrumental in directing this project.

I want to express my gratitude to Müge Gürgen, close friend, always supported me and guided me down this path from start to finish.

I would like to thank Seher Elmacı, all kept me positive and sane throughout this process and helping GIS and database studies.

I special thank my colleagues who are Ali Gökmen, Taylan, Muzaffer, Barış, and Finlay for their help during the data interpretation and field studies.

I would like to thank my assistances Akın Çil, Taner Tekin, Atilla Kılıç, and Devin Aykasım for their endless support and always answering my questions.

Last but certainly not least, I am really grateful to my family for their unwavering trust, faith, perseverance, and unadulterated love motivated me to finish this thesis. Without their affection and support, I could not have completed this thesis.

TABLE OF CONTENTS

ABSTRACT v

ÖZ vii

ACKNOWLEDGMENTS x

TABLE OF CONTENTS xi

LIST OF TABLES xiii

LIST OF FIGURES xiv

CHAPTERS

1 INTRODUCTION 1

1.1 Purpose and Scope 1

1.2 Methodology 7

1.2.1 Sampling criteria 7

1.2.2 Lithogeochemical analyses 8

1.2.3 Petrography 9

1.3 Sediment-hosted Pb-Zn deposits 10

2 GEOLOGY OF THE SOUTHEASTERN ANATOLIA 15

2.1 Regional Geological Setting 15

2.2 The geological framework of the Southeast Anatolian Orogenic Belt 16

2.3 Regional Stratigraphy of the Arabian Platform in SE Anatolia 19

3 DEPOSIT GEOLOGY 23

3.1 Introduction 23

3.2 Meskan Stratigraphy 24

3.2.1 Permian Group 25

3.2.2 Lower Çığlı Group....26
3.2.3 Middle Çığlı Group....27
3.2.4 Upper Çığlı Group....28
3.2.5 Lower Çanaklı Formation....29
3.2.6 Middle Çanaklı Formation....33
3.2.7 Upper Çanaklı Formation....35
3.3 The Meskan Zn-Pb Mineralization....36
3.3.1 Exploration history....36
3.4 Petrographic Studies....40
3.4.1 Microscopic Features of the Host Rock....40
3.4.2 Sulfide Mineralization and Ore Paragenesis....43
3.5 Lithogeochemistry....49
3.5.1 Geochemical characterization of lithostratigraphic units....49
4 DISCUSSION....97
4.1 Discussion....97
4.2 Comparison between lithogeochemical and pXRF data....108
5 CONCLUSION....119
REFERENCES....123
APPENDICES
A. XRD Analysis Results....136

LIST OF TABLES

TABLES

Table 1.1 Carbonate-hosted Pb-Zn deposits in Hakkari region (from Hanilçi and Öztürk, 2008; Santoro et al., 2013; Hanilçi et al., 2019; Karakaya Co., 2015). 6
Table 3.1 Analysis method for measured elements 49
Table 3.2 Major oxide concentrations as well as TOT/S and TOT/C values (in percentages) for each chemostratigraphic package 56
Table 3.3. HFSE, W, Mo, and Sc concentrations of all chemostratigraphic packages (n= 439). 69
Table 3.4. Total LREE, HREE, and total REE concentrations as well as Eu, Eu/ Eu* and Ce, Ce/ Ce* values of different chemostratigraphic packages 81
Table 3.5. Correlation matrix of selected major, minor, and trace elements for package 3 samples. Highly correlated elements are highlighted with green 92
Table 4.1 Measured elements in portable XRF (pXRF) 108
Table 4.2. Statistical values of major elements measured by pXRF for each package 110
Table 5.1. Suite of elements showing enrichment in each of the MVT, SEDEX, and Irish-type deposits, and in the Meskan deposit (average data for various deposit types from Wilkinson, 2014). 121

LIST OF FIGURES

FIGURES

Figure 1.1. Sketch view showing geological settings of SEDEX, MVT, and Irish-type Pb-Zn deposit in marine environment (redrawn after Kesler and Reich, 2006). 11
Figure 1.2. The Carboniferous timeline of key geological events that affected the Irish Midlands Basin (Hnatyshin et al., 2015; Wilkinson and Hitzman, 2015). 12
Figure 2.1. Map showing the main tectonic fragments and the bounding suture zones in Anatolia and in the surrounding region (Okay and Tüysüz, 1999).....15
Figure 2.2. Regional geological map of the Southeast Anatolian Orogenic Belt (after Yiğitbaş and Yılmaz, 1996a, 1996b). 17
Figure 2.3. Cross-sectional sketch showing relationship between various tectonostratigraphic units within the SEAOB (Yılmaz et al., 2022). 17
Figure 2.4. The generalized stratigraphic columnar section of the Hakkari area and the stratigraphic positions the of Pb-Zn deposits of the Hakkari district (simplified after Hanilçi, 2020). 21
Figure 2.5. Generalized stratigraphic section of the Arabian Platform in southeastern Anatolia, showing nappe zones, the formations and ages of the rock units (from Perinçek et al., 2018). 22
Figure 3.1. Google Earth view of the Meskan region showing Meskan West sector as well as the Şaho underground gallery of the Ölmezler Mining to the north of the Zap River. 23
Figure 3.2. Geological map and cross-section showing stratigraphic position of the Meskan, Üzümcü, and Karakaya carbonate-hosted Zn-Pb deposits (Hanilçi et al., 2020). 24
Figure 3.3. Shallowly-dipping limestones of the Permian Group (unpublished company report; Akın, 2023). 25
Figure 3.4. a-b) The characteristic texture (pitted texture?) of the dark grey to black colored limestones of the Permian Group (drill hole MS22DD029, 1676.80 m). ..26

Figure 3.5. a) Light green to grey colored laminated and bedded claystone with medium size calcite nodules in Lower Çığlı Group (drill hole MS22DD029, 1462.40 m) b) Bottom of the Lower Çığlı Group shows thinly bedded limestones with styloliths (drill hole MS22DD029, 1620 m). 27
Figure 3.6. a) The characteristic reddish-pinkish, thinly-bedded, fine-grained, lime mudstone layers of the Middle Çığlı Group on (drill hole MS22DD029, 1338 m), b) Bedding-parallel calcite cross-cutting green to reddish-pinkish claystone/mudstone (drill hole MS22DD029, 1361.40 m), c) Reddish-pinkish, thinly-bedded mudstone/ claystone (drill hole MS22DD029, 1310 m). 28
Figure 3.7. a) Thick carbonate vein in thinly-laminated grey-black limestone (drill hole MS22DD029, 1024 m), b) Greyish to black, millimetric to medium darker multiple limestone bands in the middle part of the Upper Çığlı Group (drill hole MS22DD029, 1029–1031 m), c) Massive, fine-grained dolostone at the upper levels of the Upper Çığlı Group (drill hole MS22DD029, 982–984 m)..... 29
Figure 3.8. Outcrop and drill core photographs of units of the Lower Çanaklı Formation. a) Intercalations of thin- to medium-bedded dark-grey limestone, b) sedimentary microbreccia, c) Thinly-laminated, fine-grained limestone (CSA unpublished report, 2020), d) Calcite-cemented vein breccia (drill hole MS23DD062-A), e) Black matrix float breccia with angular fragments (drill hole MSUGDD0003). 31
Figure 3.9. Black matrix sedimentary breccia in Lower Çanaklı Formation (drill hole MS22DD029, 903.50–906.20 m)..... 32
Figure 3.10. Dark grey to black colored, fractured, fine-grained carbonaceous limestone with irregular crackled calcite vein(let)s in the top of the Lower Çanaklı Formation (drill hole MS22DD029, 633.70–641.00 m and 598.90–601.25m). 32
Figure 3.11. a) Multiple gossanous horizons within the Middle Çanaklı Formation, with the main mineralized horizon. The prominent limestone outcrop in the ridge above the workings comprises rocks of the Middle Çanaklı Formation, b) Upper part of the Middle Çanaklı Formation showing its thinly-bedded texture with gossan layers (unpublished company report, 2020). 34

Figure 3.12. Black-colored, carbonaceous limestones with pyritic shale units (drill hole MSUGDD0023). 34
Figure 3.13. a) Barren, banded dolomite layers showing characteristic zebra texture (drill hole: MSUGDD012; 252.35 m), (b–d) Pyrite replacement of fine-grained dolomite layers in zebra-textured carbonate units of the Middle Çanaklı Formation (drill holes: MSUGDD017; 296.70 m and MSUGDD023; 247.00 m). 35
Figure 3.14. Drill core photographs of zebra textured sulfide-rich ore a) Pyrite-only semi-massive sulfide mineralization, b) Alternating bands of pyrite and calcite layers are discontinuous due to folding and local brecciation, c) Banded ore that has undergone folding and faulting, d) Bedded and layered pyrite in carbonaceous limestone (drill hole MSUGDD0035). 37
Figure 3.15. The locations of the Meskan Tepe, Meskan West, and Şaho Gallery ore zones (image looking north). Traces of studied drill holes are also shown. 38
Figure 3.16. a) View of the Meskan Tepe ore zone (looking east), b) Close-up view from irregular oxide mineralization at the northern part of Meskan Tepe. 39
Figure 3.17. Representative macro- and microphotographs of carbonaceous limestone with calcite vein (drill hole MSUGDD0025, 490.40 m). a) Macrophotograph of banded, grey- to black-colored carbonate rock. Black layers are made up of very fine-grained, micritic calcite, whereas grey layers are dominated by dolomite. Hydrothermal sparry calcite veins (white) cross-cut the original lamination, b) Microphotograph of repetitive layers of dolomite and micritic layer with sparry calcite (XPL, TL), c) Dolomitic and micritic layer includes sparry calcite at the edge of the microphotography (XPL, TL), d) Brecciated layers of coarser, dolomite-rich and micritic calcite-rich layers partly replaced by coarse-grained hydrothermal calcite (XPL, TL). 41
Figure 3.18. Macrophotograph of finely-laminated carbonaceous limestone of the Lower Çanaklı Formation (drill hole: MSUGDD0025, 423.85 m), b) Microphotograph of sparry calcite (XPL, TL), c) Microphotograph of repetitive succession of dolomitic layer and micritic layer that rich in organic carbon (XPL, TL). 42

Figure 3.19. Macrophotograph of bedded carbonaceous limestone in Lower Çanaklı Formation (drill hole: MSUGDD0025, 408.50 m), b) Microphotograph of repetitive succession of dolomitic layer and micritic layer with rich in dark-colored graphite consists of stylolite (XPL, TL). 42
Figure 3.20. a) Grey to beige, latte colored colloform-banded sphalerite, b-c) Banded pyrite and sphalerite in semi-massive sulfide mineralization, d) Color variation (latte and red-brown) in sphalerite (drill hole MSUGDD0023, 373 m). . 43
Figure 3.21. a) Hand specimen photograph of dark colored, organic-rich, carbonaceous limestone with calcite-dolomite vein (drill hole: MSUGDD0025, 306.50 m), b) Microphotograph of very fine-grained diagenetic pyrite (RL, PPL). 44
Figure 3.22. Representative hand specimen images and microphotographs of sulfide mineralization at Meskan. a) Hand specimen photograph of colloform-banded, latte-colored sphalerite with pyrite and sparry calcite layers (drill hole: MSUGDD0025, 291.85 m), b) Microphotograph of cataclasized and locally recrystallized fine-grained pyrite (py-IV) alongside sphalerite (sph-II), and galena (gn-II?) (XPL, RL), (c) Microphotograph of banded pyrite (py-III), sphalerite (sph-II), galena (gn-I) ore that has been intensely fractured and cataclastic pyrite, botryoidal? sphalerite and galena (XPL, RL), d) Moderate to highly deformed pyrite with marcasite inside the pyrite, fine grained galena and sphalerite (XPL, RL), e) Sphalerite at the edge of pyrite (pyIII) (XPL, RL), f) Colloform-banded layers of sphalerite (sph-I) and very fine-grained pyrite (py-II) surrounded by a paragenetically later generation of pyrite (py-III) (XPL, RL). 46
Figure 3.23. a) Hand specimen photograph of zebra-textured pyrite, in which alternating bands of pyrite, organic-rich limestone (black), and white, sparry calcite are visible. Sparry calcite veins also cross-cut the banding (drill hole: MSUGDD0025, 203.45 m), b) Intensely deformed, cataclastic pyrite (XPL, RL), c) Hand specimen of zebra textured, with tiny pyrite (drill hole: MSUGDD0025, 303.90 m), d) Very fine to medium grained pyrite, cataclastic marcasite, and sphalerite (XPL, RL)..... 47

Figure 3.24. Representative hand specimen images and microphotographs of sulfide mineralization. a) Hand specimen photograph of pyrite, calcite vein from carbonaceous limestone (drill hole: MSUGDD0025, 281.40 m), b) Microphotograph of pyrite (py-III), sphalerite (sph-II), galena (gn-II) (XPL, RL), c) Galena at the edge of sphalerite (sph-II) that surrounds pyrite (py-III), d) Fine-grained pyrite (py-III) with marcasite surrounded by sphalerite (sph-III) (XPL, RL), e) Moderately deformed pyrite (py-IV) with fine grained sphalerite (sph-II) (XPL, RL), f) Well-developed sphalerite inside the pyrite (XPL, RL). 48
Figure 3.25. Binary plots of CaO against (a) MgO, (b) SiO_2, (c) Al_2O_3, and (d) K_2O (in percentages) used to discriminate between different lithological units at Meskan. 51
Figure 3.26. CaO versus CaO_SF (sulfide-free; in percentages) plots used to distinguish between lithologies (up) and stratigraphic packages (down). There is a good correlation between most lithologies and identified packages except for samples from the mineralized unit. Mineralized unit samples are scattered outside the general linear trend defined by samples from the non-mineralized levels. 53
Figure 3.27. Downhole plots showing the variation of CaO and MgO (in percentages) for each package in the studied drill holes MS22DD021, MS22DD029, MS22DD030, and MSUGDD0025. 54
Figure 3.28. Downhole plots showing the variation (in percentages) of MnO (black line) and Fe_2O_3 (red line) for each package through four drill holes. 55
Figure 3.29. Downhole plots of drill hole MS22DD029 showing the variation in SiO_2 (in percentages) for each chemostratigraphic package and lithology. 57
Figure 3.30. Downhole plots showing variation of major oxide contents (in in percentages) in identified packages and lithological units in drill hole MS22DD021. Colored bars to the left represent different lithologies, whereas the ones to the right represent chemostratigraphic packages. 62
Figure 3.31. Downhole plots showing variation of major oxide contents (in percentages) in identified packages and lithological units in drill holes 30. Colored

bars to the left represent different lithologies, whereas the ones to the right represent chemostratigraphic packages. 63
Figure 3.32. Downhole plots showing variation in Al_2O_3 concentrations (in percentages) for each chemostratigraphic package in all drill holes. 64
Figure 3.33. CaO_SF (sulfide-free) versus Fe_2O_3 (up) and MnO (down) plots (in percentages) showing deviation of package 3 samples from the rest of the chemostratigraphic packages. 66
Figure 3.34. Downhole plots showing variation of major oxide contents (in percentages) in identified packages in drill hole MS22DD029 68
Figure 3.35. Downhole plots showing variation in HFSE concentrations (in ppm) in drill hole MS22DD021. 70
Figure 3.36. Downhole plots showing variation in HFSE concentrations (in ppm) in drill hole MS22DD029. 70
Figure 3.37. Downhole plots showing variation in HFSE concentrations (in ppm) in drill hole MS22DD030. 71
Figure 3.38. Downhole plots showing variation in HFSE concentrations (in ppm) in drill hole MSUGDD0025. 71
Figure 3.39. Binary plots showing variation in TiO_2 (in percentages) against Hf, Zr, Ta and Nb (in ppm) for each package through four drill holes. 74
Figure 3.40. Downhole plots showing variation in Ba and Sr concentrations (in ppm) in drill holes MS22DD021, MS22DD029, MS22DD030, and MSUGDD0025. 77
Figure 3.41. Downhole plots showing variation in Rb and Cs concentrations (in ppm) in drill holes MS22DD021, MS22DD029, MS22DD030, and MSUGDD0025. 78
Figure 3.42. Bivariate graphs of Rb and Cs (in ppm) for each chemostratigraphic package (above) and rock type (below). 79
Figure 3.43. Chondrite-normalized REE plot showing average REE contents for each lithological unit (normalization values after Boynton, 1984). Higher levels of enrichment in REEs is due to higher silt content. 80

Figure 3.44. Chondrite-normalized REE plots of samples from packages 1, 2, 4, and 5. Lines with heavier stroke represents the mean REE concentrations (in ppm) of all samples from each of the packages 1, 2, 4, and 5. Normalization values are from Boynton (1984). 82
Figure 3.45. Downhole plots showing variation in Eu/Eu* ratios for each lithology (above) and for each chemostratigraphic package (below). 83
Figure 3.46. Chondrite-normalized REE plot of samples from package 3. Green line with a heavier stroke represents the mean REE concentrations of all package 3 samples. Normalization values are from Boynton (1984). 84
Figure 3.47. Chondrite-normalized REE plot of samples from all lithological units. Lines with heavier stroke represents the mean REE concentrations (in ppm) of all samples from each different lithology. Normalization values are from Boynton (1984). 85
Figure 3.48. Downhole plots of Ag and Hg (in ppm) in drill holes MS22DD029, MS22DD030, and MSUGDD0025 87
Figure 3.49. Downhole plots showing variations in Co and Cu concentrations (in ppm) in drill holes MS22DD021, MS22DD029, and MS22DD030 88
Figure 3.50. Downhole plots showing the variation of Mo and V (in ppm) for each package in the studied drill holes MS22DD021, MS22DD029, MS22DD030, and MSUGDD0025. 89
Figure 3.51. Downhole plots showing the variation of Cd and Zn (in ppm) for each package in the studied drill holes MS22DD021, MS22DD029, MS22DD030, and MSUGDD0025. 90
Figure 3.52. Bivariate plots showing the variation of TOT/S versus Fe_2O_3, MnO (in percentage), Pb, and Zn (in ppm) graphs for each package in all drill holes. 93
Figure 3.53. Downhole plots showing the variation of As, Tl, and Sb (in ppm) for each package in the studied drill holes MS22DD021, MS22DD029, MS22DD030, and MSUGDD0025. 94
Figure 3.54. Downhole and bivariate plots showing the variation of Ge (in ppm) for package 3 in drill hole MSUGDD0025. 94

Figure 3.55. Downhole plots showing the variation of Se (in ppm) for each package in the studied drill holes MS22DD021, MS22DD029, MS22DD030, and MSUGDD0025. 95
Figure 3.56. Downhole plots showing variation of Ag, Co, Cu, Cd, Zn, and Hg (in ppm) in identified packages in drill hole MS22DD029. 96
Figure 4.1. $(Ce/Ce^*)_N$ versus $(Pr/Pr^*)_N$ graph on all lithological samples (Bau and Dulski (1996)..... 103
Figure 4.2. Downhole plots showing variation in Ni and V concentrations (in ppm) in drill holes MS22DD021, MS22DD029, MS22DD030, and MSUGDD0025. .. 107
Figure 4.3. Downhole plots showing variation in pXRF Ca and Mg concentrations (in ppm) for each package through four drill holes. 109
Figure 4.4. Downhole plots showing pXRF readings (left) and lithogeochemical analysis results (right) for Zr and Nb (in ppm) in all drill holes. 112
Figure 4.5. Downhole plots showing pXRF readings (above) and lithogeochemical analysis results (below) for Ba and Sr (in ppm) in all drill holes. 113
Figure 4.6. Downhole plots showing pXRF readings (above) and lithogeochemical analysis results (below) for Rb (in ppm) in all drill holes 114
Figure 4.7. Downhole plots showing pXRF readings (below) and lithogeochemical analysis results (above) for Mo and V (in ppm) in all drill holes 115
Figure 4.8. Downhole plots showing pXRF readings (above) and lithogeochemical analysis results (below) for As, Cd, Fe, Mn, Pb, and Zn in all drill holes 116

LIST OF ABBREVIATIONS

a.s.l	above sea level
ang	anglesite
AP	Arabian Platform
arg	argentite
ATB	Anatolide-Tauride Block
avg	average
AQ200	Aqua Regia ICP-ES/MS
brt	barite
BZSZ	Bitlis-Zagros Suture Zone
ca	calcite
carb	carbonate
cer	cerussite
°C	celsius/ centigrade
dol	dolomite
E. Triassic	Early Triassic
Fm	formation
e.g.	exempli gratia, for example
g	gram
ga	galena
goe	goethite
hem	hematite
HFSE	high field strength element

hmp	hemimorphite
HREE	heavy rare earth elements
hz	hydrozincite
lim	limonite
LILE	large ion lithophile elements
ICP-ES	Inductively Coupled Plasma- Emission Spectroscopy
ICP-MS	Inductively Coupled Plasma- Mass Spectrometry
km	kilometer
LF200	Aqua Regia ICP-ES/MS
LN	lower ophiolite nappe
LOI	loss on ignition
L.Permian	Lower Permian
L. Triassic	Late Triassic
LREE	Light rare earth elements
MA370	Multi-acid Ore Grade ICP-ES
m	meter
Ma	million years ago
mic	micrite
mm	milimeter
mrc	marcasite
mt	million ton
MVT	Mississippi Valley- type
m.y	million years
n	number

n.d.	no data
n.m.	no mining
PPL	plane polarized light
ppm	parts per million
py	pyrite
REE	rare earth element
RL	reflected light
SEDEX	sedimentary exhalative
SF	sulfide free
sid	siderite
sm	smithsonite
SEAOB	Southeast Anatolian Orogenic Belt
sph	sphalerite
TOT/C	total carbon
TOT/S	total sulfur
TL	transmitted light
TZFB	Taurus-Zagros Fold Belt
zc	zincite
qtz	quartz
XRD	X-ray diffraction analysis
XPL	cross-polarized light
~	approximately, about

CHAPTER 1

INTRODUCTION

1.1 Purpose and Scope

The Hakkari district in southeastern Türkiye contains important zinc-lead (Zn-Pb) deposits, mostly located between the city of Hakkari and the Çukurca district. These deposits are associated with the passive margin carbonates of the Arabian Platform (Hanilçi et al., 2019).

Although numerous carbonate-hosted Zn-Pb ores are present in the Hakkari district, these mineralizations are relatively understudied possibly due to their remote location and harsh topography of the region. Similarly, Hakkari district is also relatively underexplored compared to other mineral belts in Türkiye. Most exploration to date, as well as academic research, in the district focused on the potential oil resources of the region, which led to a fairly good understanding of regional tectonics and main stratigraphic relationships. Metals exploration was mostly done at the small-scale by local companies, and only a few large companies investigated the Zn-Pb ore systems of the Hakkari district. This included Cominco's work from 2001 to 2003, when the company was able to delineate a few small resources before it decided to withdraw from the region in 2008. In 2019, First Quantum Minerals (FQM) entered into an agreement with a local mining company, Ölmezler Madencilik (OM), and started detailed exploration near OM's underground Pb-Zn operations at the Meskan project site.

Meskan is one of the several carbonate-hosted Pb-Zn deposits in the Hakkari area that is actively being mined for the past two decades (since 2004). Other Pb-Zn mining operations in the Hakkari area include Üzümcü (also commenced in 2004), Kurşuntepe (2007), Karakaya (2009), Akkaya (2012), and Armutlu (2014). These

small-scale deposits have collectively produced ~1 million tons (Mt) of ore, with average grades of 22% Zn and 5% Pb since 2005 (Hanilçi et al., 2019). Table 1.1 shows some of the key features of the known Pb-Zn deposits near Hakkari/ Mineralization in all of these, except Akkaya, and Deştan, is stratabound in nature.

The Karakaya deposit, situated approximately 3-4 km southwest of the Meskan deposit, occurs within the late Triassic–Jurassic (?) Karakaya carbonates, containing ~0.2 Mt of ore at 21% Zn and 5% Pb. The deposit was mined during 2009–2018. Mineralized zones with thicknesses ranging from 5 cm up to 13 m are composed primarily of oxide ore (hydrozincite, smithsonite, cerussite, hemimorphite, anglesite, and goethite) with rare barite, pyrite, galena, and sphalerite (Hanilçi and Öztürk, 2008; Santoro et al., 2013; Hanilçi et al., 2019).

Üzümcü Pb-Zn deposit, located approximately 5 km northeast of the Meskan deposit, produced ~0.1 Mt of ore at 27% Zn and 5% Pb between 2005 and 2016. Stratabound and vein-type ores have thicknesses ranging between 1 and 5 m and are hosted in Late Triassic–Jurassic (?) Üzümcü limestone (Hanilçi et al, 2020). Primary sulfide assemblage consists of banded pyrite, galena, and sphalerite as well as oxide ores including hemimorphite, smithsonite, cerussite, hydrozincite, goethite, and limonite (Hanilçi et al., 2019).

The Kurşuntepe Pb-Zn deposit is situated ~26 km southeast of the Meskan deposit, forming approximately 7000 tons at 27% Zn and 8% Pb, mined at 2007, with length from 70 to 80 m, thickness of ore ranges from 1 to 3 m, nearby Çukurca, Hakkari (Hanilçi et al., 2019). According to Hanilçi and Öztürk (2008), the sulfide mineralization is formed between late Permian and early Triassic limestones, develop in vein-type and strata-bound type. Sphalerite, rare galena, and significant barite are the ore minerals with variable thickness from one meter up to 80 meters.

The Oğul deposit is located approximately 22 km to the southeast of Meskan deposit, and lies within the Hakkari district. Mineralization is hosted by middle-late Triassic carbonates (Figure 1.1), with the thickness of ore range from 0.3 meter to 7 meters (Hanilçi et al., 2019).

Akkaya deposit, situated ~17 km southwest of Meskan deposit, lies within the Çukurca district and produced about 7000 tons of ore at 15% Zn and 6–12 % Pb as combined sulfide and oxide ore. The thickness of the ore is ~ 2.5m with pyrite, sphalerite, and galena making up the main sulfide ore assemblage (Hanilçi et al., 2019).

Deştan deposit, is situated 25 km southeast of Meskan deposit, consists of galena, smithsonite, cerussite, and develop as cavity fills and veins ((Figure 1.1; Hanilçi et al., 2019).

As mentioned previously, the nature of Pb-Zn mineralization in the Hakkari district is poorly-known due to the scarcity of scientific research on these ore systems. In one of the early studies on the Pb-Zn ores in central and eastern Anatolia, Ceyhan (2003) analyzed Pb-Zn ores hosted in Jurassic–Cretaceous carbonate rocks for their Pb isotopic compositions. He suggested that Zn-Pb mineralization at Hakkari occurred at ~200 Ma based on model ages, and also indicated that the Pb isotope signatures of these ores are mostly non-radiogenic. Ceyhan (2003) concluded that the carbonate-hosted Pb-Zn systems in Hakkari are significantly different from the distal Pb-Zn mineralizations developed around shallow-level plutons in central and central eastern Anatolia in that they are not associated with magmatism.

While Santoro et al. (2013) investigated the mineralogy of the non-sulfide ores, Hanilçi and Öztürk (2008) outlined some of the key geological features of the primary, sulfidic Zn-Pb ores in the Hakkari district. Later, Hanilçi et al. (2020) carried out fluid inclusion, Pb and S isotope analysis, and ore petrographic studies of the Karakaya, Meskan, and Üzümcü deposits. According to this study, these deposits exhibit three distinct forms of mineralization as syn-sedimentary, sub-seafloor replacement, and as vein-type, which occur in the feeder zones. Fluid inclusion microthermometry of the sulfide-rich ores revealed low homogenization temperatures (avg.: 209°C) and moderate salinities (avg.: ~14 wt.% NaCl equiv.) for the ore-forming fluids at the Meskan deposit. Pb isotope analysis of sulfide and non-sulfide ores indicated a crustal origin for the metal source, confirming the

preliminary findings of Ceyhan (2003). Based on these, Hanilçi et al. (2020) concluded that the formation model and fluid characteristics of the Pb-Zn ores of the Hakkari district are comparable with that of sedimentary exhalative (SEDEX) deposits.

This thesis focuses on the Meskan deposit, which is one of the most notable and recently-discovered Zn-Pb prospects in southeast Anatolia. Tectonically, Meskan is situated on the Arabian Platform on the northern passive margin of Gondwana. Mineralization is stratabound and is hosted by Triassic carbonate rocks, similar to the majority of other such mineralizations near Hakkari.

At Meskan, FQM began exploration work with OM in September 2019, and > 60.000 m of drilling has been completed to date. Additionally, detailed lithological and structural mapping was carried out. A detailed biostratigraphic section of Meskan and the surrounding region was established through petrographic investigation of a large number of drill core and surface samples from various lithological units (Altıner et al., 2023).

Oyman (2023) carried out mineralogical and petrographic studies as well as preliminary fluid inclusion analyses on Zn-Pb-mineralized samples and provided an overview of ore paragenesis and textures. This study concluded that Meskan ores comprise a simple sulfide assemblage mainly dominated by several generations of pyrite and sphalerite alongside galena, marcasite, and sparse sulfosalts.

As a stratabound system, one of the key features of the Meskan Zn-Pb mineralization is the prominent control of host rock lithologies. A number of lithostratigraphic units have been identified in the deposit area, and although these units are mainly dominated by carbonate rocks Zn-Pb mineralization appears to be restricted to a specific stratigraphic level that has been identified as the Meskan Tepe Formation. This spatial relationship between the Meskan Tepe Formation and stratabound Zn-Pb sulfide mineralization can be clearly observed in drill holes at Meskan. Nevertheless, lithogeochemical markers and characterization of the different host units and mineralized layers in Meskan Zn-Pb prospect by producing both spatial

and geochemical characterization of the ore zones, establishing their continuity, identifying similarities and differences, and assessment of proximal to distal mineralization vectors have not been well-defined.

In this study, the following research questions will be answered;

- How does the lithogeochemistry relate to sedimentary facies?
- What are the main ore facies and ore paragenesis in Meskan?
- Are there any vertical and horizontal metal zonation patterns at the deposit-scale?

To answer these questions, a detailed lithogeochemical characterization study was designed. Consequently, several drill holes were carefully selected for comprehensive ICP-MS and LF200 analysis. Drill hole selection was guided by specific criteria, including the need for adequate spatial coverage across the entire project area, a thorough representation of the local stratigraphy, and the absence of any deformations related to faulting and weathering. Moreover, some drill holes were specifically selected to encompass both mineralized and non-mineralized sections. Additionally, the polished section and thin sections prepared and examined at Middle East Technical University (METU). It will help to investigate textural changes and apply the results to larger scale spatial observations. This will provide insight as to why ore zones may be distinct and carry differing mineral assemblages.

[1]Table 1.1 Carbonate-hosted Pb-Zn deposits in Hakkari region (from Hanilçi and Öztürk, 2008; Santoro et al., 2013; Hanilçi et al., 2019; Karakaya Co., 2015).

Deposit name	Coordinate (ED50 UTM)		Mineralization style	Host rock	Host rock age	Ore geometry	Ore paragenesis	Mined ore grade (%)	Mined reserve (Mt)	Ore reserve (Mt)
Karakaya	364750 E	4150750 N	Strata-bound, stratiform	Limestone	L. Triassic	Strata, veins, pockets	sm, hmp, hz, zc, cer, ang	21% Zn	0.2	4
							goe, sid, cal, dol, brt, gn, sp., py	5% Pb		
Meskan	368150 E	4150700 N	Strata-bound, stratiform	Limestone	L. Triassic	Strata, veins, pockets	sm, hz, zc, cer, ang, hmp, goe	24% Zn	0.7	A few
							sp., gn, py, brt, cal, dol, sid, qtz	6% Pb		
Üzümcü	372510 E	4150250 N	Strata-bound, stratiform	Limestone	L. Triassic	Strata, pockets	sm, hz, zc, hmp, cer, ang	027% Zn	0.1	n.d
							sp., gn, py, br, cal, dol	5% Pb		
Kurşuntepe	382900 E	4123900 N	Strata-bound, vein-fill	Limestone	L.Permian-E. Triassic	Strata, veins	sp, gn- py, brt, dol, cal, qtz	27% Zn 8% Pb	0.07	n.d
Armutlu	362750 E	4150450 N	Strata-bound, karst-fill	Limestone	L. Triassic	Strata, pocket	sm. hmp, hz, zc, cer, ang, goe	21% Zn	0.09	8
							sid, cal, dol. brt, gn, sp., py	5% Pb		
Oğul	389417 E	4145910 N	Strata-bound	Limestone	L. Triassic	Strata	gn, sp., py, sm, cer,ang, lim, goe, brt	n.p-	n.m.	n.d.
Akkaya	364300 E	4133750 N	Vein-fill	Dolomitic limestone / Dolomite	Jurassic	Vein	sm, cer, geo, lim, gn, brt	15% Zn 6-12% Pb	0.07	n.d.
Deştan	368750 E	4124000 N	Karst-fill, vein-fill	Limestone	Permian	Pocket, vein	sm, cer, gn	n.p-	n.m.	n.d.

[1] (Abbreviations: ang= anglesite, arg= argentite, brt= barite, cal=calcite, cer= cerussite, gn= galena, goe= goethite, hem= hematite, hmp= hemimorphite, hz= hydrozincite, lim= limonite, mrc= marcasite, n.d.= no data, n.m.= no mining, py= pyrite, qtz= quartz, sid= siderite, sm= smithsonite, sp= sphalerite, zc= zincite, L. Triassic= Late Triassic, E. Triassic= Early Triassic, L.Permian= Lower Permian).

1.2 Methodology

1.2.1 Sampling criteria

Four drill holes collared from the surface and another one from the underground galleries were selected for systematic lithogeochemical characterization of the stratigraphic units and the ore horizon at Meskan. A total of 439 drill core samples were analyzed for their major, minor, and trace element compositions. Sampling length was chosen as 1 m with samples getting collected at every 10 to 15 meters. Drill holes were selected based on relatively low frequency of faulting and good representation of the stratigraphy. Also, selected samples are representative of both mineralized and unmineralized intervals. At the broader scale, sampled drill holes were selected from locations characterizing the eastern and western sectors of the main mineralized area. All sampling intervals are described in terms of their contained lithology, stratigraphic positions, as well as in terms of their mineralization and alteration characteristics.

The following rules were considered during sampling;

a) Sampling from fault zones, cavities, fractures, and oxidized zones was avoided. Majority of the samples were fresh and non-weathered.

b) Chosen samples span the entire stratigraphic column. In the vicinity of ore and stratigraphic contacts, samples were collected at a higher frequency to detect even minor geochemical variations. Samples were taken from one-meter-long intervals.

c) Each cutting core sample weighs at least 100 g.

d) Variably-textured samples (brecciated, zebra-textured, banded, veined, etc.) representing the entire ore horizon were chosen to investigate the spatial zonation of the Zn-Pb mineralization.

e) The sampling density was increased within the mineralized Meskan Tepe Fm. Samples were taken up hole and downhole of the mineralization to understand how lithology and stratigraphy change in the hanging wall and footwall of mineralization.

f) Samples were collected from different ore types and assemblages in the sulfide ore zones (e.g., pyrite-dominated, colloform-banded pyrite-sphalerite, etc.).

g) Samples were chosen from calcite veins and breccia infills to understand presence and extent of dolomite alteration.

h) Samples were collected from different stacked lenses to understand whether the deposit is present at various depths or not, and also to help understand how mineralization changes with depth in the ore zone.

i) Blank, duplicate, and certified standard samples were used to implement quality accuracy and quality control measures.

1.2.2 Lithogeochemical analyses

Lithogeochemical analyses were carried out at the Bureau Veritas Laboratories in Vancouver (B.C., Canada). Selected analytical package (LF202) uses lithium metaborate fusion for near complete digestion especially of refractory minerals that contain high-field strength elements. Processed samples are combined with a $LiBO_2$/ $Li_2B_4O_7$ flux, and crucibles are subjected to fusion in a furnace. The resulting cooled bead is dissolved using ACS grade nitric acid and subsequently subjected to analysis employing ICP and/or ICP-MS techniques. The determination of Loss on Ignition (LOI) involves igniting a split sample and measuring the resultant weight loss. The assessment of total carbon (TOT/C) and total sulphur (TOT/S), possibly encompassed, are conducted through the Leco method (TC000). Additionally, within the LF202 package, concentrations of an additional suite of 14 elements including Mo, Cu, Pb, Zn, Ni, As, Cd, Sb, Bi, Ag, Au, Hg, Tl, and Se are determined via an

aqua regia digestion method (AQ200), offering insight into Au and volatile element concentrations.

Besides lithogeochemical analyses, different analytical package (MA370) was used for all drill hole assay results. Element concentrations were determined by multi-acid digestion ICP-ES for sulfide and silicate ores. The detection limit of Zn and Pb are 1 ppm and 0.1 ppm respectively for AQ200 analytical package.

For most samples, this digest roughly represents a full digest of 23 elements. Partially digested minerals include Cr and Ba, as well as oxides of Al, Fe, Hf, Mn, Sn, Ta, Zr, and REEs. As, S, Se, and Sb may be lost due to volatilization during fuming. The detection limit of Zn and Pb are 0.01% and 0.02% respectively in MA370 analyses method. A total 39 standard samples which are OREAS-21e and OREAS-22h were used.

1.2.3 Petrography

Representative drill core samples from the surface and underground drill holes in the Meskan Zn-Pb orebody were examined petrographically using a transmitted and reflected-light, polarizing microscope. Identification of ore and gangue phases was carried out through detailed petrographic examination of a total of 23 samples obtained from drill hole MSUGDD0025. Samples selected during drill core inspection were prepared into polished blocks at the facilities of the Çayeli Cu Mine in Rize and thin sections were prepared at the Minerals Research and Exploration Institute of Türkiye (MTA). Drill hole MSUGDD0025 intersects a representative section of the sulfide ore hosted within the main mineralized unit. Petrographic observations were supported by XRD analyses of the host carbonate lithologies.

1.3 Sediment-hosted Pb-Zn deposits

Sediment-hosted Pb-Zn deposits are the largest sources of lead and zinc globally. These deposits have been extensively studied over the years, and based on these sediment-hosted Pb-Zn systems are defined as sulfide-rich, stratiform to stratabound or discordant ore deposits, hosted in siliciclastic and carbonate rocks, and are not directly associated with igneous activity (Leach et. al., 2005; Fontbote and Boni, 1994; Wilkinson, 2014). Mississippi Valley-Type (MVT) and sedimentary exhalative (SEDEX) deposits are the two primary types of sediment-hosted Pb-Zn deposits (Figure 1.1). These have different features in terms of their geological setting, host rocks, and textures, as well as some similarities among each other, such as their ore mineralogy. In terms of their tectonic settings, there are some differences considered by many researchers and these differences are also reflected in their other distinctive properties, such as host rock or grain sizes of ore minerals. One of the most distinct differences between MVT and SEDEX deposits is their associated host rocks (Figure 1.2). While MVT deposits are found in carbonate-dominated sequences within platform carbonate sequences of passive margins, SEDEX deposits are primarily hosted by clastic-dominated, fine-grained siltstones, shales, and mudstones which are products of the typical shelf environment at high latitudes formed in intracontinental or failed rift basins and rifted continental margins (Leach et. al., 2010; Wilkinson, 2010; Figure 1.1). Another key feature which has been observed during many studies on these deposits is their fluid source(s). While SEDEX-type deposits form via “exhalation” of the basinal brines at the seafloor or fluid migration into poorly-consolidated sediments, precipitation from hot saline basinal brines after deposition of host sediments is accepted as the main mechanism for MVT deposit formation (Fonbote and Boni, 1994; Wilkinson, 2014). MVT and SEDEX-type Pb-Zn deposits have broadly similar ore and gangue mineral contents mainly comprised by sphalerite, galena, and pyrite as the main sulfide minerals and calcite, dolomite, siderite, barite, ankerite, and quartz as gangue minerals (Leach et al., 2005). From a structural perspective, formation of SEDEX-type deposits is

controlled generally by syn-sedimentary growth faults and associated fracture and breccia zones, where ore bodies are typically found in hanging wall of 2nd and 3rd order structures (Wilkinson, 2014). In MVT deposits, mineralization is structurally controlled by normal or trans-tensional faults (Wilkinson, 2014). It is acknowledged that syn-sedimentary fault areas supply the necessary pathways for buoyant mineralizing fluids that migrate from greater depths (Wilkinson, 2014).

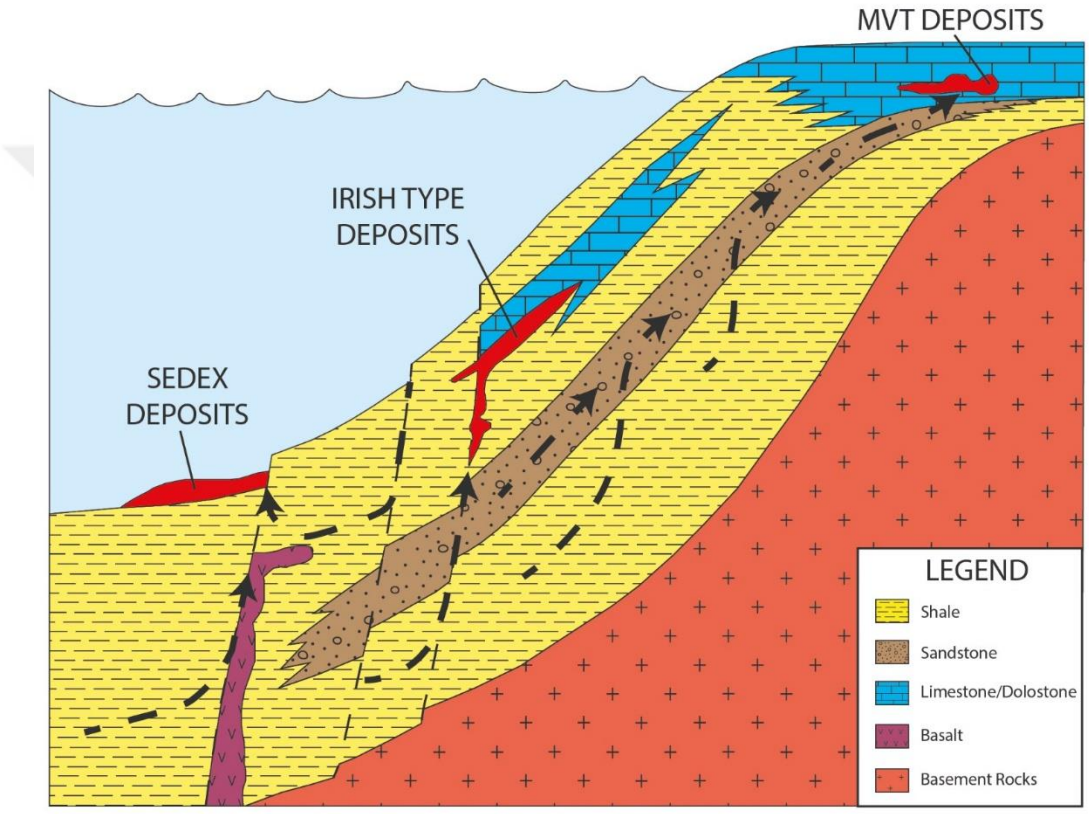


Figure 1.1. Sketch view showing geological settings of SEDEX, MVT, and Irish-type Pb-Zn deposit in marine environment (redrawn after Kesler and Reich, 2006).

While the key features of the main sedimentary-hosted Pb-Zn deposits are shortly explained above, there is another sub-type of Pb-Zn deposits that possess characteristics that do not completely conform with either of the SEDEX and MVT deposits. This type of Pb-Zn ores is called as “Irish-type deposits” named after numerous discoveries of this type in the world-known Irish Orefield (Figure 1.1).

Various authors have provided detailed descriptions of the geology of the Central Irish Orefield (Phillips and Sevastopulo, 1986; Hitzman and Beaty, 1996; Holland, 2009; Wilkinson and Hitzman, 2015). According to Philcox (1983), Irish-type deposits formed during Early Carboniferous in a marine environment and within a transgressive sequence of marl, shale, and limestone (Figure 1.2). Red-bed clastics that deposited during the Devonian–Carboniferous are conformably overlain by the Lower Carboniferous sequence, and were formed in relation to block faulting related to crustal extension (Andrew, 1992). The lowest part of the Carboniferous units in the southern part are found conformably above Devonian Old Red Sandstones. These Devonian rocks exhibit a southward thickening trend into the Munster Basin, where their thicknesses reach up to approximately 6 km (McCarthy, 1995). Devonian and Lower Paleozoic rocks were formed during Variscan folding and accompanied by an increase in east-west folding induced by the Hercynian orogeny. A distinct geological and topographic boundary emerges at the Variscan front.

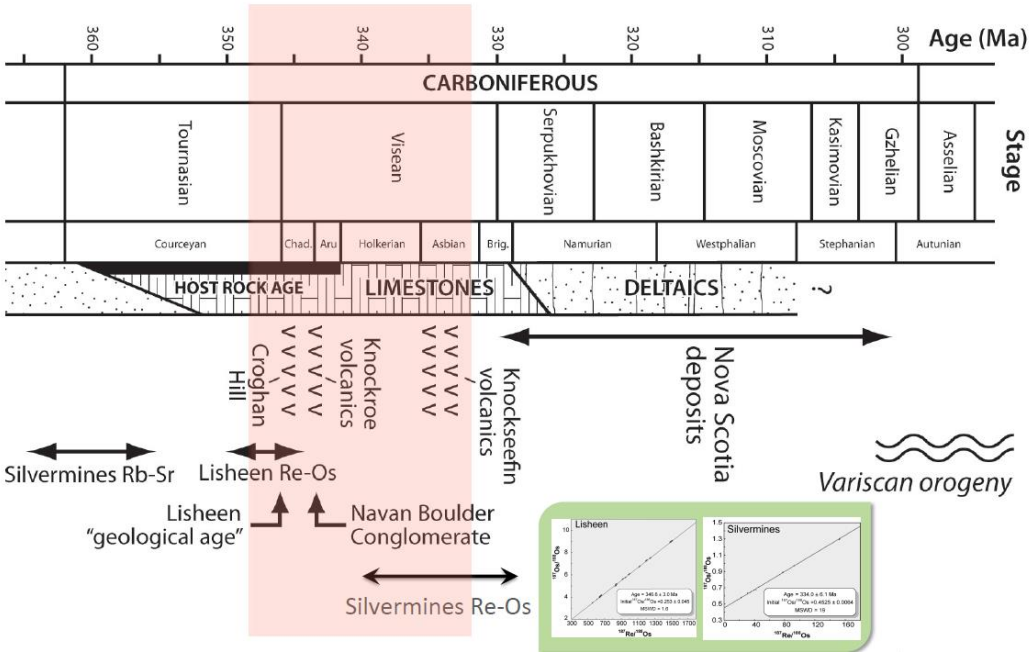


Figure 1.2. The Carboniferous timeline of key geological events that affected the Irish Midlands Basin (Hnatyshin et al., 2015; Wilkinson and Hitzman, 2015).

Irish-type deposits exhibit features close to SEDEX deposits rather than MVT deposits due to their geological characteristics (Wilkinson, 2010). Although both MVT and Irish-type deposits are hosted in carbonate lithologies, the main differences with MVT-deposits lie in the depositional environment, sulfur source and fluid temperature.

In terms of tectonostratigraphic setting at the time of mineralization, SEDEX-type deposits are formed in intracontinental rift basin (Leach et al., 2005), MVT deposits developed in platform carbonate sequences (Leach et al., 2005), and Irish-type deposits in the carbonate ramp (Wilkinson, 2003; Figure 1.1). Sulfide minerals of sphalerite, galena, pyrite, and marcasite are common in all sediment hosted Pb-Zn deposits. However, Irish-type deposits are characteristically enriched in low-Fe sphalerite (Wilkinson, 2003; 2014). Barite is a more abundant gangue mineral in Irish-type deposits than SEDEX and MVT deposits (Leach et al., 2005), whereas fluorite is rare in all three deposits. Textures in SEDEX deposits are bedding parallel, layered, and banded, whereas in Irish-type deposits massive sulfides may dominate but overall textures are may be highly variable (Leach et al., 2005; Wilkinson, 2003).

CHAPTER 2

GEOLOGY OF THE SOUTHEASTERN ANATOLIA

2.1 Regional Geological Setting

The geological evolution of Türkiye is directly linked to the development of the Tethys Ocean, which was a prolonged and complex oceanic system located between Gondwana and Laurasia. The long-lived Tethyan oceanic system is commonly sub-classified into Neotethys and Paleotethys. The present distribution of the tectonic fragments of today's Anatolia is a reflection of the gradual evolution of these oceanic basins, which are generally considered to be the primary branches of the Tethyan ocean. Based on the orogenic development of Türkiye, geological tectonic units were named in the following order from north to south: Pontides, Anatolides, Taurides, and Border Folds (Ketin, 1966; Şengör and Yılmaz, 1981; Okay and Tüysüz, 1999) (Figure 2.1). These tectonic units were encompassed by various Tethyan oceanic basins, remnants of some of which can be traced by extensive suture zones (Okay, 2008).

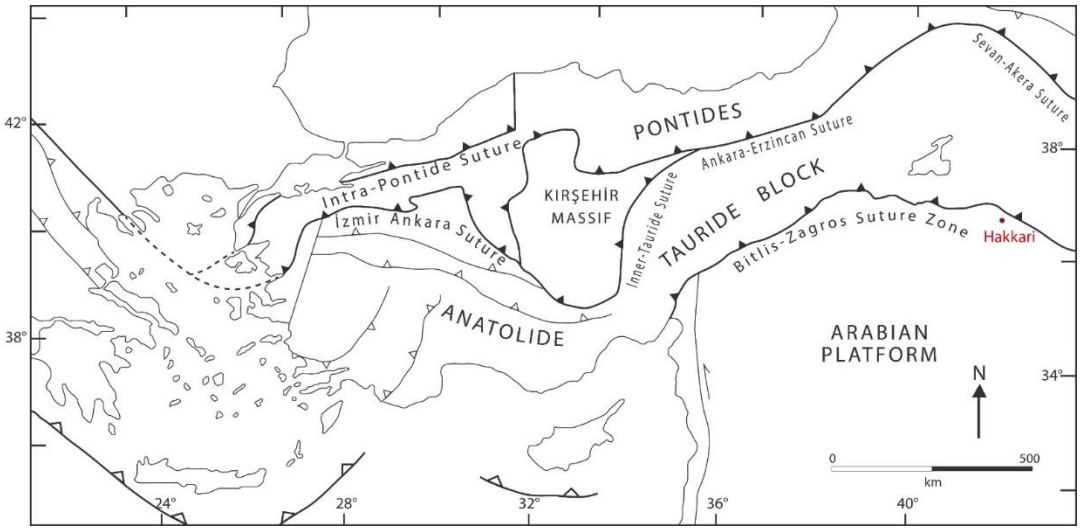


Figure 2.1. Map showing the main tectonic fragments and the bounding suture zones in Anatolia and in the surrounding region (Okay and Tüysüz, 1999).

The Anatolide-Tauride Block constitutes an important portion of the present day Türkiye and represents a continental platform that developed to the south of the Northern Neotethys ocean during the Mesozoic and Cenozoic. It remained as a part of Gondwana until the Permian, and later detached from the northern Gondwana margin through rifting (Şengör and Yılmaz 1981; Robertson and Dixon 1984; Robertson et al., 2007). This event, known as the Cimmerian orogeny, resulted in opening of the Southern Neotethys to the south of the ATB (Şengör, 1984).

In southeastern Türkiye, the ATB is juxtaposed against the Arabian Platform (AP) along the Bitlis-Zagros Suture Zone (Figure 2.1). Prior to the Southern Neotethys rifting, both ATB and AP were broadly located within a similar geological setting, and therefore their Paleozoic stratigraphies show many similarities (Okay, 2008). The Bitlis-Zagros Suture Zone is well-defined by the presence of border folds and ophiolitic mélange (Ketin, 1966).

The Southeast Anatolian Orogenic Belt (SEAOB) forms the western part of the Bitlis-Zagros Suture Zone between SE Anatolia and Iran and is comprised of a variety of tectonic units widely exposed along the collided margin between the ATB and the AP. Yılmaz (1993) sub-divided the main tectonic domains of the SEAOB into three distinct zones. These domains, separated from one another through regional thrust systems, display distinct lithological and structural characteristics largely due to their relative positions during the early evolution of the Southern Neotethys oceanic basin and its ultimate closure.

2.2 The geological framework of the Southeast Anatolian Orogenic Belt

Figure 2 shows the main tectonic sub-divisions of the SEAOB, which from the south to the north are: (1) the Arabian Platform, (2) the Imbrication Zone, and (3) the Nappe Zone (Yılmaz, 1993).

Within the SEAOB, the AP is in an autochthonous position relative to the Imbrication Zone and the Nappe Zone to its north (Figure 2.2). It consists of a Pan-African basement covered by thick Paleozoic to Tertiary sedimentary sequences that

mostly developed in a marine environment (Figures 2.2 and 2.3; Göncüoğlu et al., 1997; Elmas and Yılmaz, 2003; Okay, 2008).

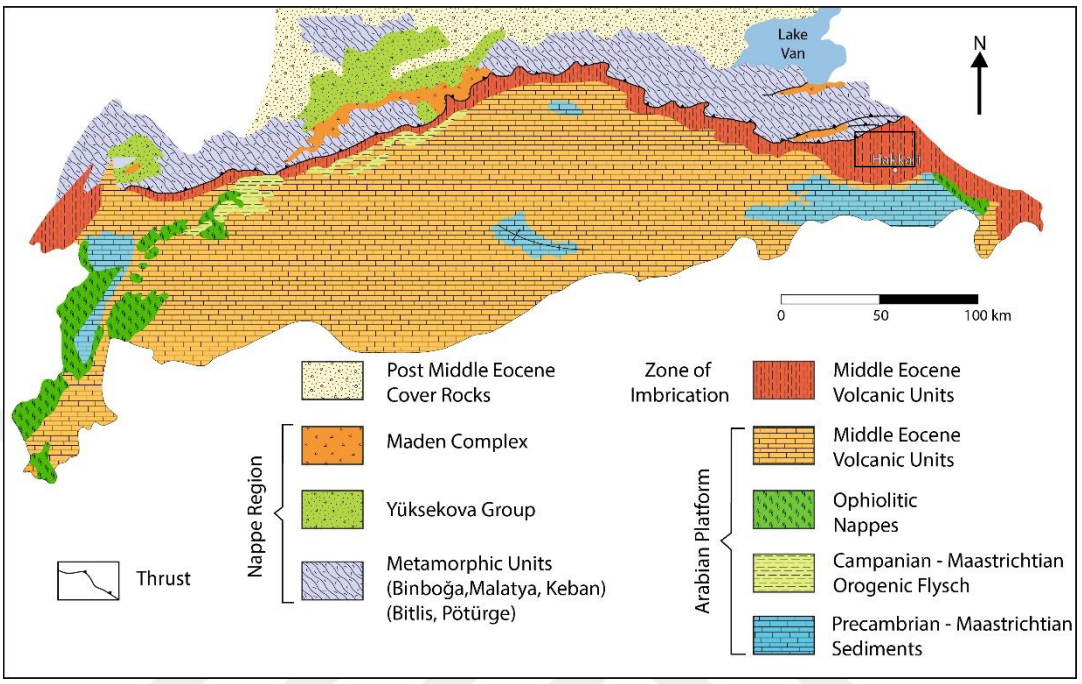


Figure 2.2. Regional geological map of the Southeast Anatolian Orogenic Belt (after Yiğitbaş and Yılmaz, 1996a, 1996b).

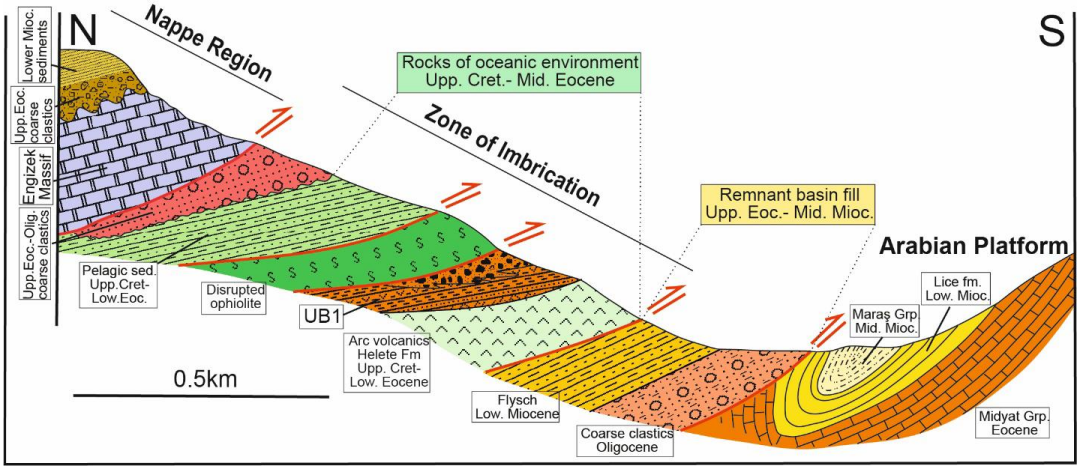


Figure 2.3. Cross-sectional sketch showing relationship between various tectonostratigraphic units within the SEAOB (Yılmaz et al., 2022).

From Permian onwards, the AP formed the passive northern margin of Gondwana until the closure of the Southern Neotethys basin in the Late Cenozoic (e.g., Şengör and Yılmaz, 1981; Yılmaz, 1993; Göncüoğlu and Kozlu, 2000; Moix et al., 2008).

The AP includes two separate successions; the northern and southern successions, representing outer and inner shelf deposits, respectively, which intergrade with one another (Yiğitbaş and Yılmaz, 1996a). The basal sandstone and conglomerate of the Terbüzek Formation indicate the base of the transgressive sequence of the southern succession (Yiğitbaş and Yılmaz, 1996a). This later passes into Besni and then into Germav Formations of Late Cretaceous–Paleocene age. The outer shelf along the northern part of the AP demonstrates a deep marine sedimentary environment with the appearance of the Cona Group (Yiğitbaş and Yılmaz, 1996a). The sedimentary sequence incorporates various regional unconformities, all relating to three distinct stages of nappe emplacement (Yılmaz, 1993; Yılmaz et al., 2022). All of this sequence is separated from the Nappe Zone through the Imbrication Zone (Figures 2.2 and 2.3).

The Imbrication Zone coincides with the main axis of the Bitlis-Zagros Suture Zone (Figure 2.2). It is developed as a complex system of E–W-trending reverse faults in the Late Cretaceous–Early Miocene (Yıldırım and Yılmaz, 1991; Yılmaz, 1993 and 2019). The Imbrication Zone broadly represents stacked thrust sheets of rock units transported from the north as the Southern Neotethyan basin progressively closed starting from the Late Mesozoic until the late Miocene. Among the thrust sheets, the arrangement of stratigraphic sequences is reversed; that is the older units are positioned above the younger ones (Yılmaz, 1993). However, the successions exhibit a complementary nature, indicating their previous formation as a continuous sequence before the imbrication process (Yılmaz, 1993). From the bottom to the top these include the Upper Cretaceous-Eocene successions is in thrust contact with the middle to late Eocene volcanics, which are predominantly composed of intermediate lavas and accompanying pyroclastic rocks with interbedded sedimentary units (Yiğitbaş and Yılmaz, 1996a). To the west, within the imbricated zone, these units disperse away from the converging boundaries of the colliding continents, expanding into a broad belt referred to as the escape zone (Yılmaz, 2019). Within this belt, the initial stratigraphic relationships of rock units engaged in the shortening and imbrication processes within the imbrication zone become distinctly visible (Yılmaz and Gürer, 1996; Robertson et al., 2004; Ünlügenç and Akıncı, 2017; Yılmaz, 2019).

The Nappe Zone, which is located at the northern part of the SEAOB, is represented by the extensive Maden Complex in the north and by the Bitlis and Pütürge metamorphic massifs in the south (Figure 2.2). Şengör and Yılmaz (1981) suggested that the two metamorphic massifs, consisting of similar Paleozoic core and Mesozoic cover rocks, together drifted away from the Arabian Platform in the Triassic. The metamorphic massifs underwent a significant phase of metamorphism subsequent to the development of the entire sedimentary succession. In the base of the nappe region, metamorphosed pillow lavas are present and are overlain by the pelagic metasedimentary rocks of the Kızılkaya formation (Yiğitbaş and Yılmaz, 1996a). This formation correlates with the well-ordered ophiolitic sequence of the Yüksekova group in Hakkari region (Yiğitbaş and Yılmaz, 1996b). Mafic volcanic intercalated with sedimentary units belongs to Maden Complex is located on Nappe zone (Yiğitbaş and Yılmaz, 1996a; Elmas and Yılmaz, 2003).

2.3 Regional Stratigraphy of the Arabian Platform in SE Anatolia

The AP comprises extensive sedimentary series that accumulated in a predominantly marine environment from the Cambrian period to the present day (Yılmaz, 1993 and 2018; Yılmaz et al., 2022; Göncüoğlu and Turhan, 1997). The sedimentary sequence has been disrupted by several unconformities that developed over three distinct periods of nappe emplacement (Figures 2.3 and 2.4; Yılmaz, 1993). Therefore, this sequence can be examined within three successions (Figure 2.4; Yılmaz, 2021). The lower ophiolite nappe (LN) was tectonically deposited onto the AP during the Late Campanian–Early Maastrichtian (Yılmaz, 1993). The ophiolites of this period exhibit suprasubduction zone affinities (Pearce, 1985; Dilek and Thy, 1992; Parlak et al., 2004). They formed above the Tethyan oceanic lithosphere which subducted northward, (Robertson 2012; Dilek 2019; Yılmaz 2019, 2021; Yılmaz et al., 2022).

The AP commonly includes a substantial shallow marine succession of Lower Paleozoic age (Yılmaz, 1993). Neritic carbonates replace clastic deposits from Devonian to Cretaceous, and also includes ophiolite nappes with Late Cretaceous–Miocene sedimentary cover rocks (Yılmaz, 1993). Regional tectonostratigraphic

units are sub-divided into three by Yılmaz (1993) as (1) the lower autochthonous unit, (2) the allochthonous unit, and (3) the upper autochthonous unit.

1) *Lower autochthonous unit:* This tectonostratigraphic unit starts with rare Neoproterozoic volcanic, volcaniclastic, and clastic lithologies of the Telbesmi Formation (Perinçek et. al., 1992). The crystalline basement is then overlain by Cambrian carbonates and siliciclastics of the Derik and sandstones of the Habur Groups, followed by the Silurian–Devonian marine deposits of the Diyarbakır Group (Perinçek et. al., 1992). The thickness is defined by geophysical data in SE Jordan and the Taurus-Zagros Fold Belt (TZFB) in eastern Türkiye as >6000 m (Alsharhan et al., 2003). The Diyarbakır Group is overlain by the Zap Group (Late Devonian-Early Carboniferous), a succession that is rich in carbonaceous limestone. Following a regional unconformity time break regionally, the Carboniferous strata gradually pass into Upper Permian sandstone and limestone of the Tanin Group (Perinçek et. al., 1992). The Lower Triassic Çığlı Group overlying is separated into three formations. The middle of carbonates in this group consists of red shale, sandstone, limestone, and siltstone. This formation has a higher siliciclastic content as it approaches the Mardin-Kahta High. Cudi Group proceed carbonate deposition until Early Cretaceous (Perinçek et. al., 1992).

2) *The allochthonous unit:* This tectonostratigraphic unit is represented by a nappe package comprising a well-preserved and ordered ophiolitic sequence known in the eastern part of the SEAOB as the Cilo ophiolite at the top (named as either Yayladağ or Kızıldağ to the west of the belt; Yılmaz, 1994; Dilek and Delaloye, 1992; Yılmaz et al., 2022). Beneath the Cilo ophiolite sequence are two distinct, internally-disordered and tectonically-separated complexes, the Koçali Complex and the Karadut Complex, which were obducted onto the AP margin during the closure of the Southern Neotethys ocean (Yılmaz, 1993). The former complex consists of an ophiolitic mélange and epiophiolitic sedimentary rocks, whereas the latter is described as a chaotic flysch unit (Yılmaz, 1993).

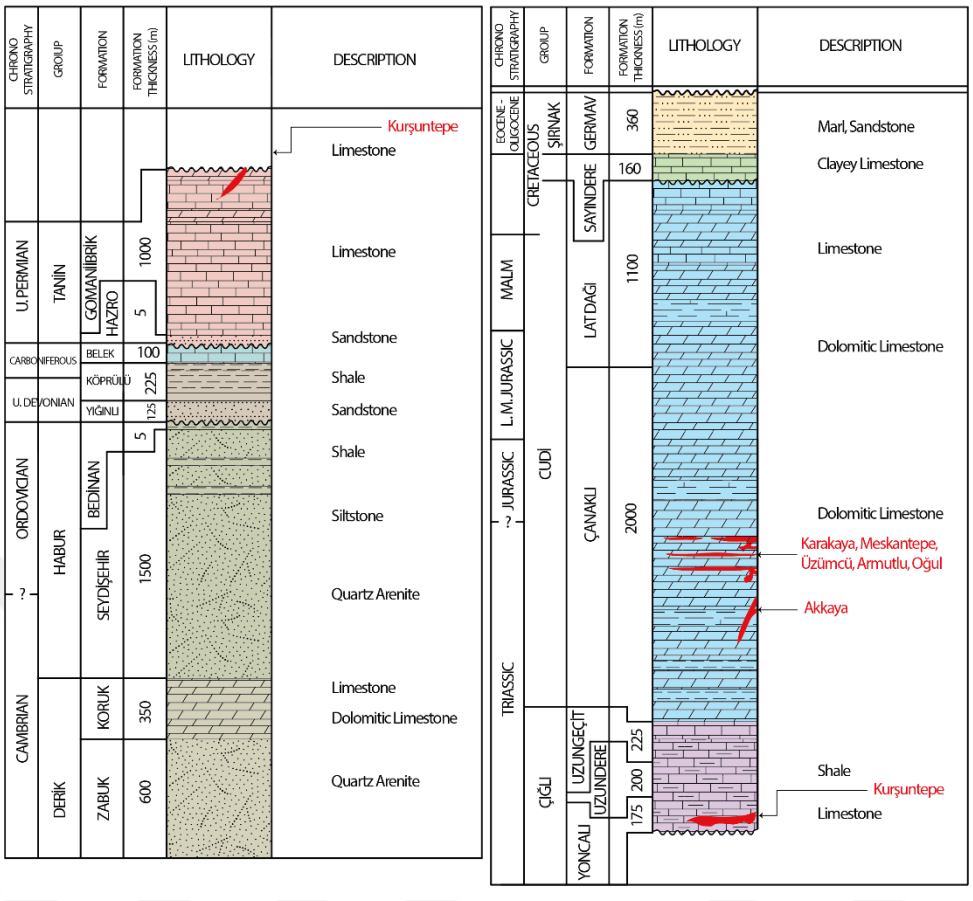


Figure 2.4. The generalized stratigraphic columnar section of the Hakkari area and the stratigraphic positions the of Pb-Zn deposits of the Hakkari district (simplified after Hanilçi, 2020).

3) *Upper allochthonous unit:* The upper part of the AP in the autochthon comprises the Mardin Group, representing a platform carbonate succession of Aptian–Cenomanian age (Perinçek et. al., 1992). It also includes the Sayındere Formation, characterized by clayey limestone from the Campanian, the Kastel Formation featuring flysch and Late Campanian to Early Maastrichtian olistostrome, the Terbüzek Formation consisting of basal sandstone to conglomerate from the upper Maastrichtian, the Besni Formation comprising Late Maastrichtian reefal limestones, the Germav Formation composed of Late Maastrichtian to Paleocene shale, the Midyat Group representing a platform carbonate sequence formed during the Eocene–Oligocene, the Fırat Formation featuring Oligocene to lower Miocene reefal limestones, and finally the Adıyaman Formation comprising Middle–Late Miocene fluvial and lacustrine sedimentary rocks (Yılmaz, 1993).

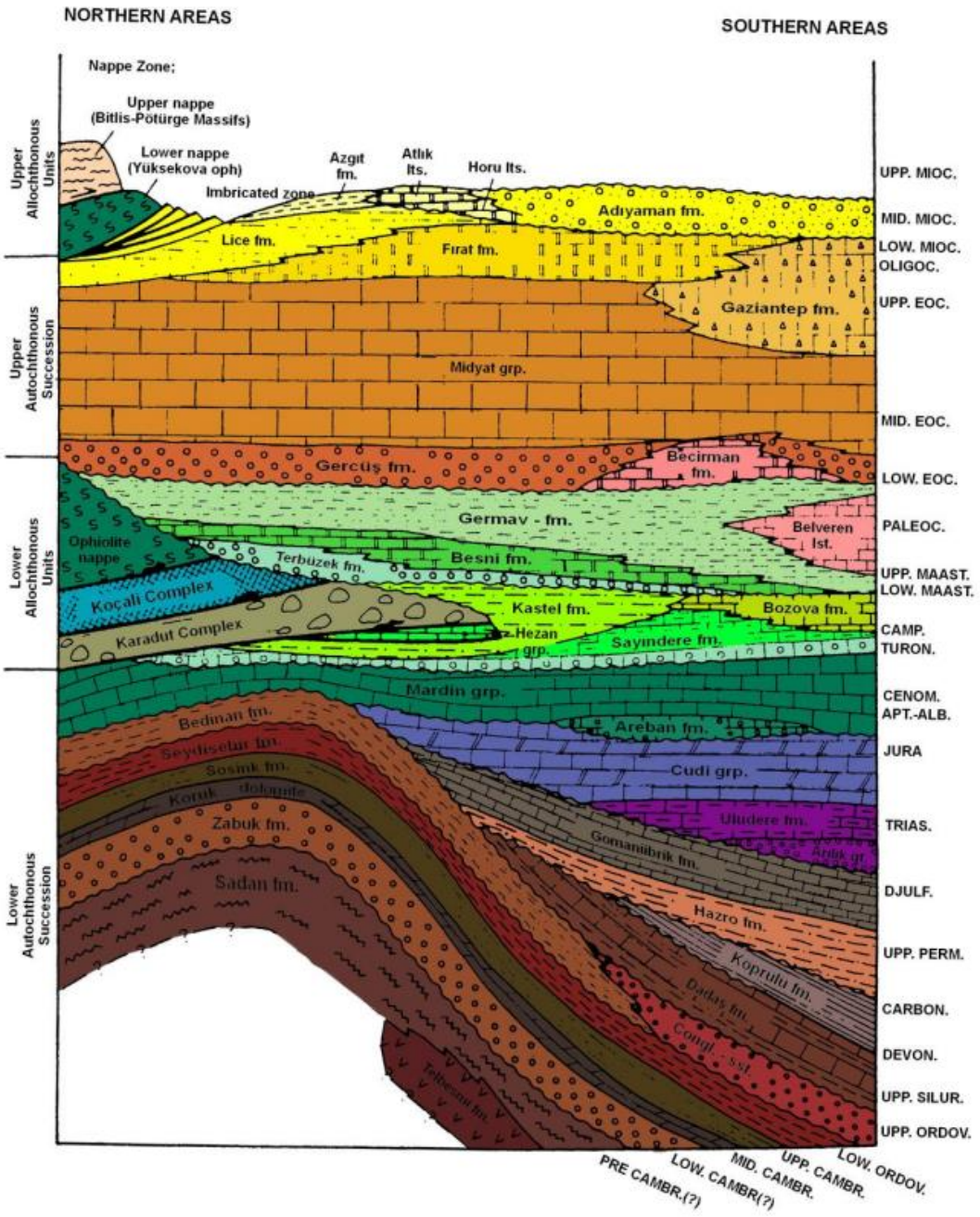


Figure 2.5. Generalized stratigraphic section of the Arabian Platform in southeastern Anatolia, showing nappe zones, the formations and ages of the rock units (from Perinçek et al., 2018).

CHAPTER 3

DEPOSIT GEOLOGY

3.1 Introduction

The Meskan deposit is situated in the Hakkari Province in southeast Türkiye (Figure 3.1), about 22 km to the west of the Hakkari city center. The Hakkari district lies on the northern edge of the AP in the Cilo Mountains. Access to the region is difficult due to its high elevation and rough topography, which includes steep peaks and deeply carved valleys. Access to Meskan from Hakkari city center is through a sealed road. The local mining company, Ölmezler Mining, site office is on the main road near the Zap River at the start of the access road into the mine site at an elevation of about 1000 m above sea level (a.s.l.). The Şaho Gallery lies at an elevation of about 1500 m a.s.l. and the Meskan Tepe military base near the Meskan West sector is at about 2000 m a.s.l. (Figure 3.1).

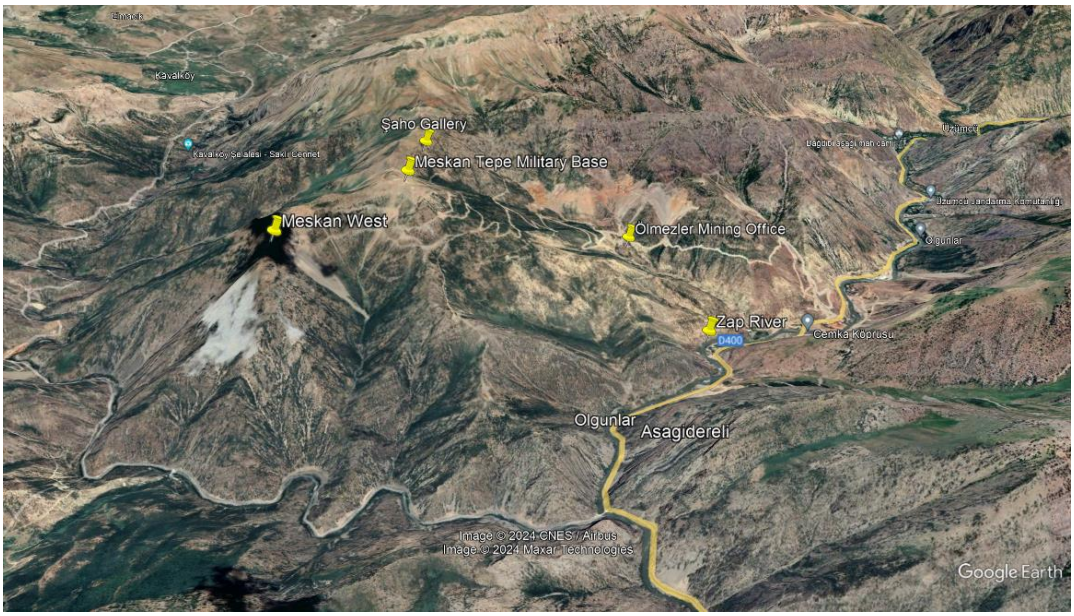


Figure 3.1. Google Earth view of the Meskan region showing Meskan West sector as well as the Şaho underground gallery of the Ölmezler Mining to the north of the Zap River.

Apart from Meskan, this area also contains several other carbonate hosted Pb-Zn deposits including Üzümcü, Karakaya, and Armutlu (Figure 3.2). These Pb-Zn systems as well as the Meskan Zn- Pb deposit are all hosted within the Middle–Late Triassic carbonate rocks of the Cudi Group (Hanilçi et al., 2020). In the absence of fossil ages, Hanilçi et al. (2020) reported a Re-Os pyrite age of 234 ± 10 Ma suggesting that sulfide mineralization occurred during the Late Triassic.

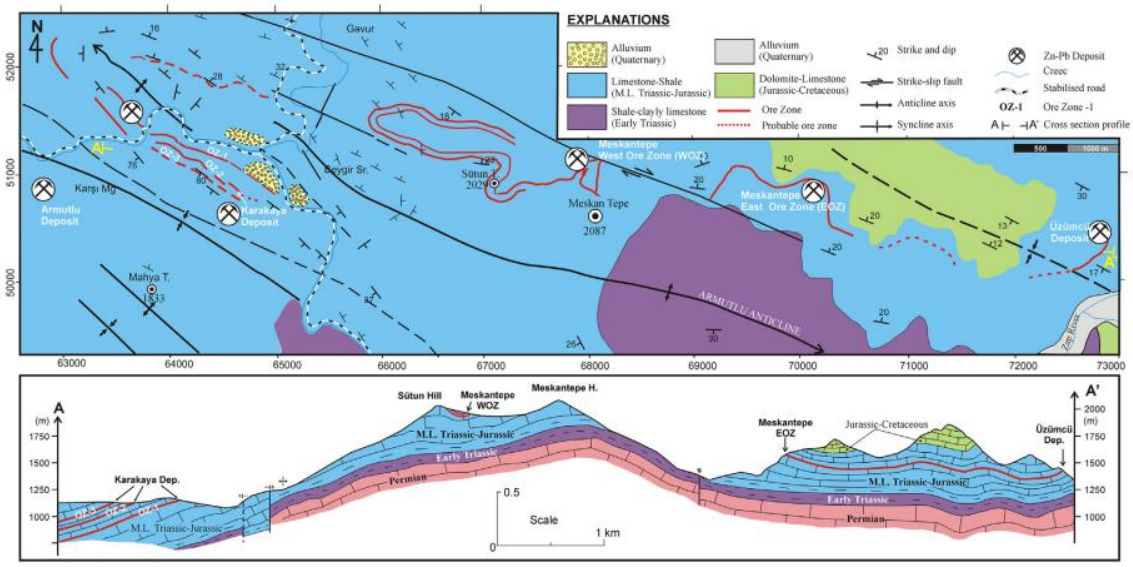


Figure 3.2. Geological map and cross-section showing stratigraphic position of the Meskan, Üzümcü, and Karakaya carbonate-hosted Zn-Pb deposits (Hanilçi et al., 2020).

3.2 Meskan Stratigraphy

The autochthonous sedimentary units, ranging in age from Precambrian to Recent, have been categorized into six distinct formations in the vicinity of the Meskan Zn-Pb deposit based on the stratigraphic relationships and nomenclature proposed by Perinçek (1990). These, from oldest to youngest, are namely the Permian Group, Lower Çığlı Group, Middle Çığlı Group, Upper Çığlı Group, Lower Çanaklı Formation, Middle Çanaklı Formation, Upper Çanaklı Formation, respectively. The main stratigraphy of Meskan is tested with three deep drill holes that are MS22DD021, MS22DD027, and MS22DD029, which intersected the entire sequence indicated above.

3.2.1 Permian Group

The Permian Group comprises the upper part of the Tanin Group. It is composed of bioclastic limestone at its base, followed by shale and coal-bearing sandstone layers, and then by dolomitic limestone and bioclastic limestone that gradually transition into a more sandy and argillaceous composition (Perinçek et. al., 1992; Figure 3.3). The age of this formation is determined as Late Permian (Fontaine, 1981; Altıner, 1989). The maximum thickness of the Permian Group in the general Hakkari region is ~1000 m (Perinçek et. al., 1992), but in the Meskan area it has a thickness of only about 50 m and it has only been intersected in one drill hole (MS22DD029). Apart from this, the lithologies of the Permian Group does not crop out in the Meskan area.

In the drill core, the carbonate rocks of the Permian Group appear as dark grey to black, and massive-looking limestones with local sandy limestone and calcite nodules as well as irregular calcite veins (Figure 3.4a). This formation is recognized in drill core by a distinct dolomite texture (pitted texture?), which likely developed by plucking of softer carbonaceous domains giving the rock a pitted appearance (Figure 3.4b).



Figure 3.3. Shallowly-dipping limestones of the Permian Group (unpublished company report; Akın, 2023).

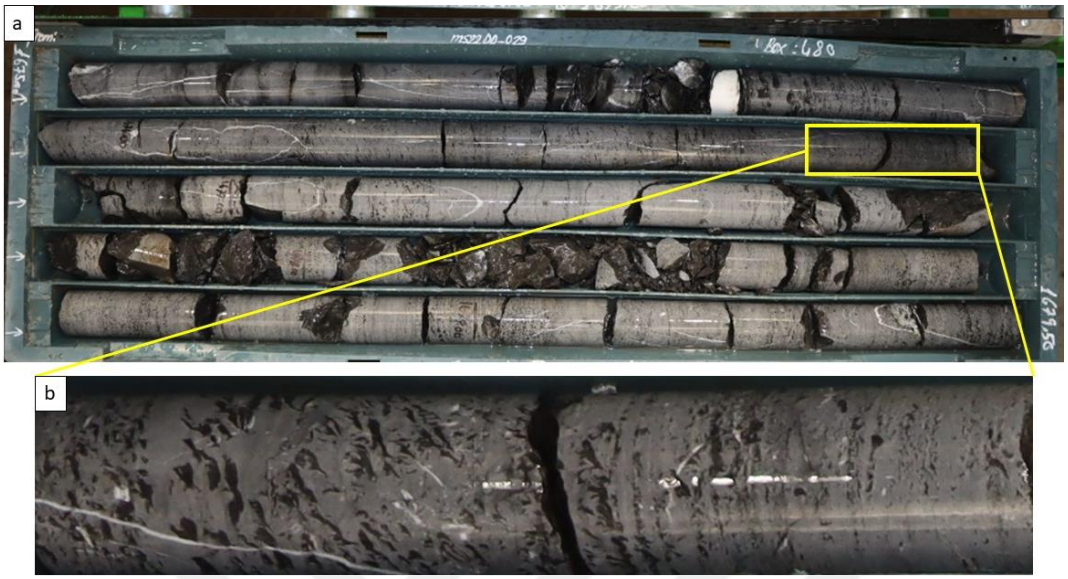


Figure 3.4. a-b) The characteristic texture (pitted texture?) of the dark grey to black colored limestones of the Permian Group (drill hole MS22DD029, 1676.80 m).

3.2.2 Lower Çığlı Group

The Permian Group is transitional upwards into the Lower Çığlı Group (Perinçek et. al., 1992; Figure 2.4). The Çığlı Group is generally observed in the southern part of the Diyarbakır-Hazro anticline and is conformable with the Middle Triassic–Lower Cretaceous Çanaklı Formation (Tuna, 1973; Perinçek, 1987; Yılmaz, 1982; Günay, 1998). Fontaine (1981) and Köylüoğlu (1986) assigned an Early Triassic age to the Çığlı Group. The lower part of this group consists of limestone and argillaceous limestone grading upwards into an alternating sequence of limestone and shale (Perinçek et. al., 1992).

Similar to the Permian Group, the Lower Çığlı Group also does not have surface exposures at Meskan. The Lower Çığlı Group is observed in the drill core as predominantly medium- to thinly-bedded and rarely massive-textured micritic limestone, dolomitic limestone, and gastropoda- and pelecypoda-rich limestone. The transition from Permian Group to Lower Çığlı Group is marked by finely-laminated grey-green claystone or mudstone layers (Figure 3.5). Dolostones are mostly grey in

color and appear massive. The maximum thickness of this formation is around 180-200 m.

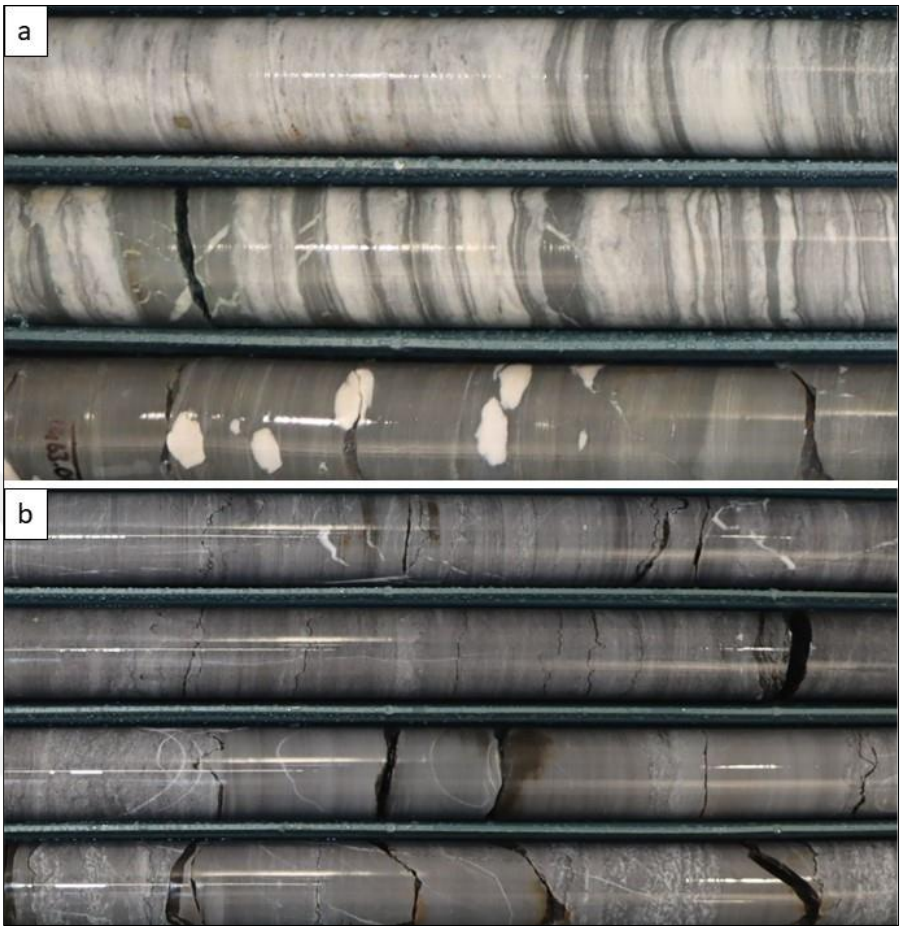


Figure 3.5. a) Light green to grey colored laminated and bedded claystone with medium size calcite nodules in Lower Çığlı Group (drill hole MS22DD029, 1462.40 m) b) Bottom of the Lower Çığlı Group shows thinly bedded limestones with styloliths (drill hole MS22DD029, 1620 m).

3.2.3 Middle Çığlı Group

The Middle Çığlı Group conformably overlies the Lower Çığlı Group and the transition between the two is marked by the appearance of reddish to brownish, clastic sedimentary layers. The emergence of these lithologies are interpreted to indicate a switch from marine to sub-aerial continental to transitional coastal plain

depositional environment (Perinçek et al., 1992). These predominantly tidal flat to sub-tidal conditions extend towards Iran to the east (Perinçek et. al., 1992).

Rocks of the Middle Çığlı Group crop out to the west of a major NW-SE structure in the central part of the study area. In drill core, the Middle Çığlı Group starts with the bedded red-pinkish, fine-grained, limey claystone/mudstone layers (Figure 3.6), which were only observed within the Middle Çığlı Group. The maximum thickness of this formation is estimated to be 120–135 m based on drill core observations.

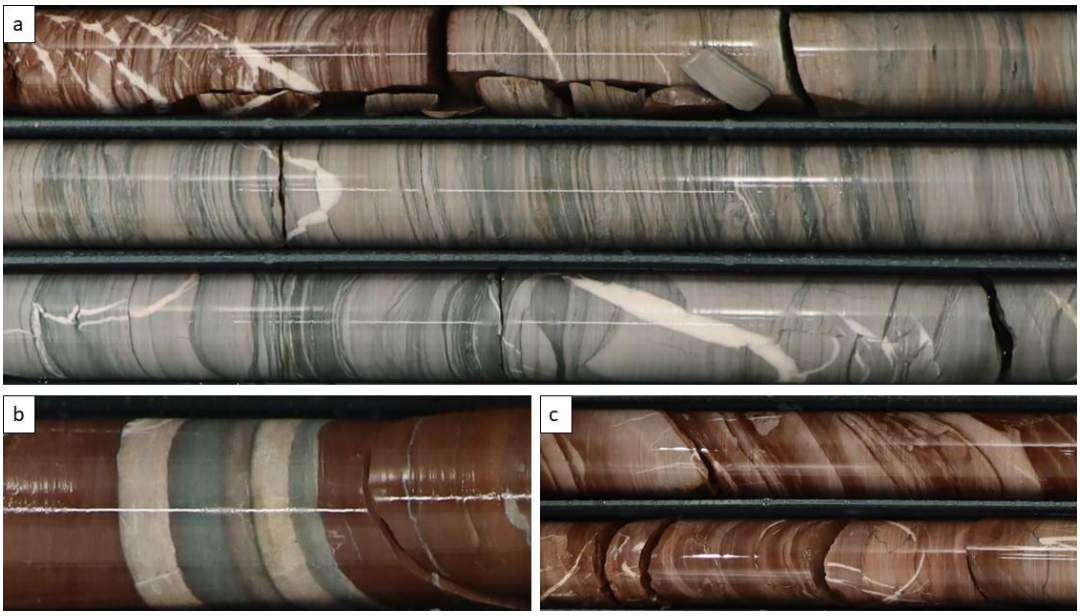


Figure 3.6. a) The characteristic reddish-pinkish, thinly-bedded, fine-grained, lime mudstone layers of the Middle Çığlı Group on (drill hole MS22DD029, 1338 m), b) Bedding-parallel calcite cross-cutting green to reddish-pinkish claystone/mudstone (drill hole MS22DD029, 1361.40 m), c) Reddish-pinkish, thinly-bedded mudstone/ claystone (drill hole MS22DD029, 1310 m).

3.2.4 Upper Çığlı Group

According to Perinçek (1992), Upper Çığlı Group proposed a shallow marine to transitional continental depositional setting for the Upper Çığlı Group similar to Middle Çığlı Group.

In and around the Meskan deposit, the Upper Çığlı Group starts with the green-colored claystone/mudstone that is rich in organic matter (Figure 3.7). Presence of

organic matter imparted a local black color to this formation. The lower part of the formation is dominated by dark grey limestone, dolomite, and dolomitic limestone. A significant increase in the siliciclastic component upward within the sequence is accompanied by a change into more greenish colors. The middle part of Upper Çığlı Group is commonly made up of medium to dark grey, thinly-laminated and well-bedded carbonates (Figure 3.7b). The maximum thickness of this formation is approximately 450–480 m.

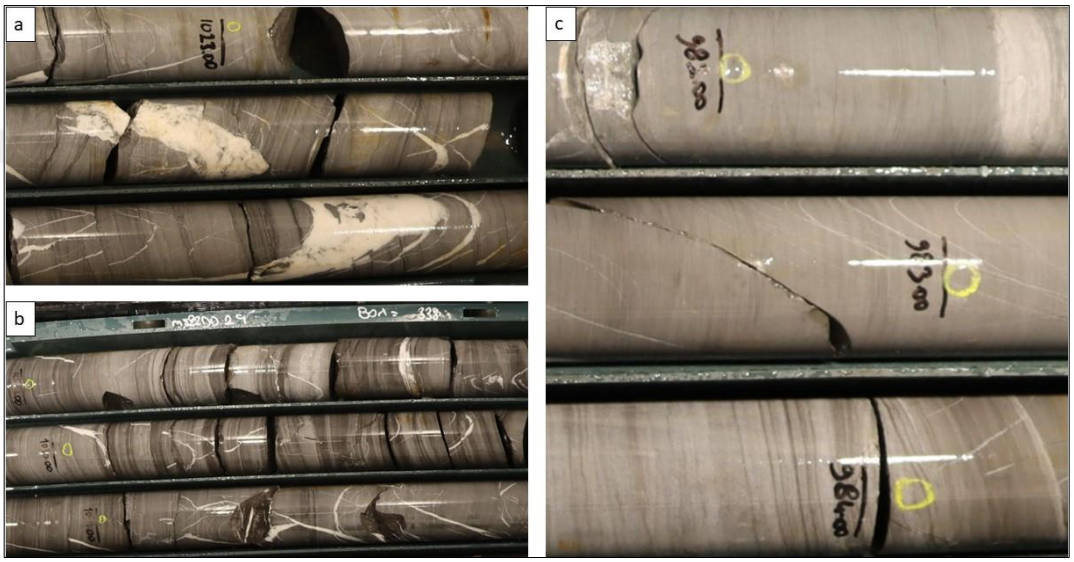


Figure 3.7. a) Thick carbonate vein in thinly-laminated grey-black limestone (drill hole MS22DD029, 1024 m), b) Greyish to black, millimetric to medium darker multiple limestone bands in the middle part of the Upper Çığlı Group (drill hole MS22DD029, 1029–1031 m), c) Massive, fine-grained dolostone at the upper levels of the Upper Çığlı Group (drill hole MS22DD029, 982–984 m).

3.2.5 Lower Çanaklı Formation

The lower part of the Çanaklı Formation is characterized by limestone and dolostone with the evaporitic layers, chert, and shale (Perinçek et. al., 1992). In Meskan deposit, the Lower Çanaklı Formation, the Middle Çanaklı Formation, and the Upper Çanaklı Formation are the three new formations that have been identified inside the Çanaklı Formation.

Lower Çanaklı Formation is predominantly made up of thin- to medium-bedded, dark colored, argillaceous, bituminous limestone interbedded with thin layers of shale-siltstone and local thick, dolomitized limestone beds (Figure 3.8). Lower Çanaklı Formation has the greatest maximum thickness compared to other formations in the study area with thicknesses reaching up to 590 m.

At the surface, massive, thinly- to thick-bedded, and finely-laminated dolomitized limestone forms prominent tower units at the base and top of the Lower Çanaklı Formation (Figure 3.10b). Thin chert bands were also locally observed. The limestone and dolostone units of the Lower Çanaklı Formation typically consist of sedimentary and collapse breccias (Figures 3.8b and 3.9). Morrow (1982) classification is used for a descriptive sub-division of breccias in the Meskan deposit. The space within interfragments, the orientation and proximity of these fragments are crucial to distinguish breccias. Different orientation (crackle, mosaic, and rubble) and different mutual proximity (pack and float) are identified in Meskan deposit. Medium size, moderately sorted, sub-angular, monomictic, clast- to matrix-supported, calcite-cemented vein breccia (Figure 3.8d) and fine- to medium-grained, very poorly-sorted, angular, polymictic, clast- to matrix-supported, angular carbonaceous or black matrix float breccia (Figure 3.8e) is observed in drill core samples. Sulfide minerals including pyrite were also detected within the Lower Çanaklı Formation in drill core.

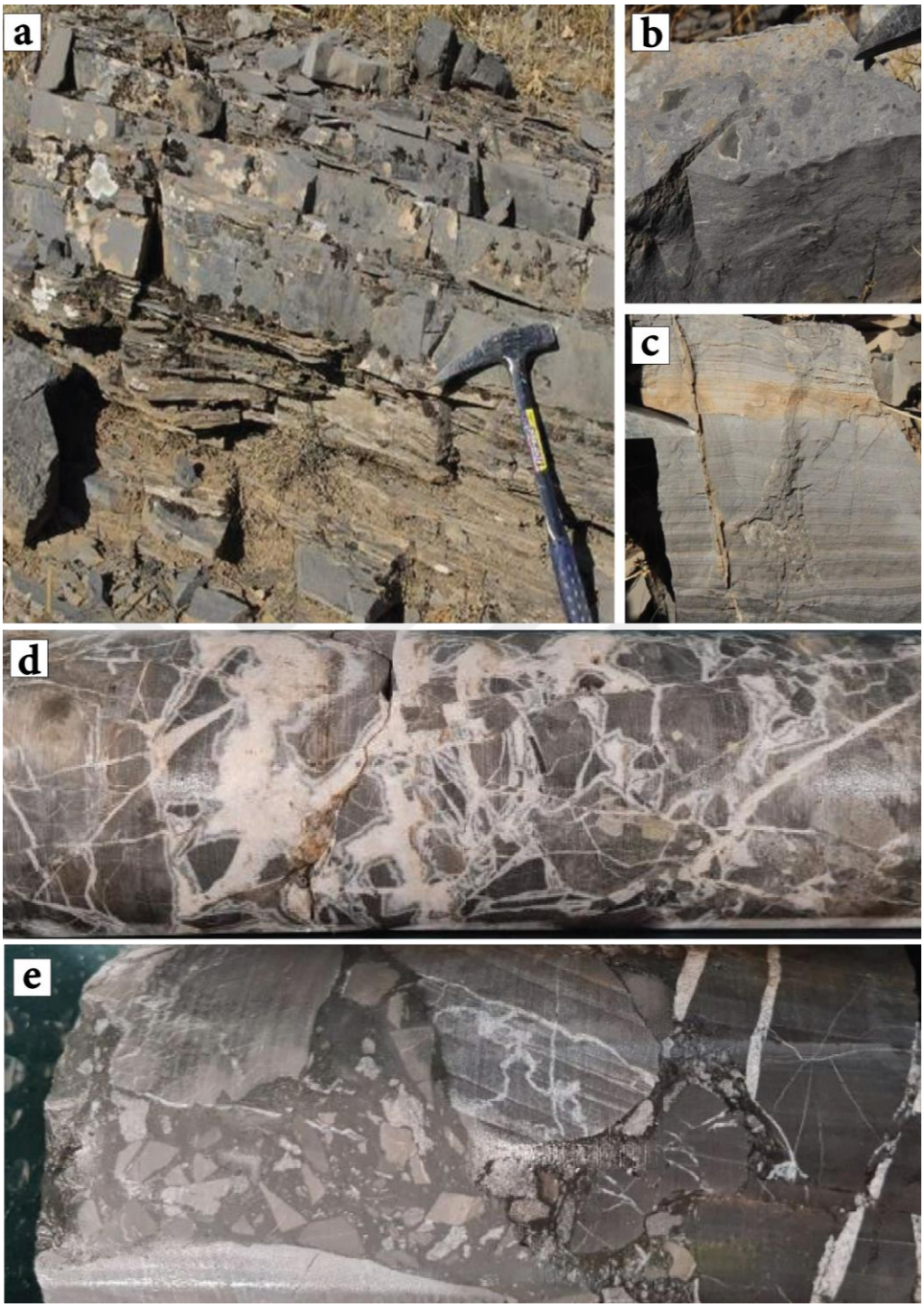


Figure 3.8. Outcrop and drill core photographs of units of the Lower Çanaklı Formation. a) Intercalations of thin- to medium-bedded dark-grey limestone, b) sedimentary microbreccia, c) Thinly-laminated, fine-grained limestone (CSA unpublished report, 2020), d) Calcite-cemented vein breccia (drill hole MS23DD062-A), e) Black matrix float breccia with angular fragments (drill hole MSUGDD0003).



Figure 3.9. Black matrix sedimentary breccia in Lower Çanaklı Formation (drill hole MS22DD029, 903.50–906.20 m).



Figure 3.10. Dark grey to black colored, fractured, fine-grained carbonaceous limestone with irregular crackled calcite vein(let)s in the top of the Lower Çanaklı Formation (drill hole MS22DD029, 633.70–641.00 m and 598.90–601.25m).

3.2.6 Middle Çanaklı Formation

Middle Çanaklı Formation is part of the stratigraphic succession in the Meskan deposit that hosts the main Zn-Pb sulfide ore body. In earlier studies by Perinçek (1990 and 1992) this formation was referred to as the Çanaklı Formation.

Middle Çanaklı Formation is distinguished by the emergence of algal-laminated sedimentary layers and also by the appearance of zebra texture, a key feature of this formation. The thickness of the main mineralized unit in the Middle Çanaklı Formation varies between 180 and 200 m. Just below the mineralization, a zone of strong brecciation commonly appears in drill core. Breccias at these levels are clast- or matrix-supported and carbonate-cemented. Breccia clasts are primarily composed of limestone and occasionally dolostone still preserving a thinly- to medium-bedded appearance. These clasts are identified as grainstone based on the classification of Dunham (1962). The formation typically exhibits bedding at a scale of 1–20 cm and is frequently finely-laminated. In the outcrop, the Middle Çanaklı Formation is also distinguished by several beds of ferruginous gossan, which presumably derived from sulfide minerals that have undergone weathering and oxidation (Figure 3.11). Such layers are particularly well-developed at the upper levels of Meskan West zone, near the military base. In the non-weathered drill core intervals, pyritic shale units are both soft and rich in organic carbon giving this unit a black appearance (Figure 3.12).

Another distinguishing feature of the Meskan Tepe Formation, the zebra texture, is defined by alternating layers of fine-grained, grey and coarse-grained, sparry white dolomite (Figure 3.13). Where mineralized, fine-grained dolomite layers have been selectively replaced by various sulfide minerals such as sphalerite, galena, pyrite, and marcasite (Figure 3.13). The oxide mineralization occurs as orange to brown colored, gossanous assemblages observed mostly within shear or fault zones. Gossans include iron oxide minerals (mainly hematite) and less commonly zincite, smithsonite, and cerussite. Contrary to sulfide mineralized levels, in the oxidized levels, zebra texture is not discernible (Figure 3.13).

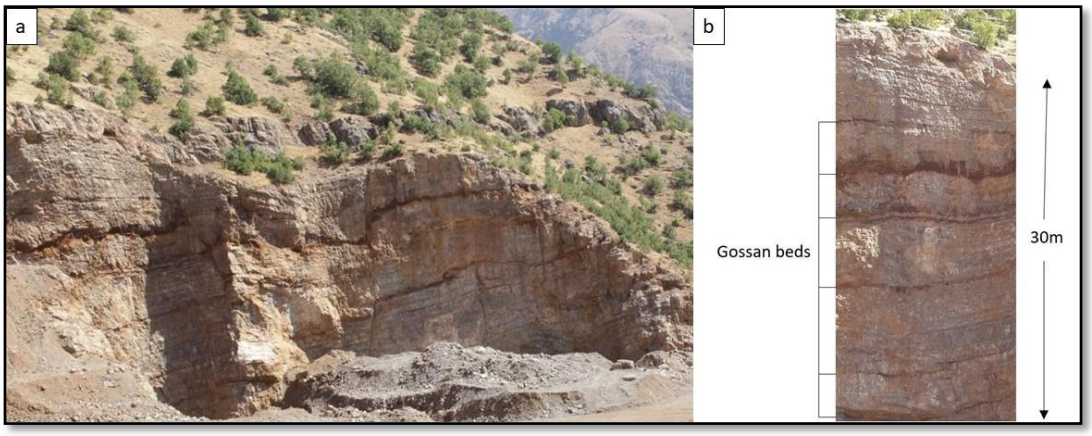


Figure 3.11. a) Multiple gossanous horizons within the Middle Çanaklı Formation, with the main mineralized horizon. The prominent limestone outcrop in the ridge above the workings comprises rocks of the Middle Çanaklı Formation, b) Upper part of the Middle Çanaklı Formation showing its thinly-bedded texture with gossan layers (unpublished company report, 2020).



Figure 3.12. Black-colored, carbonaceous limestones with pyritic shale units (drill hole MSUGDD0023).

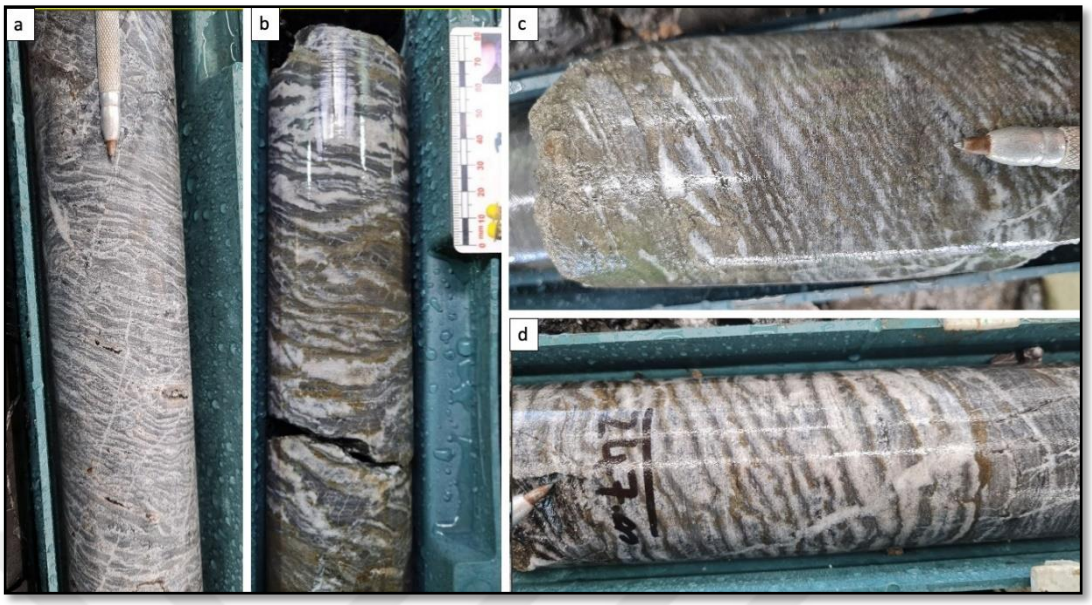


Figure 3.13. a) Barren, banded dolomite layers showing characteristic zebra texture (drill hole: MSUGDD012; 252.35 m), (b–d) Pyrite replacement of fine-grained dolomite layers in zebra-textured carbonate units of the Middle Çanaklı Formation (drill holes: MSUGDD017; 296.70 m and MSUGDD023; 247.00 m).

3.2.7 Upper Çanaklı Formation

The top of the Upper Çanaklı Formation is identified as a well-bedded sequence located above the initial extensive carbonate layer of the Upper Çanaklı Formation, situated above the mineralized zone. The maximum thickness of this formation is determined to be about 363 m in Meskan East. However, it has a greater thickness in the Meskan West as revealed by drilling. According to Allen et al. (2020; unpublished company report), this formation is composed of well-layered carbonate mudstone (micrite) with interbeds of grainstone, frequently exhibiting ripple-scale cross-lamination and layers of shale. Micritic layers typically display a dark and bituminous nature and consists of fracture-filling graphite and hematite.

The top of the Çanaklı Formation starts with massive and thick bedded carbonate level. Powder dolostone with lime-mud turns to sugary dolostone. This formation is mostly dolomitized often with a more coarse-grained recrystallized texture than the formations below. Thick irregular calcite and barite veins are observed in the drill core samples.

3.3 The Meskan Zn-Pb Mineralization

3.3.1 Exploration history

The Meskan deposit constitutes one of the most significant Zn and Pb mineralizations in the Hakkari district. The shallow, oxidized portion of the Zn-Pb ore is currently being mined by the local mining company, the Ölmezler Mining (OM), which as of date operates more than ten underground galleries.

The Meskan deposit contains stratabound carbonate replacement Zn-Pb mineralization that extends over several kilometers in the Triassic host stratigraphy. Host rocks are typically the reduced facies calcareous rocks near the base of the thick, shallow marine carbonate units of the Middle Çanaklı Formation (Hanilçi et al., 2020) overlying the dominantly clastic sequence of the Lower Çanaklı Formation.

Different types of veins are observed in the carbonate rocks of the Meskan Zn-Pb deposit during fieldwork and in drill core. Stockwork or irregular veins with crystalline carbonate (dolomite or calcite) infill are ubiquitous at Meskan. Irregular, brecciated calcite and dolomite veins are also quite common. Some of the veining appears to be associated with mineralization, as evidenced by a general increase in intensity towards the mineralized horizons and occurrence of sulfides in veins close to or within the ore zone. The intensity of veining is generally controlled by the host lithology and this is suggested to reflect the rheological properties of various units (Reynolds, 2020). Veining is best developed in the thinly-bedded, micritic and grainstone units that have been intensely dolomitized.

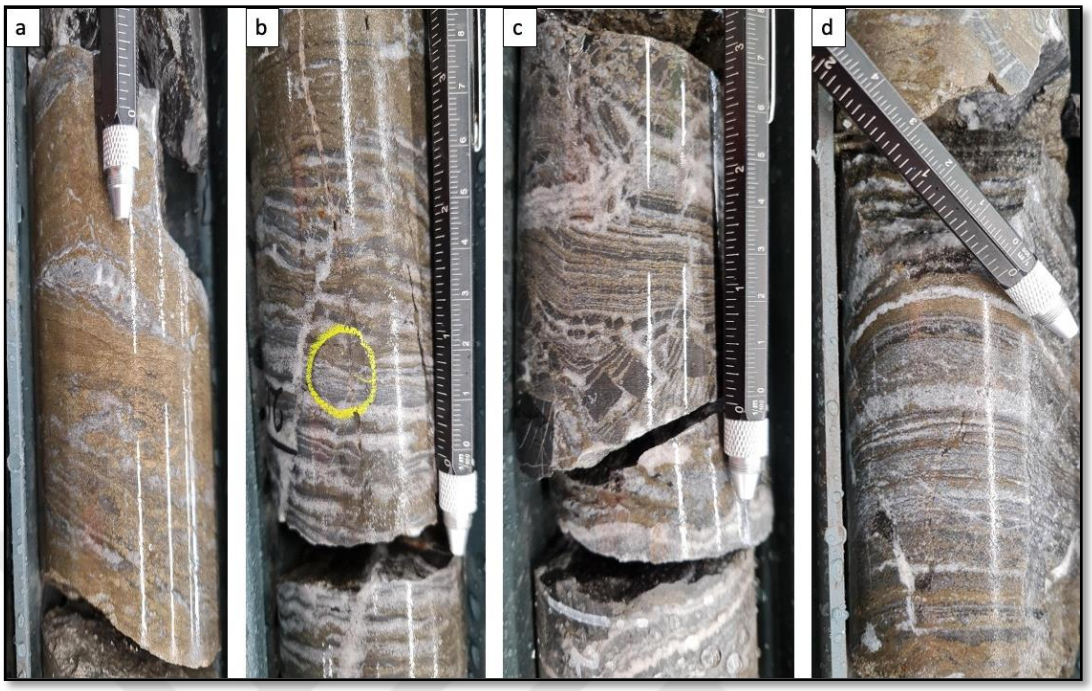


Figure 3.14. Drill core photographs of zebra textured sulfide-rich ore a) Pyrite-only semi-massive sulfide mineralization, b) Alternating bands of pyrite and calcite layers are discontinuous due to folding and local brecciation, c) Banded ore that has undergone folding and faulting, d) Bedded and layered pyrite in carbonaceous limestone (drill hole MSUGDD0035).

There are three well-developed ore zones identified at Meskan: i) Meskan Tepe, an open cut on top of Meskan Hill Tepe mountain, ii) Şaho Gallery, the primary mining region, and iii) Meskan West, the recently tested area along the western ridge at Meskan Tepe (Figure 3.1. and 3.15). These areas are separated geographically by about 1.5 km and geologically by the Meskan Tepe Fault.

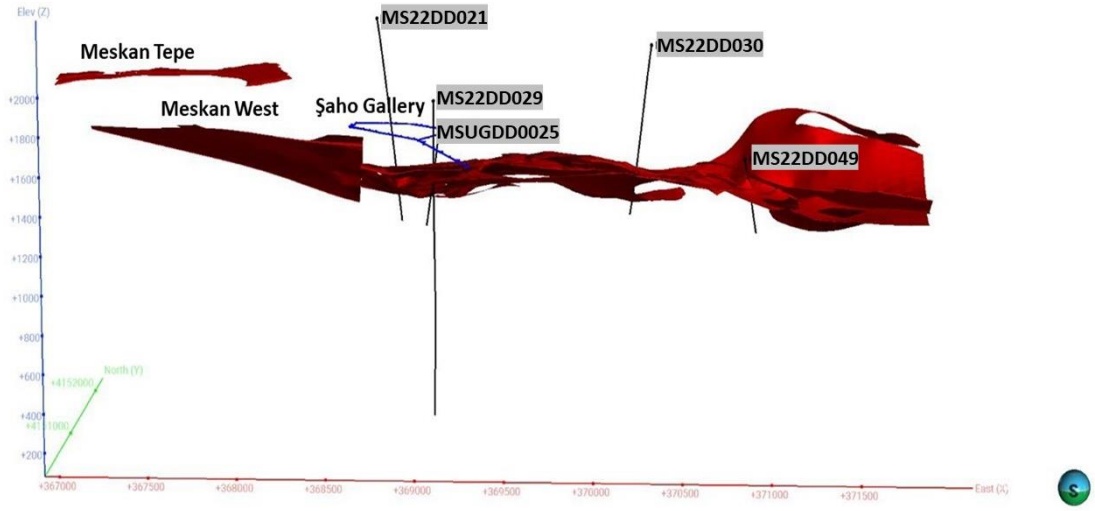


Figure 3.15. The locations of the Meskan Tepe, Meskan West, and Şaho Gallery ore zones (image looking north). Traces of studied drill holes are also shown.

The Meskan Tepe (Figure 3.16) ore zone is located ~1.5 km to the west of the Şaho Gallery (Figure 3.15). In this zone, there are several drill holes collared from the surface, near the top of the hill where oxide ore is mined. Meskan Tepe mineralization lies along the ridge to the west of the military base. On the footwall block of the Meskan Tepe Fault, the Şaho Gallery mineralization and the Meskan Tepe mineralization are aligned at the same stratigraphic level. Moving west along the Meskan Tepe ridge reveals an abundance of steeply-inclined structures and fractures, which trend from NNE to NNW, that play a crucial role in determining the present distribution of mineralization and stratigraphy (Allen et al., 2020). The mineralization in Meskan Tepe is largely stratabound. The thickness of mineralization in Meskan Tepe does not exceed 2.5–3.0 m. Nevertheless, there are more than one thick mineralized horizon is existed, in addition to thin gossanous horizons in the hanging wall of Middle Çanaklı Formation (Figure 3.16). Mineralization within Şaho Gallery is present as a tabular, stratabound ore exposed over a strike length of about 2.1 km along the northern side of the valley. The length of this gallery is 3670 m.

Mineralization in the Meskan West has been exposed in an open cut in 2018 that was operated by OM. Oxidized ore in this zone was partly mined, but the nature of

mineralization is not well-defined. Nevertheless, there are indications of both stratabound and cross-cutting oxide mineralization. Mineralization is cut by a steeply-dipping structure, but the offset in the Meskan West ore body seems to be smaller compared to that observed in the main Meskan Tepe mineralization. This resulted in a more laterally continuous stratigraphy being preserved overlying the Meskan West ore body.

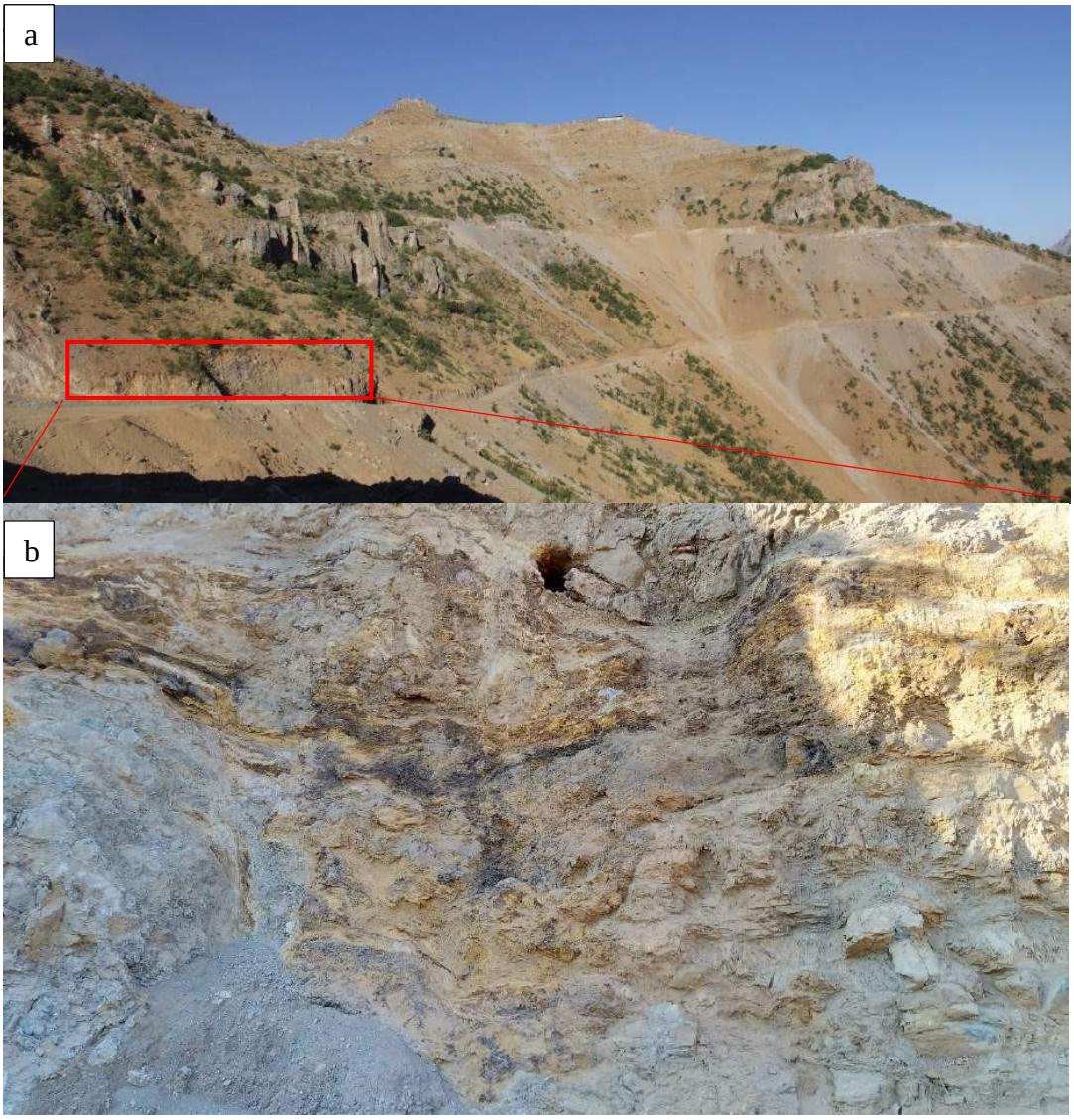


Figure 3.16. a) View of the Meskan Tepe ore zone (looking east), b) Close-up view from irregular oxide mineralization at the northern part of Meskan Tepe.

3.4 Petrographic Studies

3.4.1 Microscopic Features of the Host Rock

Host rock mineralogy is composed of micritic layers that appear texturally homogenous under the microscope. Micrite is represented by very fine-grained calcite below the main mineralized unit (Lower Çanaklı Formation; Figure 3.17). In contrast to other calcareous units, the black-colored sedimentary succession has a heterogeneous character and is also distinct in terms of composition and texture. Micritic layers consist of bitumen and/or graphite, suggesting that this succession is rich in organic matter. Thin section observations show that alternating micritic mud and dolomitic layers were deposited repetitively (Figures 3.17b and 3.18c). Apart from micritic layers, laterally extending dolomitized layers were also observed in this formation. Dolomitization is quite common in the Irish-type deposits. In the light to dark brown dolomitic layers, clasts are mostly made up of dolomite and fine-grained micrite (Figure 3.18b).

Weak fissility developed oblique to original bedding is due to the presence of stylolites as observed in the thin sections of samples from this formation (Figure 3.19b). Stylolites formed through pressure dissolution of soluble minerals, thereby reducing the overall volume of the rock (Dunham and Larter, 1981). Insoluble organic matter and minerals like pyrite, and clay remain along stylolite planes.

Diagenetic pyrite was also observed commonly within the micritic layers. This form of pyrite is very fine-grained and occurs primarily as framboidal crystals, which upon deformation, were partly recrystallized into coarser (but still fine-grained), subhedral pyrites.

XRD analysis carried out on host rock samples confirmed predominance of calcite, dolomite, and graphite at levels immediately below the mineralized unit with minor amounts of nickel-bearing oxides. Other phases tentatively identified through XRD analyses are ankerite, rutile, and argentite (Appendix A).

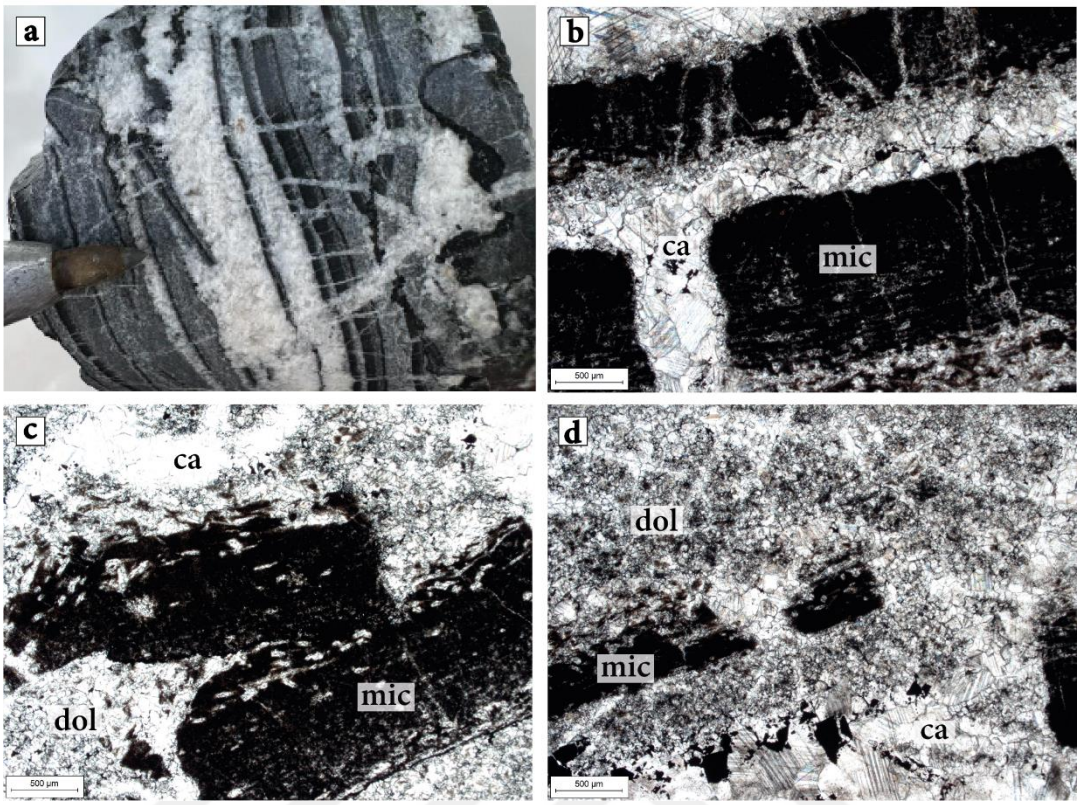


Figure 3.17. Representative macro- and microphotographs of carbonaceous limestone with calcite vein (drill hole MSUGDD0025, 490.40 m). a) Macrophotograph of banded, grey- to black-colored carbonate rock. Black layers are made up of very fine-grained, micritic calcite, whereas grey layers are dominated by dolomite. Hydrothermal sparry calcite veins (white) cross-cut the original lamination, b) Microphotograph of repetitive layers of dolomite and micritic layer with sparry calcite (XPL, TL), c) Dolomitic and micritic layer includes sparry calcite at the edge of the microphotography (XPL, TL), d) Brecciated layers of coarser, dolomite-rich and micritic calcite-rich layers partly replaced by coarse-grained hydrothermal calcite (XPL, TL).

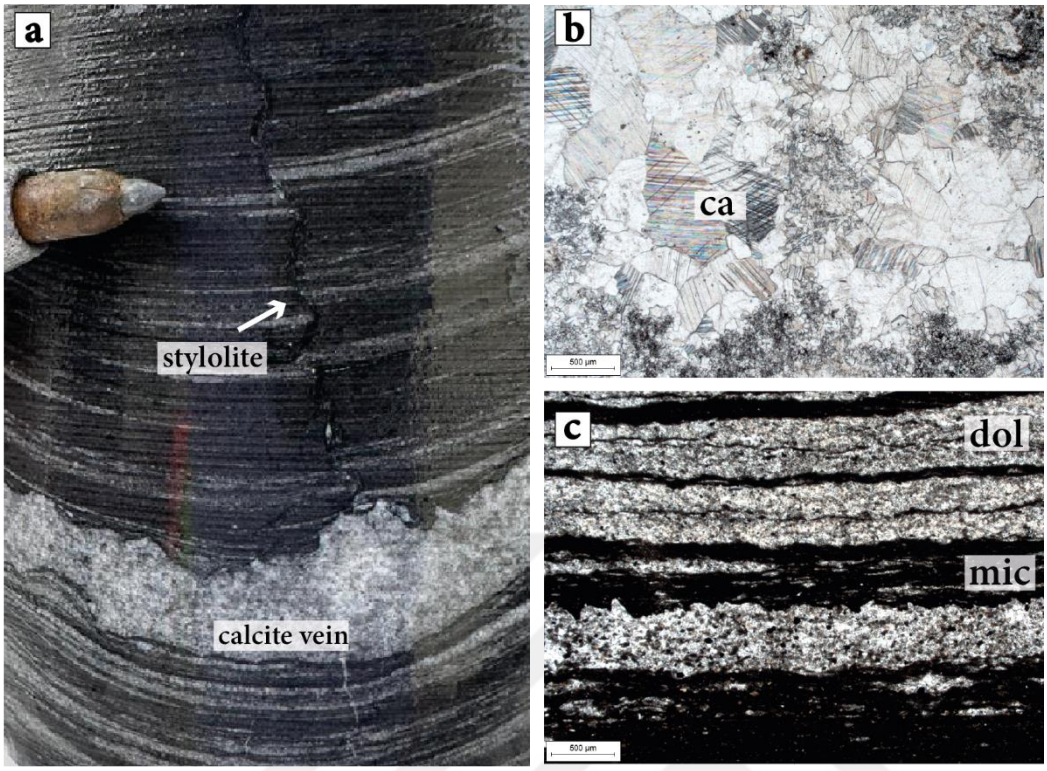


Figure 3.18. Macrophotograph of finely-laminated carbonaceous limestone of the Lower Çanaklı Formation (drill hole: MSUGDD0025, 423.85 m), b) Microphotograph of sparry calcite (XPL, TL), c) Microphotograph of repetitive succession of dolomitic layer and micritic layer that rich in organic carbon (XPL, TL).

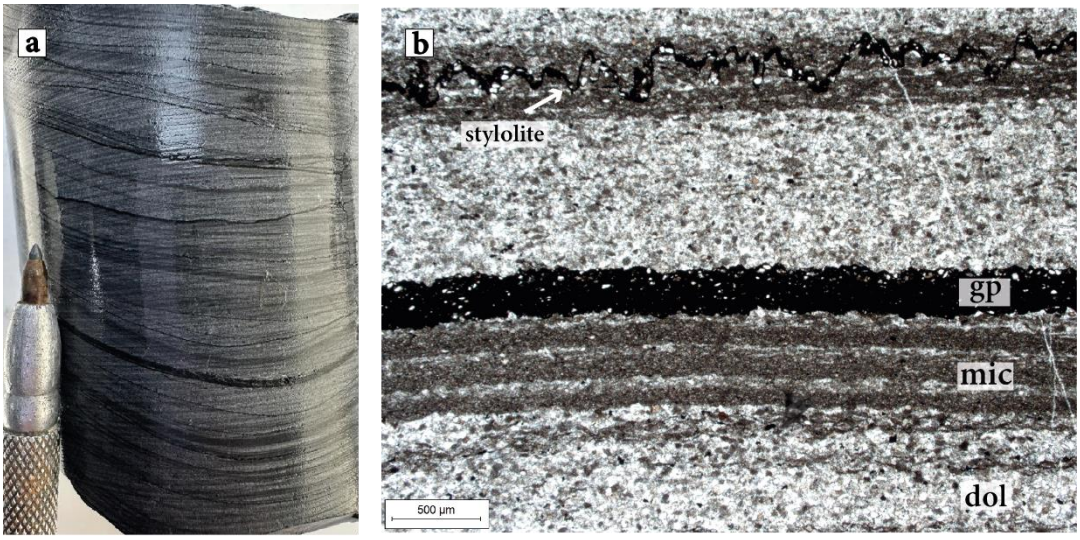


Figure 3.19. Macrophotograph of bedded carbonaceous limestone in Lower Çanaklı Formation (drill hole: MSUGDD0025, 408.50 m), b) Microphotograph of repetitive succession of dolomitic layer and micritic layer with rich in dark-colored graphite consists of stylolite (XPL, TL).

3.4.2 Sulfide Mineralization and Ore Paragenesis

The primary Pb-Zn ore at Meskan is characterized mainly by fine- to medium-grained, and occasionally coarse-grained sulfide minerals. The sulfide assemblage is mostly comprised by pyrite, with minor brown sphalerite. Ores are commonly banded, including colloform and zebra-type banded textures. Banded ores are also locally intensely-brecciated. Ore textures are highly variable and include massive, brecciated, disseminated, interbedded, and banded/zebra textures (Figure 3.20).

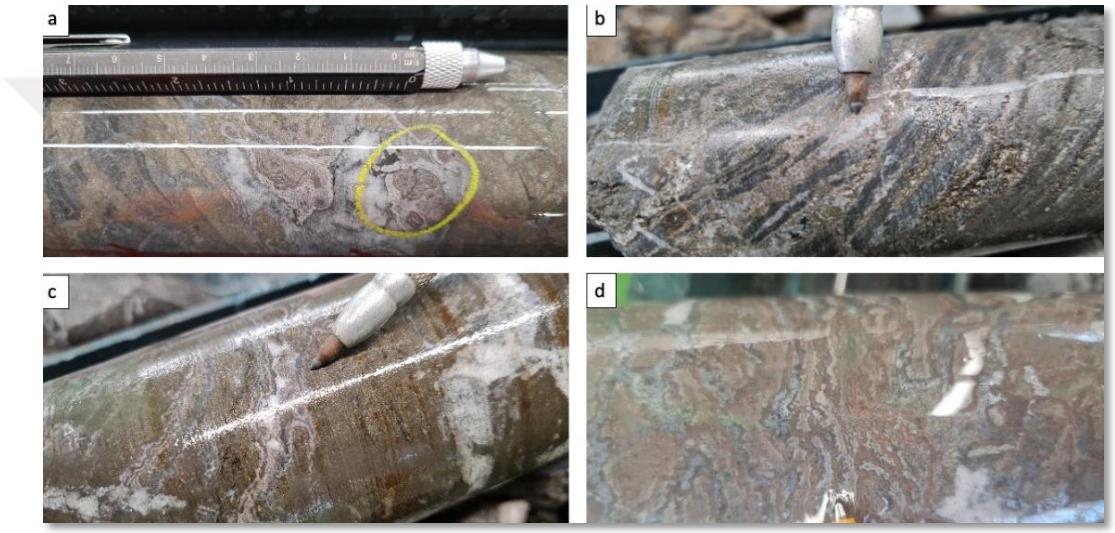


Figure 3.20. a) Grey to beige, latte colored colloform-banded sphalerite, b-c) Banded pyrite and sphalerite in semi-massive sulfide mineralization, d) Color variation (latte and red-brown) in sphalerite (drill hole MSUGDD0023, 373 m).

The sulfide mineralogy of the Meskan Pb-Zn orebody is relatively simple, containing multiple generations of pyrite, sphalerite, galena, and marcasite with rare sulfosalts (Figure 3.20). Common gangue minerals include dolomite and calcite, both from the host rocks (i.e., finely-laminated carbonaceous limestone) and also present as late stage vug/breccia infill. Barite is locally present in the ores. Apart from calcite and organic material (bitumen), this unit also contains very fine- to fine-grained, anhedral to subhedral pyrite (py-I) of probable diagenetic origin (Figure 3.21).

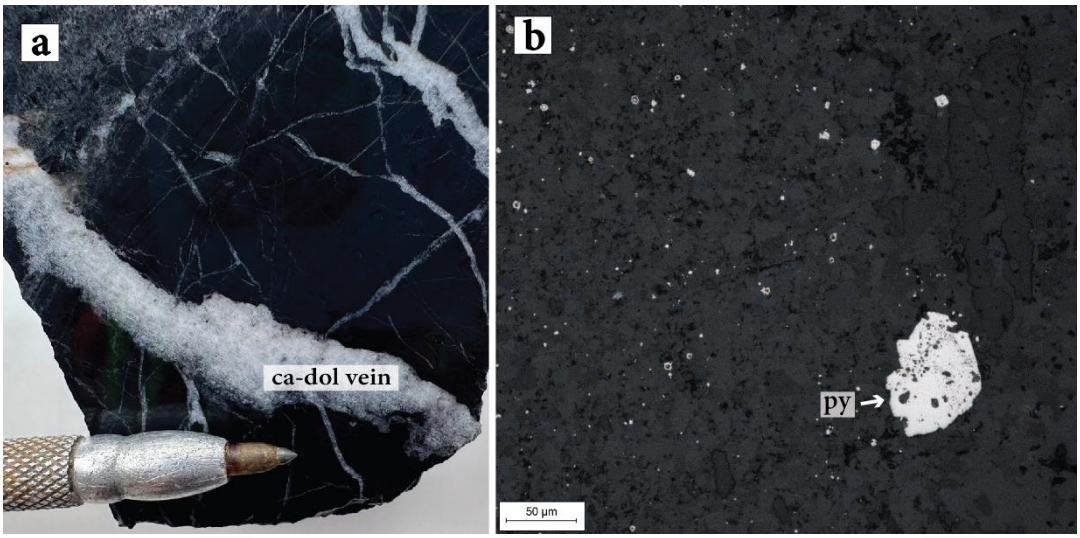


Figure 3.21. a) Hand specimen photograph of dark colored, organic-rich, carbonaceous limestone with calcite-dolomite vein (drill hole: MSUGDD0025, 306.50 m), b) Microphotograph of very fine-grained diagenetic pyrite (RL, PPL).

The proportion of sphalerite and overall sulfide minerals in the rock increases moving down the sequence, and the sulfides gradually transgress bedding as semi-massive replacement ores. Semi-massive sulfides are found at the base of this unit as replacement or matrix-fill in the dissolution breccias (Figure 3.14). The basal semi-massive sphalerite-pyrite mineralized layer contains remnant breccia fragments and late sparry dolomite. Sphalerite in most analyzed samples is medium-brown in color and is coarse-grained. A second type of sphalerite, as commonly observed in drill holes collared from underground, is pale brown to yellowish and shows regular banding (Figure 3.20a). Galena is frequently identified alongside sphalerite. Zebra texture and colloform banding including pyrite-sphalerite or pyrite-sphalerite-galena assemblages are generally observed in the semi-massive and massive sulfide zones.

Colloform-banded and zebra ores are commonly brecciated resulting in development of multiple overprinting textures. A simple sulfide paragenesis was established based on these overprinting relationships. Early colloform-banded and zebra ore is either dominated by coarse-grained sphalerite in the massive to semi-massive ores or by pyrite in barren zebra-textured intervals. Where sphalerite (sph-I) dominates it generally forms well-developed botryoidal crystals. This sphalerite is intergrown with very fine-grained pyrite (py-II; Figure 3.22b). Botryoidal intergrowths of

sphalerite and pyrite are cross-cut and enveloped by a second generation of anhedral to subhedral, fine- to medium-grained porous pyrite (py-III) and lesser marcasite alongside calcite (Figure 3.22e, f). This stage of sulfide precipitation is followed by banded sphalerite (sph-II), galena (gn-II?), pyrite (py-IV), and marcasite (Figure 3.22b, d). Pyrite of this stage (py-IV) may not actually be a late stage product, but is likely formed due to intense recrystallization due to syn- to post-mineralization deformation. A relatively minor sulfide/sulfosalt phase also appears to be intergrown with paragenetically-late galena (gn-II). This was tentatively identified as boulangerite ($Pb_5Sb_4S_{11}$), as also confirmed through XRD analyses. Other possible rare ore and gangue phases identified in the mineralized rocks based on XRD analyses include renierite ($(Cu,Zn)_{11}(Ge,As)_2Fe_4S_{16}$), strontianite ($SrCO_3$), hydrozincite ($Zn_5(CO_3)_2(OH)_6$), hemimorphite ($Zn_4(Si_2O_7)(OH)_2 \cdot H_2O$), carlinite ($Tl_2S$), germanite ($Cu_{26}Ge_4Fe_4S_{32}$), and semseyite ($Pb_9Sb_8S_{21}$) (Appendix A).

All mineralized samples studied petrographically displays textural evidence for some sort of deformation, mainly represented by cataclasized sulfide minerals. Brecciation is common both at the hand specimen and also at the microscopic scale, where host rock and sulfide clasts are surrounded within a matrix dominated by coarse-grained, sparry calcite. Apart from this, sulfide minerals of almost all stages are intensely fractured. Pyrite in particular shows the most intense deformation represented by recrystallization into coarser, pristine crystals (py-IV) followed by cataclasis. As a result, it has been locally comminuted into fine-grained, anhedral crystals (Figure 3.20a, 3.22d, 3.24b, d). Other main sulfide phases such as galena and sphalerite do not show such textures, possibly due to their lower hardness. Still, where deformation is intense, galena occurs as stretched crystals.

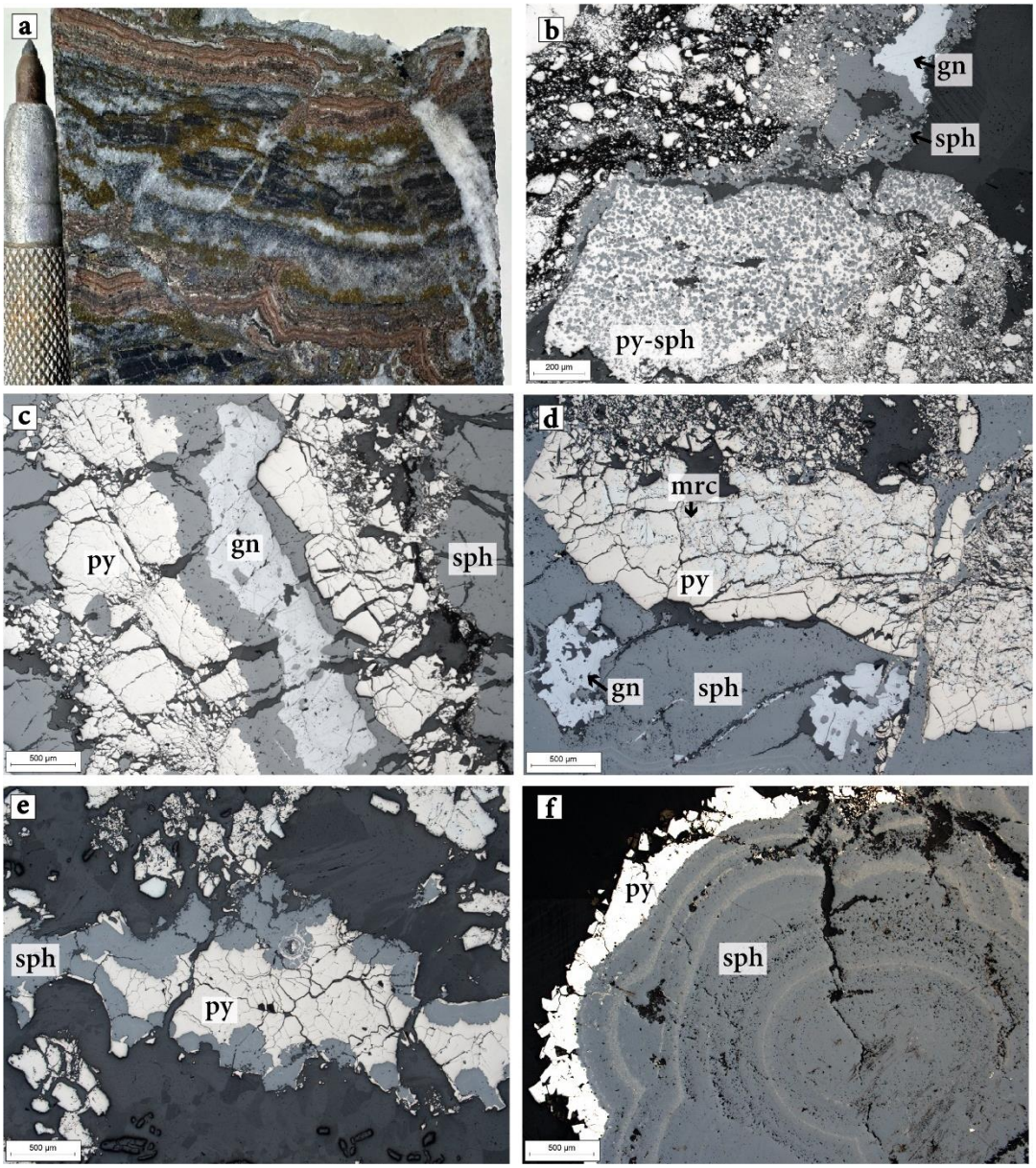


Figure 3.22. Representative hand specimen images and microphotographs of sulfide mineralization at Meskan. a) Hand specimen photograph of colloform-banded, latte-colored sphalerite with pyrite and sparry calcite layers (drill hole: MSUGDD0025, 291.85 m), b) Microphotograph of cataclasized and locally recrystallized fine-grained pyrite (py-IV) alongside sphalerite (sph-II), and galena (gn-II?) (XPL, RL), (c) Microphotograph of banded pyrite (py-III), sphalerite (sph-II), galena (gn-I) ore that has been intensely fractured and cataclastic pyrite, botryoidal? sphalerite and galena (XPL, RL), d) Moderate to highly deformed pyrite with marcasite inside the pyrite, fine grained galena and sphalerite (XPL, RL), e) Sphalerite at the edge of pyrite (pyIII) (XPL, RL), f) Colloform-banded layers of sphalerite (sph-I) and very fine-grained pyrite (py-II) surrounded by a paragenetically later generation of pyrite (py-III) (XPL, RL).

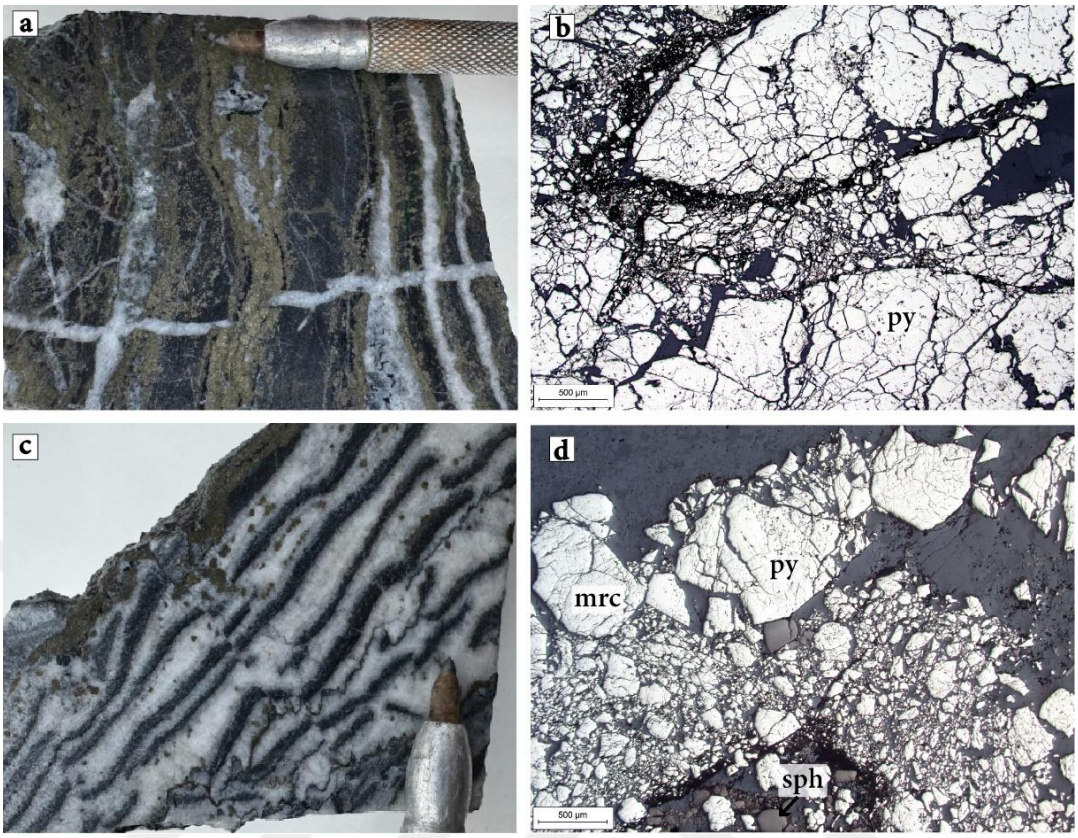


Figure 3.23. a) Hand specimen photograph of zebra-textured pyrite, in which alternating bands of pyrite, organic-rich limestone (black), and white, sparry calcite are visible. Sparry calcite veins also cross-cut the banding (drill hole: MSUGDD0025, 203.45 m), b) Intensely deformed, cataclastic pyrite (XPL, RL), c) Hand specimen of zebra textured, with tiny pyrite (drill hole: MSUGDD0025, 303.90 m), d) Very fine to medium grained pyrite, cataclastic marcasite, and sphalerite (XPL, RL).

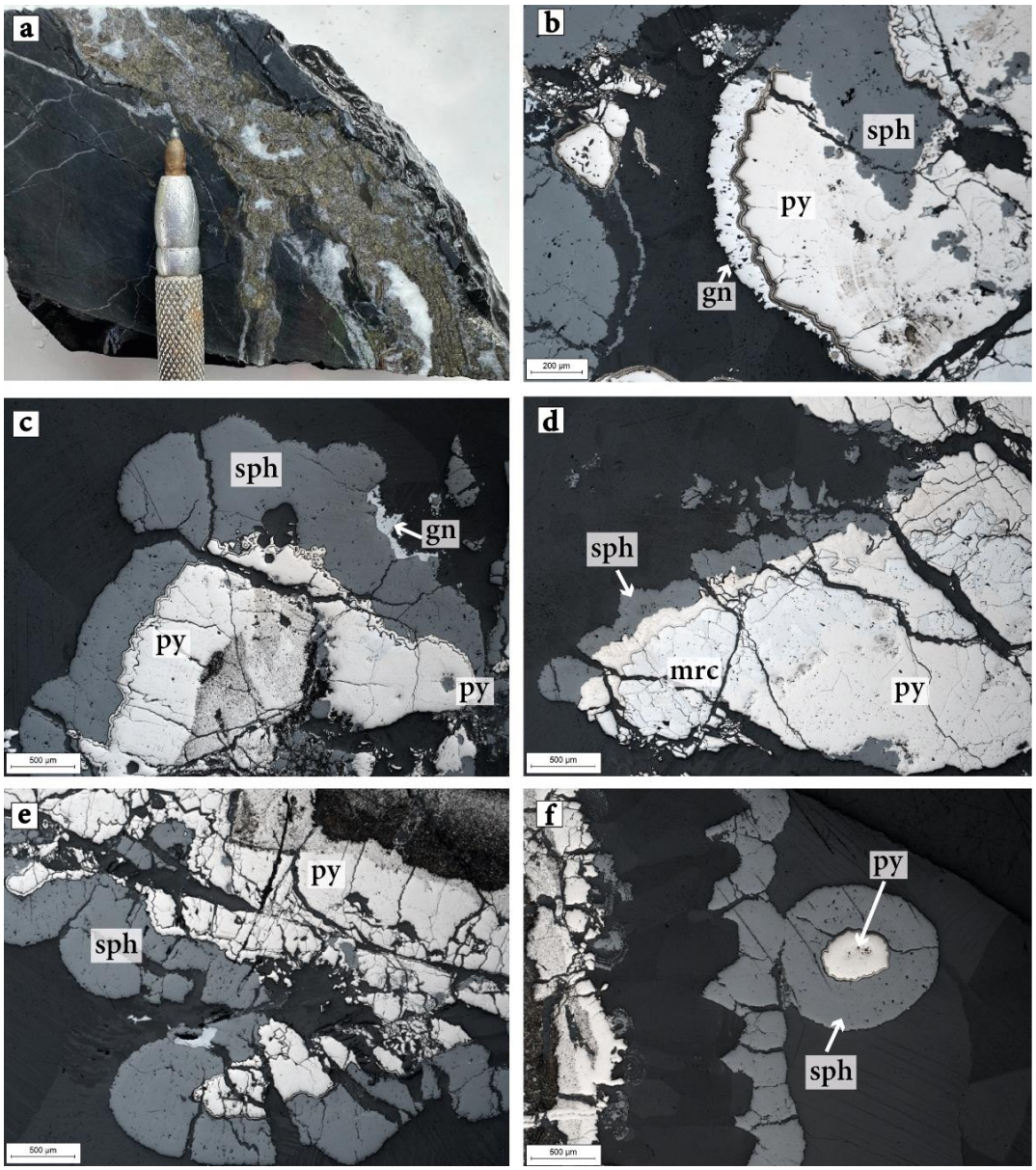


Figure 3.24. Representative hand specimen images and microphotographs of sulfide mineralization. a) Hand specimen photograph of pyrite, calcite vein from carbonaceous limestone (drill hole: MSUGDD0025, 281.40 m), b) Microphotograph of pyrite (py-III), sphalerite (sph-II), galena (gn-II) (XPL, RL), c) Galena at the edge of sphalerite (sph-II) that surrounds pyrite (py-III), d) Fine-grained pyrite (py-III) with marcasite surrounded by sphalerite (sph-III) (XPL, RL), e) Moderately deformed pyrite (py-IV) with fine grained sphalerite (sph-II) (XPL, RL), f) Well-developed sphalerite inside the pyrite (XPL, RL).

3.5 Lithogeochemistry

A total of 439 samples of mostly carbonate rocks from five different drill holes have been analyzed for their major, minor, and trace element (including rare earth elements) compositions to understand the host rock characteristics and also to understand the geochemical changes associated with hydrothermal activity responsible from stratabound Pb-Zn mineralization. Sampling of the first few meters of the drill holes was avoided due to the possible secondary effects such as weathering as well as contamination.

3.5.1 Geochemical characterization of lithostratigraphic units

Lithogeochemical data obtained from drill core samples is examined in terms of major, minor, and trace element concentrations. Major elements are presented in their oxide forms alongside their weight percentages, whereas trace elements and REE are reported in parts per million (ppm) units except for Au, which is reported in parts per billion (ppb) units (Table 3.1). Table 3.1 also shows the analysis package of Bureau Veritas for lithogeochemical analysis (LF202) carried out in this study and from 5 drill holes and assay results (MA370) from each drill hole.

Table 3.1 Analysis method for measured elements

Analysis Method (from Bureau Veritas)	Detected Elements	Units
ICP-ES (MA370)	Ag	ppm
ICP-ES (MA370)	Al, As, Bi, Ca, Cd, Co, Cr, Cu, Fe, K, Mg, Mn, Mo, Na, Ni, P, Pb, S, Sb, Sr, W, Zn	percent
ICP-MS (LF202)	Ba, Be, Ce, Co, Cs, Dy, Er, Eu, Ga, Gd, Hf, Ho, La, Lu, Nb, Nd, Ni, Pr, Rb, Sc, Sm, Sn, Sr, Ta, Tb, Th, Tm, U, W, Y, Yb, Zr	ppm

ICP-ES (LF202)	SiO_2, Al_2O_3, Cr_2O_3, CaO, Fe_2O_3, K_2O, MgO, MnO, Na_2O, P_2O_5, TiO_2	percent
AQ200 (LF202)	Ag, As, Bi, Cd, Cu, Hg, Mo, Ni, Pb, Sb, Se, Tl, Zn	ppm
AQ200 (LF202)	Au	ppb

Using data derived from both carbonates and sandy/silty lithologies, the sedimentary succession in the Meskan Zn- Pb deposit is divided into 6 different lithologies identified as dolostone, dolostone±high silt, dolostone±low silt, limestone, limestone±high silt, and limestone±low silt.

Carbonate mineralogy, and proportions of carbonate: Silt fraction shows significant variation among various calcareous units at Meskan and so it is considered as one of the main distinguishing criteria during lithological classification. For data interpretation, sulfide-free compositions of samples were calculated to remove the dilution effects of the orebody, and also major oxides were converted into elemental abundances. Reported values below the detection limits were replaced with half of the detection limit value. Although most samples show broadly similar patterns, some significant differences were noted when checking lithostratigraphic correlations between the units.

As a first step for lithological classification, samples are classified as dolostone and limestone using their CaO contents. Samples with CaO concentrations >35 wt.% are classified as limestone and those with CaO contents <35 wt.% as dolostone. The CaO concentrations of dolostone and dolostone±silt units range between 1.38 and 29.69 wt.% (mean = 26.27 wt.%, n = 241), whereas the MgO contents of same units vary from 0.02 to 21.58 wt.% (mean = 13.30 wt.%; Figure 3.25). The range of CaO abundance in limestone and limestone±silt units is between 15.87 and 47.18 wt.% (mean= 41.45 wt.%, n= 198), whereas MgO contents of the same units vary from 0.07 to 5.47 wt.% (mean= 3.48 wt.%; Figure 3.25).

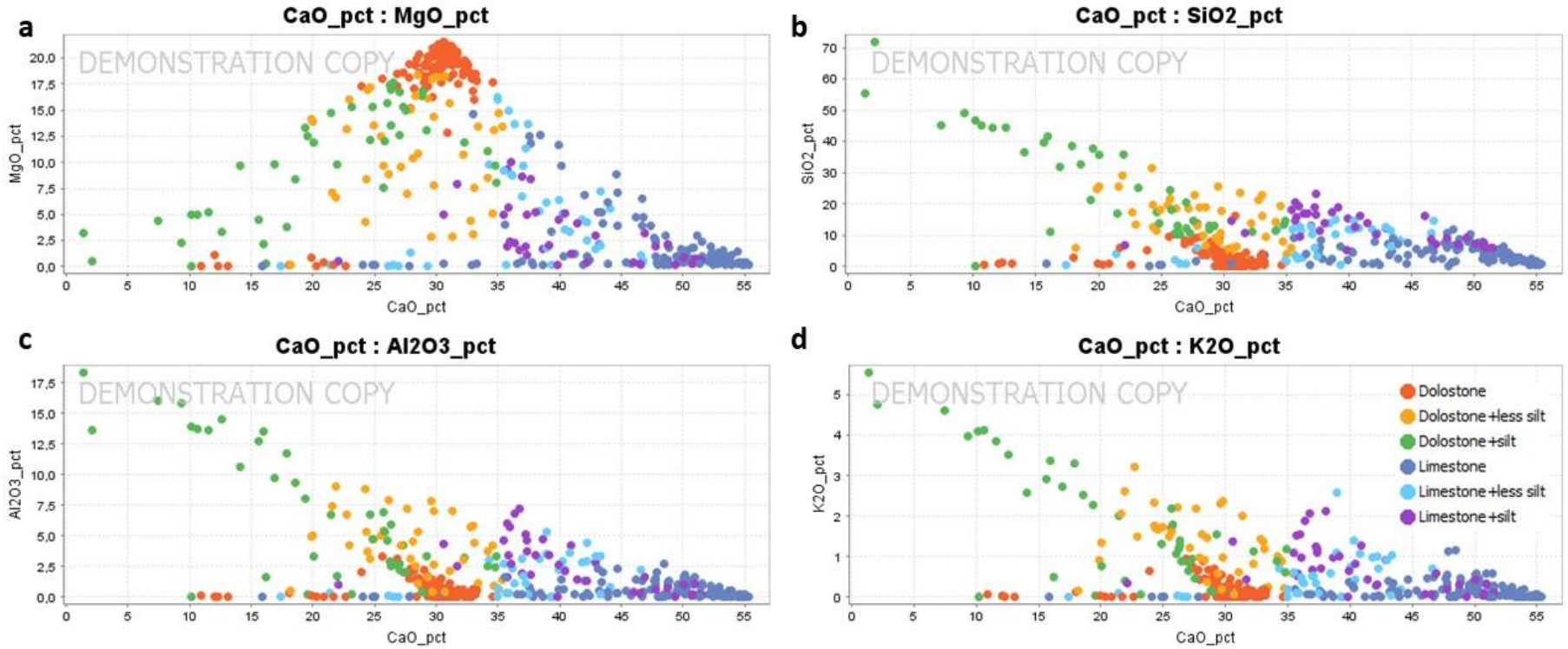


Figure 3.25. Binary plots of CaO against (a) MgO, (b) SiO_2, (c) Al_2O_3, and (d) K_2O (in percentages) used to discriminate between different lithological units at Meskan.

Following this, major oxide diagrams were plotted in order to distinguish between relatively pure limestones and dolostones. The CaO vs. MgO plot in Figure 3.25a clearly shows almost pure dolostone and limestone end members. The group of samples that lie between these two likely comprise varying proportions of calcite and dolomite (Figure 3.25a). As a next step, the silt components of calcareous rocks were determined through bivariate diagrams where CaO abundances of samples are plotted against SiO_2, Al_2O_3, and K_2O (Figure 3.25b, d). This allowed separation of clean (non-silty) limestones and dolostones from limestone/dolostone lithologies with noticeable silt fraction (dolostone±high silt, dolostone±low silt, limestone±high silt, and limestone±low silt).

A large number of samples from the mineralized sections of the stratigraphy contain sulfide minerals. In order to eliminate the dilution effect of the sulfide phases on the actual wall-rock lithogeochemistry, major oxides (SiO_2 + Al_2O_3 + Fe_2O_3 + MgO + CaO + Na_2O + K_2O + TiO_2 + P_2O_5 + MnO + Cr_2O_3) as well as loss-on-ignition (LOI) values were recalculated to sulfide-free compositions. For this purpose, total mass of each sample was calculated initially without the components of major sulfide minerals (S, Pb, Zn), and sulfide-free compositions are determined for each major element. For instance; for SiO_2, SiO_2 * (100/total mass) gives the sulfide-free abundance of SiO_2 (denoted as SiO_2_SF).

A plot of CaO concentrations of samples against sulfide-free CaO (CaO_SF) concentrations showed no significant difference between these two for most samples with the exception of samples from the main mineralized zone (Figure 3.26). The samples that lie outside the general trend represent the ore zone samples (Figure 3.26). The mineralized horizons are found in the purest or most clean limestones, which are the shallow siliciclastic-deficient limestones. This indicates that sulfide mineralization occurs within the carbonate grainstone lithotype, but not within the mudstone lithotype.

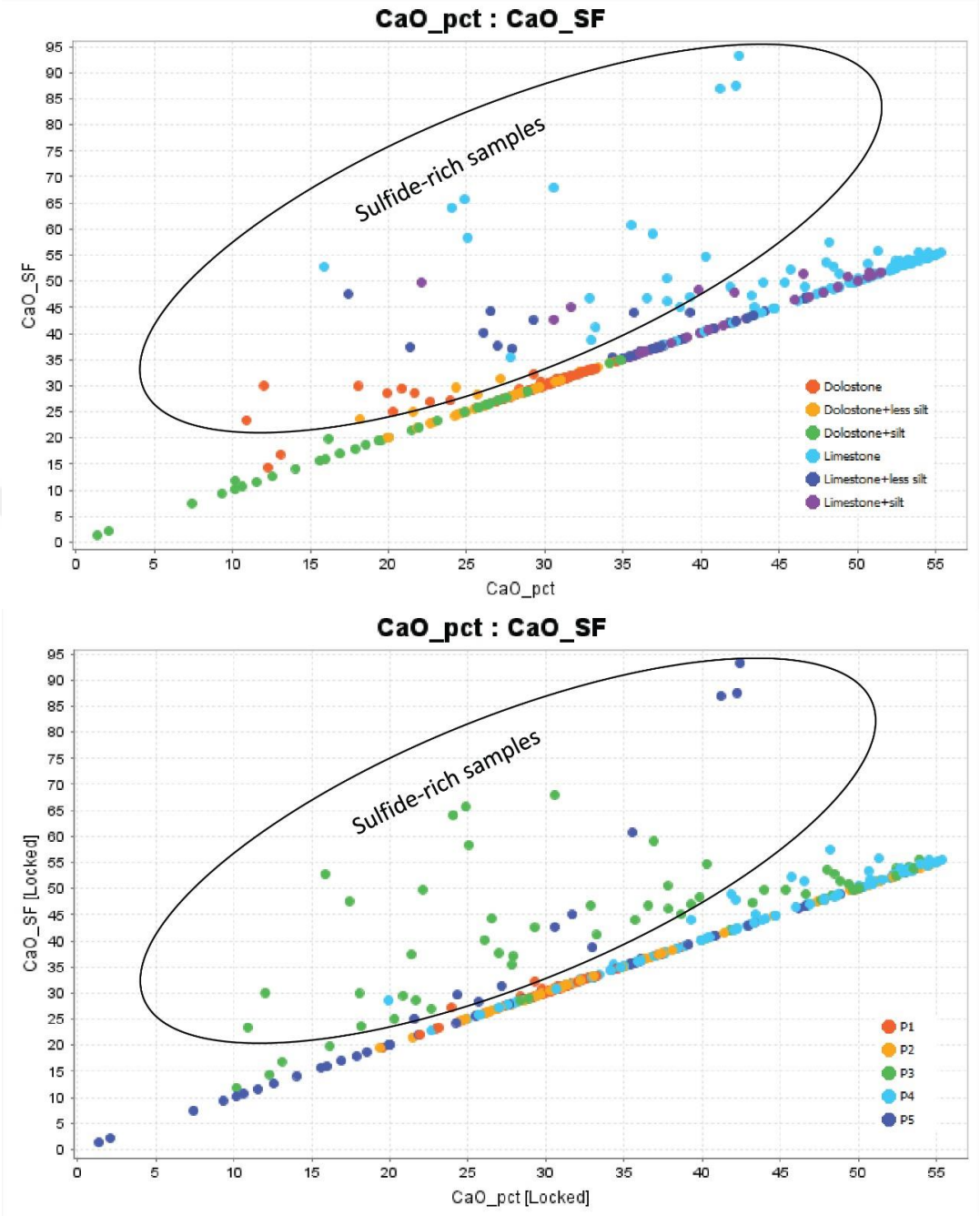


Figure 3.26. CaO versus CaO_SF (sulfide-free; in percentages) plots used to distinguish between lithologies (up) and stratigraphic packages (down). There is a good correlation between most lithologies and identified packages except for samples from the mineralized unit. Mineralized unit samples are scattered outside the general linear trend defined by samples from the non-mineralized levels.

Chemostratigraphic subdivision of the Meskan sequence: The stratigraphy encountered in the Meskan Zn-Pb deposit is divided into five chemostratigraphic

packages through lithogeochemical data obtained from four different drill holes. From the youngest (shallowest) to the oldest (deeper levels of the succession) these packages are ordered from package 1 to package 5. Each package has geochemically and lithologically distinctive features.

Package 1 is distinguished from other chemostratigraphic packages with its high overall MgO content (Figure 3.27). This is related to high-intensity dolomitization that especially developed in the upper levels of package 1. This package is characterized by intercalations of fine-grained, clean sugary dolostone and dolostone±low silt lithologies. The mean value of MgO is calculated as 19.62 wt.% for Package 1 samples through all four studied drill holes.

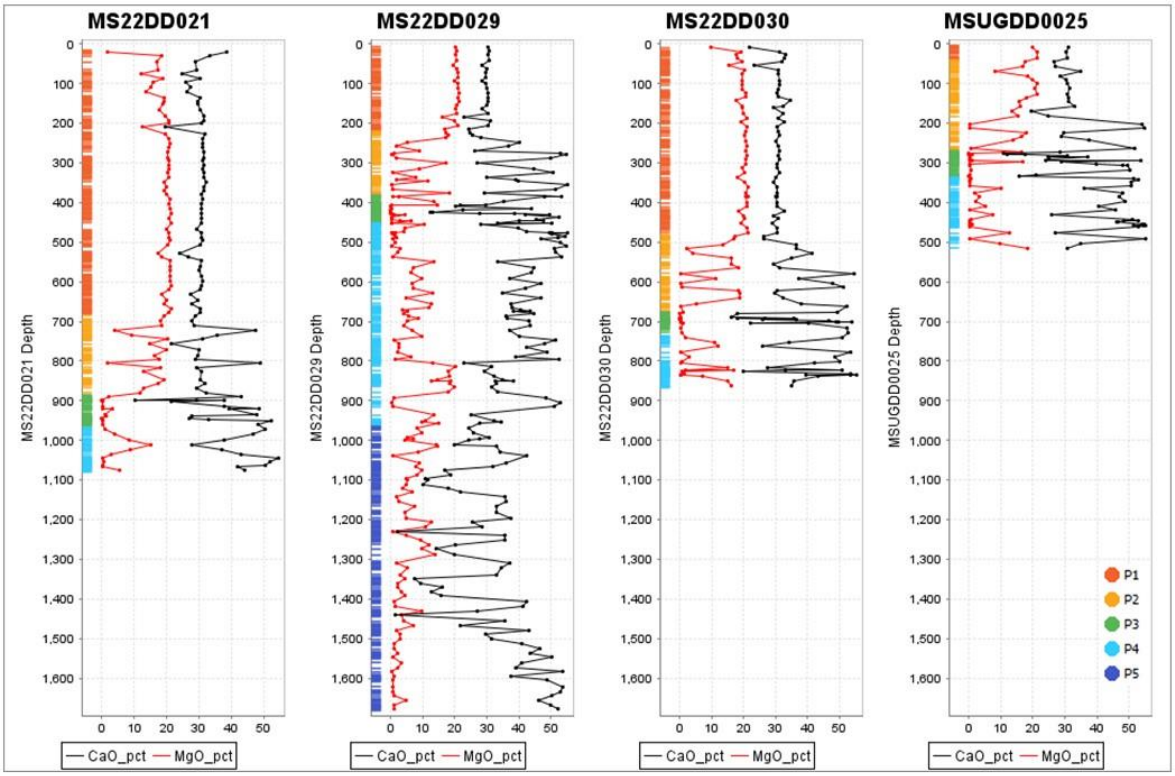


Figure 3.27. Downhole plots showing the variation of CaO and MgO (in percentages) for each package in the studied drill holes MS22DD021, MS22DD029, MS22DD030, and MSUGDD0025.

Package 2 is differentiated from package 1 by its relatively high SiO_2, Al_2O_3, and K_2O contents (Table 3.2). The top of package 2 generally starts with dolostone

followed by limestone and silty limestone. The middle part of this package is distinguished from other packages by higher proportions of clastic components. Rock samples from package 2 also typically contain very fine-grained disseminations of pyrite. The lower part of package 2 consists of dolomitic limestone and dolostones. The ore-hosting package 3 is separated from the overlying package 2 rocks and the underlying package 4 rocks mainly by its Fe_2O_3 and MnO contents. Both components are significantly higher in abundance, particularly in the upper part of package 3, even for the calculated sulfide-free compositions (Figure 3.28). Additionally, package 3 samples are characterized by a pronounced increase in TOT/S, especially in the upper part of the package. Package 3 is commonly composed of limestone, and rarely of limestone±silt and dolostone with highest TOT/S values (mean=13.82 wt.%; Table 3.2).

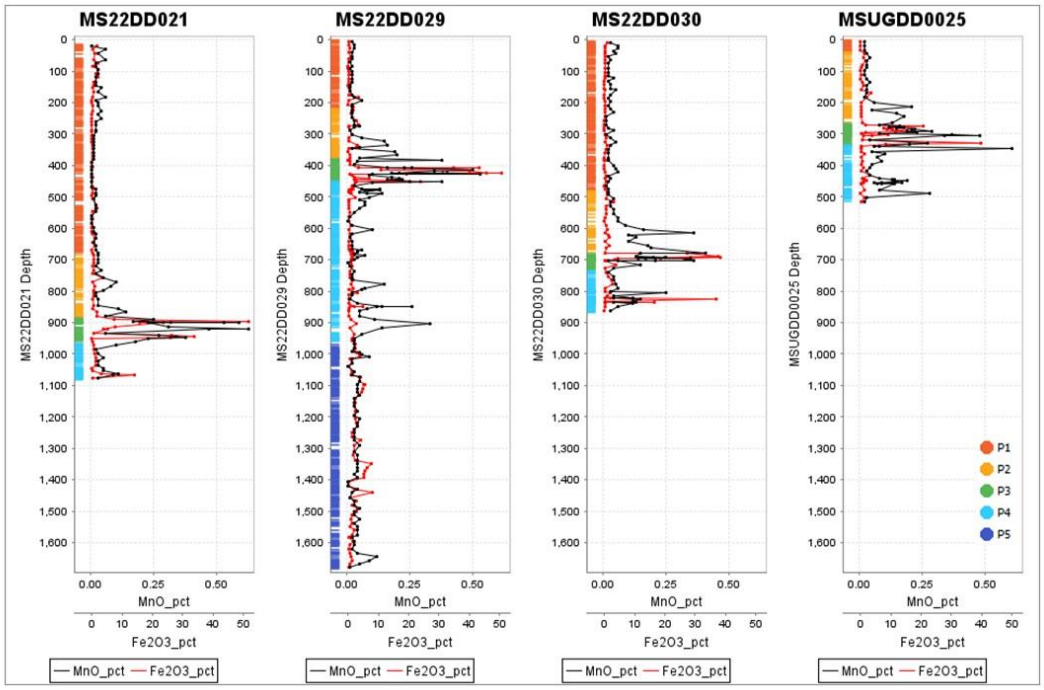


Figure 3.28. Downhole plots showing the variation (in percentages) of MnO (black line) and Fe_2O_3 (red line) for each package through four drill holes.

Table 3.2 Major oxide concentrations as well as TOT/S and TOT/C values (in percentages) for each chemostratigraphic package

439 rows - Univariate	SiO2_pct	SiO2_SF	Al2O3_pct	Al2O3_SF	Fe2O3_pct	Fe2O3_SF	MgO_pct	MgO_SF	CaO_pct	CaO_SF	K2O_pct	K2O_SF	TiO2_pct	TiO2_SF	P2O5_pct	P2O5_SF	MnO_pct	MnO_SF	TOT/C	TOT/S
[Visible] : Count Numeric	439	439	439	439	439	439	439	439	439	439	439	439	439	439	439	439	439	439	439	439
[Visible] : Minimum	0.005	0.005012	0.005	0.005004	0.02	0.020018	0.02	0.023147	1.38	1.385542	0.005	0.005002	0.005	0.005	0.005	0.005	0.005	0.005013	0.01	0.01
[Visible] : Maximum	71.92	72.063406	18.36	18.433735	51.75	59.891674	21.58	21.73338	55.35	93.211219	5.56	5.582329	0.64	0.64257	0.6	0.601094	0.63	0.769164	14.6	44.08
[Visible] : Mean	7.578303	7.800553	1.707802	1.744134	3.094579	4.100388	9.928246	10.0438	35.150843	37.204717	0.507323	0.517475	0.085068	0.087019	0.042118	0.043231	0.079385	0.092086	10.561185	2.950091
[Visible] : Median	4.36	4.665552	0.52	0.55027	0.64	0.664162	8.84	8.987557	31.61	32.791339	0.16	0.164166	0.03	0.030102	0.03	0.030104	0.04	0.040081	11.68	0.4
[Visible] : Standard Deviati...	9.659598	9.740026	2.817641	2.841668	7.709114	10.803972	8.365407	8.385656	10.740208	11.919052	0.821307	0.828488	0.125472	0.126555	0.050392	0.050496	0.102809	0.132515	2.954997	7.188408
P1 : Count Numeric	125	125	125	125	125	125	125	125	125	125	125	125	125	125	125	125	125	125	125	125
P1 : Minimum	0.005	0.005012	0.005	0.005015	0.02	0.020062	1.74	1.746532	19.55	19.594872	0.005	0.005012	0.005	0.005012	0.005	0.005012	0.005	0.005015	0.01	0.01
P1 : Maximum	37.84	37.926852	6.77	6.795415	3.59	3.620667	21.58	21.73338	38.65	38.795094	1.72	1.726457	0.32	0.321201	0.6	0.601094	0.06	0.060523	13.58	2.6
P1 : Mean	2.77524	2.792331	0.61652	0.621479	0.32448	0.32732	19.6184	19.743569	30.18616	30.373823	0.17388	0.175387	0.03404	0.034308	0.02628	0.026478	0.02308	0.023243	12.15608	0.18528
P1 : Median	0.63	0.632333	0.16	0.161013	0.12	0.120499	20.48	20.57386	30.62	30.765061	0.04	0.040201	0.005	0.00551	0.005	0.005021	0.02	0.020076	12.52	0.01
P1 : Standard Deviation	5.894095	5.913805	1.199015	1.207097	0.520933	0.526113	2.525509	2.537632	2.308787	2.267669	0.334813	0.337635	0.062691	0.063105	0.062369	0.062603	0.013793	0.013927	1.487862	0.438017
P2 : Count Numeric	72	72	72	72	72	72	72	72	72	72	72	72	72	72	72	72	72	72	72	72
P2 : Minimum	0.1	0.100567	0.02	0.020005	0.04	0.040166	0.31	0.310074	19.39	19.451272	0.005	0.005002	0.005	0.005	0.005	0.005	0.01	0.01001	8.29	0.01
P2 : Maximum	21.35	21.417465	8.07	8.095501	3.57	3.581281	21.5	21.58938	55.16	55.178761	2.59	2.59558	0.42	0.421327	0.32	0.321121	0.41	0.411353	14.6	2.83
P2 : Mean	7.503194	7.525384	1.813611	1.818943	0.904167	0.906872	11.708056	11.753506	35.686806	35.784323	0.668264	0.67023	0.092986	0.093258	0.056667	0.05684	0.072361	0.072537	11.818611	0.671528
P2 : Median	6.3	6.321115	1.095	1.098671	0.64	0.641052	15.065	15.124927	31.2	31.349367	0.385	0.386107	0.05	0.050098	0.05	0.05007	0.04	0.040118	12.23	0.485
P2 : Standard Deviation	5.401576	5.416609	2.03651	2.041926	0.88233	0.884774	7.413371	7.446984	9.698618	9.675787	0.699581	0.701455	0.10702	0.107299	0.056873	0.057064	0.076259	0.076378	1.403179	0.694726
P3 : Count Numeric	65	65	65	65	65	65	65	65	65	65	65	65	65	65	65	65	65	65	65	65
P3 : Minimum	0.15	0.173599	0.005	0.011181	0.02	0.020501	0.02	0.023147	10.18	11.781589	0.005	0.00516	0.005	0.005044	0.005	0.005044	0.02	0.030087	2.26	0.22
P3 : Maximum	11.96	15.635223	2.87	2.880254	51.75	59.891674	16.84	16.904066	53.93	68.060379	0.99	0.993746	0.2	0.200821	0.06	0.060246	0.63	0.769164	12.52	44.08
P3 : Mean	4.367077	5.108338	0.450385	0.518738	14.299231	20.681698	1.555231	1.673437	34.466769	43.341889	0.157231	0.180334	0.026846	0.031331	0.017231	0.020695	0.237538	0.318013	8.087385	13.818308
P3 : Median	3.52	3.852426	0.17	0.186476	8.41	12.377415	0.24	0.333201	35.67	47.279771	0.06	0.063244	0.005	0.013217	0.01	0.013217	0.21	0.308372	8.27	10.58
P3 : Standard Deviation	3.671932	3.951706	0.67634	0.715251	14.890377	20.286366	3.719412	3.721524	13.166238	12.469587	0.243469	0.256066	0.040731	0.042073	0.015763	0.016544	0.14099	0.188921	3.189649	12.560727
P4 : Count Numeric	114	114	114	114	114	114	114	114	114	114	114	114	114	114	114	114	114	114	114	114
P4 : Minimum	0.4	0.400677	0.005	0.005004	0.02	0.020018	0.18	0.200359	19.91	22.792309	0.005	0.005004	0.005	0.005004	0.005	0.005004	0.005	0.005013	4.86	0.06
P4 : Maximum	24.52	24.589835	6.93	6.949737	36.96	53.018892	20.16	20.236697	55.35	57.500209	3.23	3.243135	0.39	0.391111	0.17	0.171362	0.61	0.622443	13.5	31.13
P4 : Mean	6.895965	6.965724	1.235395	1.244406	1.495088	1.687151	5.72193	5.754657	43.075702	43.742837	0.354912	0.357233	0.062237	0.06269	0.051096	0.051675	0.079035	0.081152	11.515439	1.412281
P4 : Median	5.99	6.007424	0.625	0.627031	0.73	0.730907	3.09	3.095191	44.365	45.739829	0.185	0.18554	0.03	0.030111	0.05	0.050125	0.055	0.055295	11.68	0.735
P4 : Standard Deviation	5.241243	5.266932	1.421581	1.427955	3.947324	5.391658	5.965665	5.986545	9.046128	9.1481	0.488929	0.490807	0.07377	0.074084	0.032183	0.032501	0.081878	0.084711	1.265466	3.329293
P5 : Count Numeric	63	63	63	63	63	63	63	63	63	63	63	63	63	63	63	63	63	63	63	63
P5 : Minimum	0.47	1.032264	0.1	0.19036	0.08	0.175704	0.37	0.370701	1.38	1.385542	0.005	0.010982	0.005	0.010982	0.005	0.005004	0.005	0.010014	0.03	0.01
P5 : Maximum	71.92	72.063406	18.36	18.433735	7.87	7.901606	14.67	17.221746	53.72	93.211219	5.56	5.582329	0.64	0.64257	0.19	0.190576	0.12	0.120101	11.96	22.52
P5 : Mean	21.741905	22.340306	5.904286	6.054698	2.428095	2.495477	4.917937	5.241674	30.754444	34.218496	1.621984	1.659449	0.278651	0.285955	0.066349	0.068889	0.036587	0.037706	6.785238	2.609365
P5 : Median	19.32	19.77754	4.67	4.972282	1.92	2.154676	4.34	4.410409	32.99	34.237448	1.25	1.272775	0.27	0.282104	0.06	0.060451	0.03	0.036525	7.85	0.33
P5 : Standard Deviation	15.174596	15.020715	4.682875	4.65313	1.822696	1.803622	3.873865	4.119943	13.520536	18.695361	1.340091	1.340258	0.175205	0.173109	0.046535	0.046097	0.01894	0.018143	3.470165	5.595178

Package 4 is differentiated from packages 1–3 by its higher SiO_2, Al_2O_3, K_2O, TiO_2, P_2O_5, and Cr_2O_3 contents (Table 3.2). Moreover, the transition between package 3 and package 4 is detected by their low Fe_2O_3 and MnO contents, and low TOT/S ratios. The upper part of this package generally starts with dark grey to black dolostone and limestone (Figure 3.10) followed by brecciated (Figure 3.9) and laminated dolostones in the deeper levels.

Package 5, comprising the lithologies of the Lower Triassic Çığlı Group (Perinçek, 1987), is only observed in drill hole MS22DD029 and it is characterized by significantly higher SiO_2 concentrations (Figure 3.29). With increasing depth dolomitic lithologies within this package transition in to limestone and limestone ±high silt units.

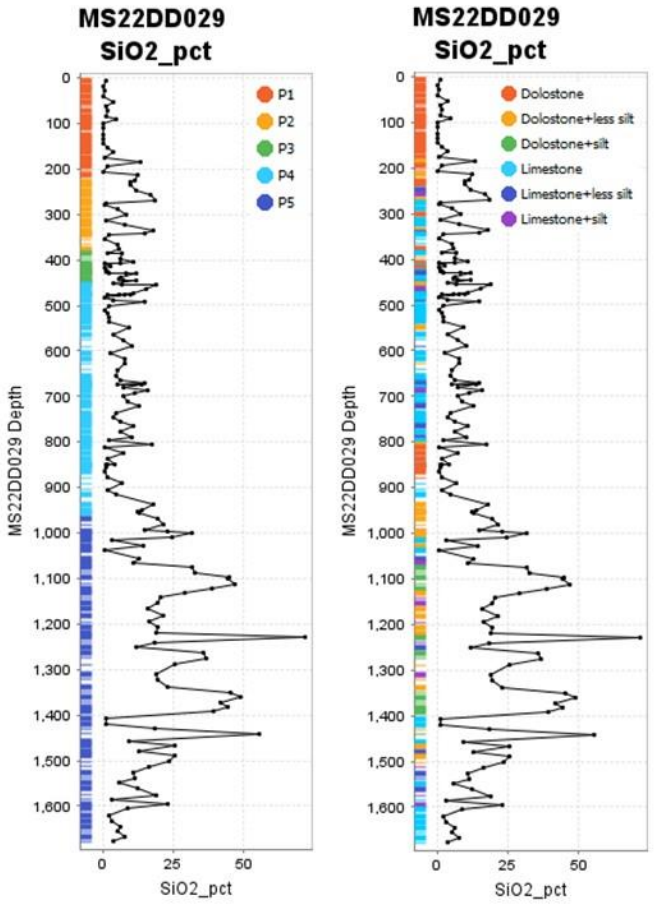


Figure 3.29. Downhole plots of drill hole MS22DD029 showing the variation in SiO_2 (in percentages) for each chemostratigraphic package and lithology.

Discrimination criteria: Certain element groups show similar geochemical behavior under specific geological conditions and therefore major, minor, and trace elements can be used to identify geochemical/mineralogical differences and similarities among distinct lithological units or stratigraphic packages. In this study, geochemical features of chemostratigraphic units are monitored using the following elements (and ratios) for data interpretation and discrimination.

Rare earth elements (REE): Rare earth elements include the lanthanide series elements (from La to Lu) as well as the pseudolanthanide yttrium since it shows similar geochemical behavior to the REEs. REEs with low atomic numbers (from La to Pm) are called as light rare earth (LREE), whereas with high atomic numbers (from Er to Lu) are called as heavy rare earth elements (HREE), and middle of REE group (from Sm to Ho) is called as middle rare earth elements (MREE; Alibo and Nozaki, 1999). The majority of REE+Y are stable in 3+ valence, with the exception of Eu (both as 2+ and 3+), and Ce (both as 3+ and 4+; Sholkovitz, 1994; Rollinson and Peace, 2021). The valence states of the latter group of elements are dictated by the oxidation state of the environment and thus these are redox sensitive (McLennan and Taylor, 2012).

Ce: Cerium anomalies have been widely used as a paleoredox indicator in petrological and provenance studies. Ce^{+3} is unique among the REE in that it is readily oxidized to relatively insoluble Ce^{+4} resulting in relative Ce depletion in oxic seawater (Baar et al. 1988). Ce in seawater is known to exhibit a behavior that is partially decoupled from that of other REEs. This is probably due to differences in the susceptibility of Ce to oxidation during chemical cycles near the Earth's surface (Liu et al., 1988). Cerium anomalies are commonly quantified through the equation, $Ce/Ce* = Ce_N / \sqrt{[(La_N) * (Pr_N)]}$ (Rollinson and Peace, 2021).

Eu: Under reducing conditions europium is stable as Eu^{+2}, rather than as Eu^{+3} (Rollinson and Peace, 2021). Eu^{+2} is similar in size and charge to Ca^{+2}, and thus is compatible in plagioclase feldspar but Eu^{+3} is not (Sinha, 1983; Tang et al., 2017). Similar to Ce, europium anomalies can also be quantified using the Eu/Eu* ratio,

where Eu* is the geometric mean of the chondrite-normalized values of Sm and Gd (Taylor and McLennan, 1985) through the equation $Eu/Eu^* = Eu_N/\sqrt{[(Sm_N) * (Gd_N)]}$. Typically, Eu/Eu* ratios <1 indicates that Eu^{+2} has been removed from samples either by plagioclase fractionation or that some amount of plagioclase has recrystallized (Bau, 1991). In siliciclastic sediments, a positive Eu anomaly often arises from a higher proportion of plagioclase feldspar (Rollinson and Peace, 2021).

High field strength elements (HFSE): Highly-charged cations with small ionic radius (Z/r >1) are called as high field strength elements HFSE (Ahrens, 1953). The HFSE includes Cr, Ti, Zr, Nb, Hf, and Ta. This group of elements are commonly known to be immobile during many geological processes including hydrothermal alteration and metamorphism (Rollinson, 1993).

Large ion lithophile elements (LILE): Elements with low field strength (Li, Be, Rb, Sr, Ba, and Cs) are referred to as large ion lithophile elements (Rollinson and Peace, 2021). This group of elements are commonly alkali metals and alkali earth metals. They are incompatible and they are also mobile during melting, crystallization, alteration, and metamorphism (Macheyeki et. al., 2020).

Transition metals (Mn, Fe, Co, Ni, Cu, Zn, Ag, Cd, Au, Hg, Re, Os) are a group of elements in the periodic table characterized by their partially filled d orbitals. They include elements from group 3 to 12, spanning periods 4 to 7. Transition metals exhibit a wide range of properties, including high melting and boiling points, metallic luster, and the ability to form colorful compounds due to their various oxidation states (Leigh, 2011).

Metalloids are elements that exhibit properties intermediate between metals and nonmetals. They are found along the staircase on the periodic table, bordering the line between metals and nonmetals. Metalloids (As, Sb, Te, Ge, etc.) possess characteristics of both metals and nonmetals, such as semiconducting behavior, brittleness, and the ability to form covalent bonds (Batley, 1998).

3.5.1.1 Major and minor oxides

Package 1 includes the younger part of the stratigraphy above the ore horizon and is investigated as two distinct levels (upper P1 and lower P1). These levels in Package 1 are commonly associated with dolostone and dolostone±silt lithologies with MgO contents generally >15 wt.%. (Figure 3.27, Table 3.2). The main difference between lithologies of the upper and lower levels of Package 1 is the silt amount. Dolostones in the upper levels have higher silt contents compared to the dolostones in the lower levels (Figure 3.30 and 3.31). In the drill hole MS22DD021, the upper P1 is 0-219.20 m, the lower P1 is 219.20-654.80 m (Figure 3.30). In the drill hole MS22DD030, the upper P1 is intersected between 0 and 65.10 m, the lower P1 between 65.10 and 475.10 m (Figure 3.31). Except drill hole MS22DD021 and MS22DD030, a clear compositional distinction in upper and lower levels was not detected in drill holes MS22DD029 and MSUGDD0025, because these begin with dolostone. In the drill core, the lower level is distinguished by intercalations of fine-grained, clean sugary dolostone and dolostone±silt units.

Table 3.2 shows a comparison between major oxide compositions of all samples (n= 439) from all chemostratigraphic packages and samples of package 1 (n= 125). Mean values for major oxide values of package 1 indicate that all major elements except MgO are relatively depleted compared to other packages (Table 3.2). The upper levels of package 1 are relatively enriched in SiO_2, Al_2O_3, K_2O, and TiO_2 with respect to lower levels in drill holes MS22DD021 (Figure 3.30) and MS22DD030 (Figure 3.31). SiO_2 contents at shallow depths reach to a maximum of 37.84 wt.% in drill hole MS22DD021 (Figure 3.30) and to 35.90 wt.% in drill hole MS22DD030 (Figure 3.31). Although enrichments in SiO_2, Al_2O_3, K_2O, and TiO_2 correlate well, the local maxima observed in SiO_2 appear as an outlier compared to these other major oxides (Figures 3.30 and 3.31). A comparison of all studied drill holes indicates that the maximum Al_2O_3 (6.77 wt.%), K_2O (1.72 wt.%), and TiO_2 (0.32 wt.%) values are observed in the upper level of MS22DD021 in package 1 (Figure 3.30). Higher abundance of these major oxides in the shallow, oxidized portions of the drill holes

likely indicate higher abundance of detrital material, whereas relative enrichments in deeper levels of package 1 suggests presence of an impure (silty) dolostone unit.

Package 2 generally consists of dolostone at the top followed by limestone and silty limestone with increasing depth. The middle part of this package is distinguished by increased clastic component and also by the highest total organic sulfur (TOT/S) contents. Additionally, very fine-grained disseminations of diagenetic pyrite are present in all lithologies in Package 2. The lower part of Package 2 consists of less silty dolomitic limestone and dolostones. Mean MgO concentrations show a sharp drop as passing from package 1 (19.6 wt.%, n= 125) into package 2 (11.7 wt.%, n= 72; Table 3.2), whereas mean CaO concentrations increase from about 30.2 wt.% in package 1 to 35.7 wt.% in package 2 (Table 3.2). Figure 3.28 clearly illustrates this change in MgO and CaO contents in all four drill holes. Fe_2O_3 abundances on the other hand does not show significant variation among packages 1 and 2 (both at 3.6 wt.%; Table 3.2). In addition to CaO, package 2 samples also have higher overall MnO, SiO_2, Al_2O_3, K_2O, and TiO_2 contents compared to package 1 samples (Figure 3.26, 3.30, and 3.31). MnO concentrations reach up to a maximum of 0.41 wt.% (MS22DD030, 677.50 m; Figure 3.27), and K_2O concentrations locally reach up to about 8 wt.% in drill hole intervals where silt components are markedly high (Figure 3.30 and 3.31).

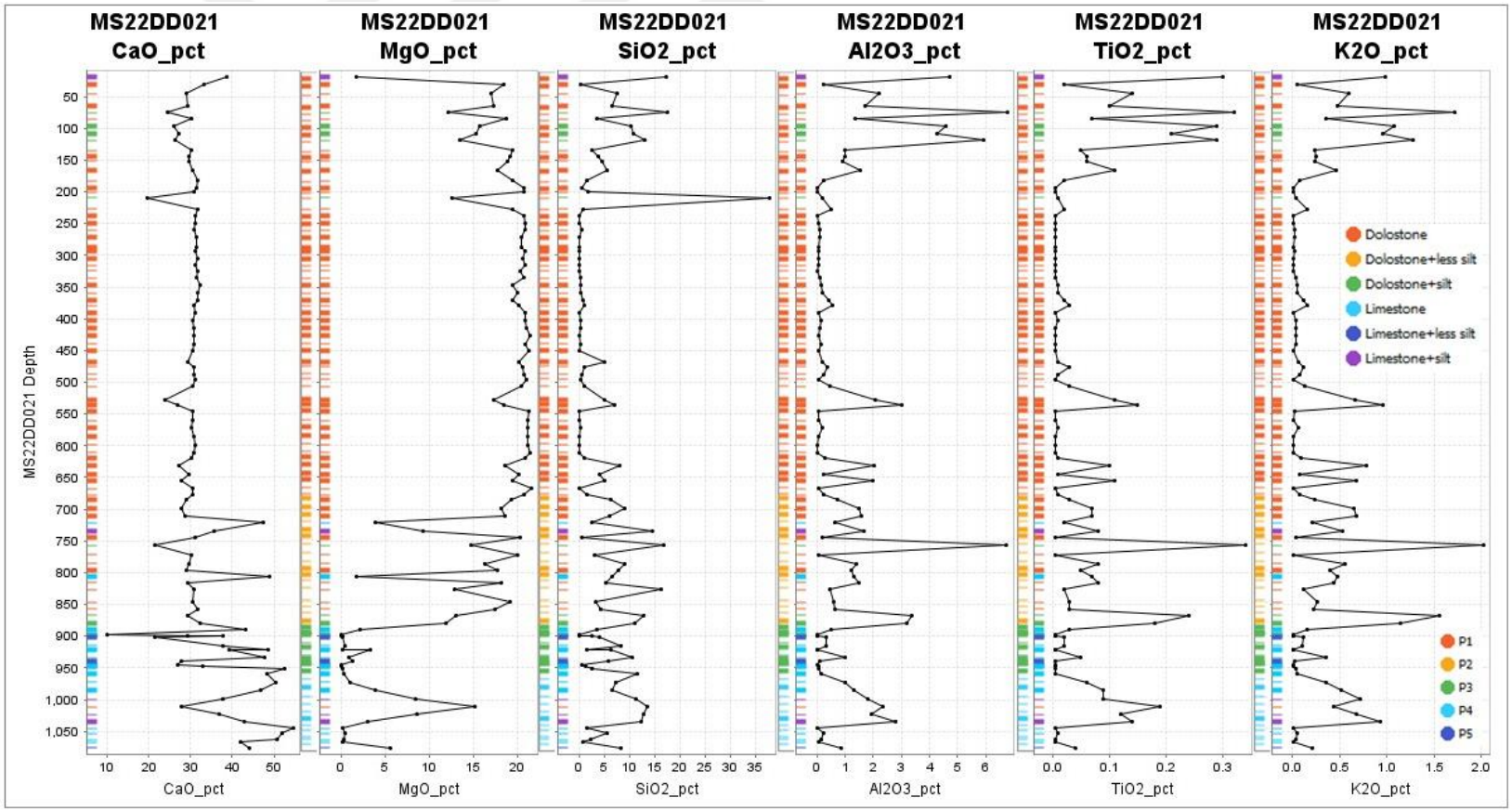


Figure 3.30. Downhole plots showing variation of major oxide contents (in in percentages) in identified packages and lithological units in drill hole MS22DD021. Colored bars to the left represent different lithologies, whereas the ones to the right represent chemostratigraphic packages.

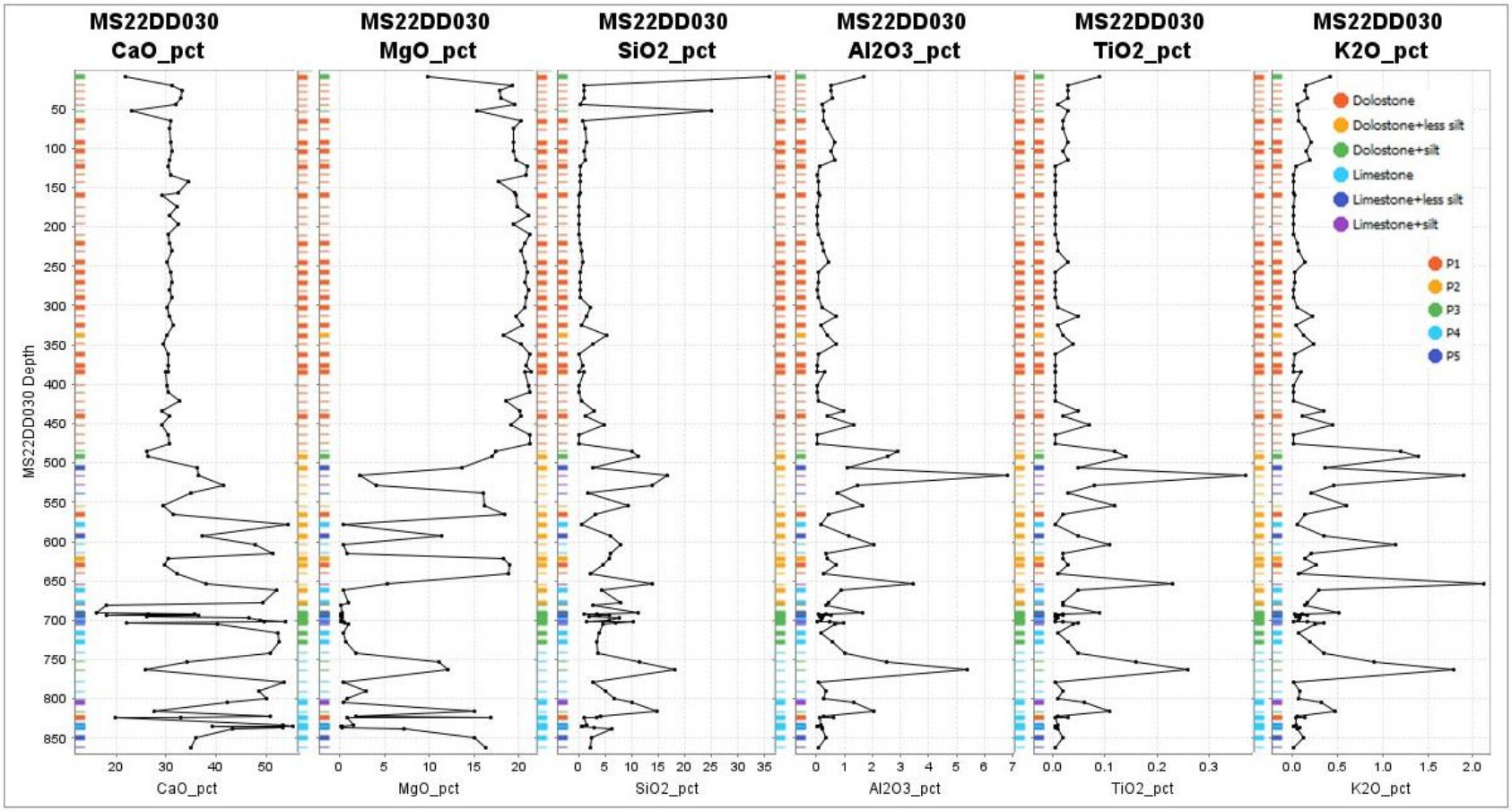


Figure 3.31. Downhole plots showing variation of major oxide contents (in percentages) in identified packages and lithological units in drill holes 30. Colored bars to the left represent different lithologies, whereas the ones to the right represent chemostratigraphic package

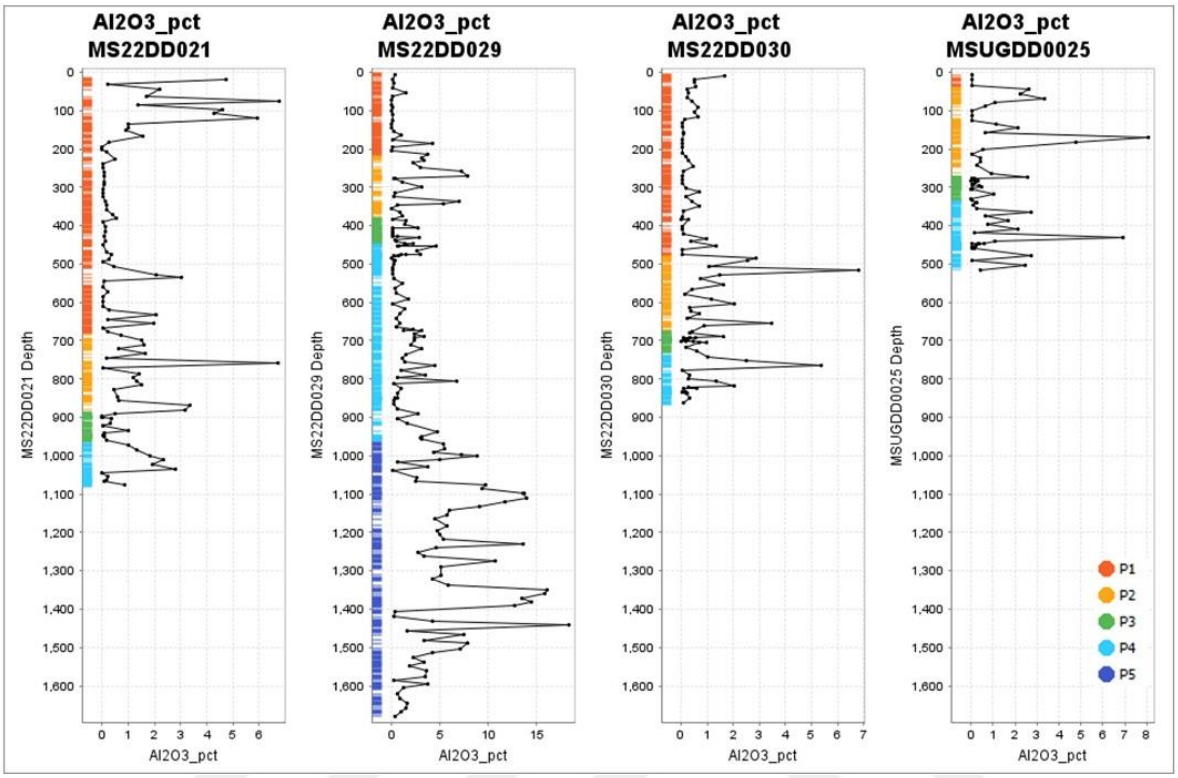


Figure 3.32. Downhole plots showing variation in Al_2O_3 concentrations (in percentages) for each chemostratigraphic package in all drill holes.

Package 3 comprises the part of the Meskan stratigraphy that hosts the Zn-Pb sulfide mineralization. This package is mainly composed of clean limestone and less commonly of limestone±high silt and dolostone units. Zebra-textured, banded intervals of barren or mineralized rocks are characteristic of Package 3, and it is also abundant in ore minerals such as pyrite, sphalerite, galena, and marcasite. Therefore, this package is called as the "main mineralized zone" or as the "ore zone". Package 3 samples are characterized by overall low MgO (mean= 1.55 wt.%) and locally very high CaO contents that range from 10.2 to 53.9 wt.% (mean= 34.5 wt.%; n= 65; Table 3.2). The range of CaO_SF contents in package 3 is between 11.78 wt.% and 68.06 wt.%, whereas MgO_SF contents of the same package vary from 0.02 wt.% to 16.90 wt.% in package 2 (Table 3.2). Although some of the CaO is probably sourced from the calcareous protolith, there is likely some hydrothermal contribution to the

relatively high CaO abundances of this package through vein and breccia matrix calcite. Plots of CaO_SF versus Fe_2O_3 and CaO_SF versus MnO indicate a strong relationship between Fe_2O_3 (mean= 14.29 wt.%) and MnO (mean= 0.24 wt.%) in package 3 compared to other packages (Table 3.2, Figure 3.33). Since package 3 is mostly characterized by clean (relatively pure) carbonate (either dolomite or limestone) horizons, relative proportion of the siliciclastic component is quite low especially in drill holes MS22DD021 and 30 (Figures 3.30 and 3.31). Package 3 samples have the lowest average SiO_2, Al_2O_3, TiO_2, and K_2O among all identified chemostratigraphic packages (Figures 3.30 and 3.31; Table 3.2). The carbonate sequence is commonly dolomitized above the package 3. Package 3 is characterized with the highest TOT/S (mean= 13.82 wt.%; n = 65) and the lowest TOT/C (mean= 8.09 wt.%) contents with respect to the overlying P2 and underlying P4 samples (Table 3.2). Moreover, package 3 is separated from the overlying and the underlying packages mainly by its significantly higher in abundance Fe_2O_3 (mean= 14.3 wt.%) and MnO (mean= 0.24 wt.%) contents (Table 3.2). Enrichment of these major oxides predominantly might be associated with the prevalence of manganoan carbonates or barite within the ore zone.

Package 4, representing the part of stratigraphy immediately below the mineralized horizon (package 3), starts at the top with dark grey to black dolostone and limestone followed by brecciated and laminated dolostones. This package presents striking differences compared to the package 3 samples in terms of major, minor, and trace element geochemistry. Package 4 samples commonly have high CaO abundances and as such the predominant lithologies are clean limestone and limestone±high silt with only minor dolostone components. In this respect, it differs from relatively shallow package 1 and package 2 lithologies. However, MgO contents (avg= 5.72 wt.%; n = 114) and thus dolomite proportions are higher compared to package 3 (Figure 3.27, Table 3.2). Package 4 is also differentiated from underlying package 3 with its relatively high MgO contents (avg: 5.72 wt.%, n=114) and overlying package (P2) with relatively low Fe_2O_3 (avg: 1.50 wt.%) and MnO (avg: 0.08 wt.%) values (Figure 3.28; Table 3.2). Average TOT/C content of package 4 (11.5 wt.%)

is comparable with that of package 2 (11.8 wt.%), but is significantly higher compared to the TOT/C values of package 3 (Table 3.2). In contrary, TOT/S shows a prominent decrease in package 4 (avg: 1.4 wt.%) compared to package 3 (avg: 13.8 wt.%) due to a lack of sulfide minerals (possibly except that of minor diagenetic pyrite), but TOT/S values are still relatively higher compared to package 2 samples (Table 3.2).

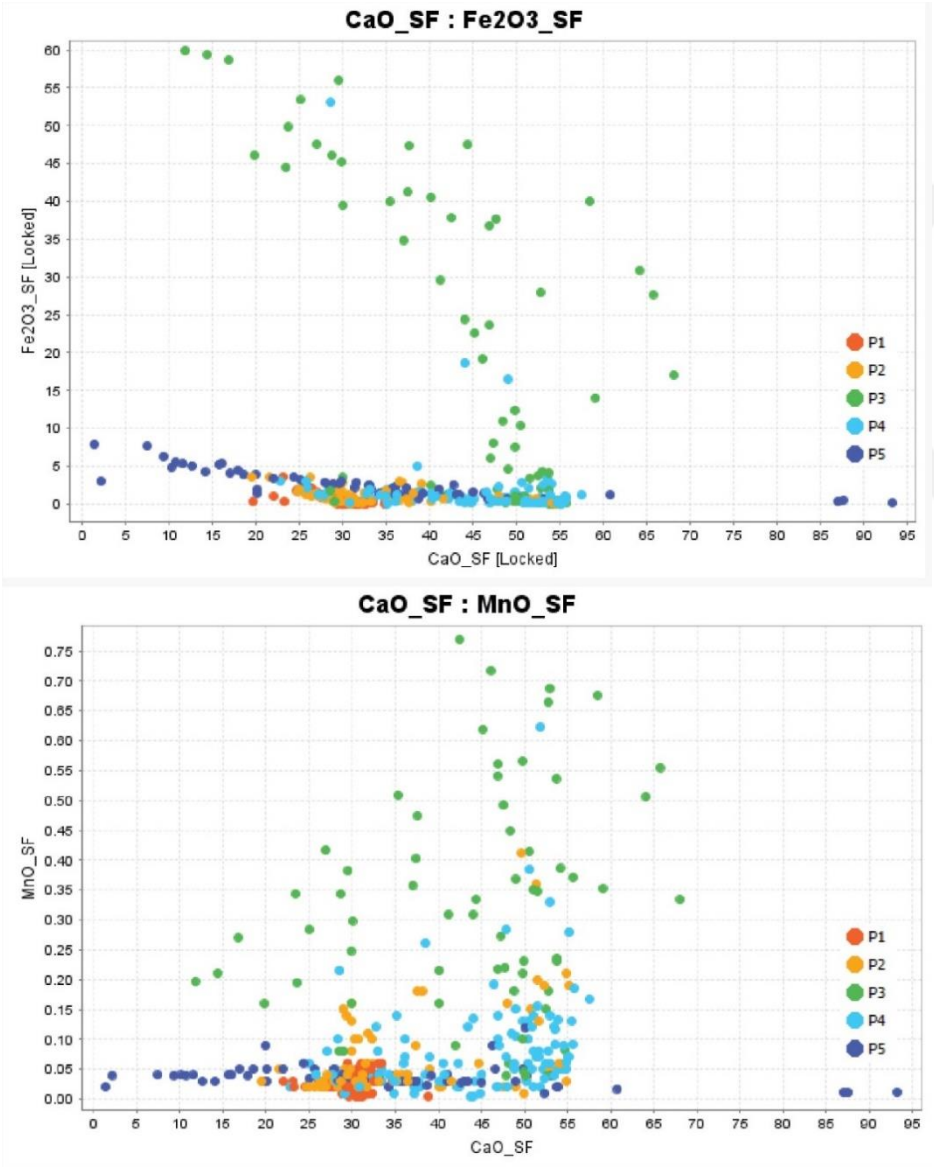


Figure 3.33. CaO_SF (sulfide-free) versus Fe_2O_3 (up) and MnO (down) plots (in percentages) showing deviation of package 3 samples from the rest of the chemostratigraphic packages.

Following package 3, which has the lowest concentrations of the element suite of SiO_2, Al_2O_3, K_2O, TiO_2, and P_2O_5, package 4 samples show prominent increases in concentrations of these elements. In this respect, package 4 seems to be relatively well-correlated with package 2 but average abundances of Al_2O_3 (1.24 wt.%), TiO_2 (0.06 wt.%), and K_2O (0.36 wt.%) are about 1.5 to 2 times higher in package 2 samples (Table 3.2). Highest Al_2O_3 (6.9 wt.%, Figure 3.32) and TiO_2 (0.39 wt.%) values are observed in drill hole MSUGDD025, whereas the maximum K_2O (3.23 wt.%) value is observed in MS22DD029 (Figure 3.30). MnO (avg= 0.08 wt.%) is relatively depleted compared to package 3 (avg= 0.24 wt.%; Table 3.2) possibly due to absence of hydrothermal phases (such as carbonate) that commonly incorporate Mn. Similarly, Fe_2O_3 is also significantly depleted with respect to package 3 due to absence of Fe-sulfide phases of pyrite and marcasite as well as due to absence of sphalerite.

Package 5, the lowermost chemostratigraphic package identified in this study, was only intersected in MS22DD029 and as such all interpretations below are based on lithogeochemical data obtained from this drill hole. The CaO (avg: 30.75 wt.%) and MgO (avg: 4.92 wt.%) content in package 5 is relatively depleted with respect to package 4 (Table 3.2). Package 5 is distinguished from other chemostratigraphic packages with its significantly higher contents of SiO_2 (avg: 21.74 wt.%), Al_2O_3 (avg: 5.90 wt.%), K_2O (avg: 1.62 wt.%), TiO_2 (avg: 0.27 wt.%; Table 3.2, n= 63). This indicates a markedly high proportion of siliciclastic component in the lower part of the Meskan stratigraphic sequence, represented by the Çığlı Group. Positive anomalies of SiO_2, Al_2O_3, K_2O, and TiO_2 mostly comes from sandy and argillaceous composition. A significant increase in the siliciclastic component upward within the upper Çığlı group (Figure 3.29) is accompanied by a change into more greenish colors. No significant enrichment or depletion trends were observed in package 5 in terms of Fe_2O_3 and MnO (Figure 3.28).

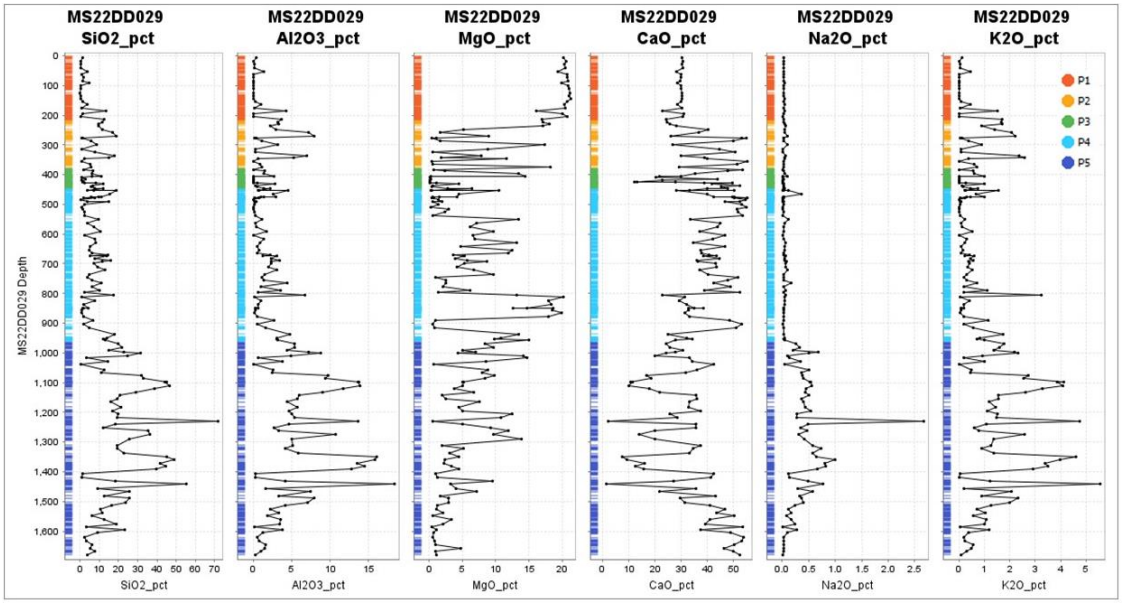


Figure 3.34. Downhole plots showing variation of major oxide contents (in percentages) in identified packages in drill hole MS22DD029

3.5.1.2 High field strength elements (HFSE)

Compatible, immobile HFSE including Nb, Hf, Zr, Ta, W, V, and Sc are relatively depleted in package 1 with respect to the mean HFSE concentrations of all other identified packages (Table 3.3). In contrast, hexavalent molybdenum is relatively enriched in package 1 with respect to the mean HFSE concentrations of all other identified packages. The upper ~120 meters of P1, which correspond to near surface rocks that have undergone weathering and oxidation, generally have higher abundances of HFSEs that can be observed in the downhole plot of drill hole MS22DD021 (Figure. 3.35). HFSE contents below the weathering zone in P1 are generally low except minor local positive peaks (Figure 3.35). Within the first 150 meters of drill hole MS22DD021 and also at 536.50 m depth, similar variations were observed for Zr, Hb, Hf, and Ta (Figure 3.35). Two samples (depth: 527.50 m and 536.50 m) show positive HFSE anomalies at the lower part of package 1 in MS22DD021. In MS22DD029, HFSE are relatively depleted in package 1 (Figure 3.36). Pronounced abrupt increases are evident in Zr, Nb, Hf, Ta, and W at 53.20 m

and 184.80 m depth with Ta content reaching to a maximum of 0.8 ppm within P1 at 92.00 m depth in MS22DD021 (Figure 3.36). Similarly, HFSE concentrations in drill hole MS22DD030 are also relatively low in package 1 (Figure 3.37).

It was noted that enrichment trends in HFSE in this drill hole are less well-defined compared to other three drill holes especially for Nb (Figure 3.37). Ta reaches to a maximum of 1.6 ppm at 159.50 m, but this does not seem to correlate well particularly with Zr, Nb, and W (Figure 3.37). Only 3 samples were selected and analyzed from Package 1 from the underground drill hole MSUGDD0025, which precluded detailed lithogeochemical characterization and identification of elemental trends (Figure 3.38).

Table 3.3. HFSE, W, Mo, and Sc concentrations of all chemostratigraphic packages (n= 439).

439 rows - Univariate	Nb_ppm	Hf_ppm	Zr_ppm	Ta_ppm	W_ppm	Mo_ppm	V_ppm	Sc_ppm
[Visible] : Count Numeric	439	439	439	439	439	439	439	439
[Visible] : Minimum	0.05	0.05	0.4	0.05	0.25	0.05	4	0.5
[Visible] : Maximum	27.2	7.5	292.1	3.6	19.4	150	413	17
[Visible] : Mean	2.973121	0.682574	26.189522	0.230638	0.484169	5.280638	39.558087	1.673121
[Visible] : Median	0.9	0.2	7.5	0.05	0.25	1.8	27	0.5
[Visible] : Standard Deviation	4.375826	1.007131	38.958069	0.329506	1.036538	12.135698	43.158735	2.37079
P1 : Count Numeric	125	125	125	125	125	125	125	125
P1 : Minimum	0.05	0.05	0.4	0.05	0.25	0.1	4	0.5
P1 : Maximum	9.4	1.9	74.8	1.6	2.4	150	413	6
P1 : Mean	1.0928	0.2524	9.3416	0.1184	0.3228	6.7104	25.976	0.844
P1 : Median	0.2	0.05	3	0.05	0.25	1.3	11	0.5
P1 : Standard Deviation	1.897172	0.394256	15.304017	0.193913	0.26201	19.699213	52.191407	0.938461
P2 : Count Numeric	72	72	72	72	72	72	72	72
P2 : Minimum	0.05	0.05	0.6	0.05	0.25	0.3	4	0.5
P2 : Maximum	27.2	4.6	187.5	1.7	2.5	47.1	253	7
P2 : Mean	5.384722	0.977083	39.248611	0.338194	0.438889	8.309722	53.708333	1.604167
P2 : Median	2.45	0.5	18.6	0.2	0.25	4.4	35.5	1
P2 : Standard Deviation	7.067485	1.210574	49.170734	0.430075	0.366773	9.771346	47.502835	1.650731
P3 : Count Numeric	65	65	65	65	65	65	65	65
P3 : Minimum	0.05	0.05	0.4	0.05	0.25	0.4	4	0.5
P3 : Maximum	8.5	2.1	59.4	3.6	5.6	7.9	64	3
P3 : Mean	1.054615	0.271538	8.632308	0.219231	0.441538	2.289231	21.353846	0.684615
P3 : Median	0.4	0.1	3.2	0.05	0.25	1.7	20	0.5
P3 : Standard Deviation	1.818712	0.381401	13.270316	0.486754	0.744593	1.691072	14.729255	0.534506
P4 : Count Numeric	114	114	114	114	114	114	114	114
P4 : Minimum	0.05	0.05	0.9	0.05	0.25	0.3	4	0.5
P4 : Maximum	16.9	3.1	127.1	0.9	19.4	48.3	195	6
P4 : Mean	2.557456	0.500877	20.350877	0.172807	0.587281	6.212281	51.657895	1.22807
P4 : Median	1.1	0.2	9.9	0.05	0.25	3.1	40	0.5
P4 : Standard Deviation	3.274197	0.603382	24.528381	0.183879	1.859499	7.460695	38.961026	1.197601
P5 : Count Numeric	63	63	63	63	63	63	63	63
P5 : Minimum	0.05	0.05	1.6	0.05	0.25	0.05	4	0.5
P5 : Maximum	14.9	7.5	292.1	1.1	2.2	3.4	125	17
P5 : Mean	6.679365	1.952381	73.373016	0.446825	0.713492	0.38254	47.222222	5.222222
P5 : Median	6.6	1.7	64	0.4	0.6	0.1	41	4
P5 : Standard Deviation	3.98776	1.418724	52.803315	0.284955	0.542932	0.661691	29.251107	4.041895

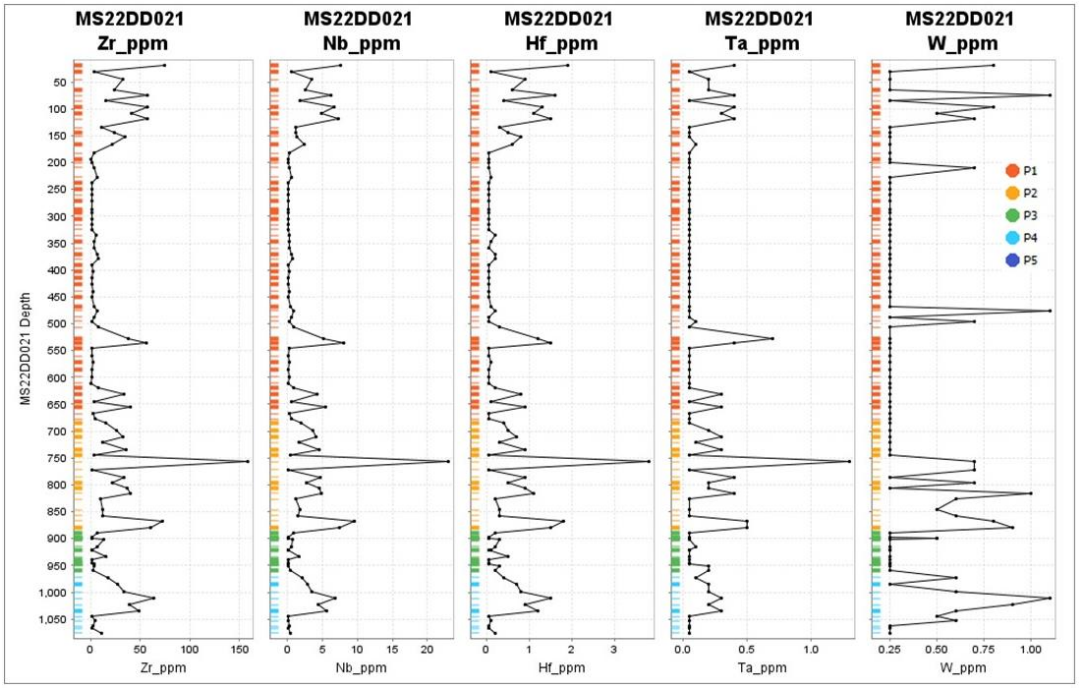


Figure 3.35. Downhole plots showing variation in HFSE concentrations (in ppm) in drill hole MS22DD021.

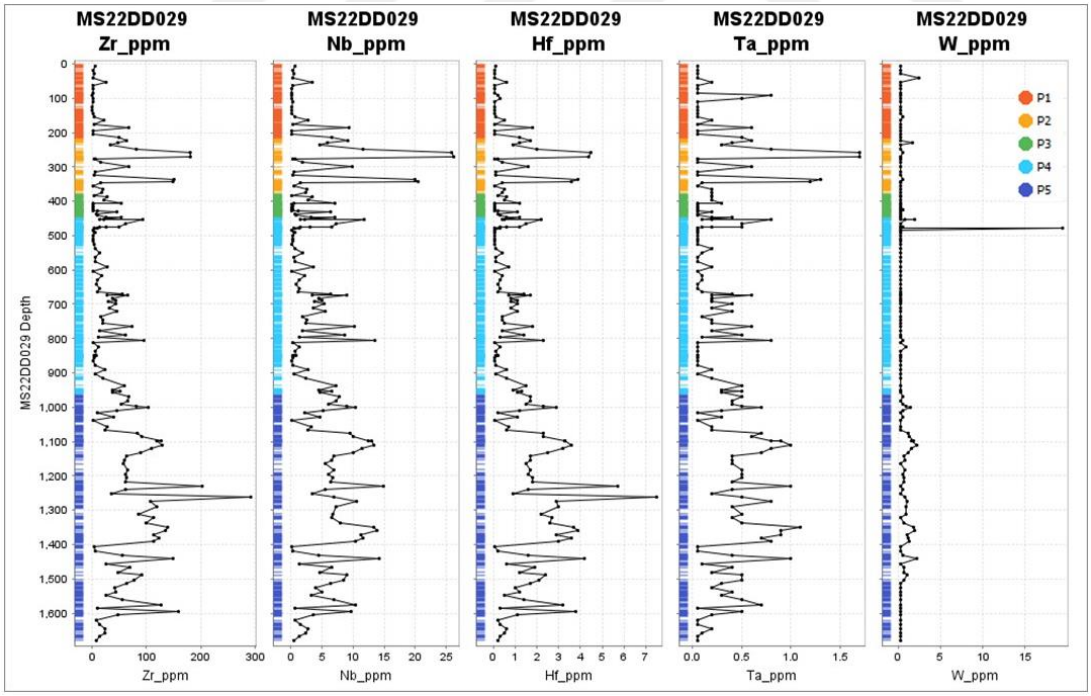


Figure 3.36. Downhole plots showing variation in HFSE concentrations (in ppm) in drill hole MS22DD029.

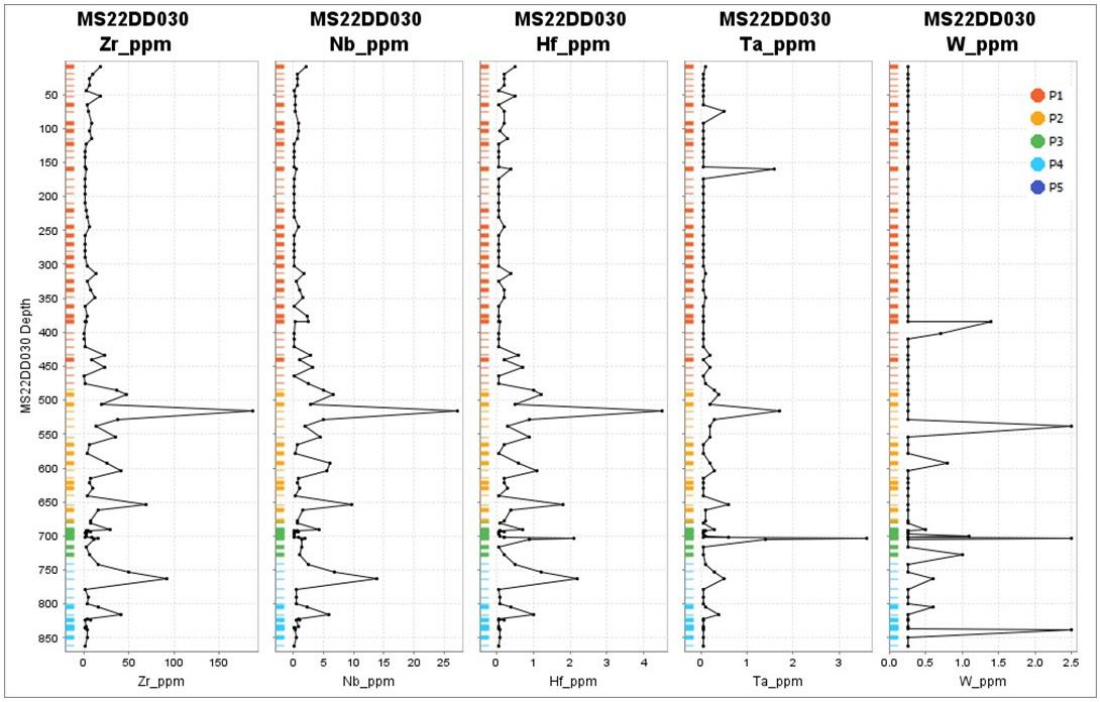


Figure 3.37. Downhole plots showing variation in HFSE concentrations (in ppm) in drill hole MS22DD030.

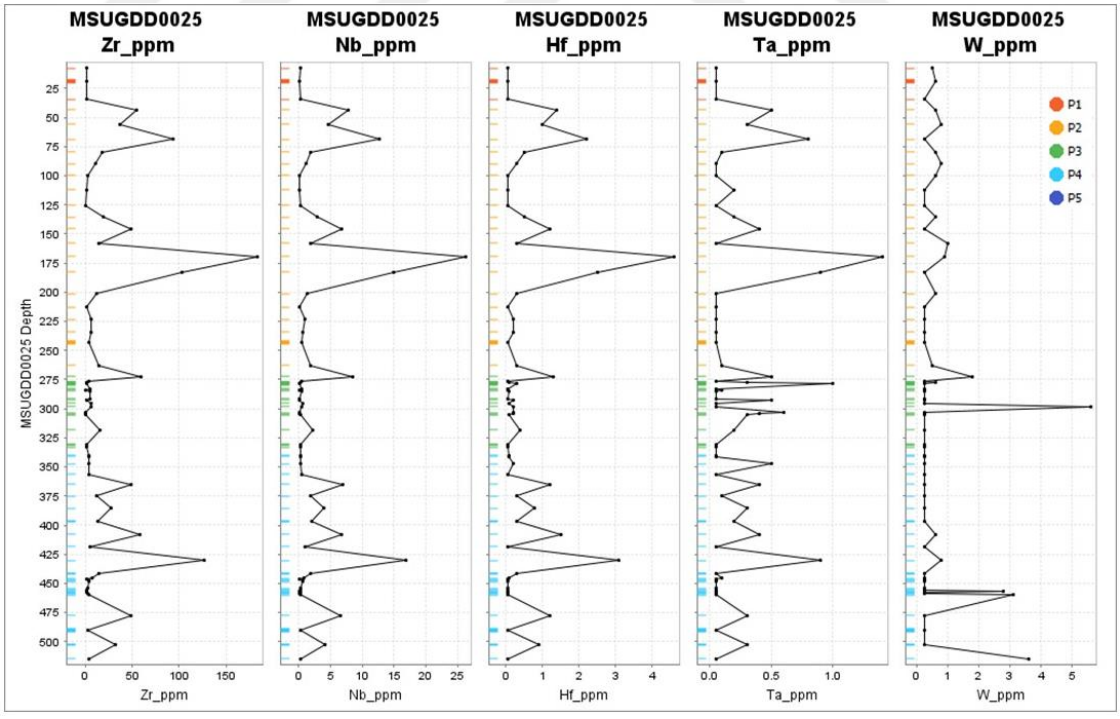


Figure 3.38. Downhole plots showing variation in HFSE concentrations (in ppm) in drill hole MSUGDD0025.

In package 2, HFSE abundances are highly variable. However, overall all HFSE including Hf, Nb, Ta, and Zr have relatively higher concentrations in package 2 samples with respect to package 1 samples (Table 3.3). This is similar to the general increasing trend observed for Al_2O_3, SiO_2, K_2O, and TiO_2. Table 3.3 shows the mean values of Zr (39.25 ppm), Hf (0.98 ppm), Nb (5.38 ppm), and Ta (0.34 ppm) in package 2 (n= 72). In drill hole MS22DD021, the maximum values of Zr (158.20 ppm), Nb (23.00 ppm), Hf (3.8 ppm), and Ta (1.3 ppm) is observed at 756.90 m depth (Figure 3.35). In the drill hole MS22DD029, the maximum values of Zr (181.60 ppm), Nb (26.20 ppm), Hf (4.4 ppm), and Ta (1.7 ppm) is observed at the depth 269.50 m (Figure 3.36). In the drill hole MS22DD030, positive trend of Zr (187.50 ppm), Nb (27.20 ppm), Hf (4.5 ppm), and Ta (1.7 ppm) is observed at the depth 516.00 m (Figure 3.37).

Package 3 is relatively depleted in HFSE with respect to all other chemostratigraphic packages in all drill holes except for package 1 samples (Table 3.3; Figures 3.35–3.38). Overall, most HFSE have low contents but Ta and W shows occasional positive peaks in downhole plots for MS22DD030 and MSUGDD0025 (Figures 3.37 and 3.38). Specifically, the abundances of Zr, Hf, Nb, and Y exhibit a decrease of >70% compared to package 2 (Table 3.3). However, only one sample from drill hole MS22DD030 (depth: 703.00 m) shows relatively high Hf (2.1 ppm), Ta (3.6 ppm), and W (2.5 ppm) with respect to other samples in package 3 (Figure 3.38). Another sample from drill hole MSUGDD0025 (depth: 278.25 m) also indicates above detection limit Ta (1 ppm) and relatively high W (depth: 298.10 m, 5.6 ppm) values in package 3 (Figure 3.38).

Similar to most major and minor elements, mean concentrations of HFSE are also generally higher in package 4 compared to package 3, but they are about 2–3 times lower compared to package 2. In individual drill holes, however, HFSE behavior appears to be highly variable. In MS22DD021 and MSUGDD0025, the suite of HFSE including Zr, Nb, Hf, and Ta are visibly more enriched in this package relative to package 3 samples in downhole plots (Figures 3.35 and 3.38), whereas in others

this relationship is not clear. W separates from this group of elements as it does not show an apparent enrichment or depletion trend among packages 3 and 4.

Plots of TiO_2 against Nb, Zr, Hf, and Ta shows similar trends (Figure 3.39). The mean of Zr (20.35 ppm) values are three times higher than that of package 3 (Table 3.3). The maximum values of Zr (127.10 ppm), Nb (16.90 ppm), Hf (3.1 ppm), and Ta (0.9 ppm) are observed at 430.00 m depth in drill hole MSUGDD0025 in package 4 (Figure 3.38).

Another distinguishing feature of package 5 is its significantly higher HFSE contents (Table 3.3). The increasing rate of each HFSE is variable in package 5 comparing with the value of overall packages. The mean values are reach to maximum in HFSE, Zr (73.37 ppm), Hf (1.95 ppm), Ta (0.45 ppm), and Nb (6.68 ppm) respectively (Table 3.3). In the figure 3.36 indicates that the highest Zr (292.10 ppm) and Hf (7.5 ppm) are observed at 1262.50 m (Figure 3.31).

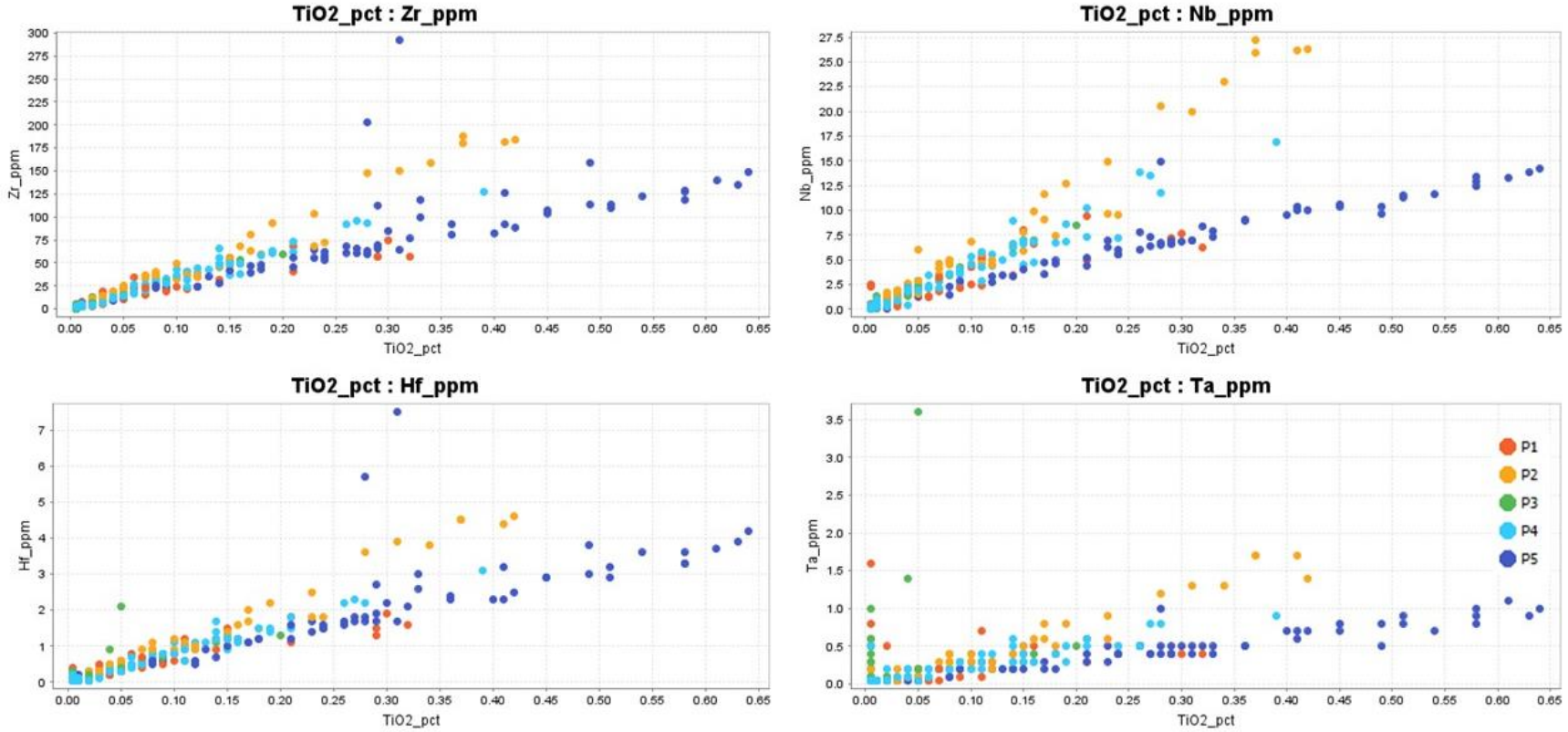


Figure 3.39. Binary plots showing variation in TiO_2 (in percentages) against Hf, Zr, Ta and Nb (in ppm) for each package through four drill holes.

3.5.1.3 Large ion lithophile elements (LILE)

Among LILE, Ba and Sr positively correlate with each other in all of the studied drill holes (Figure 3.41). On the other hand, both Ba and Sr contents show some variation among three drill holes (Figure 3.40). Sr abundances are generally low (<168 ppm) for most of the P1 samples in drill hole MS22DD021 except for a prominent increase ~527.50 m depth, approximately 408 meters before the lower boundary of P1 (Figure 3.41). A similar trend is also observable in drill hole MS22DD029, whereas in MS22DD030 there are at least three distinct intervals (75.00 m, 159.50 m, 341.20 m) at which Sr contents show significant increases (Figure 3.40). Ba concentrations reach up to 2.4 wt.% in MS22DD029 (100.50 m depth), and exceed 5 wt.% in MS22DD030 (at 159.50 m depth) suggesting presence of barite.

Ba and Sr contents of package 2 are relatively lower with respect to package 1 samples (Figure 3.40). Ba values reach up to 4689 ppm in MS22DD021 (785.10 m), and > 8400 ppm in drill hole MSUGDD0025 (111.70 m), whereas there is not observed high values in drill holes MS22DD029 and MS22DD030 in package 2 (Figure 3.40).

Ba and Sr abundances are generally high in package 3 and these also are strongly correlated with each other. Ba content reaches up to 5 wt.% in all four drill holes (Figure 3.40) likely due to presence of barite gangue in the sulfide ore. An increase in Cs concentrations is observed at the transition from package 2 into package 3 in drill holes MS22DD030 (7.2 ppm) and MSUGDD0025 (11.7 ppm; Figure 3.40).

For Rb and Cs, the highest values are observed in the dolostone±high silt unit in package 1 as 47.30 ppm and 7.9 ppm, respectively in the upper levels of MS22DD021 (Figure 3.41). Rb and Cs are correlated with each other in the three drill holes are plotted in Figures 3.41 and 3.42. Significant enrichments in Rb (locally >30 ppm) are generally associated with dolostone±silt levels.

Both Rb and Sr are relatively enriched (around 2 times) in package 4 with respect to package 3, whereas Cs and Ba are relatively depleted (Figures 3.40 and 3.41). Depletion in the latter are possibly due to the absence or low abundance of hydrothermal phases in this package. Sr values are generally consistent within package 4 except three samples with significant enrichments of up to 4.8 wt.% (Figure 3.40). The highest Rb value is observed at the drill hole MS22DD030 (depth: 763.50 m) and drill hole MSUGDD0025 (depth: 430.50m) as 55 ppm (Figure 3.41).

A plot of Rb vs. Cs indicates significantly higher Cs abundances for package 3 samples, while Rb contents remain low (Figures 3.41 and 3.42).

The mean Rb (56.96 ppm) and Cs (3.22 ppm) abundances in package 5 are >four times higher with respect to other packages. The highest Rb (200.80 ppm) and Cs (16.8 ppm) values are observed in dolostone+ silt at 1440.40 m depth (Figure 3.41). The maximum Sr concentration of 2.27 wt.% corresponds to a silty interval at the transition between packages 4 and 5 (Figure 3.41).

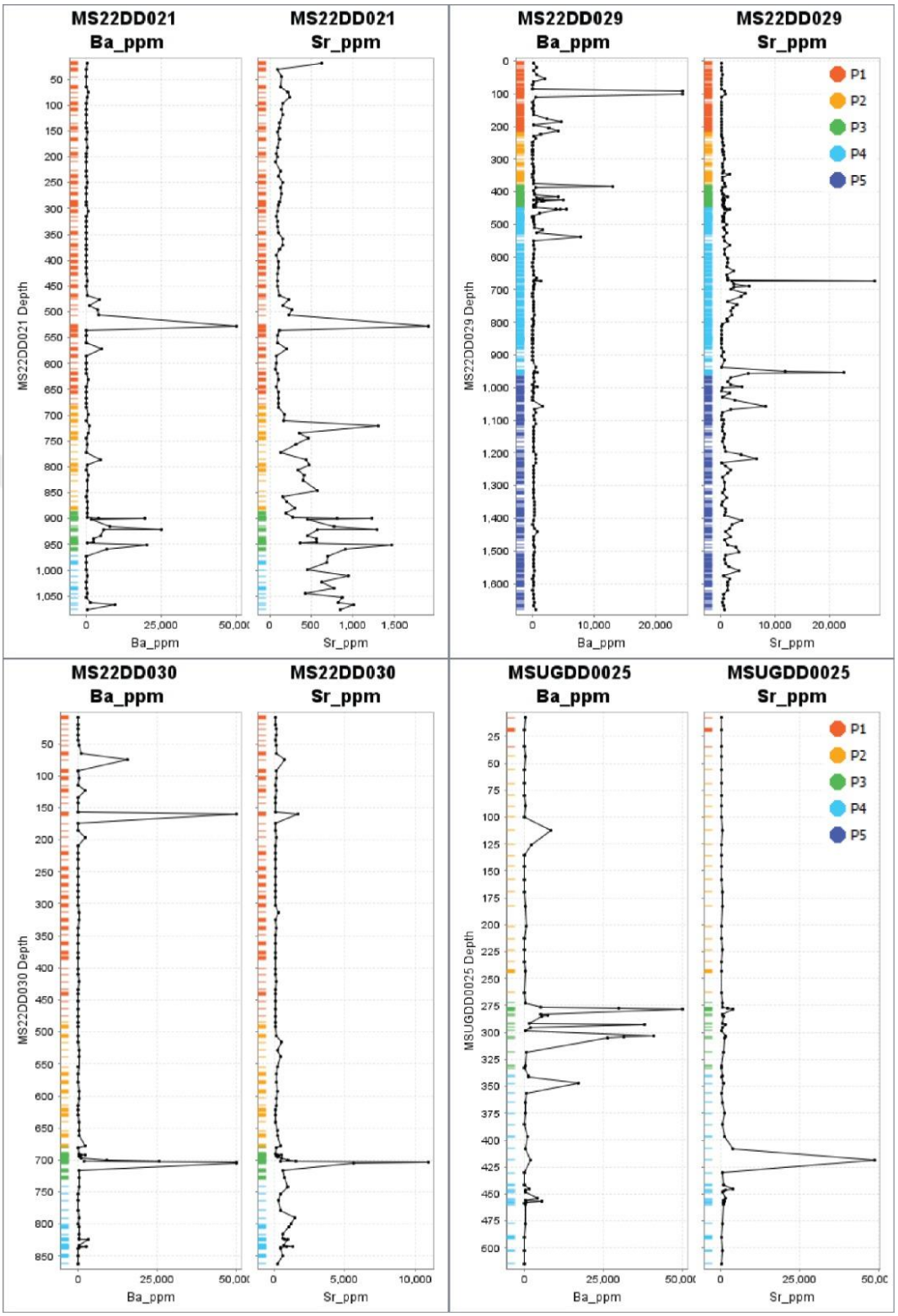


Figure 3.40. Downhole plots showing variation in Ba and Sr concentrations (in ppm) in drill holes MS22DD021, MS22DD029, MS22DD030, and MSUGDD0025.

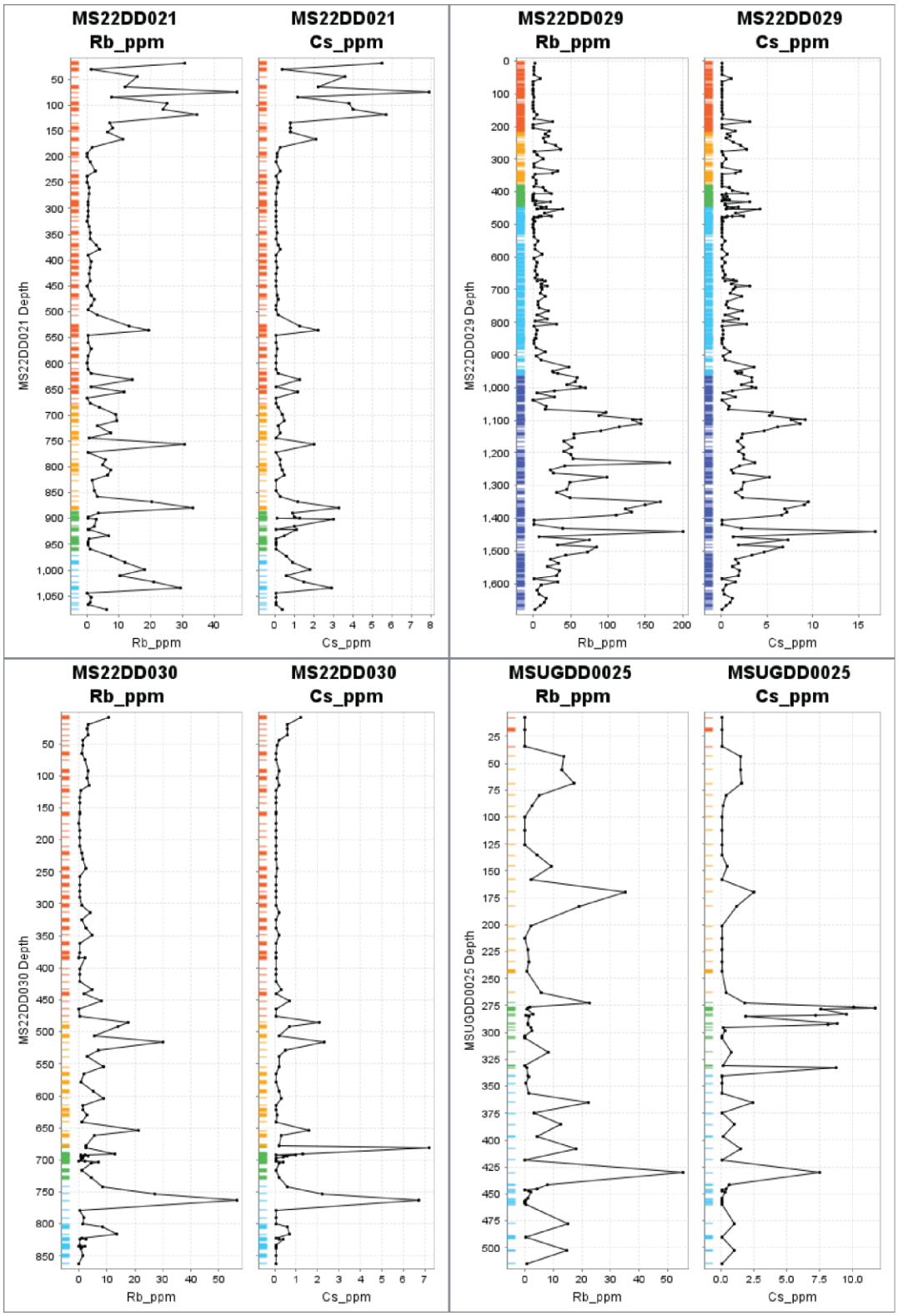


Figure 3.41. Downhole plots showing variation in Rb and Cs concentrations (in ppm) in drill holes MS22DD021, MS22DD029, MS22DD030, and MSUGDD0025.

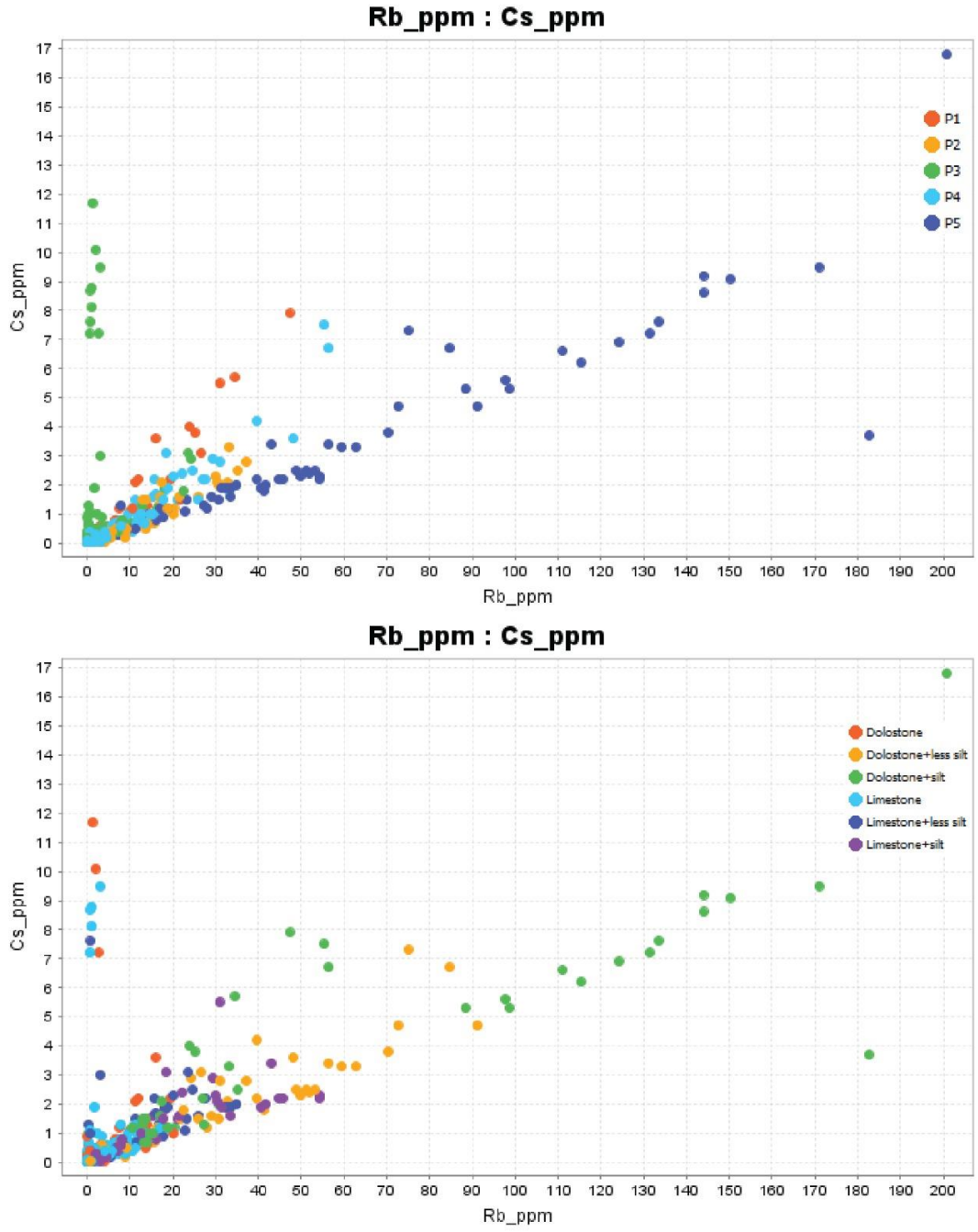


Figure 3.42. Bivariate graphs of Rb and Cs (in ppm) for each chemostratigraphic package (above) and rock type (below).

3.5.1.4 Rare earth elements (REE)

Figure 3.43 shows average of chondrite-normalized REE plots of different lithologies comprising the stratigraphic succession at Meskan. Figure 3.44 shows the REE patterns of individual samples from all packages except samples of package 3. Average REE patterns for all chemostratigraphic packages are broadly similar such that they are relatively enriched in LREE compared to MREE and HREE with significant negative Eu anomalies (Figure 3.43). Dolomitic carbonates of package 1 are relatively less enriched in all REE compared to most other lithologies and these show broadly similar enrichment levels with pure limestones (Figure 3.43; Table 3.4). In fact, slight depletions relative to chondritic values can be observed for some of the HREE including Tm, Yb, and Lu (Figure 3.43).

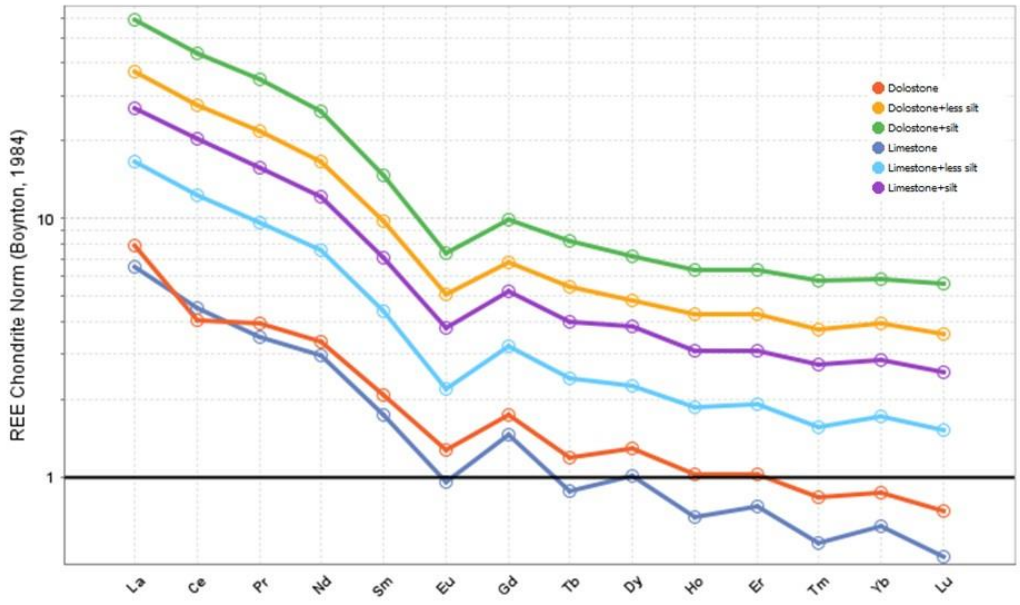


Figure 3.43. Chondrite-normalized REE plot showing average REE contents for each lithological unit (normalization values after Boynton, 1984). Higher levels of enrichment in REEs is due to higher silt content.

REE concentrations of package 1 samples vary widely, but these in general show similar patterns on the chondrite-normalized plot (Figure 3.43 and 3.44). Negative Ce and Eu anomalies are noted in most samples, but individual samples with positive Ce and Eu anomalies are also present (Figure 3.44). The range of Eu/Eu* ratios in

dolostone and dolostone+silt units is between 0.03 and 1.04 (mean= 0.20, n= 125), whereas Ce/Ce* ratios of the same units vary from 0.46 to 2.6 (mean= 1.45, n= 109; Table 3.4) in package 1.

Table 3.4. Total LREE, HREE, and total REE concentrations as well as Eu, Eu/ Eu* and Ce, Ce/ Ce* values of different chemostratigraphic packages

439 rows - Univariate	Sum LREE	Sum HREE	SumREE	Eu_ppm	Eu/Eu*	Ce_ppm	Ce/Ce*
[Visible] : Count Numeric	439	439	439	439	439	439	411
[Visible] : Minimum	0.8	0.115	1.095	0.01	0.008224	0.05	0.458333
[Visible] : Maximum	238.03	14.96	253.02	1.33	2.817181	117.3	3.375
[Visible] : Mean	21.76426	1.945239	23.887312	0.177813	0.210779	9.939522	1.79088
[Visible] : Median	10	0.98	11.095	0.09	0.197164	3.7	1.928571
[Visible] : Standard Deviation	31.509308	2.492122	34.181002	0.230961	0.20641	15.18405	0.447867
P1 : Count Numeric	125	125	125	125	125	125	109
P1 : Minimum	0.91	0.115	1.095	0.01	0.029128	0.2	0.458333
P1 : Maximum	63.02	5.53	68.16	1.18	1.043309	28.8	2.6
P1 : Mean	10.59104	1.1764	11.87904	0.1116	0.200644	4.0664	1.446933
P1 : Median	7.13	0.95	8.15	0.08	0.209529	2.5	1.509202
P1 : Standard Deviation	11.452324	1.045975	12.544358	0.141052	0.120754	5.158268	0.512126
P2 : Count Numeric	72	72	72	72	72	72	71
P2 : Minimum	1.66	0.17	1.985	0.01	0.04	0.5	0.9375
P2 : Maximum	99.49	8.35	107.92	0.7	1.474087	47.5	2.318182
P2 : Mean	21.217639	1.943681	23.329931	0.168611	0.219091	9.886111	1.929543
P2 : Median	12.05	1.075	13.32	0.1	0.194248	5.55	1.946809
P2 : Standard Deviation	23.782463	2.091651	26.01793	0.171992	0.175136	11.337614	0.210208
P3 : Count Numeric	65	65	65	65	65	65	59
P3 : Minimum	0.92	0.115	1.245	0.01	0.008224	0.05	0.535714
P3 : Maximum	40.78	3.99	45.12	0.5	2.817181	19.1	3.375
P3 : Mean	7.235077	0.730231	8.040692	0.0753846	0.274884	3.173077	1.779819
P3 : Median	4.74	0.43	5.24	0.04	0.169031	1.9	1.8
P3 : Standard Deviation	7.947847	0.862041	8.780174	0.0969871	0.434457	3.766122	0.501527
P4 : Count Numeric	114	114	114	114	114	114	110
P4 : Minimum	0.8	0.13	1.14	0.01	0.039223	0.3	0.775862
P4 : Maximum	80.12	7.26	87.98	0.6	1.427306	37.9	3
P4 : Mean	15.182895	1.39136	16.695658	0.121404	0.186684	6.923684	1.893574
P4 : Median	10.13	0.8175	10.9875	0.08	0.18051	3.9	1.961084
P4 : Standard Deviation	15.171538	1.409281	16.675584	0.12635	0.137908	7.193302	0.366177
P5 : Count Numeric	63	63	63	63	63	63	62
P5 : Minimum	1.47	0.17	1.795	0.01	0.05	0.3	1.451613
P5 : Maximum	238.03	14.96	253.02	1.33	0.27948	117.3	2.435644
P5 : Mean	71.457619	5.728333	77.713413	0.52746	0.198848	34.092063	2.065097
P5 : Median	63.29	5.1	69.24	0.5	0.203629	30.4	2.074026
P5 : Standard Deviation	50.565927	3.800544	54.626229	0.338169	0.0371927	24.338721	0.158266

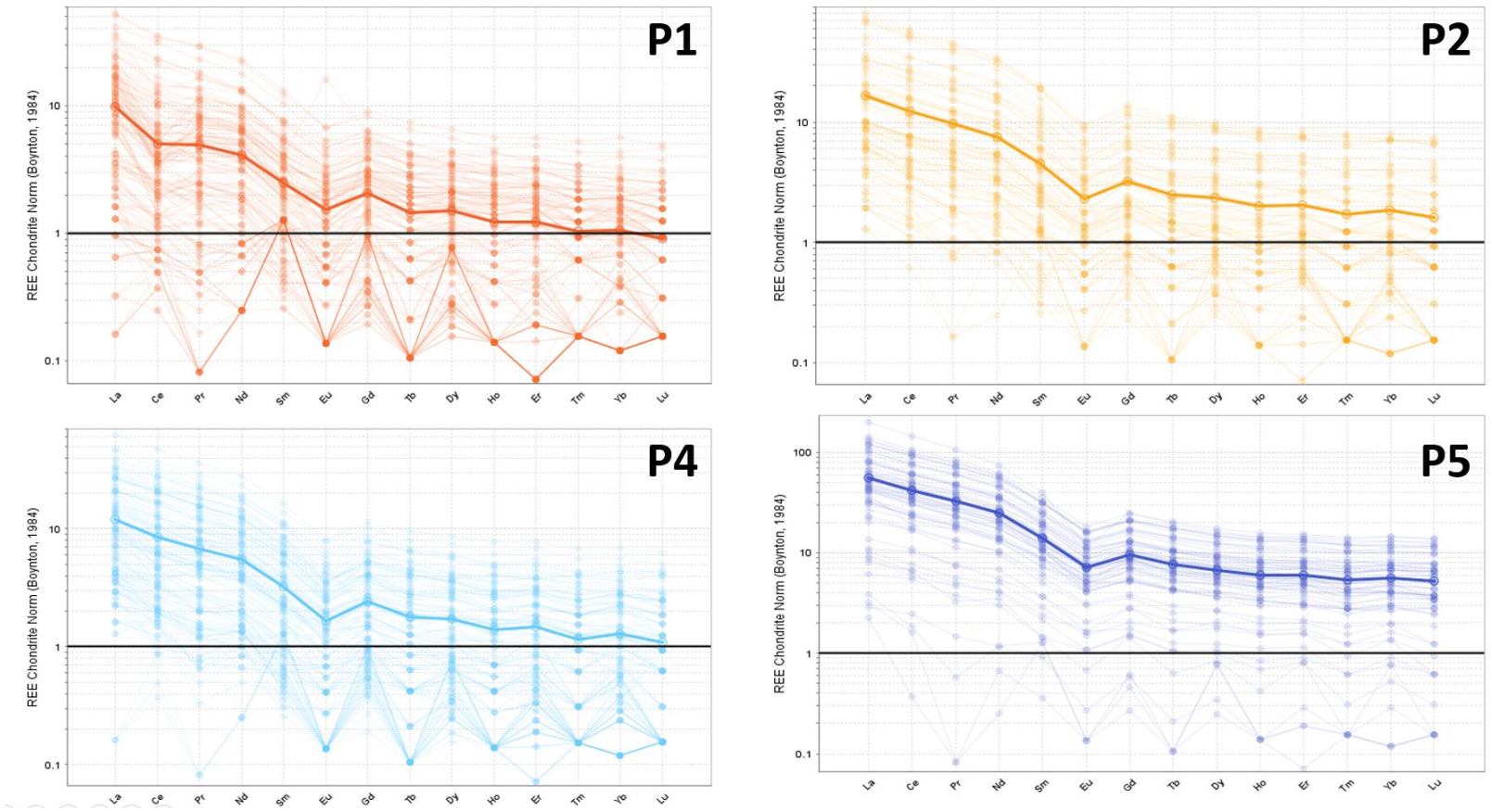


Figure 3.44. Chondrite-normalized REE plots of samples from packages 1, 2, 4, and 5. Lines with heavier stroke represents the mean REE concentrations (in ppm) of all samples from each of the packages 1, 2, 4, and 5. Normalization values are from Boynton (1984).

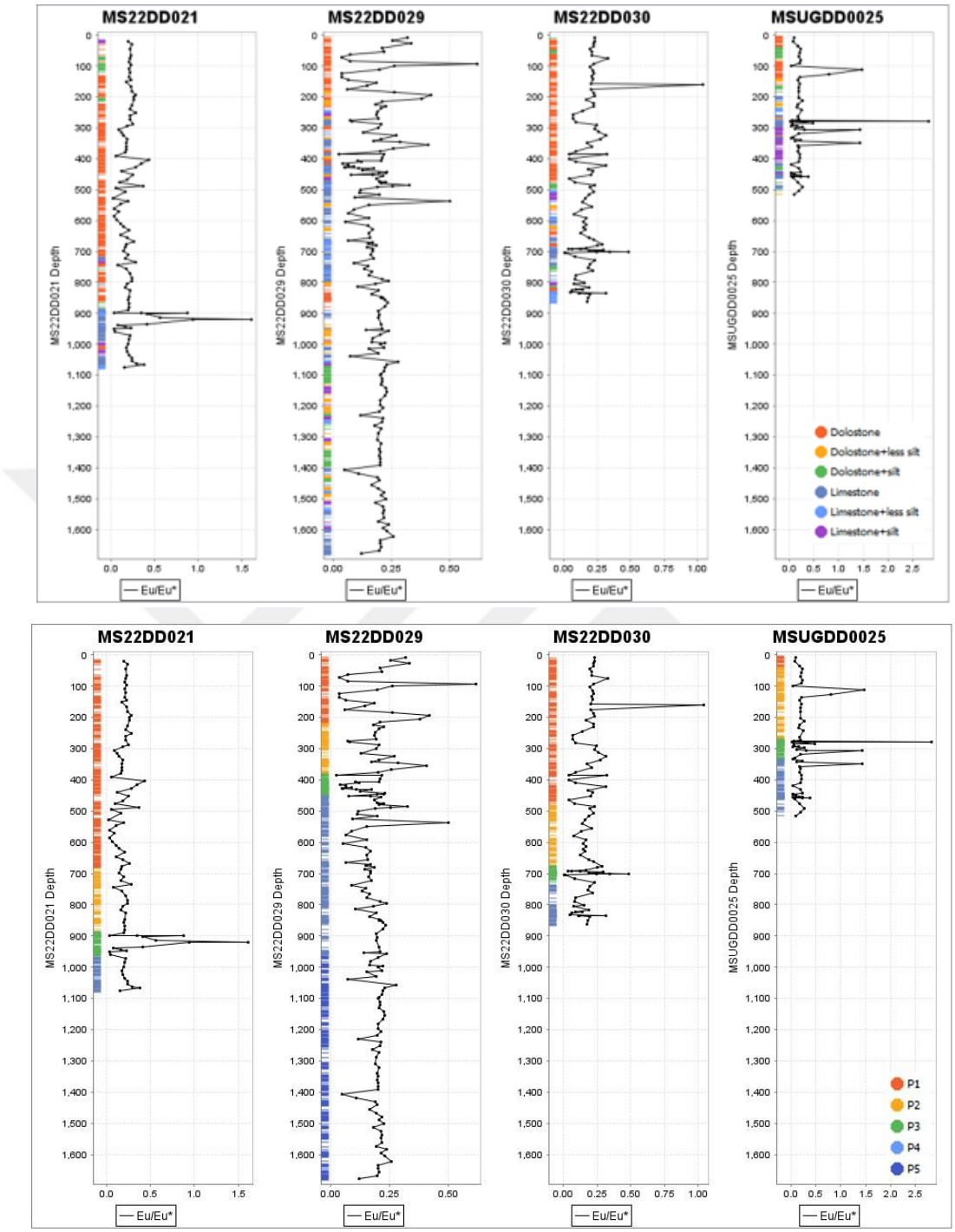


Figure 3.45. Downhole plots showing variation in Eu/Eu* ratios for each lithology (above) and for each chemostratigraphic package (below).

Package 2 samples show similar trends with package 1 samples on a chondrite-normalized REE plot such that LREE are relatively more enriched compared to MREE and HREE (Figure 3.44). The mean total REE concentrations in package 2

samples (23.33 ppm), however, are slightly higher compared to that of package 1 samples (11.88 ppm; Table 3.4). Majority of samples display negative Eu anomalies, but Ce anomalies are not as well-developed (Figure 3.44). The range of Eu/Eu* values in package 2 is between 0.01 and 0.70 (mean= 0.17; n= 72), whereas Ce/Ce* ratios vary from 0.94 to 2.32 (mean= 1.93; n= 71; Table 3.4).

The behavior of REE within package 3 is quite different than other identified chemostratigraphic packages (Figure 3.46). Average REE concentrations are lower in package 3 compared to other packages. Samples that belong to package 3 are strongly depleted in REE with respect to other packages. Additionally, samples from sulfide zone with zebra/banded-textured limestone are quite different from non-mineralized (relatively sulfide-free) samples within Package 3 (Figure 3.47).

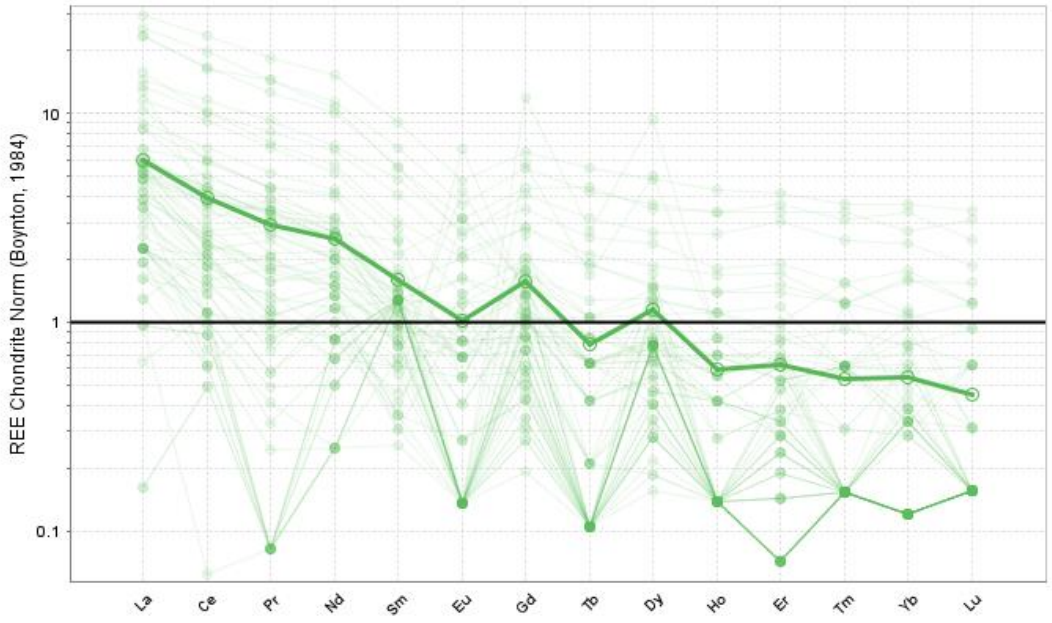


Figure 3.46. Chondrite-normalized REE plot of samples from package 3. Green line with a heavier stroke represents the mean REE concentrations of all package 3 samples. Normalization values are from Boynton (1984).

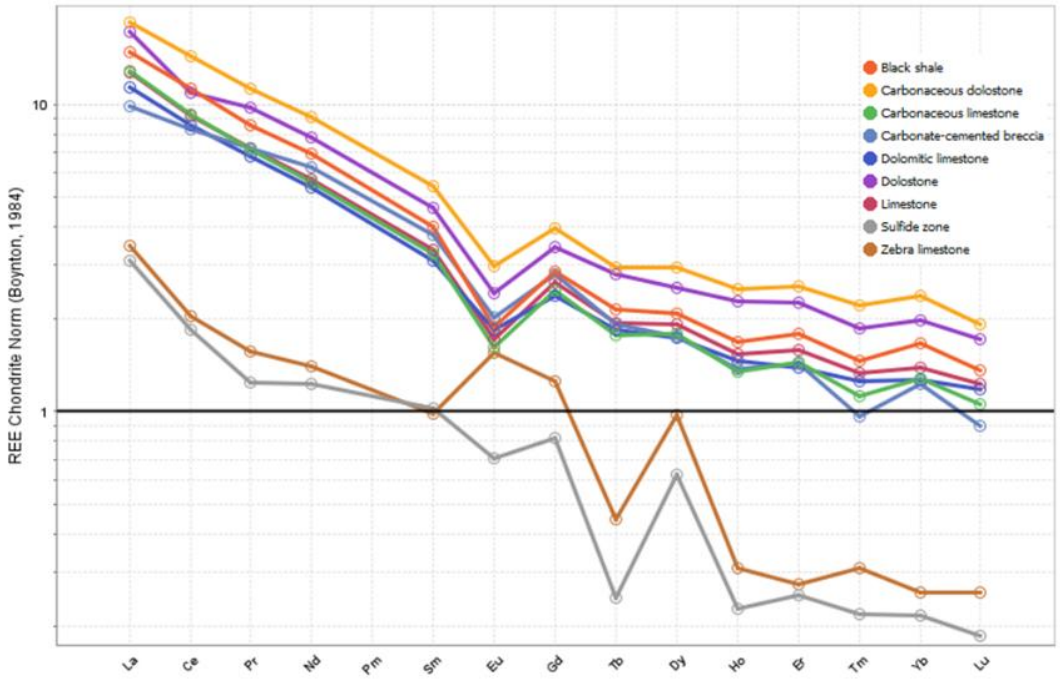


Figure 3.47. Chondrite-normalized REE plot of samples from all lithological units. Lines with heavier stroke represents the mean REE concentrations (in ppm) of all samples from each different lithology. Normalization values are from Boynton (1984).

Chondrite-normalized REE plot in Figure 3.44 indicates that package 4 samples have broadly similar REE patterns with samples from all other chemostratigraphic packages (with the sole exception of sulfide-rich samples in package 3) such that LREE are relatively more enriched compared to MREE and HREE. The range of Eu/Eu* values in package 4 is between 0.04 and 1.43 (mean= 0.19; n= 114), while Ce/Ce* ratios vary from 0.78 to 3.00 (mean= 1.89; n= 110; Table 3.4). Negative Eu anomalies for most samples is also conformable with the general trend in Meskan. A comparison of REE contents against other chemostratigraphic packages indicates that package 4 samples are generally enriched at least about 2 to 3 times in all REE with respect to other packages (Figure 3.44).

Package 5 samples also show relative enrichments in LREE compared to MREE and HREE and these also consistently display negative Eu anomalies (Figure 3.44; Table 3.4). In addition, the highest REE enrichments are observed in this package (up to

10 times enriched compared to clean limestone or dolostone samples; Figure 3.44) likely reflecting the relatively siliciclastic rich and carbonate deficient nature of the lithologies. (Figure 3.47). The range of Eu/ Eu* values in package 5 is between 0.05 and 0.28 (mean= 0.20; n= 63), whereas Ce/Ce* ratios vary from 1.45 to 2.43 (mean= 2.07; n= 62; Table 3.4).

3.5.1.5 Transition metals and metalloids

Package 1 samples do not show apparent trends for a number of metals/metalloids including Ag, Au, Cd, Hg, Zn, and Pb. There is higher concentrations in Ag and Hg in drill hole MS22DD021 and MS22DD029 (Figure 3.48). Ag reaches up to 0.4 ppm, whereas Hg reaches up to 22.11 ppm at 421.60 m depth in drill hole MS22DD030 (Figure 3.49). In drill hole MS22DD029, the maximum Hg value is detected at 100.50 m as 1.31 ppm in package 1 (Figure 3.48). Cu and Co correlate well for all three drill holes. Abundances of both metals are generally low (mean for Co= 0.82 ppm and for Cu= 2.97 ppm; Figure 3.49), but particularly in drill hole MS22DD021 these two elements are relatively enriched (up to 11.30 ppm for Cu and 33.50 ppm for Cu) at shallow depths (Figure 3.49, drill hole- 21, depth 96.50 m). Both metals, on the other hand, have quite low concentrations in drill holes MS22DD029 and MS22DD030 (Figure 3.49).

Ag, Au, Cd, Hg, and Zn are not significantly enriched in package 2 samples (Figure 3.49). Besides Ag and Hg are relatively low apart from one sample that belongs to drill hole MSUGDD0025 at 79 m depth as 1.15 ppm (Figure 3.48). The highest Co (8.8 ppm, 270 m) and Cu (39.40 ppm, 335.50 m) are observed in the MS22DD029 (Figure 3.49). Package 2 samples are markedly more enriched in V in all drill holes compared to samples from other packages (Figure 3.50). Although the highest V value of 413 ppm is observed in drill hole MS22DD021 in package 1, the highest mean V concentrations are encountered in package 2 with a mean V abundance of 53.71 ppm.

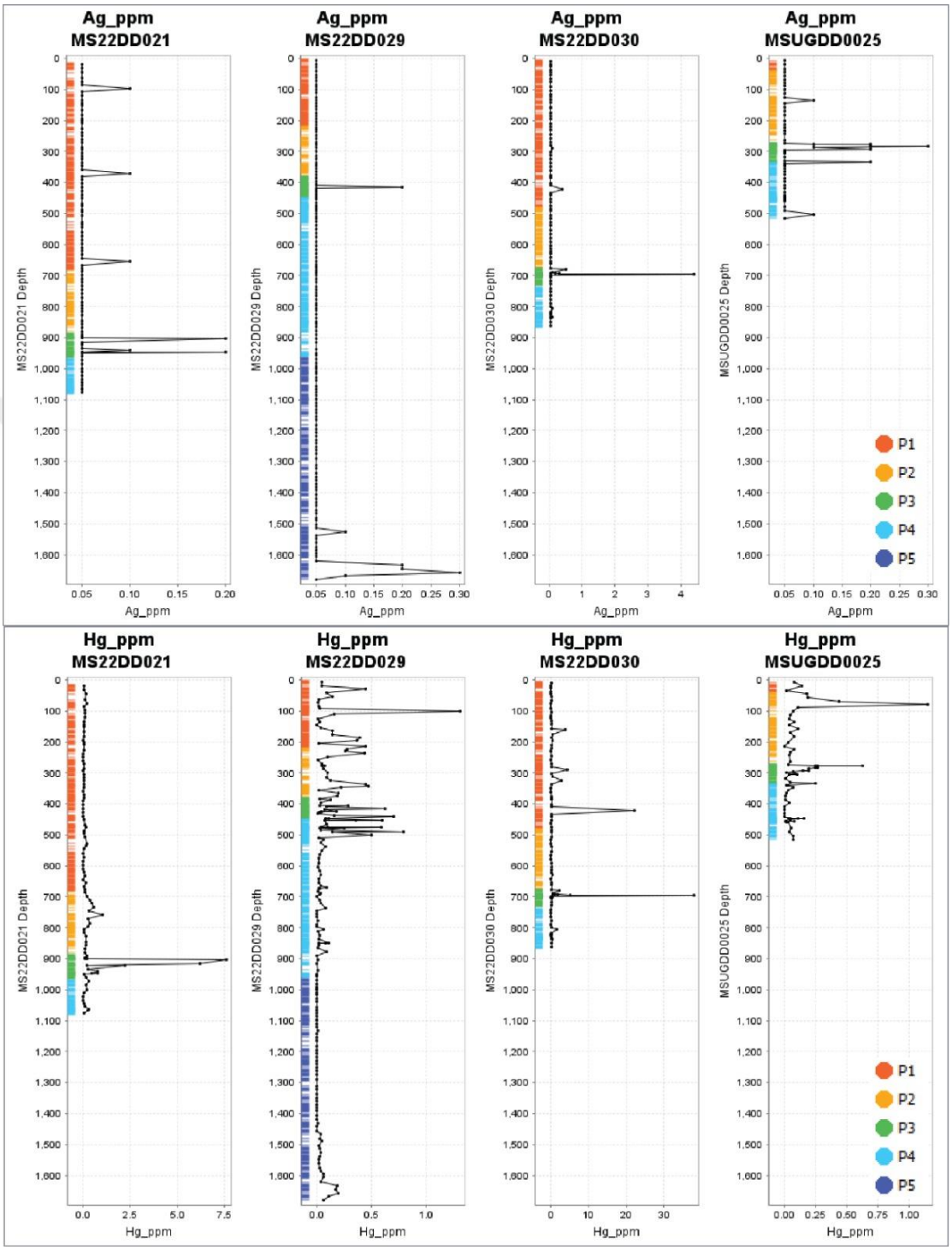


Figure 3.48. Downhole plots of Ag and Hg (in ppm) in drill holes MS22DD029, MS22DD030, and MSUGDD0025

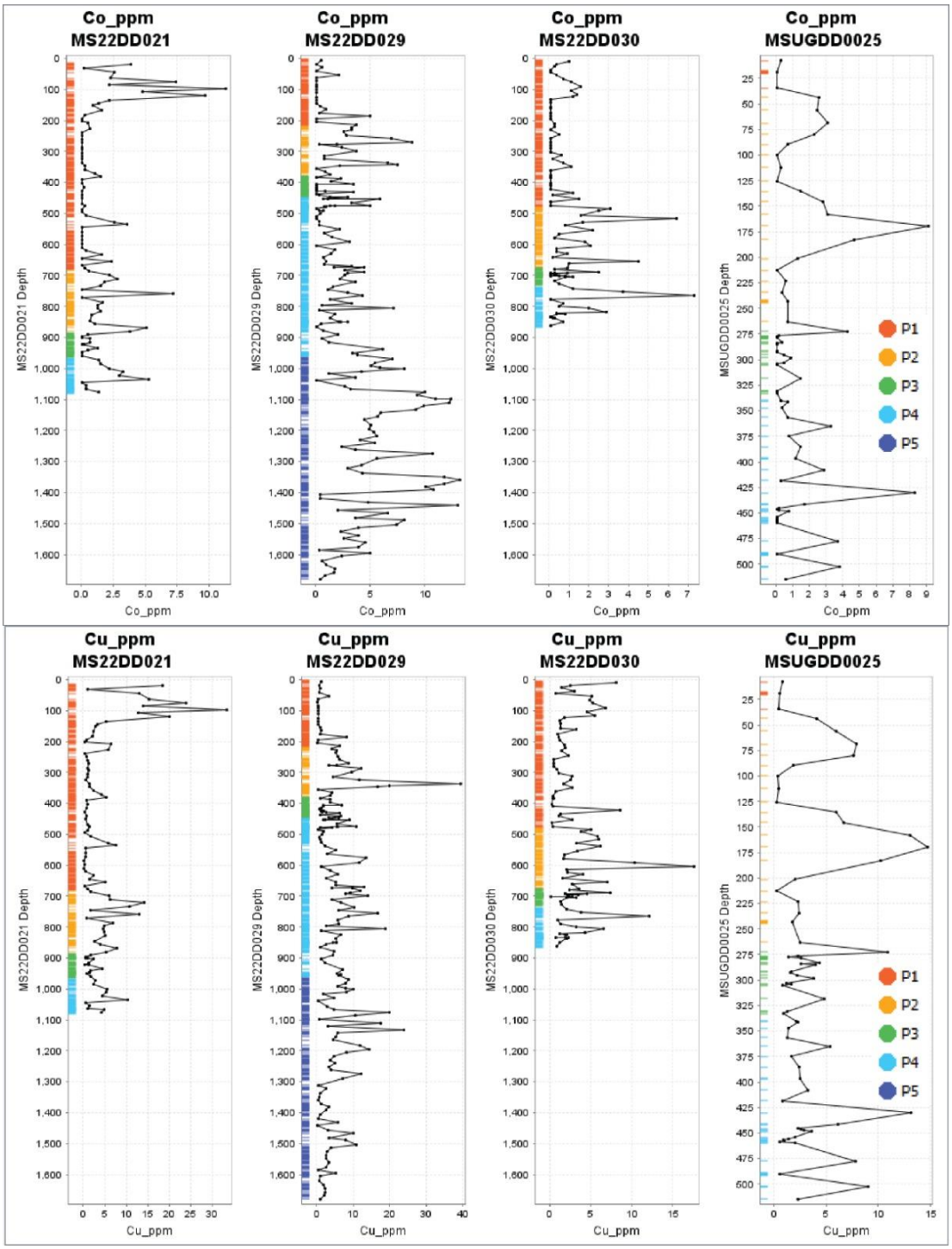


Figure 3.49. Downhole plots showing variations in Co and Cu concentrations (in ppm) in drill holes MS22DD021, MS22DD029, and MS22DD030

The strong positive V anomalies are particularly associated with the carbonaceous limestone and black shale units with high bitumen/graphite contents. Similarly, Mo

concentrations are also higher in package 2 compared to package 1 (Figure 3.50), the latter characterized by very low Mo concentrations close to lower detection limit. Among the package 2 samples, the highest Mo (47.10 ppm, depth: 157.50 m) and V (253.00 ppm, depth: 345.50 m) are observed in drill holes MSUGDD0025 and MS22DD021, respectively (Figure 3.50).

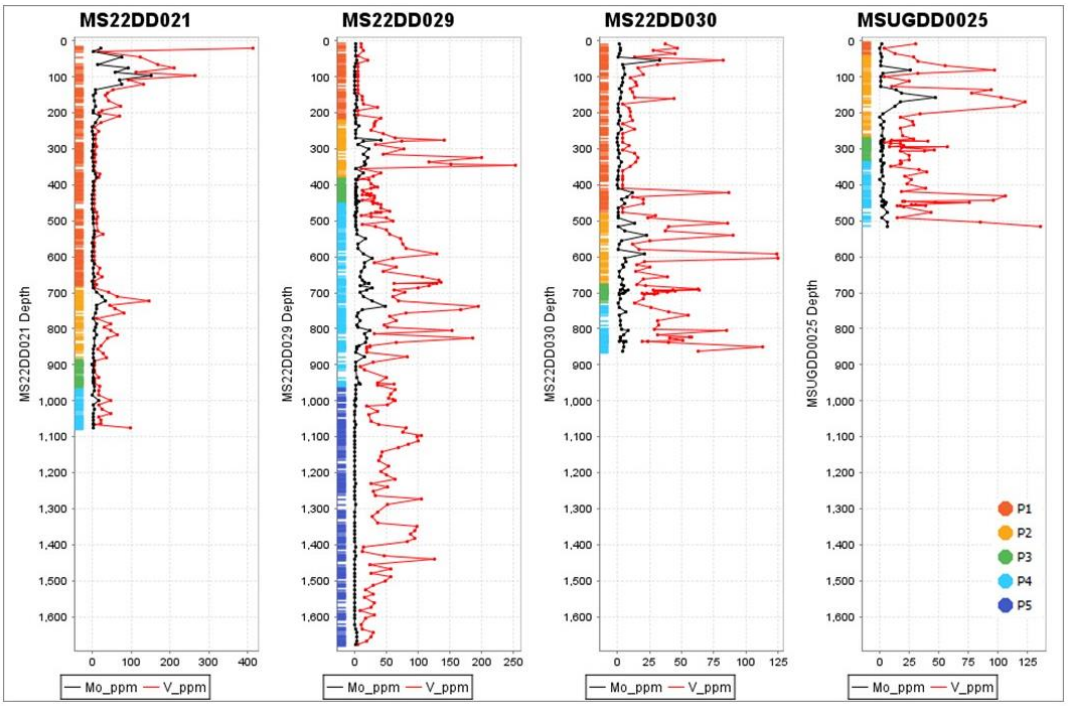


Figure 3.50. Downhole plots showing the variation of Mo and V (in ppm) for each package in the studied drill holes MS22DD021, MS22DD029, MS22DD030, and MSUGDD0025.

A correlation matrix for a suite of 36 selected elements was constructed for package 3 samples to understand their relationship to the Meskan Zn-Pb mineralization (Table 3.5). Since package 3 comprises the host lithologies of the base metal sulfide ore, it has the highest concentrations of a variety of base metals and metalloids. As expected, package 3 samples are highly enriched in Zn and are also relatively enriched in Cd, two metals that are strongly associated with sphalerite (Figure 3.51). A fairly strong correlation exists between Fe_2O_3 and Zn, whereas Pb is less correlated with Fe_2O_3 (Table 3.5). Similarly, MnO values only show positive correlation with Zn at 0.098 (Table 3.5). The highest Zn values exceed the upper detection limit of

10,000 ppm, whereas the highest Cd value reaches to 496.1 ppm as observed in drill hole MSUGDD0025. Moreover, the correlation matrix of P3 shows that there is a good correlation between Zn, Cd, and As (Table 3.5). On the other hand, some of the transition metals including Cu and Co show rather high correlation with TiO_2, P_2O_5, and HFSE, rather than with ore metals such as Pb and Zn (Table 3.5).

Hg contents of most rock units at Meskan are generally quite low. Nevertheless, there is an increase in Hg in package 3 samples with a maximum Hg concentration of 38.0 ppm as observed in drill hole MS22DD030 (depth: 695.00 m; Figure 3.49).

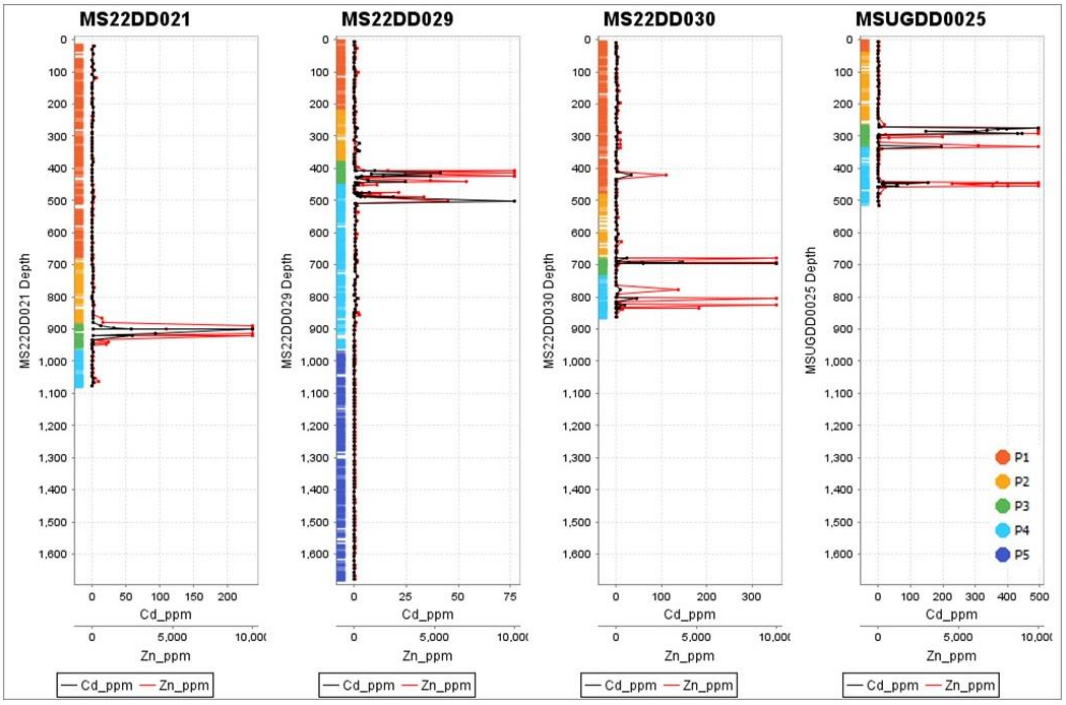


Figure 3.51. Downhole plots showing the variation of Cd and Zn (in ppm) for each package in the studied drill holes MS22DD021, MS22DD029, MS22DD030, and MSUGDD0025.

Generally, there is a strong correlation between Fe_2O_3 + MnO + Zn + Pb and TOT/S (Figure 3.52). This indicates that, these elements primarily reside in pyrite, sphalerite, and galena, sulfide phases that commonly occur together in the mineralized samples. A significant number of the TOT/S values are frequently above the upper detection limit (30 wt.%) in the mineralized unit, particularly in intervals of semi-massive and massive sulfide mineralization. A comparison of downhole

geochemistry in terms of sulfide-mineralized intervals in each drill hole indicates a gradual increase in pyrite amounts with depth followed by an abrupt peak in sphalerite + galena + pyrite abundance in the main mineralized horizon.

Table 3.5. Correlation matrix of selected major, minor, and trace elements for package 3 samples. Highly correlated elements are highlighted with green

	SiO2_pct	Al2O3_pct	Fe2O3_pct	MnO_pct	CaO_pct	MgO_pct	Na2O_pct	K2O_pct	TiO2_pct	P2O5_pct	Cr2O3_pct	Pb_ppm	Zn_ppm	As_ppm	Cd_ppm	Sb_ppm	Ag_ppm	Tl_ppm	Se_ppm	Ba_ppm	Mo_ppm	Cu_ppm	Sc_ppm	Co_ppm	Cs_ppm	Hf_ppm	Nb_ppm	Rb_ppm	Sr_ppm	Ta_ppm	Th_ppm	U_ppm	V_ppm	W_ppm	Zr_ppm	Y_ppm
SiO2_pct	1,00																																		
Al2O3_pct	0,68	1,00																																	
Fe2O3_pct	-0,45	-0,33	1,00																																
MnO_pct	-0,36	-0,49	0,13	1,00																															
CaO_pct	0,34	0,11	-0,75	0,16	1,00																														
MgO_pct	0,50	0,65	-0,31	-0,32	0,00	1,00																													
Na2O_pct	0,08	0,37	-0,28	-0,28	-0,28	0,55	1,00																												
K2O_pct	0,67	1,00	-0,35	-0,50	0,12	0,67	0,39	1,00																											
TiO2_pct	0,63	0,97	-0,30	-0,44	0,08	0,67	0,39	0,97	1,00																										
P2O5_pct	0,71	0,84	-0,37	-0,49	0,21	0,63	0,24	0,83	0,81	1,00																									
Cr2O3_pct	0,18	0,23	-0,19	-0,27	-0,07	0,01	0,03	0,22	0,17	0,12	1,00																								
Pb_ppm	-0,47	-0,31	0,20	-0,12	-0,54	-0,23	0,44	-0,30	-0,29	-0,26	-0,11	1,00																							
Zn_ppm	-0,51	-0,41	0,47	0,10	-0,59	-0,29	0,17	-0,42	-0,38	-0,32	-0,21	0,79	1,00																						
As_ppm	-0,45	-0,30	0,40	-0,11	-0,68	-0,23	0,34	-0,29	-0,27	-0,37	-0,12	0,75	0,71	1,00																					
Cd_ppm	-0,42	-0,25	0,09	-0,13	-0,47	-0,18	0,52	-0,25	-0,23	-0,26	-0,07	0,90	0,61	0,74	1,00																				
Sb_ppm	-0,18	-0,13	0,15	-0,15	-0,24	-0,11	0,08	-0,13	-0,13	-0,01	0,07	0,50	0,34	0,32	0,52	1,00																			
Ag_ppm	-0,12	-0,09	0,13	-0,10	-0,15	-0,08	-0,05	-0,10	-0,10	0,00	0,08	0,35	0,23	0,13	0,35	0,94	1,00																		
Tl_ppm	-0,45	-0,31	0,69	-0,03	-0,73	-0,24	0,05	-0,31	-0,28	-0,40	-0,14	0,48	0,64	0,76	0,39	0,21	0,15	1,00																	
Se_ppm	-0,33	-0,23	-0,04	-0,10	-0,29	-0,19	0,37	-0,23	-0,22	-0,23	-0,09	0,82	0,59	0,52	0,68	0,22	0,15	0,23	1,00																
Ba_ppm	-0,16	-0,19	-0,28	0,11	0,04	-0,18	0,02	-0,19	-0,18	-0,25	0,52	0,07	-0,07	0,09	0,19	-0,04	-0,07	-0,07	0,10	1,00															
Mo_ppm	0,38	0,17	-0,04	-0,22	0,07	0,01	-0,20	0,15	0,11	0,34	0,01	0,03	0,03	-0,07	-0,04	0,31	0,33	-0,06	0,03	-0,25	1,00														
Cu_ppm	0,57	0,82	-0,19	-0,51	-0,05	0,59	0,37	0,81	0,83	0,71	0,09	-0,05	-0,20	-0,14	-0,07	0,00	-0,02	-0,20	0,02	-0,24	0,29	1,00													
Sc_ppm	0,54	0,89	-0,13	-0,29	-0,04	0,59	0,31	0,87	0,90	0,69	0,09	-0,22	-0,28	-0,20	-0,17	-0,09	-0,06	-0,17	-0,20	-0,20	0,11	0,78	1,00												
Co_ppm	0,68	0,97	-0,29	-0,45	0,07	0,67	0,36	0,97	0,97	0,82	0,20	-0,30	-0,41	-0,29	-0,23	-0,10	-0,06	-0,30	-0,21	-0,17	0,17	0,84	0,90	1,00											
Cs_ppm	-0,30	-0,04	0,01	-0,22	-0,50	-0,03	0,68	-0,03	-0,02	-0,17	-0,05	0,77	0,51	0,76	0,84	0,19	0,04	0,44	0,66	0,15	-0,12	0,07	0,02	-0,04	1,00										
Hf_ppm	0,55	0,80	-0,36	-0,46	0,04	0,47	0,29	0,79	0,79	0,63	0,67	-0,28	-0,41	-0,28	-0,22	-0,14	-0,11	-0,31	-0,20	0,25	0,04	0,63	0,64	0,78	-0,06	1,00									
Nb_ppm	0,63	0,97	-0,28	-0,43	0,07	0,66	0,38	0,97	0,99	0,80	0,16	-0,28	-0,38	-0,26	-0,23	-0,12	-0,09	-0,26	-0,22	-0,20	0,12	0,83	0,92	0,97	-0,02	0,78	1,00								
Rb_ppm	0,62	0,99	-0,32	-0,48	0,07	0,69	0,44	0,99	0,97	0,81	0,19	-0,26	-0,37	-0,25	-0,20	-0,11	-0,09	-0,27	-0,19	-0,19	0,11	0,81	0,89	0,96	0,02	0,77	0,97	1,00							
Sr_ppm	-0,01	0,01	-0,24	-0,14	-0,03	-0,11	0,01	0,01	-0,01	-0,05	0,86	-0,04	-0,15	-0,04	0,03	-0,06	-0,07	-0,13	-0,03	0,76	-0,15	-0,07	-0,12	-0,01	0,01	0,57	-0,03	-0,02	1,00						
Ta_ppm	0,12	0,19	-0,24	-0,25	-0,08	0,04	0,06	0,19	0,18	0,09	0,88	-0,09	-0,20	-0,08	-0,02	-0,06	-0,06	-0,14	-0,06	0,69	-0,08	0,11	0,06	0,18	0,00	0,72	0,16	0,17	0,96	1,00					
Th_ppm	0,57	0,94	-0,28	-0,36	0,07	0,70	0,44	0,94	0,97	0,77	0,10	-0,28	-0,36	-0,25	-0,21	-0,12	-0,08	-0,25	-0,22	-0,18	0,07	0,77	0,88	0,94	0,00	0,74	0,98	0,95	-0,06	0,12	1,00				
U_ppm	0,70	0,54	-0,41	-0,43	0,40	0,34	-0,02	0,55	0,48	0,74	0,07	-0,34	-0,35	-0,42	-0,35	-0,07	-0,05	-0,44	-0,21	-0,25	0,60	0,51	0,30	0,51	-0,30	0,38	0,47	0,48	-0,08	0,02	0,43	1,00			
V_ppm	0,30	0,33	0,06	-0,31	-0,05	0,10	-0,12	0,31	0,29	0,25	0,25	-0,14	-0,17	-0,09	-0,13	0,19	0,20	-0,05	-0,17	-0,06	0,40	0,36	0,34	0,33	-0,12	0,24	0,31	0,29	-0,01	0,11	0,23	0,28	1,00		
W_ppm	0,30	0,13	-0,17	-0,22	-0,10	0,56	0,22	0,12	0,13	0,23	0,25	-0,15	-0,20	-0,13	-0,11	-0,07	-0,05	-0,14	-0,13	0,06	0,03	0,22	0,08	0,18	-0,08	0,27	0,11	0,10	0,25	0,29	0,08	0,13	0,02	1,00	
Zr_ppm	0,64	0,97	-0,29	-0,42	0,08	0,66	0,40	0,97	0,99	0,81	0,17	-0,26	-0,38	-0,26	-0,21	-0,13	-0,09	-0,28	-0,19	-0,20	0,13	0,82	0,90	0,97	-0,01	0,79	0,99	0,97	-0,02	0,16	0,97	0,48	0,28	0,11	1,00
Y_ppm	0,62	0,93	-0,44	-0,45	0,18	0,65	0,37	0,93	0,95	0,79	0,31	-0,31	-0,45	-0,32	-0,23	-0,12	-0,08	-0,37	-0,23	0,00	0,08	0,74	0,80	0,92	-0,05	0,87	0,94	0,93	0,19	0,35	0,93	0,49	0,21	0,15	0,95	1,00

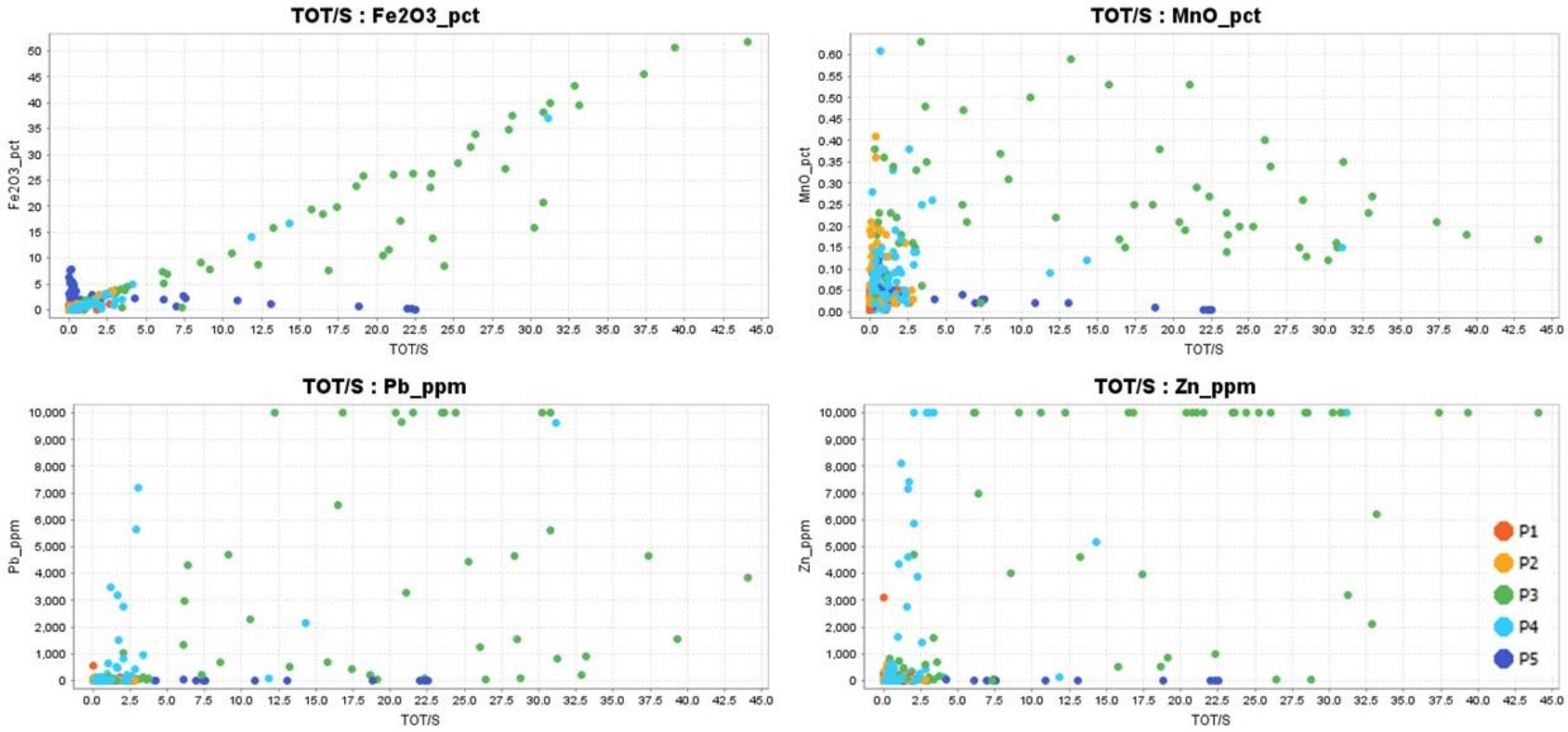


Figure 3.52. Bivariate plots showing the variation of TOT/S versus Fe_2O_3, MnO (in percentage), Pb, and Zn (in ppm) graphs for each package in all drill holes.

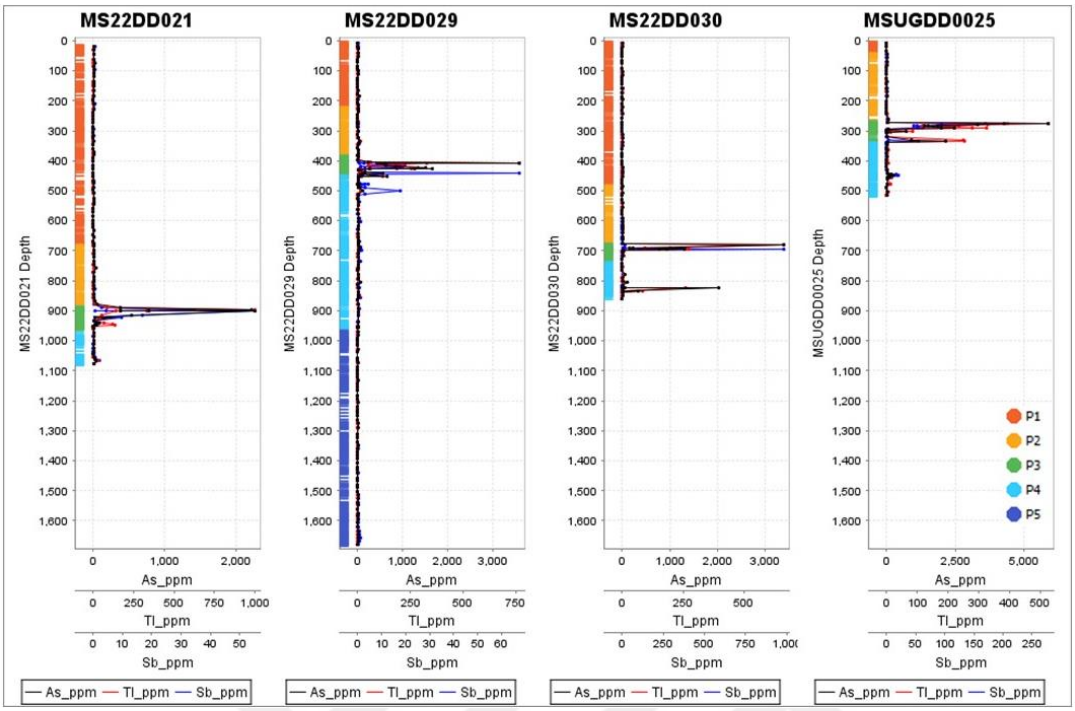


Figure 3.53. Downhole plots showing the variation of As, Tl, and Sb (in ppm) for each package in the studied drill holes MS22DD021, MS22DD029, MS22DD030, and MSUGDD0025.

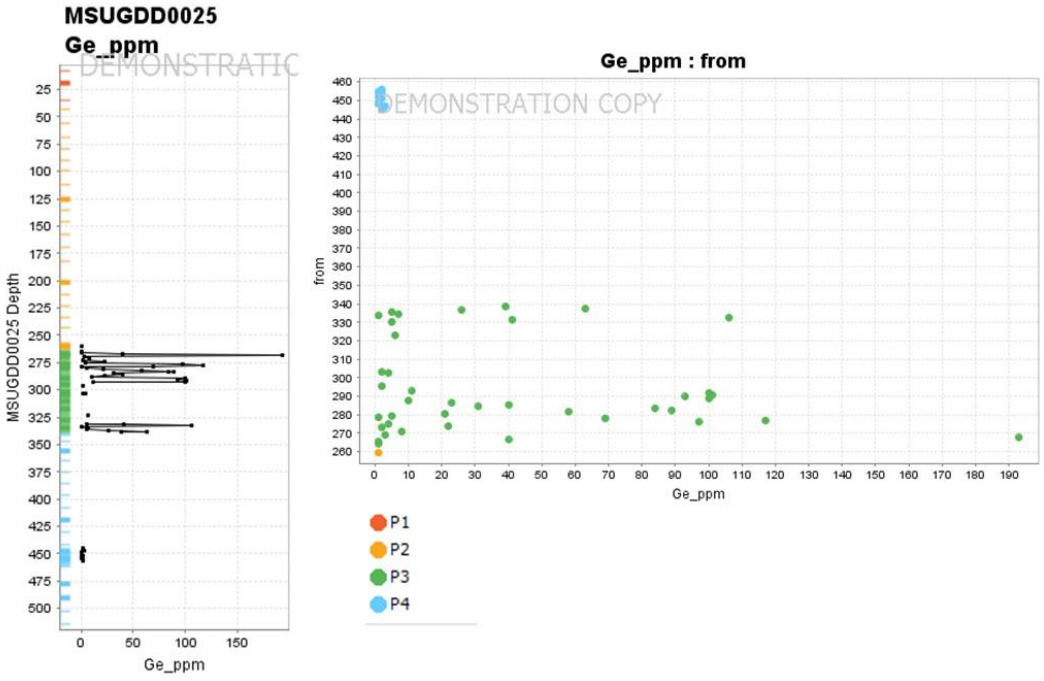


Figure 3.54. Downhole and bivariate plots showing the variation of Ge (in ppm) for package 3 in drill hole MSUGDD0025.

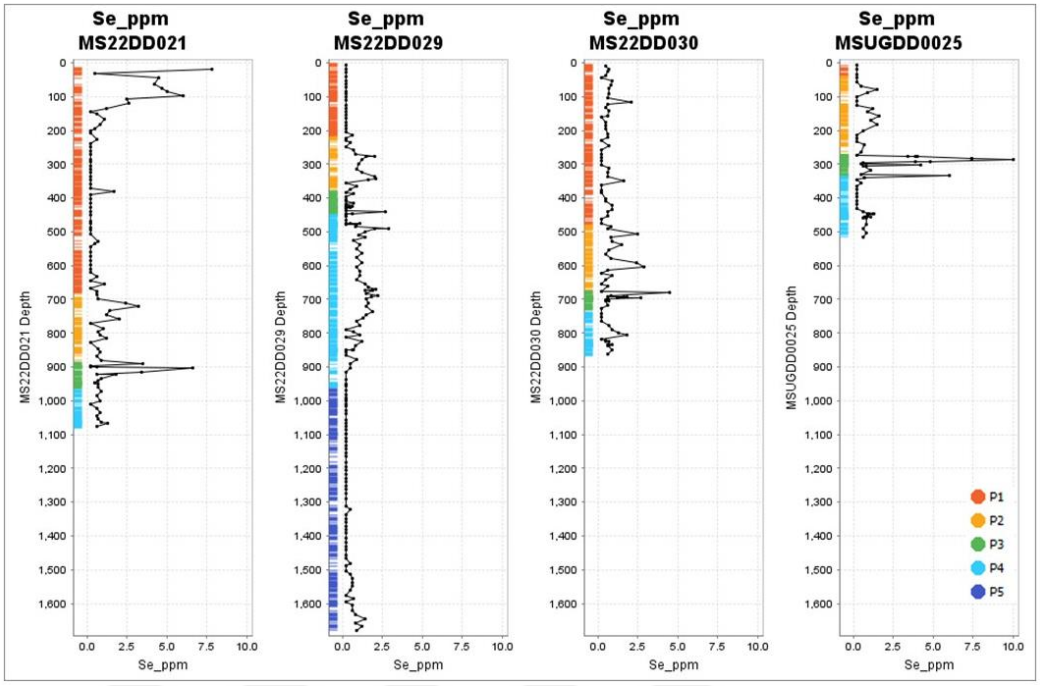


Figure 3.55. Downhole plots showing the variation of Se (in ppm) for each package in the studied drill holes MS22DD021, MS22DD029, MS22DD030, and MSUGDD0025.

Although base metal mineralization is observed mostly within the main mineralized zone (package 3), package 4 also has locally high Zn contents (>10 wt.%) drill holes MSUGDD0025 (depth: 449.90 m) and MS22DD030 (depth: 824 m; Figure 3.51). As expected, intervals of high Zn content also have relatively high Cd with a maximum concentration of 153.40 ppm in MSUGDD025 (depth: 445.90 m; Figure 3.51). Mean concentrations of highly-charged cations are also generally higher in package 4 compared to package 3; i.e., they are about 2 times more enriched compared to package 3 in Mo and about 3 times more enriched in V (Table 3.3). The strong positive Mo (48.30 ppm) and V (195.00 ppm) anomalies are detected in MS22DD029 at 736 m (Figure 3.50) in package 4.

Package 5 has markedly higher concentrations of a number of transition metals mainly including Cu and Co (Figure 3.56). Highest measured Co value is 13.2 ppm (depth: 1440 m), whereas for Cu the highest measured value is 23.9 ppm (depth: 1131.50 m; Figure 3.56). Elements such as Zn, Cd, Ag, Hg, and Pb are not

particularly enriched in this package, except minor relative enrichments in Ag (0.3 ppm) and Hg (0.2 ppm) in the lower part of the package intersected in MS22DD029 (depth: 1656.50 m; Figure 3.56).

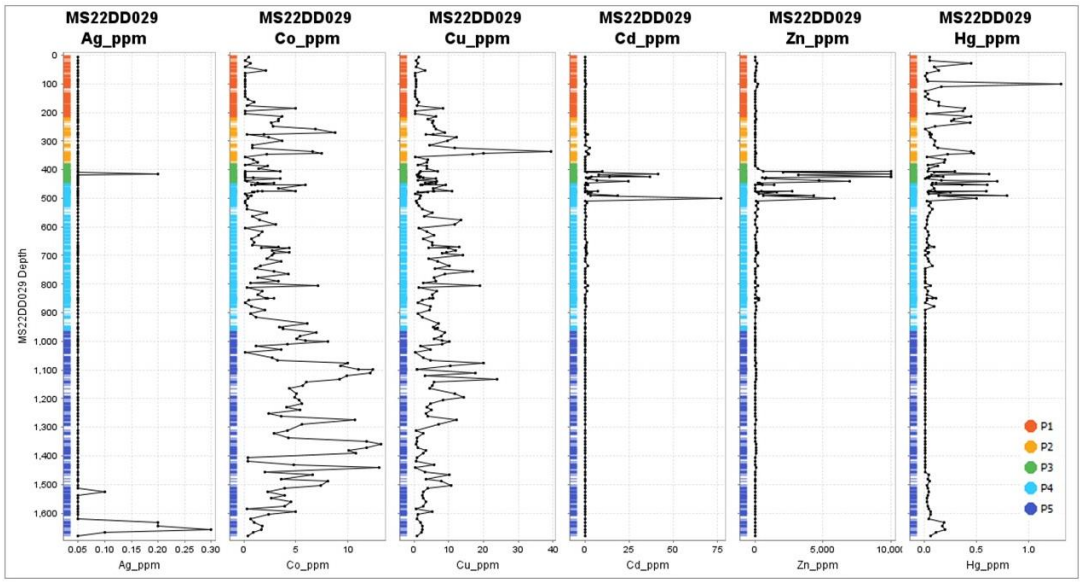


Figure 3.56. Downhole plots showing variation of Ag, Co, Cu, Cd, Zn, and Hg (in ppm) in identified packages in drill hole MS22DD029.

CHAPTER 4

DISCUSSION

4.1 Discussion

The carbonate-hosted Pb-Zn deposits, which may be Pb- or Zn-rich (Sangster, 1983), are divided into three subgroups as MVT (Leach and Sangster, 1993), Irish-type (Hitzman and Large, 1986; Wilkinson, 2003), and SEDEX deposits (Carne and Cathro, 1982). There are many studies focus on the overall mineralogical, genetic, stratigraphic, structural, and mineralization features of sediment hosted Zn-Pb deposits (Sangster, 1983; Goodfellow et al., 1993; Hitzman et al., 1992 and 2002; Leach et al., 2001 and 2005 b; Lydon, 2004; Kesler and Reich, 2006; Ashton et al., 2010). Despite the existence of a large number of such studies, lithogeochemical features of sediment-hosted Pb-Zn deposits are relatively less studied (Hitzman et al., 2002; Leach et al., 2005; Wilkinson, 2014). Therefore, the present study on lithogeochemical characterization of the sedimentary sequence at Meskan provides some significant findings on element mobility, metal associations, and host rock geochemical features.

In this study, 439 samples from 4 different drill holes have been chosen for comprehensive total whole-rock characterization by ICP-ES/MS including determination of total carbon and sulfur contents. Based on their distinct geochemical signatures, the sedimentary sequence at Meskan is divided into 5 chemostratigraphic packages; package 1 being the youngest and package 5 is the oldest, and 6 lithostratigraphic units as dolostone, limestone, and their high or low silt counterparts. Typically, lithostratigraphic units in each package are defined according to their silt amount, and each package boundary is determined by abrupt changes in major elements (as well as C and S) concentrations. Identified chemostratigraphic packages based on lithogeochemistry correlates well with

stratigraphic sub-divisions proposed in the literature by Perinçek (1992), which were also the basis of drill core logging at the Meskan project. This indicates that observed changes in Meskan stratigraphy are well-reflected in the major, minor, and trace element characteristics properties, which are in turn controlled by parameters such as sediment source/input and paleoenvironmental conditions including changes in redox conditions.

Prior to determining the extent and degree of lithogeochemical changes that occurred at Meskan due to hydrothermal activity, a comprehenive characterization of the host lithologies of package 3 was completed through petrographic investigations complimented by whole-rock XRD analyses. Accordingly, the host rocks are found to be mainly comprised by carbonate micrite mudstones and claystones accompanied by a smaller portion of interlaminated grainstone-mudstone lithologies. Main mineral constituents of these rock units are calcite and lesser dolomite, which have been overprinted and partly replaced by hydrothermal phases such as sulfides, barite, and carbonates (mainly calcite).

Major and minor elements: Package 3 is commonly composed of limestone, limestone±high silt and rarely of dolostones, with distinct major oxide compositions. These rocks have significantly low MgO contents even without normalizing to sulfide-free concentrations (avg MgO= 1.55 wt.%, n= 65) relative to other chemostratigraphic packages (avg= 9.93 wt.%, n= 439; Table 3.2).

When the studied part of the stratigraphy within and around Pb-Zn mineralization is considered, it can be seen that dolomitization is not an integral part of the Meskan succession. This is in contrast with most MVT and Irish-type Pb-Zn systems, which commonly are characterized by extensive dolomitization through replacement of a large proportion of limestone layers occurring at regional- to district-scales (Sverjensky, 1986; Leach et al., 2005; Hitzman et al., 1998; Wilkinson, 2003). Petrographic and XRD analyses of host rock samples also confirm that dolomite is only a minor constituent of the altered and mineralized rocks locally occurring as a hydrothermal replacement phase within zebra-textured rocks.

In striking contrast to MgO, average CaO contents of the ore-hosting units within package 3 are significantly high, especially even when the sulfide-free compositions are considered (avg. CaO_SF: 43.34 wt.%; Table 3.2). This is in keeping with the observation that calcite is both the main primary constituent of the host rocks and is also commonly found as a hydrothermal component as breccia, vein or open space fill, at higher proportions compared to dolomite.

Samples in package 3 have relatively high Fe_2O_3 (avg: 20.68 wt.%) and high MnO (avg: 0.32 wt.%) contents (Table 3.2). One of the major characteristics of the carbonate rocks in package 3 is their high MnO contents. This is particularly evident stratigraphically through the ore zone in all selected drill holes, where MnO contents exceed 0.5 wt.% (Figure 3.28). The great variations in the Fe_2O_3 and MnO values in this package reflect variations in hydrothermal input. MnO-rich samples in also have increased Zn and Ba concentrations. In contrary, most transition metals and metalloids do not correlate with main ore metals such as Zn and Pb (Table 3.6). Elevated levels of Mn in and around the ore horizon could be due to presence of manganoan carbonates such as kutnohorite ($Ca,Mn(CO_3)_2$). A pilot study completed by FQM and investigating the UV fluorescence characteristics of hydrothermal carbonates also indicated relatively higher Mn concentrations in these minerals. In addition, some Mn may also reside in sphalerite, where Mn^{+2} can substitute for Fe^{+2} or Zn^{+2} (Muntyan, 1999). The evaluation of Fe_2O_3 and MnO indicate that samples of pure limestone or dolostone with very low silt have Fe and Mn enrichments relative to other chemostratigraphic packages. High MnO contents (up to 0.61 wt.%) are also detected in drill hole MSUGDD0025 in package 4 distal from sulfide mineralization, but overall MnO contents of all chemostratigraphic packages except for Package 3 are low (Figure 3.28).

According to major and minor element mobility and sulfide-free compositions of major and minor elements given in Figure 3.25, the mineralized samples that are located outside the general trend are found in the purest or most clean limestones, which are the shallow siliciclastic-deficient lithological components. The samples in package 3 have the lowest average SiO_2 (4.36 wt.%), Al_2O_3 (0.45 wt.%), TiO_2 (0.03

wt.%), and K_2O (0.16 wt.%) contents among all identified chemostratigraphic packages (Table 3.2).

Total organic carbon contents (TOT/C; avg= 8.08 wt.%) are relatively low in package 3 with respect to packages 2 and 4, whereas the highest amount of total sulfur (TOT/S; avg= 13.82 wt.%) are observed in package 3 (Table 3.2). The observation that the ore host rocks are relatively lower in abundance in organic material compared to the enclosing strata may give clues about possible ore forming processes at Meskan. Interaction between oxidized, metal-rich brines and a reductant such as hydrocarbon-bearing lithologies is regarded as one of the possible ore precipitation mechanisms, particularly in MVT systems (Leach et al., 2005). However, the relatively low TOT/C contents of package 3 samples suggest that reduction of oxidized fluids may not be a plausible model for Zn-Pb mineralization at Meskan.

HFSE: Higher abundances of HFSEs in package 1 are detected between 0–119.20 m and at the 536.50 m depth in drill hole MS22DD021 (Figure 3.35), with minor local positive peaks at 53.20 m and 184.80 m in drill hole MS22DD029 (Figure 3.36), and at 52.80 m, 75.00 m and 159.50 m depths in drill hole MS22DD030 (Figure 3.37). Especially, the beginning of drill hole MS22DD021 between 0 and 119.20 m is significantly enriched in HFSE. This interval consists of weathered and oxidized carbonate rocks, which suggests that HFSE enrichment is likely associated with presence of detrital heavy mineral grains (such as rutile/anatase) or with clastic input in these levels. The increase in clastic input is also demonstrated with positive trends of Al_2O_3, TiO_2, and K_2O at the same intervals in MS22DD021 and MS22DD030 (Figures 3.30 and 3.31). These elements are incompatible, resistant to alteration and are not easily affected by weathering. HFSEs can be found in accessory minerals such as zircon, ilmenite, apatite, and rutile (Belousova et al. 2002a; Morton and Yaxley 2007). Therefore, HFSE enrichments in package 1, which has been affected from weathering and oxidation, are closely related with the increase in resistate minerals possibly alongside with an increase in silt proportions in the upper level of package 1 in drill holes MS22DD021 and MS22DD029 (Figures 3.35 and 3.36).

In package 2, a strong positive trend of HFSE is observed at the depth of 757.40 m in drill hole MS22DD021 (Figure 3.35), at 270 m in drill hole 29 (Figure 3.36), at 516.50 m in drill hole MS22DD030 (Figure 3.37), and at 169.50 m in drill hole MSUGDD0025 (Figure 3.38). The lithology of these four samples are dolostone+ silt except MSUGDD0025 sample that is limestone±silt. All of them have silt input, so rich in terms of HFSE. In the package 3, all the HFSE are relatively deficient except only one limestone±silt sample from drill hole MS22DD030 (depth= 703.25 m) shows strong positive Hf (2.1 ppm), Ta (3.6 ppm), and W (2.5 ppm) values with respect to other samples in package 3 (Figure 3.37). Lack amount of HFSE may imply that these carbonates are mostly pure and depleted in silt amount. The highest Zr (292.10 ppm) and Hf (7.5 ppm) are detected dolostone+ silt sample in package 5, that is observed only drill hole MS22DD029 (Figure 3.36).

LILE: In terms of LILE compositions, Barium values locally exceed the upper detection limit (>5 wt. %) in dolostone samples at 527 m in the drill MS22DD021 and 159 m in the drill hole MS22DD030 in the package 1 (Figure 3.40). The highest Ba concentration of 8404 ppm is detected at 111.70 m in drill hole MSUGDD0025 in package 2. Ba is relatively enriched in package 3 (avg= 8024.77 ppm) with respect to all packages (1967.22 ppm). This Ba enrichment in package 3 is mostly detected in limestone, and rarely in limestone±silt units. In package 4, the highest Ba (17058 ppm) is observed in limestone±silt at 347.00 m in the drill hole MSUGDD0025 (Figure 3.41). Ba and Sr positively correlate with each other in all of the studied drill holes. Although the average of Sr (945.12 ppm) values for all packages are relatively close to Sr values of package 3 (avg= 928.44 ppm), higher Sr values are abundant in package 4 and package 5 (Figure 3.40).

For Rb and Cs, the highest values are observed in the dolostone±high silt unit in the package 5 as 200.80 ppm and 16.8 ppm respectively in package 5 (Figure 3.41). Rb is enriched in carbonate samples that rich in terms of silt amount (Figure 3.41). Rb values are correlated with the packages except package 3. Cs is found to be enriched in pyrite, sphalerite, galena samples (Figure 3.20a) with respect to barren (but pyritic) zebra carbonates (Figure 3.20c) in main sulfide mineralization zone (P3).

There are strongly positive Cs anomalies in package 3, whereas Rb is relatively depleted with respect to other packages (Figure 3.41). Although, Rb and Cs values are correlated with stratigraphy, the correlation with lithology is not certainly defined. Relatively less amount of Cs samples that belongs to unmineralized zebra texture limestone are usually enriched in MnO (mostly > 0.20 wt. %, with the highest at 0.63 wt. %) and CaO (generally > 40 wt. %). Positive Cs values might indicate that it is hydrothermal, correlated with Pb, Zn, As, Cd, Sb, Tl and Se (Table 3.5).

REE: The average ∑REE contents in the package 3 (mineralized ore zone) are significantly low compared to all packages (Table 3.2). The general REE patterns indicate that HREEs are depleted relative to the LREEs; Eu anomaly (avg= Eu/Eu*: 0.27); and Ce anomaly (avg= Ce/ Ce*: 1.78). Eu/ Eu* values in package 3 are relatively higher than package 2 and package 4.

Ce: Many studies shows that cerium can be used as an indicator for determination of paleoredox conditions in marine carbonates (Liu et al., 1988). According to De Baar et al. (1991), the absence of Ce anomalies with respect to its neigbour REEs can be interpreted by oxidation of Ce^{+3} into less soluble than Ce^{+4}. Positive Ce anomalies can be associated with an increase in detrital material (Nath et al., 1997), diagenesis, and paleo-redox conditions (Liu et al., 1988). The ratio of Ce/Ce* varies from 0.1 to 0.4 for oceanic seawater (Wang et al., 1986), and approaches to 1 with an increase in the proportion of clastic material (Murray et al., 1991). At the same time, carbonates precipitated in equilibrium with seawater retain the negative Ce anomalies, as commonly observed in marine limestones (Palmer, 1985). In this study, most samples yielded Ce/Ce* ratios often < 1. The highest mean value of Ce is detected package 5 (0.98 ppm) and package 2 (0.93 ppm), respectively. This may imply that package 5 and package 2 are relatively enriched in silt with respect to other packages. On the other hand, there is a sharp decrease in Ce abundances in the transition between package 2 and package 3 in MS22DD021 (0.1 ppm), and MS22DD029 (0.28 ppm). This was interpreted to be a consequence of a decrease in silt proportion in package 3. A plot of $(Ce/Ce^*)_N$ against $(Pr/Pr^*)_N$ is suggested to be useful to understand the enrichment of La because artificial negative Ce anomalies

might occur because of possible positive La anomalies (Bau and Dulski, 1996; Kamber and Webb, 2001). Figure 4.1, therefore, indicates that samples are not clustered at the modern seawater region. Instead, most of these samples are clustered as outliers on stronger negative Ce anomalies and positive La anomalies.

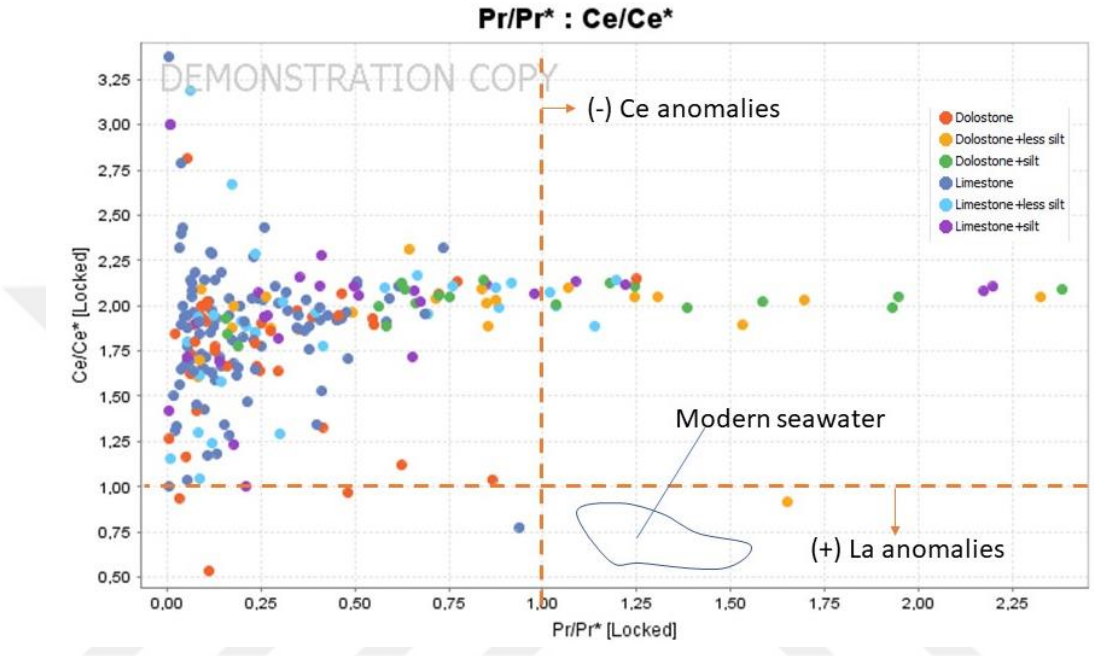


Figure 4.1. $(Ce/Ce^*)_N$ versus $(Pr/Pr^*)_N$ graph on all lithological samples (Bau and Dulski (1996).

Eu: The reduction from Eu^{+3} to Eu^{+2} is commonly thought to be a marker for a high temperature hydrothermal environment in sedimentary rocks (Bau and Dulski, 1996; Bau and Alexander, 2006). In carbonates, negative Eu anomalies are associated with diagenetic processes, ruling out the possible role of hydrothermal fluids (Wang et al., 2017). Positive Eu anomalies develop at temperatures >200–250 °C, and contrasting anomalies of Ce and Eu (positive Eu, negative Ce) cannot develop under the same physico-chemical conditions (Bau and Möller, 1992). This contrast between anomalies of Eu and Ce may give clues on variations in redox conditions as hydrothermal fluids migrate.

In this study, the Eu/Eu* values vary from 0.57 to 0.66 in all packages except for package 3. The highest Eu/Eu* value (0.84) is detected in package 3. Except

MS22DD029, package 3 samples have relatively high Eu/Eu* values compared to other chemostratigraphic packages. Such higher values are interpreted to be a contribution of hydrothermal carbonates probably precipitated from fluids that are relatively oxidized in comparison to the existing carbonate rocks. Although package 3 samples are not themselves particularly reduced, as indicated these do not have significantly higher proportions of organic carbon but their redox states may still be possibly relatively low in comparison to the ore fluids. Thus higher Eu/Eu* values are directly attributed to precipitation of sparry calcite, which was commonly observed as a fracture-fill phase in the mineralized horizon. The mean value of all lithological units among each package except for zebra textured carbonates in package 3 show negative Eu anomalies on chondrite-normalized REE plots. However, Eu/Eu* are relatively higher in the upper levels of package 1 in MS22DD029 (1.88; 92.00 m) and in MS22DD030 (3.19; 159.50 m; Figure 3.45). These higher values probably reflect the role of oxidized, shallow, surficial waters convecting within the weathered and oxidized horizon.

Barren zebra-textured limestone in package 3 is characterized by high Eu/Eu* ratios with respect to other packages (avg. between 0.19 and 0.21). At the same samples are depleted in Cs with respect to other sulfide-rich samples in package 3 (Figure 3.42).

According to chondrite-normalized REE plot of all samples for each package, LREE is enriched in silt dominated carbonates with respect to pure dolostone and limestones. LREEs is relatively enriched in all packages with respect to HREE. The enrichment of LREE with respect to HREE is typical feature of terrigenous inputs of different diagenetic history and depositional environment (Wang et al., 2017). Moreover, according to the correlation matrix, Rb contents of all Meskan samples strongly correlate with Al_2O_3 (0.99), K_2O (0.99), and TiO_2 (0.97) in package 3 (Table 3.5). A strong correlation between Rb and K are already expected as Rb commonly substitutes for K in minerals, and in this case, possibly in K-bearing detrital clay minerals of terrigenous origin.

At Navan deposit in the Irish Midlands, the zoning of Zn, Pb, Mn, and As create an intensive halo over the mineralization (Peace et al., 2003). In the Meskan deposit, around the semi-massive and/ or massive sulfides, positive trends across transition metals such as Fe_2O_3_SF (avg= 20.68 wt.%), Mn (avg= 0.18 wt.%), Zn (avg= 0.45 wt.%), Cd (avg= 68.41 ppm) are observed in package 3. Cd correlates with Zn, and may imply the higher amount of sphalerite with respect to other sulfide minerals. Cd values may enrich in sphalerite than rather than galena in Meskan deposits.

The most prevalent ore minerals of Irish-type deposits are pyrite, sphalerite and galena, with minor proportions of chalcopyrite, tennantite, and sulfosalts; and barite as a gangue (Hitzman and Beaty, 1996). At Meskan, the main sulfide assemblage is characterized by pyrite, sphalerite, galena, and marcasite with local boulangerite. Package 3 samples typically show enrichments in a number of metals/metalloids such as Pb (avg = 0.26 wt.%), As (avg = 827.31 ppm), Sb (avg = 38.32 ppm), and Tl (avg = 134.09 ppm), Ge (avg = 16.67 ppm, n= 102) with respect to other packages (Figures 3.51–3.53). The most frequent source of Pb comes from the galena, which can be found in a variety of ore bodies of base metals that commonly form MVT and SEDEX (Large and McGoldrick, 1998). In the meantime, Pb isotopic compositions of galena from Pb-Zn systems in the Irish Midlands are multiply-sourced (Wilkinson, 2014). In the Lisheen deposit, the distribution of As strongly correlates with Fe and Cu, Ni, Ag, and Co (Torremans et al., 2018). It is thought that As is associated with Fe-sulfide rich domains within arsenian pyrite and arsenopyrite (Hitzman et al., 2002; Wilkinson et al., 2005b, Torremans et al., 2018).

Tl presents one of the most noticeable trace element halos in the Australian SEDEX deposits, with Tl contents ranging from 100 to 1000 ppm in the ore zones (Pirajno, 2010).

Germanium is an element with very low (~1.5 ppm) average continental crust abundances (Smith and Huyck, 1999), but it commonly occurs in Zn-rich deposits. Ge is a relatively important element for Pb-Zn deposit classification, and it is often abundant in the majority of MVT deposits. It typically resides in sphalerite in low-

temperature Pb-Zn deposits that are not related to magmatism (Cook et al., 2009). Ge may be a by-product of extraction and refining of Zn ores from Pb-Zn deposits (Gunn, 2014; Licht et al., 2015; Mondillo et al., 2018), and it may be enriched in sphalerite as Ge^{+4} (Bernstein, 1985). It is most likely that the increase in Ge concentrations in mineralize samples from Package 3 is directly associated with sphalerite precipitation. In the Meskan deposit, significant Ge enrichment is particularly detected in domains of colloform-banded sphalerite-pyrite ores in the massive sulfide mineralization zone in Package 3.

According to Scott and Lyons (2012), the existence of Mo is a robust paleo-redox proxy in shale and mudstone, In these rocks, Mo abundances of less than 25 ppm is taken as an indication of sulfidic porewater and non-sulfidic bottom waters. These authors suggested that Mo>100 ppm in euxinic bottom waters, whereas abundances between 25 and 100 ppm is related to seasonal sulfidic bottom waters. Large et al. (2011) also noted that under reducing conditions Mo exists as the relatively insoluble Mo^{+4} and becomes incorporated in sedimentary rocks in a reducing environment. In the present study, Mo abundances are significantly low and range from 0.4 to 7.9 ppm within the main mineralized zone (avg= 2.29 ppm). The highest value of Mo (150.00 ppm) is detected at 96.50 m depth in MS22DD021 in package 1 (Figure 3.50) and package 2 and locally package 4 have higher Mo contents compared to package 3 samples. This is taken as an additional indication of relatively oxidizing conditions that prevailed during deposition of ore host rocks of the Meskan Tepe Formation.

According to Jones and Manning (1994) and Ross and Bustin (2009), Co and Cr are unaffected by redox conditions, while Ni and V are easily sequestered into sediments under reducing environment. The maximum Ni (128 ppm) value is observed at package 2 (depth= 276.50 m, MS22DD029), whereas the maximum V (413 ppm) value is detected at package 1 (depth= 19.20 m, MS22DD021) (Figure 4.2). Ni values are relatively correlated with V. Ni (avg=10.32 ppm) and V (avg= 21.35 ppm) are depleted in package 3 with respect to other drill holes (Figure 4.2). Package 3 does not indicate strongly crucial gains or losses in terms of Sc (max 3 ppm), Sn

(max 8 ppm), W (max 5.6 ppm), Mo (max 7.9 ppm), and V (max 64 ppm) (Figure 4.2).

Besides the other elements, Bi is in- sensitive in all drill holes in package 3. Ag, Au, Co, Ga, Ni, Se, Ta, Th, Y are relatively depleted in package 3 with respect to other packages. Although, Cu is common at Silvermine deposit (Torremans et al., 2018), it is not common in the mineralized zone (P3) at Meskan deposit.

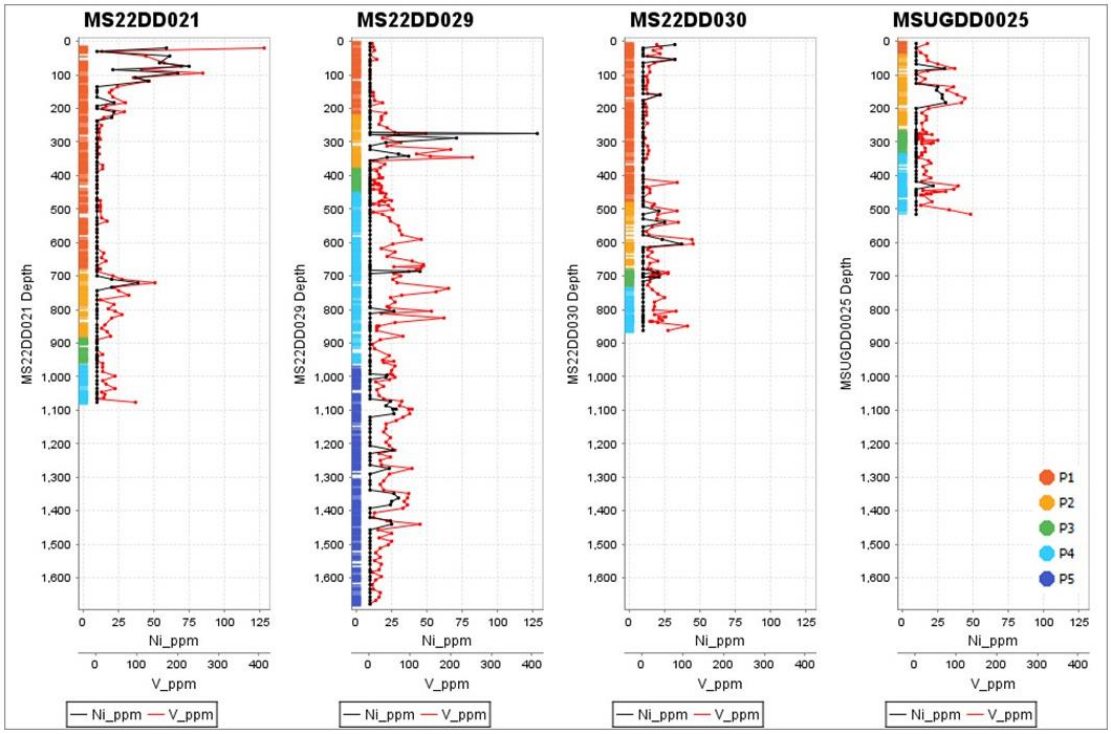


Figure 4.2. Downhole plots showing variation in Ni and V concentrations (in ppm) in drill holes MS22DD021, MS22DD029, MS22DD030, and MSUGDD0025.

Based on geochemical analyses of sulfide ore, Hanilçi et al. (2020) stated that Meskan mineralization is characterized by increased levels of As, Ba, Tl, Cd, Sb, Mo, and Hg, and that this trace element signature points out to a SEDEX-like system. They supported this assertion also by relatively high (>200ºC) homogenization temperatures obtained from liquid-rich, two-phase fluid inclusions, which would rule out the presence of an MVT system. Lithogeochemical data presented here also partly confirmed similar enrichments in package 3 samples with the addition of Mn and Ge, but significant enrichments in Hg and Mo were not detected. In fact, Mo was

found to be relatively depleted in comparison to some other chemostratigraphic packages identified. This is most evident in package 1, where together with some other transition metals such as Ni and V, Mo was found to be particularly higher in concentration. This was interpreted to be associated with the relatively high TOT/C levels in this unit and thus its reduced character, due to which these metals become stabilized in their reduced and relatively insoluble states.

4.2 Comparison between lithogeochemical and pXRF data

At Meskan, portable energy-dispersive X-ray fluorescence (pXRF) is used to produce a large geochemical dataset of drill cores from both surface and underground drilling operations. pXRF data helps to evaluate stratigraphic correlations, interpret, lithogeochemistry, and also to interpret preliminary mineralogy of the measured rock samples. Measurements were routinely taken at every 2 meters from entire drill holes and from rocks of different compositions, stratigraphic positions, and textures. The pXRF readings are taken for 40 different elements (Table 4.1). The quality control protocols of XRF readings were performed by using standards in every 30 samples, and the device is calibrated at every 50 samples. Here, obtained pXRF data is compared to the results of lithogeochemical analysis using analytical packages MA370 and LF202. This comparison is expected to provide an understanding of the utilization of pXRF data in the absence of detailed assay results.

Table 4.1 Measured elements in portable XRF (pXRF)

Analysis Method	Detected Elements	Units
Portable X-ray fluorescence (pXRF)	P, S, K, Ca, Ti, V, Cr, Mn, Fe, Co, Ni, Cu, Zn, As, Se, Rb, Sr, Zr, Mo, Ag, Cd, Sn, Sb, Ba, W, Hg, Pb, Bi, Th, U, Al, Ce, La, Mg, Nb, Si, Y, Pr, Nd, LE	ppm

Routine collection of pXRF readings from drill core is significant to understand stratigraphic sequence and geochemistry easily. Compared to analytical methods, it gives so fast results and economically low cost. After collection of data for each selected drill hole, all elements are compared on bivariate graphs and downhole plots.

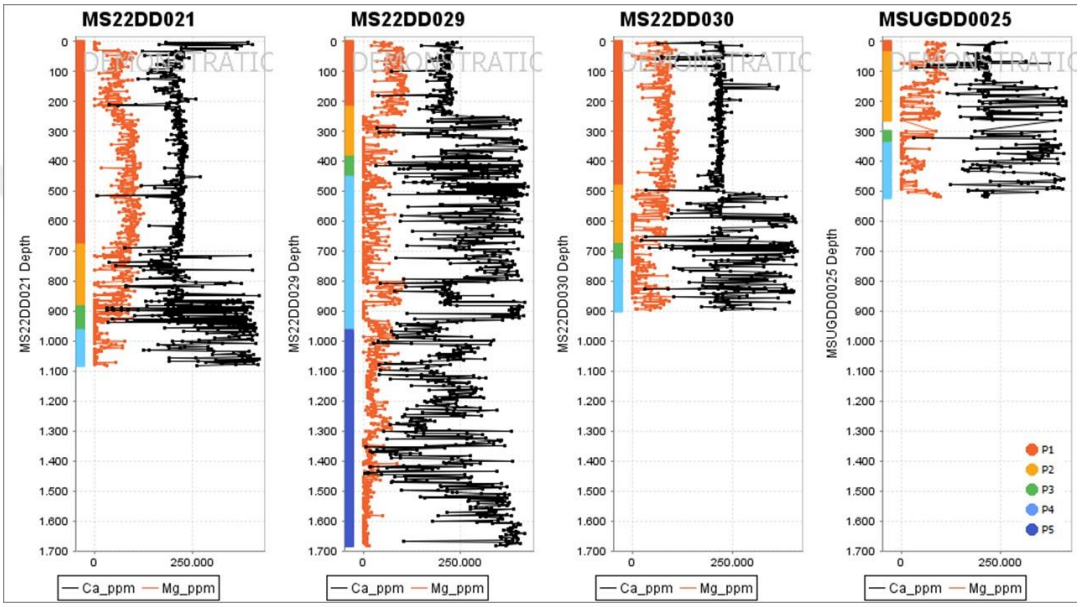


Figure 4.3. Downhole plots showing variation in pXRF Ca and Mg concentrations (in ppm) for each package through four drill holes.

The results of pXRF readings demonstrate that Ca and Mg show strong positive correlations with lithogeochemistry assay results (LF202). The value of Mg can be used to differentiate between packages 1 and 2, similar study with assay results in high MgO content (Figure 3.27 and 4.3). The mean value of Mg is calculated as 7.7 wt.%, in the package 1 through all 4 drill holes. At the same time, Ca and Mg amount and their ratios relative to each other helps to understand lithology as limestone and dolostone while logging of active drill holes before the assay results. Package 2 might differentiate from package 1 by its relatively high Si, Al, and K contents (Table 4.2). Package 3 can separate from the overlying package 2 rocks and the underlying package 4 rocks mainly by high Fe and Mn contents. Both components are

significantly higher in abundance. Package 4 is differentiated from above package by their high value of Si, Al, K, and Ti. The increasing of silt amount is detected from package 3 to package 4 (Table 4.2). Moreover, the transition between package 3 and package 4 is detected by their low Fe and Mn contents. Package 5 is separated package 4 by their very high value of Si value (Table 4.2).

Table 4.2. Statistical values of major elements measured by pXRF for each package

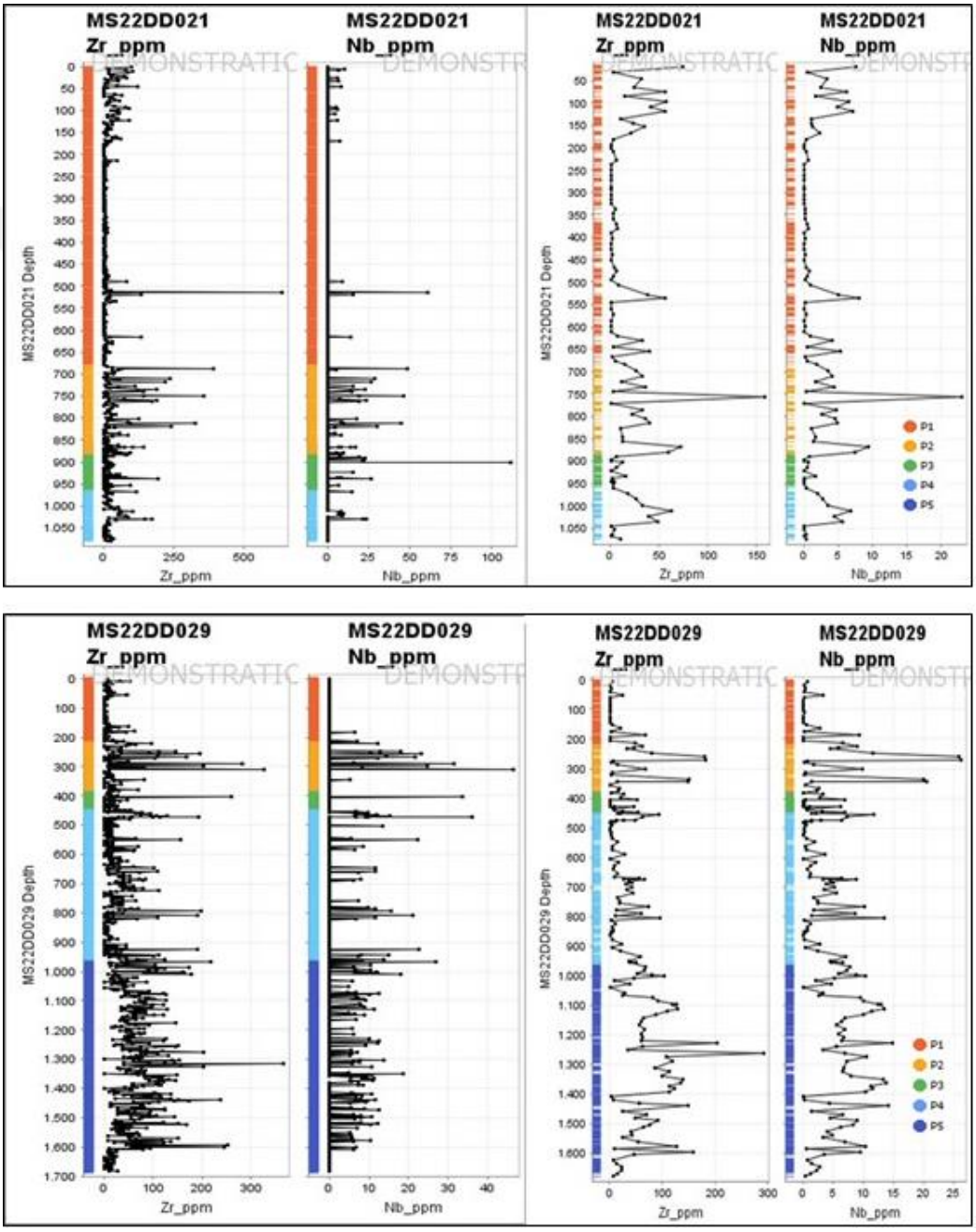
2527 rows - Univariate	Ca_ppm	Mg_ppm	Si_ppm	Al_ppm	K_ppm	Ti_ppm	Fe_ppm	Mn_ppm	S_ppm
[Visible] : Count Numeric	2527	2527	2527	2527	2527	2527	2527	2527	2527
[Visible] : Minimum	5546.34	0	0	0	0	0	101.59	0	0
[Visible] : Maximum	423360.21	125503.98	304901.04	114641.45	52014.29	11364.04	382699.01	81793.77	315531.95
[Visible] : Mean	251973.347922	39133.314879	32857.3496	9181.352311	3584.513364	712.807072	15337.261713	581.530625	16294.593621
[Visible] : Median	224262.8	28933.48	17018.33	3807.74	1045.39	478.62	3315.5	266.08	2867.02
[Visible] : Standard Deviati...	88277.553641	36999.443934	39865.251232	13367.197316	6001.826448	1035.289282	41440.985179	2039.929807	41051.535159
P1 : Count Numeric	710	710	710	710	710	710	710	710	710
P1 : Minimum	5737.5	0	0	0	0	0	112.91	0	0
P1 : Maximum	404649.46	125503.98	277288.03	114641.45	52014.29	11364.04	80066.69	901.24	104686.39
P1 : Mean	213175.956746	76975.310577	18884.774437	6480.195197	1436.819915	382.929775	3191.177535	191.752634	2537.862183
P1 : Median	218080.01	82993.025	9466.76	3143.135	315.16	0	1458.745	158.81	754.02
P1 : Standard Deviation	32516.702423	25486.426455	28248.609658	9486.157948	3280.963311	774.30177	5244.674923	123.255041	6978.140747
P2 : Count Numeric	442	442	442	442	442	442	442	442	442
P2 : Minimum	24520.25	0	0	0	0	0	179.45	64.48	0
P2 : Maximum	421559.79	116758.68	304901.04	94599.01	45072.36	8378.8	250545.12	81793.77	245546.3
P2 : Mean	248115.026267	45858.331199	34624.838891	10031.045113	4510.59267	761.000452	8855.301697	985.972443	8536.112511
P2 : Median	220203.54	52964.465	23350.42	5195.31	1705.24	496.97	3183.555	298.5	2500.2
P2 : Standard Deviation	87294.79655	35569.492404	37859.528053	13326.643162	6382.818472	1132.816871	18205.389006	4633.840045	20660.158295
P3 : Count Numeric	392	392	392	392	392	392	392	392	392
P3 : Minimum	18152.99	0	0	0	0	0	387.39	65.38	99.11
P3 : Maximum	412521.36	104206.34	254683.2	62397.57	35058.45	7206.24	382699.01	5720.87	305517.59
P3 : Mean	272961.915689	9653.614592	21804.280969	3797.4975	1981.011556	420.639719	53686.992806	1288.11602	55202.465281
P3 : Median	295887.555	0	10118.53	1475.85	700.28	0	8221.275	906.675	12662.825
P3 : Standard Deviation	105719.851617	21142.599213	32528.254341	7408.560003	3803.840167	783.110415	87185.304988	1082.240947	77544.056594
P4 : Count Numeric	623	623	623	623	623	623	623	623	623
P4 : Minimum	31481.75	0	0	0	0	0	101.59	0	0
P4 : Maximum	423360.21	107644.31	259941.13	71132.58	36181.84	8510.74	349877.2	4271.38	315531.95
P4 : Mean	297849.818989	20164.821268	31334.419872	7372.886372	3081.405746	666.515329	9835.432937	475.090353	11357.960032
P4 : Median	317726	6944.5	19636.99	3012.82	964.94	522.19	3075.99	318.33	4878.39
P4 : Standard Deviation	87717.292034	26122.498443	33375.923359	10989.187948	5059.517484	954.008034	26437.195137	488.701739	23007.858797
P5 : Count Numeric	360	360	360	360	360	360	360	360	360
P5 : Minimum	5546.34	0	2576.89	0	0	0	413.01	0	0
P5 : Maximum	414062.34	89777.49	258775.32	84093.3	39286.19	8568.47	55124.46	1130.12	202924.06
P5 : Mean	230981.586444	21169.814528	72915.366889	22457.470917	9299.9135	1702.475861	15013.069583	268.502583	19128.385306
P5 : Median	232192.315	16509.83	65142.92	17576.93	6467.06	1553.815	12978.29	243.575	3852.5
P5 : Standard Deviation	101533.149037	18477.239074	51250.277912	19051.47283	8709.729233	1113.171519	11419.593731	135.85131	40238.994033

In terms of HFSE, only pXRF values of Zr and Nb are compared to assay results in all selected drill holes. The elements consist of Zr and Nb are highly correlated in all drill holes (Figure 4.4). Zr and Nb are relatively depleted in package 1 with respect to other identified packages except upper ~120 meters of drill hole MS22DD021. Rb is enriched in package 5 with respect to other packages (Figure 4.6). Weathered and oxidized samples that located in the upper part of drill hole MS22DD021 have higher values of Zr, Nb, and Rb.

In terms of LILE, pXRF values of Ba and Sr are compared to assay results in all identified drill holes (Figure 4.5). Most of the pXRF values of Ba and Sr are positively correlated with assay results. Although pXRF readings shows specific

point, whereas assay results show the interval; the general trend and strongly positive values are nearly the same.

Mo and V are correlated each other in all packages (Figure 4.7). The strong positive Mo and V concentrations are also higher in package 2 compared to other packages (Figure 4.7).



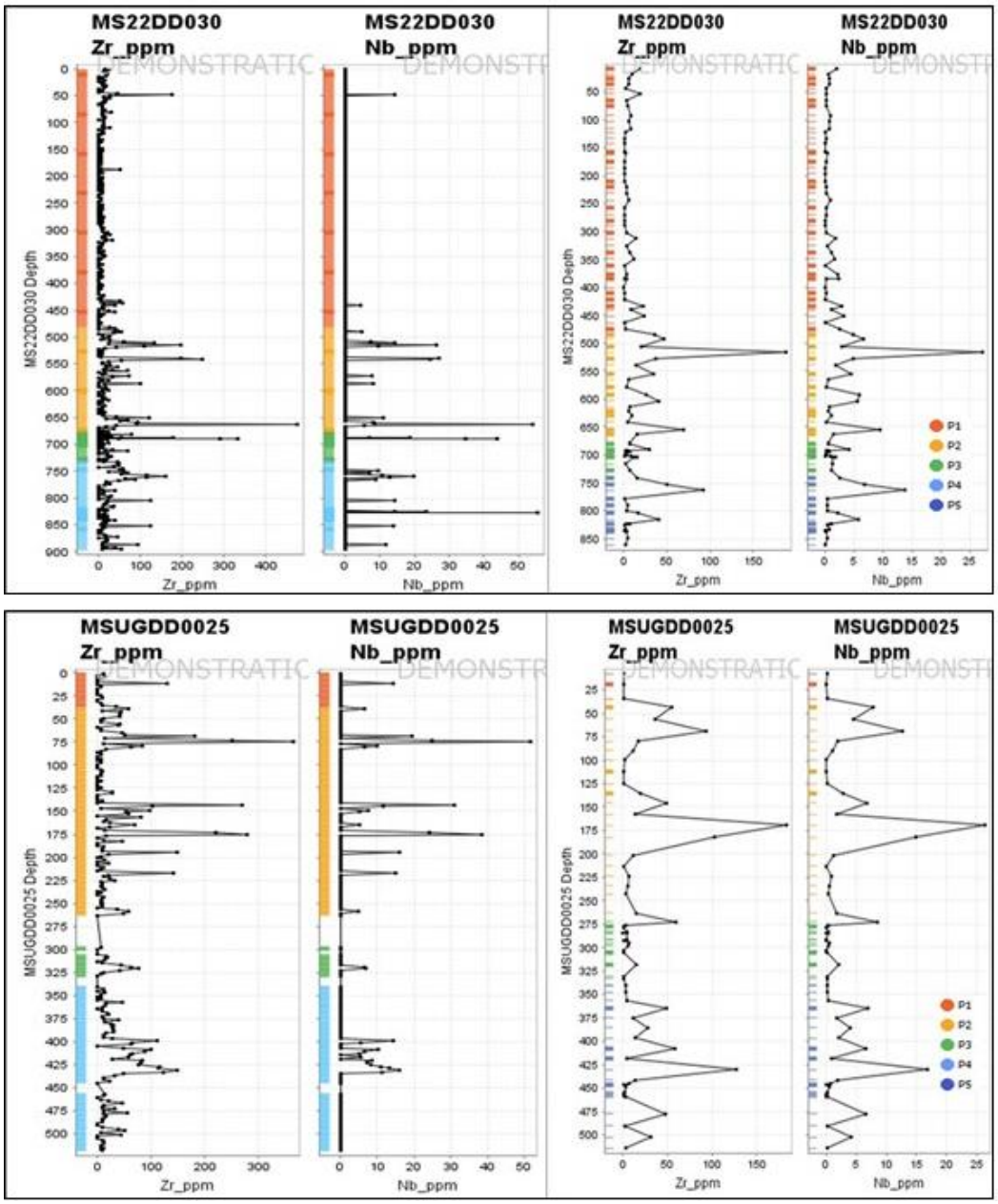


Figure 4.4. Downhole plots showing pXRF readings (left) and lithogeochemical analysis results (right) for Zr and Nb (in ppm) in all drill holes.

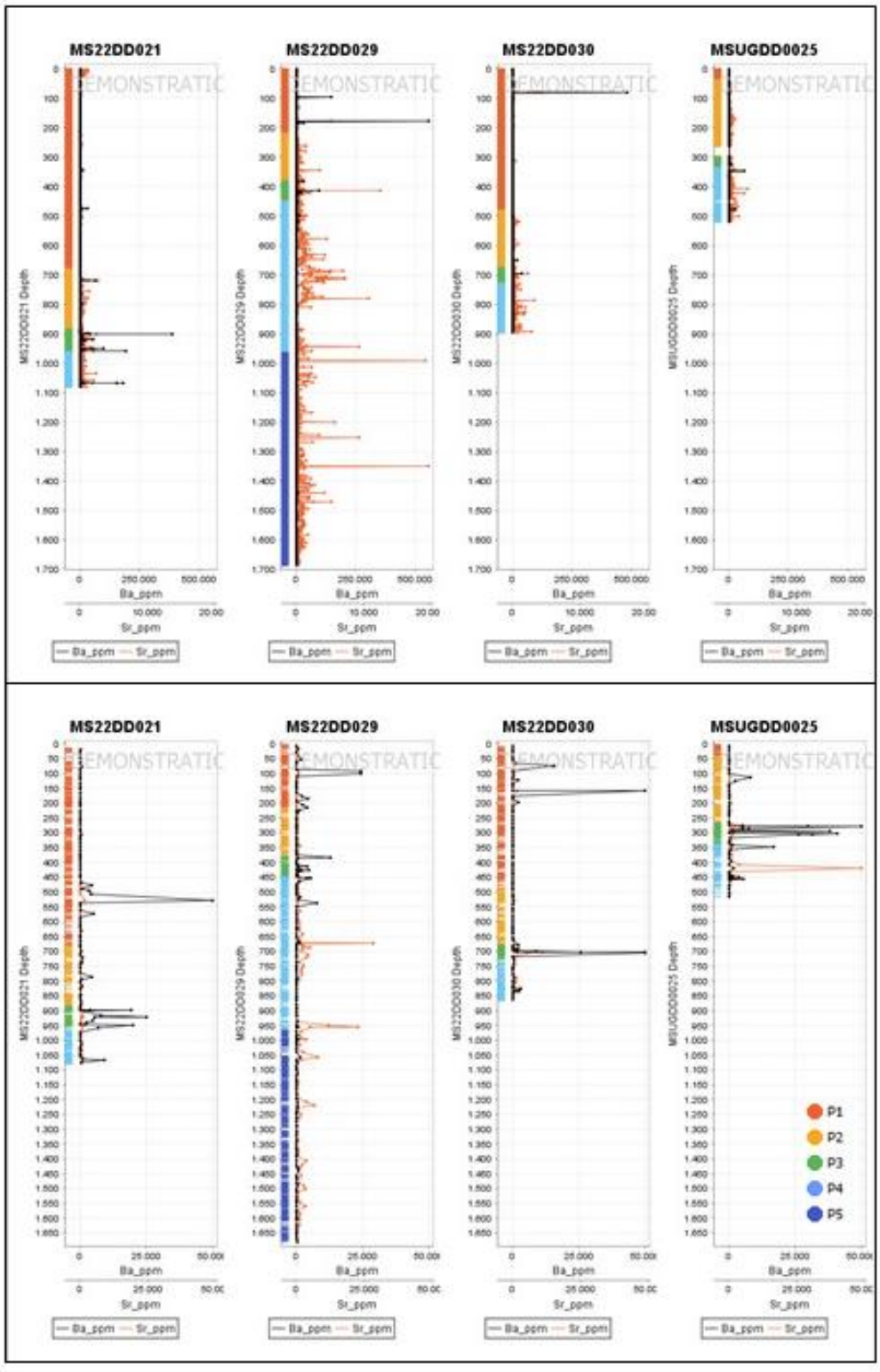


Figure 4.5. Downhole plots showing pXRF readings (above) and lithogeochemical analysis results (below) for Ba and Sr (in ppm) in all drill holes.

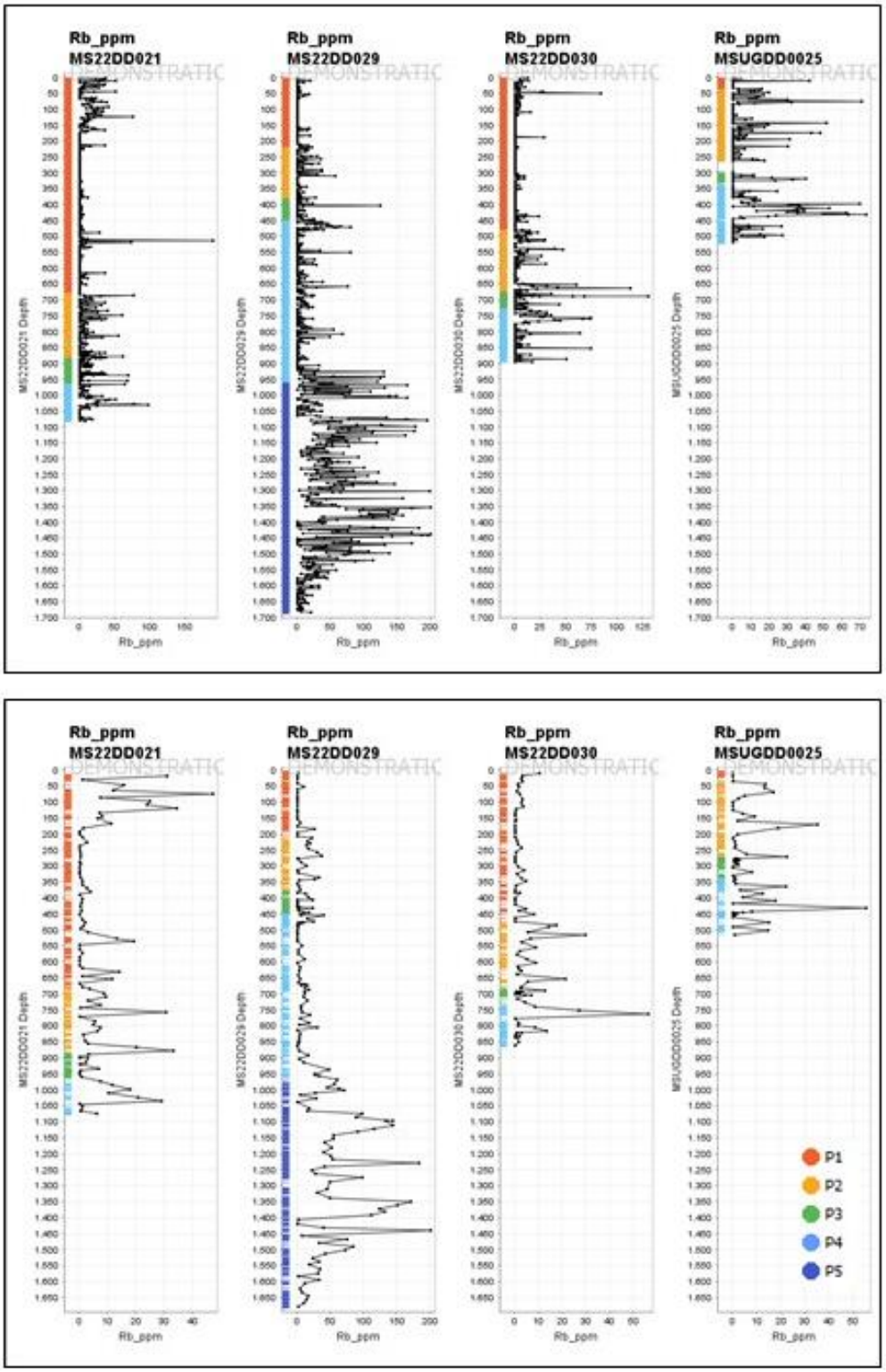


Figure 4.6. Downhole plots showing pXRF readings (above) and lithogeochemical analysis results (below) for Rb (in ppm) in all drill holes

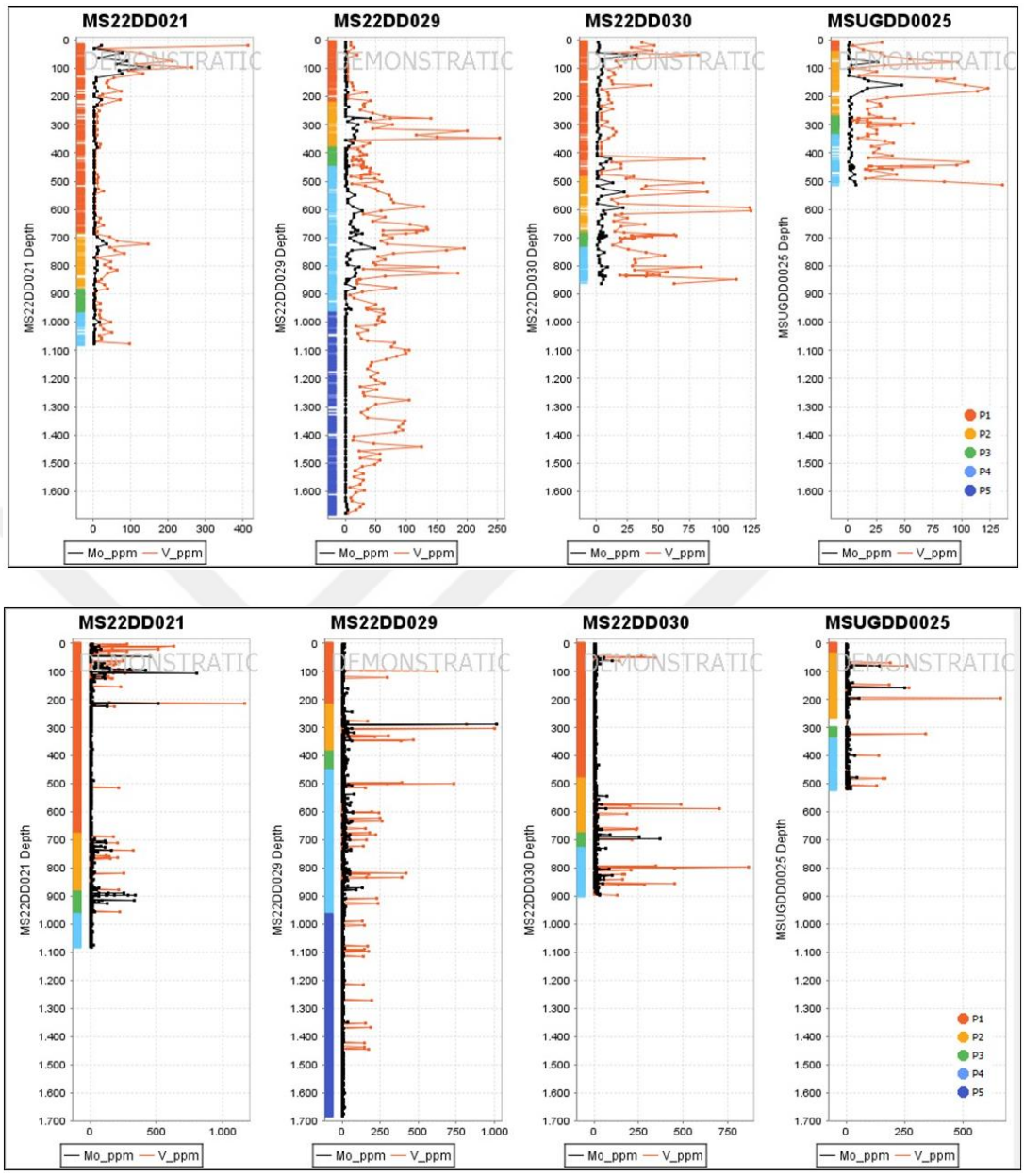


Figure 4.7. Downhole plots showing pXRF readings (below) and lithogeochemical analysis results (above) for Mo and V (in ppm) in all drill holes

Although transition element and metals/ metalloids are generally below the detection limit, the highest concentration of As, Cd, Pb and Zn are observed through all drill holes in the mostly package 3 and rarely package 4 (Figure 4.8). These elements indicate relatively enrichment especially at the package 3 and correlate with assay results.

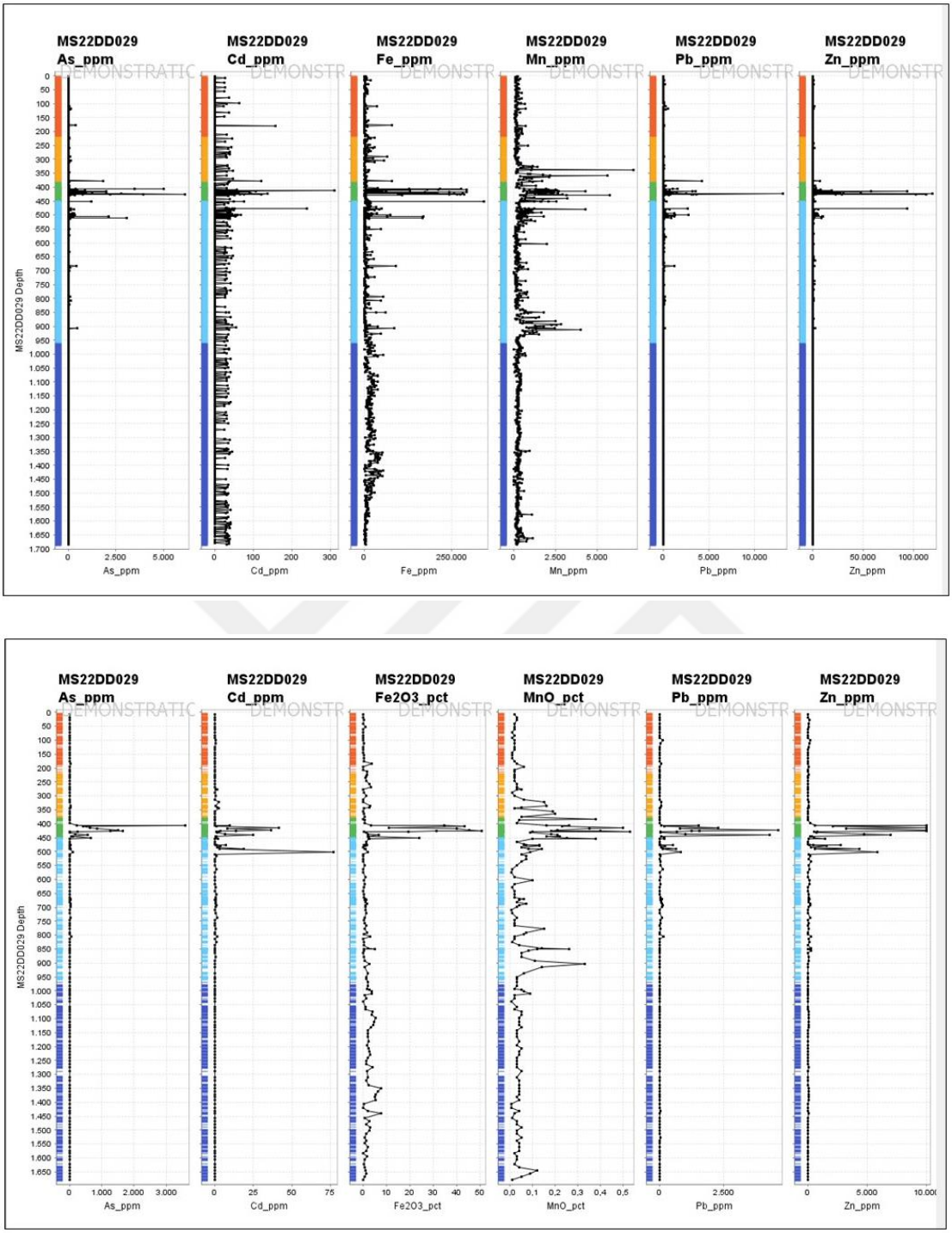


Figure 4.8. Downhole plots showing pXRF readings (above) and lithogeochemical analysis results (below) for As, Cd, Fe, Mn, Pb, and Zn in all drill holes

The fundamental differences between the different lithologies can cause incorrect interpretation while measuring each element that fall outside the common range. At

the same time, pXRF are measuring the single point, not the entire interval. Therefore, this type error is so expectable.

CHAPTER 5

CONCLUSION

Meskan Zn-Pb deposit that is located at Hakkari, SE of Türkiye, has been identified carbonate±silt dominated different lithostratigraphic units. The sulfide mineralization of Meskan deposit is characterized by mostly very fine to medium-grained pyrite dominated, marcasite, sphalerite, and galena. Mineralized units also include renierite, marcasite, strontianite, carlinite, hemimorphite, celestine, germanite, boulangerite, semseyite. Textures of mineralization mostly consists of massive, disseminated, interbeds and banded zebra texture, brecciated, and colloform banding. Besides them, nice recrystallization textures with cataclastic deformation, and framboidal pyrite is observed in the thin and polished sections. The thickness of sulfide ore mineralization ranges from 0.5 to 8 m.

Mineralization shows characteristics of Irish-type deposits, in the broad sense, in terms of basin setting, lithostratigraphy, and mineralization style and deposition. Although the Irish type of model is based on the deposits of the central midlands of Ireland, it includes a range of deposits settings and styles, all characterized by mineralization that is dominantly replacive rather than open-space fill, typically with strong direct structural control, and that formed during basin extension or inversion. Irish type deposits are typically preferentially hosted by clean, often micritic, limestone that may be reduced and is usually dolomitized. Dolomitization associated with mineralization is generally ferroan and there is a common association with hydrothermal dolomitic rock-matrix breccias, termed black-matrix breccias.

The characteristics of Irish type deposits commonly hosted on the hanging wall of normal fault zones, frequently overlying transtensional basement shear zones. Host rocks, more permeable than other lithologies in the sequence, are typically the first major clean carbonate unit in the sequence. Faults are syn-depositionally active

during late rifting and these faults control margins of intra-platform basins, marked by significant carbonate facies thickness variations. This type deposits comprise single or multiple stacked lenses; are stratabound and display generally stratiform morphologies. Mineralogically they are relatively comprising sphalerite, galena, Fe sulfides, barite in a gangue of calcite, dolomite, and silica. Meskan Zn-Pb deposit have most of these features however some other properties have not known yet.

The content of SiO_2 (0.01– 71.92 %, avg = 7.58 %), Al_2O_3 (0.01– 18.36 %, avg= 1.71 %), Fe_2O_3 (0.02– 51.75 %, avg= 3.09 %), CaO (1.38-55.35 %, avg= 35.15 %), and MgO (0.02-21.58 %, avg= 9.93) between the analyzed samples (n= 439) is variable. Generally, the CaO and MgO content of all the samples is the highest, followed by SiO_2, Fe_2O_3 and Al_2O_3 whereas the Na_2O, K_2O, TiO_2, P_2O_5, MnO and Cr_2O_3 contents are relatively low with respect to other major elements (Table 3.2). MgO is relatively enriched in package 1 (avg= 19.62 %, n= 125). In addition, the SiO_2, Al_2O_3, K_2O, TiO_2, P_2O_5, and Cr_2O_3 values suddenly increase from package 1-2 and package 4-5. At the same time, SiO_2 is relatively enriched in package 5 (avg= 21.74 %, n= 63). The enrichment of SiO_2, Al_2O_3, TiO_2, and K_2O in these samples comes from terrigenous origins, and rich in terms of silt amount. Moreover, the transition between package 3 and package 4 is detected by their low content of Fe_2O_3, MnO, and TOT/ S values.

The depletion of MgO in the ore zone (P3) with respect to other packages might indicate that the host rock lithology of package 3 is mostly limestone rather than dolostone. Irish type deposits are generally enriched in Ag, As, Cd, Cu, Co, Ni and MVT deposits are enriched in Ag, Cd, Cu, Co, Ge, Ga, Ni, Sb whereas SEDEX-type deposits are enriched in As, Bi, Cd, Cu, Ge, Hg, Ni, Se, Sb, Tl. (Wilkinson, 2014). The meaningful correlation in the study between As, Cd, Fe, Mn, Sb, Pb, Tl, and Zn may indicate substitution of these elements in the structure of pyrite, sphalerite, galena, which give the most important geochemical anomalous patterns. The ore zone is relatively depleted in Ag, Cu, Co, and Ni with respect to other packages (Table 5.1). This suggest that metals come from continental crust. According to Hanilçi and others (2020) studies about Pb isotope and trace element correlations

between sulfide and non-sulfide ore show that As, Hg, Tl, Mn, and Sb indicate fluids are circulating in continental crust, and those fluids are also the source of metals.

In general, the highest concentrations of Zn and Pb are up to > 1 wt.% and occur at the mostly package 3 and rarely package 4 within hydrothermally mineralized-dolomitized carbonates. The sulfide mineralization occurs purest or most clean limestones, which are the shallow siliciclastic-deficient component.

HFSE, including Ti, Cr, Zr, Nb, Hf, Ta, and highly charged cations, that are Sc, V, Mo, W are associated with detrital heavy mineral grains or clastic input. The increasing of clastic input is also demonstrated with positive trend of Al_2O_3, TiO_2, and K_2O. These positive anomalies of HFSEs are generally affected by weathering and oxidation. High correlation in terms of HFSE may imply that these carbonates are mostly pure and depleted in silt amount.

In terms of LILE, Ba and Sr positively correlate with each other. Although, Rb and Cs values are correlated with stratigraphy in all packages except P3, the correlation with lithology is not certainly defined. Strongly positive Cs anomalies is hydrothermal, and correlated with sulfide mineralization. Unmineralized zebra texture limestones are depleted in Cs, but enriched in terms of MgO with respect to other mineralized samples in package 3.

Table 5.1. Suite of elements showing enrichment in each of the MVT, SEDEX, and Irish-type deposits, and in the Meskan deposit (average data for various deposit types from Wilkinson, 2014).

Deposit type	**Enriched elements**
MVT	Ag, Cd, Cu, Co, Ge, Ga, Ni, Sb
SEDEX	As, Bi, Cd, Cu, Ge, Hg, Ni, Se, Sb, Tl
Irish type	Ag, As, Cd, Cu, Co, Ni
Meskan	As,Ba, Cd, Fe,Ge, Mn, Sb, Pb, Tl, Zn

Meskan lithogeochemical samples are relatively enriched in LREE relative to HREE on chondrite normalized diagram. According to REE+ Y values for package 2 (n= 72), package 3 (n= 65), and package 4 (n= 114) samples, the lithological units REE (∑REE+ Y) concentration in dolostone average is 13.14 ppm (n= 43); in dolostone±low silt average 39.78 ppm (n = 21); in dolostone±high silt average 121.03 ppm (n= 20); in limestone 9.81 ppm (n= 110); in limestone±low silt 22.16 ppm (n= 31), while the average of ∑REE+ Y is 29.69 ppm in limestone±high silt (n = 26).

The carbonates of Meskan deposit show Ce and Eu anomalies. Ce anomalies are generally less than 1. The variations in Ce anomalies in package 3 is controlled by the silt input. The high content of Ce suggest that these carbonates are deposited under package 5 and package 2, that are rich in clastic input.

The relatively increasing of Eu/ Eu* values with respect to other packages are marker for high temperature hydrothermal environment in package 3. The highest Eu/ Eu* values are detected in unmineralized zebra texture sulfide mineralization zone.

REFERENCES

Ahrens, L. H. (1953). The use of ionization potentials. Part 2. Anion affinity and geochemistry. *Geochimica et Cosmochimica Acta*, *3*(1), 1–29.

Alibo, D. S., & Nozaki, Y. (1999). Rare earth elements in seawater: Particle association, shale-normalization, and Ce oxidation. *Geochimica et Cosmochimica Acta*, *63*, 363–372.

Alsharhan, A.S. and C.G.S. Kendal 1986. Precambrian to Jurassic Rocks of Arabian Gulf and Adjacent Areas: Their Facies, Depositional Setting and Hydrocarbon Habitat. The American Association of Petroleum Geologists Bulletin, v. 70, p. 977-1002.

Anderson, I. K., Ashton, J. H., Boyce, A. J., Fallick, A. E., & Russell, M. J. (1998). Ore depositional processes in the Navan Zn + Pb deposit, Ireland. Economic Geology, 93, 535–563.

Andrew, C. J. (1992). Basin development chronology in the lowermost Carboniferous strata in the Irish North-central Midlands. In A. A. Bowden, G. Earls, P. G. O'Connor, & J. F. Pyne (Eds.), *The Irish Minerals Industry 1980-1990* (pp. 143–169). Dublin, Irish Association for Economic Geology.

Ashton, J. H., Black, A., Geraghty, J., Holdstock, M., & Hyland, E. (1992). The geological setting and metal distribution patterns of the Zn-Pb-Fe mineralization in the Navan Boulder Conglomerate. In A. A. Bowden, G. Earls, P. G. O'Connor, & J. F. Pyne (Eds.), *The Irish Minerals Industry 1980-1990* (pp. 171–210). Dublin, Irish Association for Economic Geology.

Batley, G.E. (1998). Elements: Metalloids . In: Geochemistry. Encyclopedia of Earth Science. Springer, Dordrecht. https://doi.org/10.1007/1-4020-4496-8_106

Bau, M. (1991). Rare-earth element mobility during hydrothermal and metamorphic fluid-rock interaction and the significance of the oxidation state of europium. *Chemical Geology, 93*(3–4), 219–230. doi:10.1016/0009-2541(91)90115-8

Bau, M., & Möller, P. (1992). Rare Earth Element Fractionation in Metamorphogenic Hydrothermal Calcite, Magnesite and Siderite. Hahn-Meitner-Institut Berlin, Federal Republic of Germany.

Bau, M., & Dulski, P. (1996). Distribution of yttrium and rare-earth elements in the Penge and Kuruman iron-formations, Transvaal Supergroup, South Africa. Precambrian Research, 79, 37–55.

Bau, M., & Alexander, B. (2006). Preservation of primary REE patterns without Ce anomaly during dolomitization of Mid-Paleoproterozoic limestone and the potential re-establishment of marine anoxia immediately after the "Great Oxidation Event." *South African Journal of Geology, 109*, 81–86.

Blakeman, R., Ashton, J. H., Boyce, A. J., Fallick, A. E., & Russell, M. J. (2002). Timing of interplay between hydrothermal and surface fluids in the Navan Zn+Pb orebody, Ireland: Evidence from metal distribution trends, mineral textures and δ34S analyses. Economic Geology, 97, 73–91.

Boyce, A. J., Little, C. T. S., & Russell, M. J. (2003). A new fossil vent biota in the Ballynoe barite deposit, Silvermines, Ireland: Evidence for intracratonic sea-floor hydrothermal activity about 352 Ma. Economic Geology, 98, 649–656.

Carboni, V., Walsh, J. J., Stewart, D. R. A., & Güven, J. F. (2003). Timing and geometry of normal faults and associated structures at the Lisheen Zn-Pb deposit, Ireland - investigating their role in the transport and the trapping of metals. In D. G. Eliopoulos et al. (Eds.), *Proceedings of the 7th Biennial SGA Meeting - Mineral Exploration and Sustainable Development* (pp. 665–668). Millpress Science Publishers, Rotterdam.

Caulfield, J. B. D., LeHuray, A. P., & Rye, D. M. (1986). A review of lead and sulfur isotope investigations of Irish sediment-hosted base metal deposits with new

data from the Keel, Ballinalack, Moyvoughly and Tatestown deposits. In C. J. Andrew, R. W. A. Crowe, S. Finlay, W. M. Pennell, & J. Pyne (Eds.) Geology and Genesis of Mineral Deposits in Ireland (pp. 591–615). Dublin: Irish Association for Economic Geology.

Ceyhan, N. (2003). Lead isotope geochemistry of Pb-Zn deposits from Eastern Taurides, Türkiye. Unpublished master's thesis. Graduate School of Natural and Applied Sciences, Middle East Technical University, Ankara, Türkiye.

De Baar, H. J. W., Schijf, J., & Byrne, R. H. (1991). Solution chemistry of the rare earth elements in seawater. *European Journal of Solid State and Inorganic Chemistry*, *28*, 357–373.

Dilek, Y., & Delaloye, M. (1992). Structure of the Kızıldağ ophiolite, a slow spread Cretaceous ridge segment north of the Arabian promontory. Geology, 20, 19–22. https://doi.org/10.1130/00917613 (1992)

Dunham J.B.; Larter S. (1981). "Association of Stylolitic Carbonates and Organic Matter: Implications for Temperature Control on Stylolite Formation". AAPG Bulletin. 65.

Elmas, A. (1992). Erçek Gölü (Van) dolayının jeoloji incelemesi [Geological study of the Erçek Lake (Van) region]: Unpublished doctoral dissertation, University of Istanbul, 372 pages.

Elmas, A., & Yılmaz, Y. (2003). Development of an oblique subduction zone—tectonic evolution of the Tethys Suture Zone in southeast Türkiye. *International Geology Review, 45*(9), 827–840. https://doi.org/10.2747/0020-6814.45.9.827

Elmas. (1996). The Late Oligocene nappe emplacement in the Southeast Anatolian orogenic belt. *Turkish Journal of Earth Sciences, 5*, 89–98.

Erdogan, B. (1977). Geology, geochemistry, and genesis of the sulfide deposits of Ergani-Maden region, SE Türkiye [Geology, geochemistry, and genesis of

the sulfide deposits of the Ergani-Maden region, SE Türkiye]: Unpublished doctoral dissertation, University of New Brunswick, 288 pages.

Fallick, A. E., Ashton, J. H., Boyce, A. J., Ellam, R. M., & Russell, M. J. (2001). Bacteria were responsible for the magnitude of the world-class hydrothermal base metal sulfide orebody at Navan, Ireland. Economic Geology, 96, 885–890.

Feely, M., Coleman, D., Baxter, S., & Miller, B. (2004). U-Pb zircon geochronology of the Galway Granite, Connemara, Ireland: implications for the timing of late Caledonian tectonic and magmatic events and for correlations with Acadian plutonism in New England. *Atlantic Geology, 39*, 175–184.

Fontaine, J. M. (1981). La Plate-forme Arabe et sa marge passive au Mésozoïque. L'exemple D'Hazro (SE Turkey): A. L'Université de Paris-sud., Thèse, 211 p.

Fontboté, L., & Boni, M. (1994). Sediment-Hosted Zinc-Lead Ores — An Introduction. In Special Publication of the Society for Geology Applied to Mineral Deposits (MINERAL DEPOS., volume 10).

Fusciardi, L. P., Güven, J. F., Stewart, D. R. A., Carboni, V., & Walshe, J. J. (2003). The geology and genesis of the Lisheen Zn-Pb deposit, Co. Tipperary, Ireland. In J. G. Kelly et al. (Eds.), *Europe's Major Base Metal Deposits* (pp. 455–481). Dublin, Irish Association for Economic Geology.

Goodfellow, W. D., Lydon, J. W., & Turner, R. J. W. (1993). Geology and genesis of stratiform sediment-hosted (SEDEX) zinc-lead-silver sulphide deposits. In R. V. Kirkham, W. D. Sinclair, R. I. Thorpe, & J. M. Duke (Eds.), *Mineral Deposit Modeling* (pp. 201–251). Geological Association of Canada Special Paper 40. Ottawa, ON: Geological Association of Canada.

Göncüoğlu, M.C., Kozlu, H., Dirik, K., (1997). Pre- Alpine and Alpine terranes in Turkey: explanatory notes to the terrane map of Turkey. Annales Géologiques des Pays Helleniques, 37, 515-536.

Göncüoğlu, M. C., & Kozlu, H. (2000). Early Paleozoic evolution of the NW Gondwanaland: Data from southern Türkiye and surrounding regions. *Gondwana Research, 3*(3), 315–324. 937x(05)70290-2

Hanilçi, N., & Öztürk, H. (2008). Hakkari region Zn-Pb deposits: preliminary evidence for their geological features and formation. In H. Öztürk, N. Hanilçi, A. Kahriman, & Ş. G. Özkan (Eds.), *Proceedings symposium on geology and mining of Pb-Zn deposits of Türkiye* (pp. 244–264). Istanbul University, Istanbul.

Hanilçi, N., Öztürk, H., & Kasapçı, C. (2019). Carbonate-hosted Pb-Zn deposits of Türkiye. In F. Pirajno, C. Dönmez, & M. B. Şahin (Eds.), *Mineral Resources of Türkiye, Modern Approaches in Solid Earth Sciences* (pp. 497–533). Springer Nature, Switzerland.

Hanilçi, N., Öztürk, H., & Banks, D. (2020). Geological, geochemical and microthermometric characteristics of the Hakkari region Zn-Pb deposits, SE Turkey.

Hitzman, M. W., Redmond, P. B., & Beaty, D. W. (2002). The carbonate-hosted Lisheen Zn–Pb–Ag deposit, County Tipperary, Ireland. *Economic Geology, 97*, 1627–1655.

Hitzman, M. W., & Beaty, D. W. (1996). The Irish Zn-Pb-(Ba) orefield. In D. F. Sangster (Ed.), Carbonate-Hosted Lead-Zinc Deposits, Society of Economic Geologists Special Publication 4 (pp. 112–143). Littleton, CO: Society of Economic Geologists, Inc.

Hitzman, M. W., O'Connor, P., Shearley, E., Schaffalitzky, C., Beaty, D. W., Allan, J. R., & Thompson, T. B. (1992). Discovery and geology of the Lisheen Zn–Pb–Ag prospect, Rathdowney Trend, Ireland. In A. A. Bowden, G. Earls, P. G. O'Connor, & J. F. Pyne (Eds.), *The Irish Mineral Industry* (pp. 227–246). Dublin: Irish Association for Economic Geology.

Holland, C. H., & Sanders, I. (2009). *The Geology of Ireland*. Dunedin Academic Press.

Johnson, A. W., Shelton, K. L., Gregg, J. M., Somerville, I. D., Wright, W. R., & Nagy, Z. R. (2009). Regional studies of dolomites and their included fluids: Recognizing multiple chemically distinct fluids during the complex diagenetic history of Lower Carboniferous (Mississippian) rocks of the Irish Zn-Pb ore field. Mineralogy and Petrology, 96, 1–18.

Kamber, B. S., & Webb, G. E. (2001). The geochemistry of late Archaean microbial carbonate: implications for ocean chemistry and continental erosion history. *Geochimica et Cosmochimica Acta, 65,* 2509–2525.

Karakaya Co. (2015). The ore zones of Karakaya Pb-Zn deposits and Ore Potential (Unpublished report, p. 25). August 2015.

Kesler, S. E., & Reich, M. (2006). Precambrian Mississippi Valley-type deposits: Relation to changes in the atmosphere and hydrosphere. In S. E. Kesler & H. Ohmoto (Eds.), *Evolution of Early Earth's Atmosphere, Hydrosphere, and Biosphere – Constraints from Ore Deposits* (pp. 185–204). Geological Society of America Memoirs 198. Boulder, CO: Geological Society of America.

Ketin, İ. (1966). Tectonic units of Anatolia. *Maden Tetkik ve Arama Bulletin, 66,* 23–34.

Kennan, P. S., Phillips, W. E., & Strogen, P. (1979). Pre-Caledonian basement to the paratectonic Caledonides in Ireland. *Geological Society, London, Special Publications, 8*(1), 157–161. https://doi.org/10.1144/gsl.sp.1979.008.01.15

Köylüoğlu, M. (1986). Güneydoğu Anadolu otokton birimlerinin kronostratigrafisi, mikrofasiyes ve mikrofosilleri [Chronostratigraphy, microfacies, and microfossils of the Southeast Anatolian autochthonous units]. Turkiye Petrolleri Anonim Ortakligi, Araştırma Eğitim Yayınları no. 9.

Large, D. E. (1983). Sediment-hosted massive sulphide lead-zinc deposits: An empirical model. In D. F. Sangster (Ed.), *Sediment-Hosted Stratiform Lead-Zinc Deposits* (pp. 1–29). Mineralogical Association of Canada Short Course Series, vol. 9. Quebec: Mineralogical Association of Canada.

Large, R. R., Bull, S. W., Cooke, D. R., & McGoldrick, P. J. (1998). A genetic model for the HYC deposit, Australia: Based on regional sedimentology, geochemistry, and sulfide-sediment relationships. *Economic Geology, 93*, 1345–1368.

Large, R. R., Bull, S. W., McGoldrick, P. J., Walters, S., Derrick, G. M., & Carr, G. R. (2005). Stratiform and stratabound Zn-Pb-Ag deposits in Proterozoic sedimentary basins, northern Australia. In J. W. Hedenquist, J. F. H. Thompson, R. J. Goldfarb, & J. P. Richards (Eds.), *Economic Geology 100th Anniversary Volume, 1905–2005* (pp. 931–963). Littleton, CO: Society of Economic Geologists, Inc.

Leach, D. L., Bradley, D., Lewchuk, M. T., Symons, D. T. A., de Marsily, G., & Brannon, J. (2001). Mississippi Valley-type lead-zinc deposits through geological time: Implications from recent age-dating research. *Mineralium Deposita, 36*, 711–740.

Leach, D. L., Bradley, D., Lewchuk, M., et al. (2002). Reply to Discussion on "Mississippi Valley-type lead–zinc deposits through geological time: implications from recent age-dating research" by S.E. Kesler and C.W. Carrigan (2001). *Mineralium Deposita, 37,* 803–805.

Leach, D. L., & Sangster, D. F. (1993). Mississippi Valley-type lead-zinc deposits. In R. V. Kirkham, W. D. Sinclair, R. I. Thorpe, & J. M. Duke (Eds.), *Mineral Deposit Modeling* (pp. 289–314). Geological Association of Canada Special Paper 40. Ottawa, ON: Geological Association of Canada.

Leach, D. L., Sangster, D. F., Kelley, K. D., et al. (2005). Sediment-hosted lead-zinc deposits: A global perspective. In J. W. Hedenquist, J. F. H. Thompson, R. J.

Goldfarb, & J. P. Richards (Eds.), *Economic Geology 100th Anniversary Volume, 1905–2005* (pp. 561–607). Littleton, CO: Society of Economic Geologists, Inc.

Leach, D. L., Taylor, R. D., Fey, D. L., Diehl, S. F., & Saltus, R. W. (2010). A deposit model for Mississippi Valley-type lead-zinc ores: Chapter A of mineral deposit models for resource assessment. US Geological Survey Scientific Investigations Report 2010–5070–A. Reston, VA: US Geological Survey.

Leigh, G. J. (2011). Principles of Chemical Nomenclature: A guide to IUPAC recommendations. Royal Society of Chemistry

Liu, Y. G., Miah, M. R. U., & Schmitt, R. A. (1988). Cerium, a chemical tracer for paleo-oceanic redox conditions. *Geochimica et Cosmochimica Acta, 52*, 1361–1371.

Lydon, J. W. (2004). Genetic models for Sullivan and other SEDEX deposits. In M. Deb & W. D. Goodfellow (Eds.), *Sediment-Hosted Lead-Zinc Sulphide Deposits: Attributes and Models of Some Major Deposits in India, Australia and Canada* (pp. 149–190). Delhi: Narosa Publishing House.

Macheyeki, A. S., Li, X., Kafumu, D. P., & Yuan, F. (2020). Chapter 1 - Elements of exploration geochemistry. In A. S. Macheyeki, X. Li, D. P. Kafumu, & F. Yuan (Eds.), Applied Geochemistry (pp. 1-43). Elsevier. https://doi.org/10.1016/B978-0-12-819495-9.00001-3

Masuzawa, T., & Koyama, M. (1989). Settling particles with positive Ce anomalies from the Japan Sea. *Geophysical Research Letters, 16,* 503–506.

McCarthy, I. A. J. (1995). Devonian and Carboniferous successions of the Munster and South Munster basins, southern Ireland. In K. Anderson, J. Ashton, G. Earls, M. Hitzman, & S. Tear (Eds.), *Irish Carbonate-hosted Zn-Pb Deposits* (Guidebook Series, v.21, pp. 95–102). Society of Economic Geology.

Moix, P., Beccaletto, L., Kozur, H. W., Hochard, C., Rosselet, F., & Stampfli, G. M. (2008). A new classification of the Turkish terranes and sutures and its implication for the paleotectonic history of the region. *Tectonophysics*, *451*(1–4), 7–39.

Morrow, D. W. (1982). Descriptive field classification of sedimentary and diagenetic breccia fabrics in carbonate rocks.

Muntyan, B. L. (1999). Colorado Sphalerite. Rocks & Minerals, 74(4), 220–235. doi:10.1080/00357529909602545

Murray, R. W., Buchholtz, M. R., & Brumsack, H. J. (1991). Rare earth elements in Japan Sea sediments and diagenetic behavior of Ce/Ce*, results from ODP leg 127. *Geochimica et Cosmochimica Acta, 55*, 2453–2466.

Nath, B. N., Bau, M., Ramalingeswara, R. B., & Rao, C. M. (1997). Trace and rare earth elemental variation in Arabian Sea sediments through a transect across the oxygen minimum zone. *Geochimica et Cosmochimica Acta, 61*, 2375–2388.

Okay, A. I. (2008). Geology of Türkiye: A synopsis. *Anschnitt, 21*, 19–42.

Okay, A. I., & Tüysüz, O. (1999). Tethyan sutures of northern Türkiye Major continental blocks of Türkiye. *The Mediterranean Basins: Tertiary Extension within the Alpine Orogen*, 475–515.

O'Connor, P. J., Aftalion, M., & Kennan, P. S. (1989). Isotopic U–Pb ages of zircon and monazite from the Leinster Granite, southeast Ireland. *Geological Magazine, 126*, 725–728.

Palmer, M. R. (1985). Rare earth elements in foraminifera tests. *Earth and Planetary Science Letters, 73*, 285–298.

Palmer, M. R. (1985). Rare earth elements in foraminifera tests. Earth and Planetary Science Letters, 73, 285–298.

Perinçek, D. 1990. Hakkari ili dolayinin stratigrafisi, Guneydogu Anadolu, Turkey: TPJD Bull.,v.2,.no.1, s.21-68.

Perinçek, D., Duran, O., Bozdoğan, N., & Çoruh, T. (1992). Stratigraphy and paleogeographical evolution of the autochthonous sedimentary rocks in Southeast Turkey. In Paleogeographic Evolution of the Northern Arabian Plate.

Phillips, W. E. A., & Sevastopulo, G. D. (1986). The stratigraphic and structural setting of Irish mineral deposits. In C. J. Andrew, R. W. A. Crowe, S. Finlay, W. M. Pennell, & J. F. Pyne (Eds.), Geology and Genesis of Mineral Deposits in Ireland (pp. 1–30). Dublin: Irish Association for Economic Geology.

Reynolds, N. R. (2010). Assessment of Hakkari Projects, Hakkari, Türkiye. Unpublished CSA Global Report No. R238.2010 to Meskan Ölmez Madencilik.

Robertson, A. H. F., & Dixon, J. E. (1984). Introduction: aspects of the geological evolution of the Eastern Mediterranean. In J. E. Dixon & A. H. F. Robertson (Eds.), The Geological Evolution of the Eastern Mediterranean (Geological Society of London Special Publication, 17, pp. 1–74).

Robertson, A. H., Parlak, O., Rízaoğlu, T., Ünlügenç, İnan, N., Tasli, K., & Ustaömer, T. (2007). Tectonic evolution of the South Tethyan Ocean: Evidence from the Eastern Taurus Mountains (Elaziğ region, SE Turkey). Geological Society, London, Special Publications, 272(1), 231–270. https://doi.org/10.1144/gsl.sp.2007.272.01.14.

Rollinson, H. R. (1993). *Using Geochemical Data: Evaluation, Presentation and Interpretation*. Taylor and Francis.

Santoro, L., Boni, M., Herrington, R., Cleeg, A., 2013. The Hakkari nonsulfide Zn–Pb deposit in the context of other nonsulfide Zn–Pb deposits in the Tethyan Metallogenic Belt of Turkey. Ore Geol. Rev. 53, 244–260.

Santoro, L. (2015). The Jabali, Hakkari and Reef Ridge nonsulfide Zn (Pb) deposits: An evaluation by QEMSCAN® technology, and comparison to other analytical methods. PhD thesis.

Sholkovitz, E. R., Landing, W. M., & Lewis, B. L. (1994). Ocean particle chemistry: The fractionation of rare earth elements between suspended particles and seawater. *Geochimica et Cosmochimica Acta, 58*, 1567–1579.

Sinha, S. P. (1983). The Europium anomaly. In North Atlantic Treaty Organization Scientific Affairs Division (Ed.), *Systematics and the properties of the lanthanides* (pp. 550–553). ISBN 978-90-277-1613-2.

Strogen, P. (1974). The sub-Palaeozoic basement in central Ireland. *Nature, 250*, 562–563.

Şengör, A. M. C., & Yılmaz, Y. (1981). Tethyan evolution of Türkiye: A plate tectonic approach. *Tectonophysics, 75*(3–4).

Tang, M., McDonough, W. F., & Ash, R. A. (2017). Europium and strontium anomalies in the MORB source mantle. *Geochimica et Cosmochimica Acta, 197*, 132–141.

Tuna, D. (1973). VI. Bolge litostratigrafi birimleri adlamasinin aciklayici raporu [Explanatory report on the lithostratigraphic units of the VI. Region]. Turkiye Petrolleri Anonim Ortakligi, Rapor no. 813, 131 s.

Ünlügenç, U. C., & Akıncı, A. C. (2017). Kızıldere-Güveloğlu (Ceyhan-Adana) Civarının Tektono-Stratigrafisi [Tectono-Stratigraphy of the Kızıldere-Güveloğlu (Ceyhan-Adana).

Yılmaz, Y. (1993). New evidence and model on the evolution of Southeast Anatolia orogen. *Geological Society of America Bulletin, 105*, 251–271.

Yılmaz, Y. (2019). Southeast Anatolian orogenic belt revisited (geology and evolution). *Canadian Journal of Earth Sciences, 56*(11), 1163–1180. doi:10.1139/cjes-2018-0170.

Yıldırım, M., & Yılmaz, Y. (1991). Güneydoğu Anadolu Orojenik Kuşağının Ekaylı Zonu [The sliced zone of the Southeast Anatolian Orogenic Belt]. *TPJD Bülteni, 3*, 57–73.

Yılmaz, Y., Yiğitbaş, E., & Genç, C. (1993). Ophiolitic and metamorphic assemblages of Southeast Anatolia and their significance in the geological evolution of the Orogenic Belt. *Tectonics, 12*(5), 1280–1297.

Yılmaz, Y., & Gürer, Ö. F. (1996). The geology and evaluation of Misis-Andırın Belt, Aroun Andırın (Kahramanmaraş). Turkish Journal of Earth Sciences, 5(3), 39-55.

Yılmaz, Y., Yiğitbaş, E., & Çemen, İ. (2022). Tectonics of the Southeast Anatolian orogenic belt [Preprint]. doi:10.1002/essoar.10510308.1.

Yiğitbas, E., & Yılmaz, Y. (1996a). New evidence and solution to the Maden complex controversy of the Southeast Anatolian orogenic belt (Türkiye). *Geologische Rundschau, 85*, 250–263.

Yiğitbas, E., & Yılmaz, Y. (1996b). Post-Late Cretaceous strike-slip tectonics and its implications for the Southeast Anatolian orogen, Türkiye. *International Geology Review, 38*, 818–831.

Yiğit, O. (2009). Mineral Deposits of Türkiye in relation to Tethyan Metallogeny: Implications for future mineral exploration. *Economic Geology, 104*, 19–51.

Wang, Z. F., Huang, K. K., Zhang, D. J., & You, L. (2017). Maturation of Neogene dolomite from Xuande Atoll of Xisha archipelago, the South China Sea. *Journal of Sedimentary Research*.

Wang, Z., Li, Y., Wei, G., Zhou, Y., & Wang, P. (2017). Rare earth element and yttrium (REY) geochemistry of Cenozoic carbonates on the Xuande Atoll of the Xisha Archipelago, the South China Sea: Implications of the impact of dolomitization on REY. *Geochemistry, Geophysics, Geosystems, 18*(11), 4149-4167.

Wilkinson, J. J., & Lee, M. J. (2003). Cementation, hydrothermal alteration, and Zn–Pb mineralization of carbonate breccias in the Irish Midlands: Textural evidence from the Cooleen Zone, near Silvermines, County Tipperary — A reply. *Economic Geology*, *98*, 194–198.

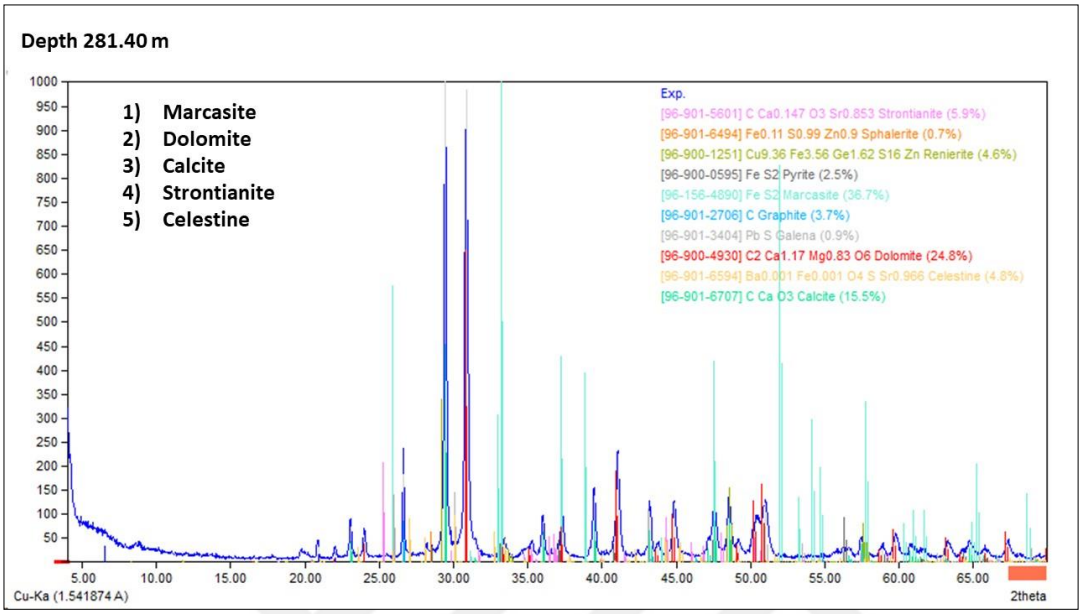
Wilkinson, J. J., Eyre, S. L., & Boyce, A. J. (2005a). Ore-forming processes in Irish-type carbonate-hosted Zn-Pb deposits: Evidence from mineralogy, chemistry and isotopic composition of sulfides at the Lisheen Mine. Economic Geology, 100, 63–86.

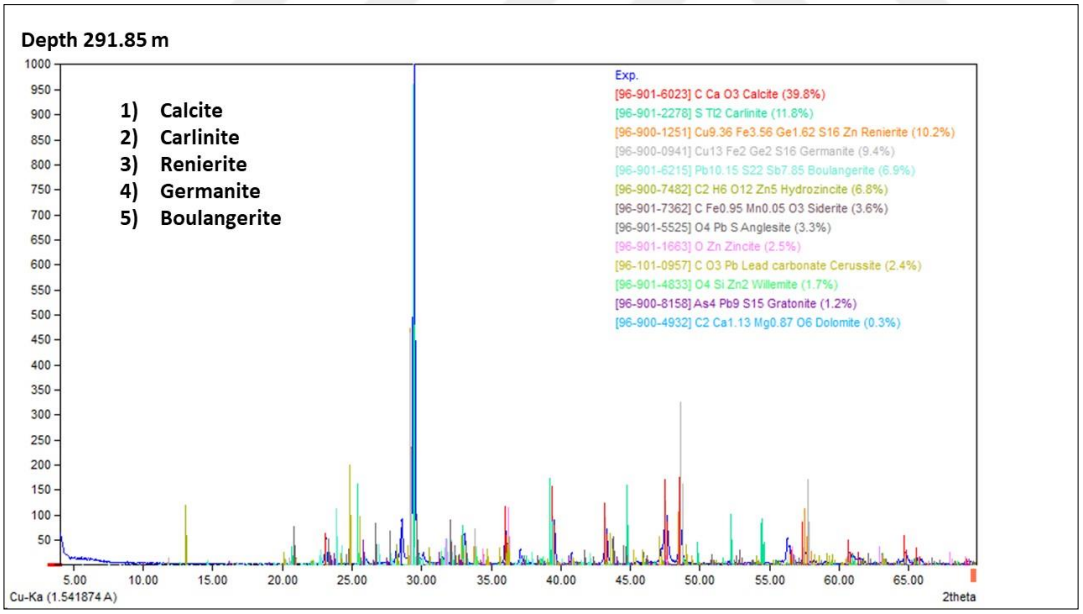
Wilkinson, J. J., (2014). Sediment- Hosted Zinc- Lead Mineralization: Processes and Perspectives, In Treatise on Geochemistry (Second Edition), edited by Heinrich D. Holland and Karl K. Turekian, Elsevier, Oxford, p. 219-249.

Wilkinson, J. J., & Hitzman, M. (2015). A new genetic model for mineralization in the Irish Zn-Pb orefield.

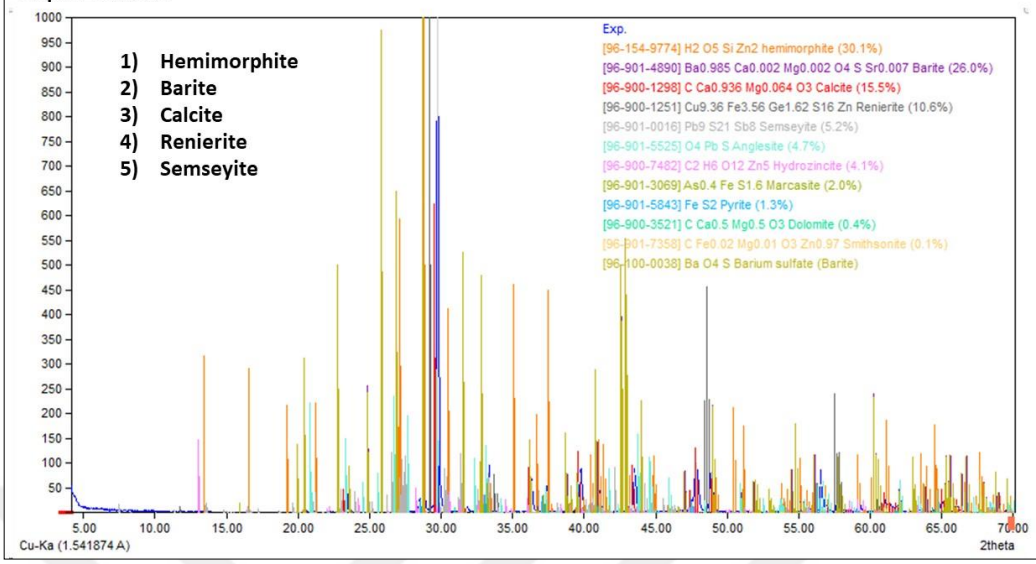
Wilkinson, J. J., & Redmond, P. B. (2010). Irish Zn-Pb: New insights, new discoveries. In Proceedings of the 13th Quadrennial IAGOD Symposium, Adelaide, Australia, 6-9 April 2010.

A. XRD Analysis Results

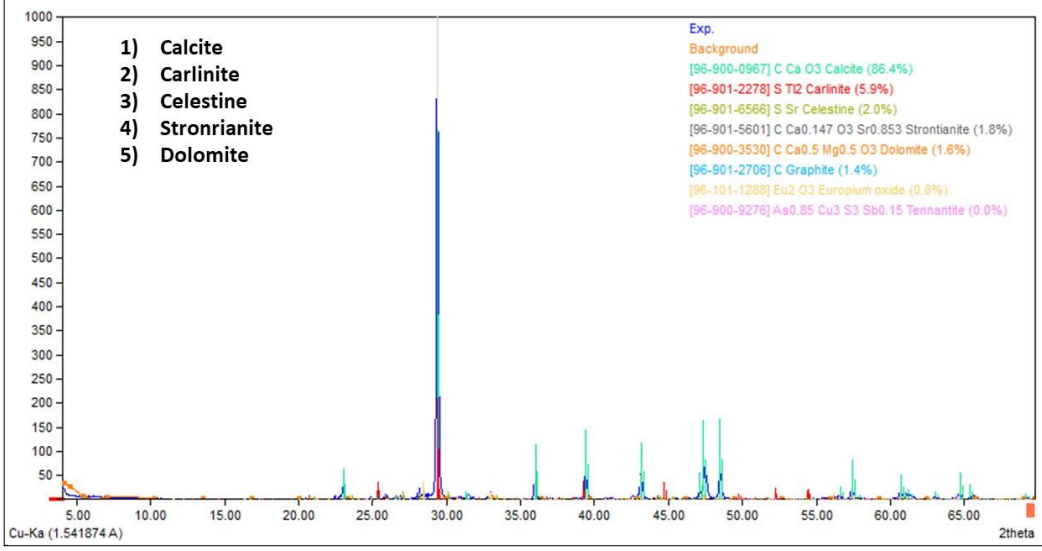




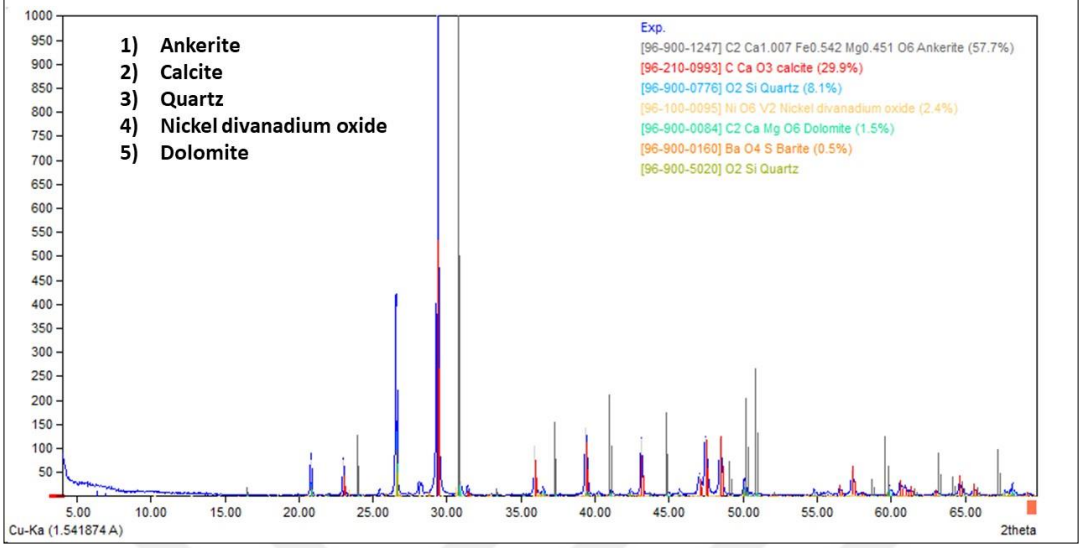
Depth 293.45 m



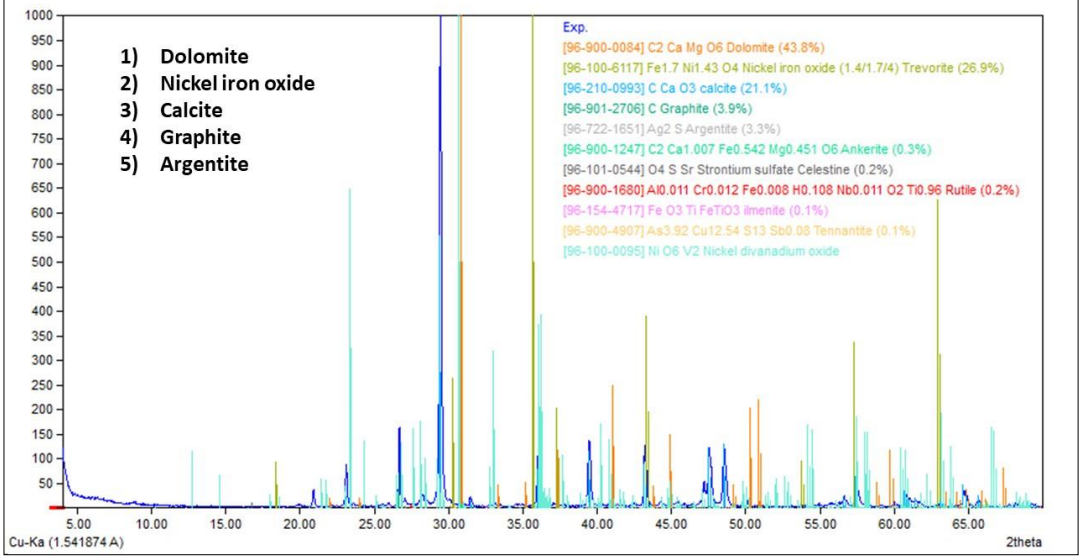
Depth 303.90 m



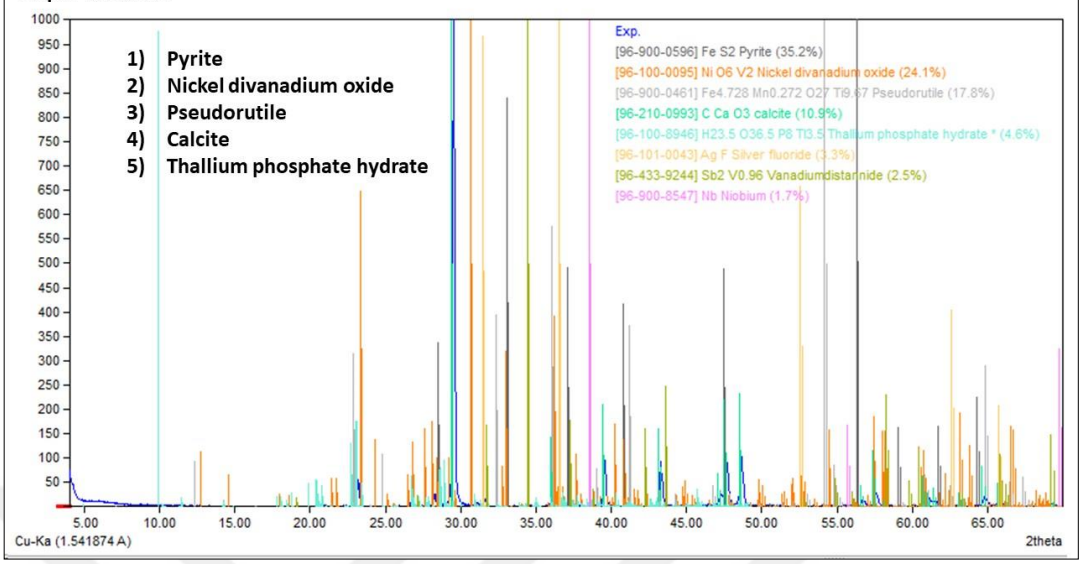
Depth 306.50 m



Depth 408.50 m



Depth 461.05 m



Depth 512 m

